University of Nottingham
UK | CHINA | MALAYSIA

Electronic Structure Methods for Large Molecular Systems and Materials in Strong Magnetic Fields

PhD Thesis, Submitted September 2022

Benjamin T. Speake

Supervised by Prof. Andrew M. Teale

School of Chemistry

University of Nottingham

Contents

Abstract

The high-rank polynomial scaling of modern electronic structure methods can present significant limitations on the size of molecular systems that can be accurately studied. This issue is further exasperated when using non-perturbative approaches for studying systems within arbitrary strength magnetic fields due to the requirements for complex algebra and reduced permutational symmetry. One such attempt at overcoming this issue is the concept of fragmentation, which has shown promise in recent years for accurately determining the electronic structure of systems that can be sensibly fragmented into smaller subunits. The main aim in this work is to combine the concepts of one such method, the embedding fragment method (EFM), with recent advances in non-perturbative treatment of external fields, enabling the study of increasingly large or complex systems. The implementation of this approach is presented for systems in strong magnetic fields. The method is applied to determine energetic, structural and magnetic response properties of systems beyond the scope of more conventional methods. The EFM is shown to provide an accurate electronic structure approximation when studying systems within extremely strong magnetic fields, with errors generally $< 0.001\%$ compared to conventional all electron methods, maintaining accuracy up to fields on the order of $\gtrsim$70000 Tesla. Its application to large water clusters is presented showing how external magnetic fields strengthen intermolecular interactions, as has previously been demonstrated through experiment, but that the origin of this strengthening is not as straightforward as the altering of the hydrogen bonding present at zero field, a rational often considered alongside experimental results. Also demonstrated is how this approach can be used to accurately model solvation effects when calculating magnetic properties of solute molecules. In this work the calculation of nuclear magnetic resonance chemical shifts is considered, using the EFM and comparing to both gas phase calculations and calculations including solvent effects using the polarisable continuum method. To aid in the interpretation of results, two additional tool sets have been development. The first is a suite of tools to analyse the complex current vector field induced by exposing a molecule to an external field. The second is a new molecular viewer software package, improving the ability to analyse the effects of external magnetic fields on molecular systems.

Benjamin T. Speake

January 13, 2023

Acknowledgements

Firstly, I thank Prof. Andy Teale for all his support and supervision over the past few years. His insights and mentorship have been invaluable in the development of this work and in my development as a researcher. Additionally, I would like to thank the entire Teale research group for their friendship and support. In particular, I will be forever grateful for the input, advise and friendship from both Dr. Tom Irons and Dr. Grégoire David.

I am also grateful for all the friends and colleagues I have made along the way, the entire computational chemistry department has always made life welcoming and fun whilst providing an incredibly useful network of support. Special mention has to go to Dr. Josh Baptiste and Dr. Abi Miller, I couldn't have asked for better housemates, you really helped me find a home over the past four years, especially whilst locked down during a global pandemic.

I'd like to thank the Royal Society, ERC and the University of Nottingham for the funding that made this project, and all the experiences that came with it possible.

Finally, I am especially grateful to my family, for all the love and support throughout my entire journey so far. You have always believed in me and without you, I couldn't have achieved all I have.

Publications

1. Irons T. J. P., David G., Speake B. T., Helgaker T., Teale A. M., 'Analysing Magnetically Induced Currents in Molecular Systems Using Current-Density-Functional Theory', *Journal of Physical Chemistry A*, **124**(7), 1321-1333, 2020.
2. Speake B. T., Irons T. J. P., Wibowo M., Johnson A. G., David G., Teale A. M., 'An Embedded Framgent Method for Molecules in Strong Magnetic Fields', *Journal of Chemical Theory and Computation*, **18**(12), 7412-7427, 2022.

1 Introduction and Background

The paradigm of modern chemistry is shifting away from the traditional laboratory based experiments. Although experimental based studies are still vital and will never be completely replaced, advances in computational methods and resources have enabled the more accurate modelling of an increasingly wide range chemical systems, enabling certain aspects chemical behaviour to be studied without the need for physical experiments. Even in cases where experiments are still required or desirable, computational modelling is often used to enhance the overall analysis and provide a more complete understanding of the chemistry taking place. Typically, computational modelling methods fall into two categories, those that only consider the classical interactions within a system, and those that also consider the quantum mechanical interactions. To truly understand the chemistry taking place, the quantum nature of the electrons and nuclei that make up the system must be considered, however, this is not straightforward except for the most simple systems. The field of electronic structure theory strives to provide methods to accurately model the quantum nature of the fundamental particles that make up a system, and control the chemistry it exhibits.

As theoretical methods and available computational resources have improved over time however, researchers have set their sights on modelling even more complex chemical systems, whether it be studying complex protein interactions, intermolecular interactions in liquids and large clusters or solid state chemistry involving periodicity. Therefore, one of the most important areas of research, within the development of electronic structure theories, is in the development of novel approaches to remove the restrictive high-rank polynomial computational scaling of the underlying fundamental methods.[1;2] Many approaches to overcoming the limitations on system size that can be studied have been developed; these include the introduction of approximations such as density fitting[3;4] or the chain-of-spheres approximation,[5] embedding methods in which certain parts of the system are treated with a higher level of theory embedded in a more approximate treatment for the rest of the system[6–8] and fragmentation approaches in which the system is treated as a set of smaller subsystems from which the results are combined, yielding a description of the whole system.[9;10] Such methods have become increasingly popular as the subsystem calculations are readily parallelisable whilst the limited size of each individual calculation allows higher level methods to be applied to the system,[11] and form much of the focus of this work.

In recent years, there has also been a growing interest in the behaviour of electronic systems in the presence of strong magnetic fields.[12–26] Much of this has been examining the effects of magnetic fields stronger than those accessible in the laboratory but which are found to exist for example, on the surface of white dwarf stars,[27;28] which has proven essential for identifying the spectra originating from these stellar objects.[29–31] The treatment of electronic structure within an external magnetic field is typically studied through perturbation theory, where the system can be assumed to be accurately approximated as the zero field case plus

a small perturbation. This approach however, breaks down as the electronic structure of the system begins to depend more heavily on the external field resulting in the zero field case no longer providing a suitable approximate solution. The study of much stronger field strengths therefore, requires a non-perturbative treatment of the external magnetic field, requiring new software packages to be developed which can efficiently perform this type of treatment.[32–36] The use of such methods has provided invaluable insight into the exotic chemistry that takes place in such environments, where the familiar chemistry observed at zero field, may no longer apply. Of particular note was the discovery of a new bonding regime whereby bonding within simple molecules shifts from typical covalent bonding to a paramagnetic bonding mechanism, generated by the stabilisation of antibonding orbitals within an external magnetic field orientated perpendicular to the bond.[37] Until now however, the focus of modelling electronic systems in strong magnetic fields has been restricted to atoms and small molecules. Many experimental studies however, have suggested that a comparatively small external magnetic field can create a measurable change in the properties of systems where the dominant binding is through weak intermolecular interactions, such as bulk liquid structures.[38–46] Furthermore, the use of a magnetic field to alter the properties of liquids within various industrial applications is well documented.[47–49] The rationale behind these changes and in some cases the nature of the changes however, is still a topic of substantial debate.

The following chapters aim to address the computational scaling issues when performing London Atomic Orbital based electronic structure calculations on increasingly large molecular systems, by combining these methods within an embedded fragment approximation. This would present a method for going beyond simple molecules when studying systems within arbitrary strength magnetic fields. This is particularly desirable since the response of molecular systems and materials to an external field is known to be governed by the area perpendicular to the magnetic flux. In addition, many large systems are composed of molecular subunits, for example clusters and molecular crystals, in which weak interactions such as hydrogen bonding play a decisive role and may be susceptible to the influence of external fields. In the present work, methods are developed to exploit the molecular nature of these systems to enable calculations of energetic, structural and response properties beyond the scope of currently available conventional approaches.

2 Electronic Structure Theory

2.1 Foundations of Electronic Structure Theory

The fundamental aspect of any electronic structure problem is finding a solution to the Schrödinger Equation[50] for a given system, which in its simplest form it is given by,

$$\hat{\mathcal{H}}\Psi_i = \mathcal{E}_i\Psi_i, \tag{2.1}$$

where Ψ_i is the molecular wavefunction describing a given state of the system, $\mathcal{E}_i$ is its corresponding energy and $\hat{\mathcal{H}}$ is the Hamiltonian operator. This forms an eigenvalue equation, where Ψ_i is an eigenfunction of $\hat{\mathcal{H}}$ with corresponding eigenvalue $\mathcal{E}_i$. In practice $\hat{\mathcal{H}}$ varies depending on the problem being considered, for most electronic structure problems the non-relativistic molecular Hamiltonian is considered. For a system of N nuclei, with atomic numbers Z_α and masses M_α and n electrons, it has the form,

$$\begin{aligned}\hat{\mathcal{H}} = &-\sum_{\alpha=1}^{N}\left(\frac{\hbar^2}{2M_\alpha}\nabla_\alpha^2\right) - \sum_{i=1}^{n}\left(\frac{\hbar^2}{2m_e}\nabla_i^2\right) - \sum_{i=1}^{n}\sum_{\alpha=1}^{N}\left(\frac{e^2}{4\pi\epsilon_0}\frac{Z_\alpha}{|\mathbf{r}_i - \mathbf{R}_\alpha|}\right) \\ &+ \sum_{i>j}^{n}\left(\frac{e^2}{4\pi\epsilon_0}\frac{1}{|\mathbf{r}_i - \mathbf{r}_j|}\right) + \sum_{\alpha>\beta}^{N}\left(\frac{e^2}{4\pi\epsilon_0}\frac{Z_\alpha Z_\beta}{|\mathbf{R}_\alpha - \mathbf{R}_\beta|}\right)\end{aligned} \tag{2.2}$$

Here m_e is the rest mass of an electron, e is the elementary charge, $\mathbf{r}_i$ and $\mathbf{R}_\alpha$ are the positions of the i^{th} electron and α^{th} nucleus respectively, ∇_i^2 is the Laplacian operator and ϵ_0 is the permittivity of free space. It can be split into its five constituent components, the nuclear kinetic energy $\hat{T}_N$, the electron kinetic energy $\hat{T}_e$, the electron-nuclear attraction $\hat{V}$, the electron-electron repulsion $\hat{W}$ and the nuclear-nuclear repulsion $\hat{V}_{NN}$ operators respectively. It is often written in a more concise form using these definitions,

$$\hat{\mathcal{H}} = \hat{T}_N + \hat{T}_e + \hat{V} + \hat{W} + \hat{V}_{NN}. \tag{2.3}$$

It is also common to define the non-relativistic molecular Hamiltonian in terms of *atomic units*, rather than *Systéme International* (SI) units, allowing several constants (m_e, e and $4\pi\epsilon_0$) to be removed from the equation, greatly simplifying the expression. Atomic units are used throughout this work unless otherwise stated.

2.1.1 The Born-Oppenheimer Approximation

The eigenfunctions of Eq. (2.2) describe a molecular system by defining a wavefunction $\Psi(\mathbf{r}, \mathbf{R})$ that depends on the electron coordinates $\mathbf{r}$ and the nuclear coordinates $\mathbf{R}$. This presents a challenging problem to solve therefore, simplifications are often made. One such simplification is the *Born-Oppenheimer Approximation*[51] where the electrons are assumed to respond adiabatically to the motion of the nuclei, due to the nuclei having a far greater

mass. The wavefunction can therefore be written as a product of a nuclear and electronic wavefunction,

$$\Psi(\mathbf{r},\mathbf{R}) \approx \Xi(\mathbf{R})\,\Phi(\mathbf{r};\mathbf{R}), \tag{2.4}$$

where the electronic wavefunction $\Phi(\mathbf{r};\mathbf{R})$ is only parametrically dependent on the nuclear coordinates, through the electron-nuclear attraction term. At a given fixed nuclear geometry $\hat{V}(\mathbf{r};\mathbf{R})$ can be reduced to a one-electron operator, dependent on fixed parameters representing the fixed nuclear point charges. An electronic Hamiltonian can be constructed at a fixed molecular geometry, $\mathbf{R}$,

$$\hat{\mathcal{H}}_{\text{elec}}(\mathbf{r};\mathbf{R}) = \hat{T}_e(\mathbf{r}) + \hat{V}(\mathbf{r};\mathbf{R}) + \hat{W}(\mathbf{r}) \tag{2.5}$$

with a corresponding electronic Schödinger equation,

$$\hat{\mathcal{H}}_{\text{elec}}(\mathbf{r};\mathbf{R})\,\Phi_i(\mathbf{r};\mathbf{R}) = \mathcal{E}_i(\mathbf{R})\,\Phi_i(\mathbf{r};\mathbf{R}), \tag{2.6}$$

where the electronic wavefunctions $\Phi_i(\mathbf{r};\mathbf{R})$ are eigenfunctions of $\hat{\mathcal{H}}_{\text{elec}}(\mathbf{r};\mathbf{R})$ with corresponding eigenvalues, $\mathcal{E}_i(\mathbf{R})$, representing the electronic energies at a given nuclear geometry. The electronic wavefunctions form a complete orthonormal basis, constituting the electronic energy levels of the system. The remaining terms from $\hat{\mathcal{H}}$ constitute the operator for the nuclear Schrödinger equation,

$$\hat{\mathcal{H}}_{\text{nuc}}(\mathbf{R})\,\Xi(\mathbf{R}) = \mathcal{E}_{\text{nuc}}\Xi(\mathbf{R}). \tag{2.7}$$

The corresponding Hamiltonian for which can be written as,

$$\hat{\mathcal{H}}_{\text{nuc}} = \hat{T}_N(\mathbf{R}) + \hat{V}_{NN}(\mathbf{R}) + \mathcal{E}(\mathbf{R}), \tag{2.8}$$

where $\mathcal{E}$ is the potential energy resulting from the solution to the electronic Schrödinger equation with nuclei at positions ($\mathbf{R}$). Within the Born-Oppenheimer approximation, it is assumed that the energy gap between the different electronic states is large enough that the electronic and nuclear wavefunctions exhibit no coupling. This results in the total wavefunction evolving through the same electronic state as the nuclear geometry changes, therefore, the electrostatic potential experienced by the nuclei is represented by a potential energy function of the given electronic state, $\mathcal{E}_i(\mathbf{R})$. Focusing on the electronic structure at a fixed geometry only requires the consideration of the electronic Schrödinger equation significantly simplifying the problem. In some very simple cases it can be solved analytically however, most systems of chemical interest still require further approximations.

2.1.2 *ab Initio* Theory

Due to the complexity of the final term in Eq. (2.5), which couples the motion of the electrons, it is not possible to solve the electronic Schrödinger equation analytically for systems with more than one electron, therefore, when treating a multi-electron system, modern electronic structure techniques attempt to numerically approximate the solutions to the electronic Schrödinger equation. One common approach for approximating these

solutions is *ab initio* theory, where an *ansatz* for the many-electron wavefunction of a given system is formulated from the known behaviour of electrons. Usually this is formulated using the exact solution for the one-electron system as a starting point.

One-Electron Orbitals

The eigenfunctions of the one-electron Hamiltonian are known as spatial orbitals, $\varphi_i(\mathbf{r})$, representing the spatial orbital at position, $\mathbf{r}$, of an electron,

$$\left(-\frac{1}{2}\nabla_{\mathbf{r}}^2 - \sum_{\alpha}\frac{Z_\alpha}{|\mathbf{r}-\mathbf{R}_\alpha|}\right)\varphi_i(\mathbf{r}) = \varepsilon_i\varphi_i(\mathbf{r}), \tag{2.9}$$

All the spatial orbitals of a given system constitute an orthonormal set,

$$\int_{\mathbb{R}^3}\varphi_i^*(\mathbf{r})\,\varphi_j(\mathbf{r})\,d\mathbf{r} = \delta_{ij}. \tag{2.10}$$

On its own however, a spatial orbital does not fully describe the quantum state of an electron as it neglects its intrinsic angular momentum, referred to as electron spin which creates a magnetic moment. It is known that the magnetic momentum can occupy two possible states, and when quantised along a Cartesian axis, these can be determined as eigenfunctions of the spin angular momentum operator $\hat{s}_z$,

$$\hat{s}_z\alpha(\sigma) = \frac{1}{2}\alpha(\sigma) \qquad \hat{s}_z\beta(\sigma) = -\frac{1}{2}\beta(\sigma), \tag{2.11}$$

where the spin functions α and β have spin quantum numbers of $+1/2$ and $-1/2$ respectively and σ is the spin variable. A complete description for a given electron can therefore be obtained as a product of the spatial orbital and its spin function, η, giving a total *spinorbital*,

$$\phi_i(\mathbf{r}_i,\sigma_i) = \varphi(\mathbf{r}_i)\,\eta(\sigma_i) \tag{2.12}$$

which is both an eigenfunction of the Hamiltonian and the spin angular momentum operator. An orthonormal basis can be made from the resulting spinorbitals which, if complete, can be used to form a general wavefunction ψ,

$$\psi(\mathbf{r}_i,\sigma_i) = \sum_i \phi_i(\mathbf{r}_i,\sigma_i)\,c_i \tag{2.13}$$

where c_i is the expansion coefficient for the i^{th} function and $\sum_i c_i^* c_i = 1$. This expression is often written in *Dirac* notation, also known as bra-ket notation,

$$\phi_i(\mathbf{x}) \to |i\rangle \qquad \phi_i^*(\mathbf{x}) \to \langle i| \qquad \langle i|j\rangle = \int \phi_i^*(\mathbf{x})\,\phi_j(\mathbf{x})\,d\mathbf{r}d\sigma = \delta_{ij}, \tag{2.14}$$

where $\mathbf{x}$ has been used to refer to the combined spin and spatial coordinates, $\mathbf{x} = (\mathbf{r},\sigma)$. Here δ_{ij} is the Kronecker delta function,

$$\delta_{ij} = \begin{cases} 0 & \text{if } i \neq j, \\ 1 & \text{if } i = j. \end{cases} \tag{2.15}$$

Therefore, the linear expansion in Eq. (2.13), becomes,

$$|\psi\rangle = \sum_i |i\rangle c_i \tag{2.16}$$

The Slater Determinant

The simplest *ansatz* for an n-electron wavefunction assumes that all the electrons are non-interacting and therefore the many-electron Hamiltonian, can be constructed by considering a sum of one-electron Hamiltonians,

$$\hat{\mathcal{H}} = \sum_{i=1}^{n} \hat{h}(i) \qquad \text{where} \qquad \hat{h}(i) = -\frac{1}{2}\nabla^2_{\mathbf{r}_i} - \sum_{\alpha} \frac{Z_\alpha}{|\mathbf{r}_i - \mathbf{R}_\alpha|}. \tag{2.17}$$

The corresponding wavefunction for such as system is the *Hartree product* wavefunction.[52] This represents a non-physical solution however, as it depicts distinguishable particles assigned to individual spinorbitals. This violates the Pauli exclusion principle which requires the wavefunction to be antisymmetric on exchange of indistinguishable fermions, such as electrons.

Although in itself, the Hartree product is unphysical, it presents a logical starting point for building a suitable *ansatz* for a many-electron wavefunction. Given a complete set of spinorbitals $\{\phi_i\}$, a function of the electron coordinates can be constructed from a linear combination of spinorbitals. For a single electron system it is given by,

$$\psi(\mathbf{r}_1, \sigma_1) = \sum_i c_i \phi_i(\mathbf{r}_1, \sigma_1) \tag{2.18}$$

This can be extended to consider a two-electron system,

$$\psi(\mathbf{r}_1, \sigma_1, \mathbf{r}_2, \sigma_2) = \sum_i \sum_j d_{ij} \phi_i(\mathbf{r}_1, \sigma_1)\, \phi_j(\mathbf{r}_2, \sigma_2) \tag{2.19}$$

where d_{ij} is the expansion coefficient for the i^{th} and j^{th} spinorbitals in electron coordinates $(\mathbf{r}_1, \sigma_1)$ and $(\mathbf{r}_2, \sigma_2)$ respectively. From this we can generalise any many-electron wavefucntion as a linear combination of Hartree products. For two electrons we have,

$$\begin{aligned}\psi(\mathbf{r}_1, \sigma_1, \mathbf{r}_2, \sigma_2) =& d_{11}\phi_1(\mathbf{r}_1, \sigma_1)\, \phi_1(\mathbf{r}_2, \sigma_2) + d_{12}\phi_1(\mathbf{r}_1, \sigma_1)\, \phi_2(\mathbf{r}_2, \sigma_2) \\ &+ d_{21}\phi_2(\mathbf{r}_1, \sigma_1)\, \phi_1(\mathbf{r}_2, \sigma_2) + d_{22}\phi_2(\mathbf{r}_1, \sigma_1)\, \phi_2(\mathbf{r}_2, \sigma_2).\end{aligned} \tag{2.20}$$

For this wavefunction to satisfy the Pauli exclusion principle, d_{11} and d_{22} must be zero and $d_{12} = -d_{21}$ giving the following normalised wavefunction,

$$\psi(\mathbf{r}_1, \sigma_1, \mathbf{r}_2, \sigma_2) = \frac{1}{\sqrt{2}} \left[\phi_1(\mathbf{r}_1, \sigma_1)\, \phi_2(\mathbf{r}_2, \sigma_2) - \phi_2(\mathbf{r}_1, \sigma_1)\, \phi_1(\mathbf{r}_2, \sigma_2)\right]. \tag{2.21}$$

This has the form of a determinant. In general, for a system with n electrons, this expression

is a *Slater determinant* wavefunction,

$$\Phi = \frac{1}{\sqrt{n!}} \begin{vmatrix} \phi_1(\mathbf{r}_1, \sigma_1) & \phi_1(\mathbf{r}_2, \sigma_2) & \cdots & \phi_1(\mathbf{r}_n, \sigma_n) \\ \phi_2(\mathbf{r}_1, \sigma_1) & \phi_2(\mathbf{r}_2, \sigma_2) & \cdots & \phi_2(\mathbf{r}_n, \sigma_n) \\ \vdots & \vdots & \ddots & \vdots \\ \phi_n(\mathbf{r}_1, \sigma_1) & \phi_n(\mathbf{r}_2, \sigma_2) & \cdots & \phi_n(\mathbf{r}_n, \sigma_n) \end{vmatrix} \tag{2.22}$$

The Variation Principle

A Slater determinant wavefunction is not exact, however. Therefore, it is vital to identify a method to systematically improve the approximation. The variational principle is one such approach. Assuming the eigenfunctions of $\hat{\mathcal{H}}$ constitute a complete set, such that the trial wavefunction ϕ mat be expanded in the basis of eigenfunctions, it can be shown that the ground state eigenvalue of $\hat{\mathcal{H}}$ is a lower bound to the expectation value of the trial wavefunction. The result being that the lower energy wavefunction is assumed the more correct solution, presenting a basis for a systematic search for the ground-state. This can be expressed as,

$$\langle \Psi | \hat{\mathcal{H}} | \Psi \rangle = \mathcal{E} \geq \mathcal{E}_0 = \langle \Psi_0 | \hat{\mathcal{H}} | \Psi_0 \rangle, \tag{2.23}$$

where Ψ_0 and $\mathcal{E}_0$ define the exact solution for a given system.

2.1.3 Hartree-Fock Theory

The simplest approximation for a many-electron wavefunction is the Hartree-Fock (HF) method, where the wavefunction is represented by constructing a single Slater determinant. The electrons are treated as being independent, whilst experiencing an *effective* potential due to the other $n-1$ electrons, resulting in a one-electron mean-field approximation. The electronic Hamiltonian can be decomposed into its one-electron component,

$$\hat{\mathcal{H}}_1 = \sum_i \hat{h}(i) = \sum_i -\frac{1}{2}\nabla_i^2 - \sum_i \sum_\alpha \frac{Z_\alpha}{|\mathbf{r}_i - \mathbf{R}_\alpha|}, \tag{2.24}$$

containing the kinetic energy and nuclear interaction terms, and a two-electron component, $\hat{w}(i,j)$,

$$\hat{\mathcal{H}}_2 = \hat{W} = \sum_i \sum_{j \neq i} \hat{w}(i,j) = \sum_i \sum_{j \neq i} \frac{1}{|\mathbf{r}_i - \mathbf{r}_j|} \tag{2.25}$$

The expectation value of the normalised Slater determinant is then given by,

$$\mathcal{E}_{\text{HF}} = \langle \Phi | \hat{\mathcal{H}} | \Phi \rangle = \sum_i \langle i | \hat{h} | i \rangle + \sum_i \sum_{j \neq i} \langle ij | ij \rangle - \langle ij | ji \rangle. \tag{2.26}$$

The one-electron component here is the expectation value of the one-electron Hamilatonian on a given spinorbital,

$$\langle \Phi | \hat{\mathcal{H}} | \Phi \rangle = \int \phi_i^*(\mathbf{r}\sigma)\, \hat{h} \phi_i(\mathbf{r}\sigma)\, d\mathbf{r} d\sigma = \hat{h}_i. \tag{2.27}$$

The remaining two terms refer to the electron-electron interactions which can be written in terms of two contributions. The first is the Coulomb integral, $\langle ij|ij\rangle = J_{ij}$, which can be physically interpreted as the classical electrostatic interaction between the two electrons. The second is the exchange integral, $\langle ij|ji\rangle = K_{ij}$, which results from the anti-symmetry of the wavefunction, discussed in 2.1.2, and is interpreted as the energy arising from electrons with parallel spins having different spatial wavefunctions. These two terms can be combined and written as a single antisymmetrised integral term $\langle ij||ij\rangle = J_{ij} - K_{ij}$. The following integral notation has been used for simplification,

$$\langle pq|rs\rangle = \int\int \frac{\phi_p^*(\mathbf{r}_1\sigma_1)\,\phi_q(\mathbf{r}_2\sigma_2)\,\phi_r^*(\mathbf{r}_1\sigma_1)\,\phi_s(\mathbf{r}_2\sigma_2)}{|\mathbf{r}_1 - \mathbf{r}_2|} d\mathbf{r}_1 d\boldsymbol{\sigma}_1 d\mathbf{r}_2 d\sigma_2. \tag{2.28}$$

This is commonly known as *physicist's* notation for two-electron integrals, however, often these integrals will be written in what is referred to as *chemist's* or *Mulliken* notation where $(pr|qs) = \langle pq|rs\rangle$.

The Hartree-Fock Equations

Given a Slater determinant, the ground state HF energy for a given molecular system can be found by exploiting the variational principle, discussed in 2.1.2, on a set of orthonormal basis of spin-orbitals, $\{\phi_i\}$ where $\langle i|j\rangle = \delta_{ij}$. This leads to a constrained optimisation that can be carried out using the method of Lagrange undetermined multipliers, where the Lagrangian is,

$$\mathcal{L}(\{\phi_i\}) = \mathcal{E}(\{\phi_i\}) - \sum_{ij} \epsilon_{ij}\left(\langle i|j\rangle - \delta_{ij}\right), \tag{2.29}$$

where ϵ_{ij} are a set of real Lagrange multipliers. Given a small perturbation, $\phi_i \to \phi_i + \delta\phi_i$, the change in the Lagrangian can be written as,

$$\delta\mathcal{L} = \delta\mathcal{E} - \sum_{ij} \epsilon_{ij}\delta\langle i|j\rangle. \tag{2.30}$$

From the variational principle, setting $\delta\mathcal{L} = 0$, it can be determined that, for a given electron p,

$$\delta\mathcal{L} = \sum_i \int \delta\phi_i^*(\mathbf{x}_p)\left[\hat{h}(p)\,\phi_i(\mathbf{x}_p) + \sum_j \left(\hat{J}_j(p) - \hat{K}_j(p)\right)\phi_i(\mathbf{x}_p) - \sum_j \epsilon_{ij}\phi_j(\mathbf{x}_p)\right] d\mathbf{x}_p + \text{c.c.} = 0, \tag{2.31}$$

where c.c. denotes the corresponding complex conjugate expression, where $\mathbf{x}_p$ has been used to denote a set of combined spatial and spin coordinates, as previously defined, and $\hat{J}$ and $\hat{K}$ are the one-electron Coulomb and exchange operators respectively,

$$\hat{J}_j(p)\,\phi_i(\mathbf{x}_p) = \left[\int \phi_j^*(\mathbf{x}_q)\,\hat{w}(p,q)\,\phi_j(\mathbf{x}_q)\,d\mathbf{x}_q\right]\phi_i(\mathbf{x}_p) \tag{2.32}$$

$$\hat{K}_j(p)\,\phi_i(\mathbf{x}_p) = \left[\int \phi_j^*(\mathbf{x}_q)\,\hat{w}(p,q)\,\phi_i(\mathbf{x}_q)\,d\mathbf{x}_q\right]\phi_j(\mathbf{x}_p) \tag{2.33}$$

Given that the perturbation is an arbitrary value, for Eq (2.31) to hold requires,

$$\left[\hat{h}(p) + \sum_j \left(\hat{J}_j(p) - \hat{K}_j(p)\right)\right]\phi_i(\mathbf{x}_p) = \sum_j \epsilon_{ij}\phi_j(\mathbf{x}_p) \tag{2.34}$$

which defines a one-electron generalised-eigenvalue problem, since the matrix ϵ_{ij} is not diagonal. This can be re-written in terms of the Fock operator $\hat{f}$,

$$\hat{f}|\phi_i\rangle = \sum_j \epsilon_{ij}|\phi_j\rangle. \tag{2.35}$$

It can be shown that a unitary transform always exists that diagonalises ϵ_{ij}, hence there always exists a set of spinorbitals for which ϵ_{ij} is diagonal,

$$\hat{f}|\phi_i\rangle = \epsilon_i|\phi_i\rangle, \tag{2.36}$$

where ϵ is now a diagonal matrix of Lagrange multipliers. The problem is now simplified to that of a standard eigenvalue problem, forming the canonical Hartree-Fock equations.

Restricted and Unrestricted Formalisms

Two formalisms are typically employed when performing calculations over orbitals. The first is restricted Hartree-Fock (RHF) theory which requires electrons in the same spin orbital to have the same spatial component,

$$\phi_i(\mathbf{x}) = \begin{cases} \varphi(\mathbf{r})\,\alpha(\sigma) \\ \varphi(\mathbf{r})\,\beta(\sigma) \end{cases} \tag{2.37}$$

This enforces double occupation of all spatial orbitals. It provides a good model for studying closed shell systems as it requires a reduced computational cost due to the number of spatial orbitals being half the number of spinorbitals. However, it cannot accurately capture the dissociation of closed shell molecules into open shell systems. A common example is the dissociation of H_2 as RHF will produce the ionic dissociation state, $H_2 \rightarrow H^+ + H^-$ due to the enforced shared spatial function. RHF can be generalised to restricted open-shell Hartree-Fock theory (ROHF)[53] to account for unpaired electrons, where the expectation value for the energy is given by,

$$\begin{aligned} \mathcal{E} =& 2\sum_k h_k + \sum_{k,l}(2J_{kl} - K_{kl}) \\ &+ f\left[2\sum_m h_m + f\sum_{m,n}(2aJ_{mn} - bK_{mn}) + 2\sum_{km}(2J_{km} - K_{km})\right], \end{aligned} \tag{2.38}$$

where k and l are the indices of the closed-shell orbitals, m and n are the indices of the open-shell orbitals and a, b and f are numerical constants specific to the system being studied. The first two sums constitute the closed-shell energy as in RHF, the next two

constitute the open-shell energy and the last is the interaction energy between the closed and open shells.

The second formalism is unrestricted Hartree-Fock (UHF) theory which removes the imposed restriction of RHF, allowing electrons in multiple spatial functions for the same spin orbital,

$$\phi_i(\mathbf{x}) = \begin{cases} \varphi^{\alpha}(\mathbf{r})\,\alpha(\sigma) \\ \varphi^{\beta}(\mathbf{r})\,\beta(\sigma) \end{cases} \tag{2.39}$$

This approach removes the limitation of RHF to closed shell systems however at slightly increased cost.

Linear Combination of Atomic Orbitals

In general, when solving the canonical HF equations, the molecular orbitals are expanded in a finite basis of atom-centred atomic orbitals (AOs), giving a linear combination of atomic orbitals (LCAOs),

$$\varphi_i(\mathbf{r}) = \sum_{\nu} c_{\nu i}\chi_{\nu}(\mathbf{r}). \tag{2.40}$$

where $\{\chi_\nu\}$ are a set of AOs with corresponding linear expansion coefficients $\{c_{\nu i}\}$. This forms the basis for the Roothaan-Hall approach.[54;55] Rewriting the canonical HF equation in LCAO form,

$$\hat{f}\sum_{\nu} c_{\nu i}|\chi_\nu\rangle = \epsilon_i \sum_{\nu} c_{\nu i}|\chi_\nu\rangle. \tag{2.41}$$

Left-multiplying this by $\langle\chi_\mu|$ gives,

$$\sum_{\nu} c_{\nu i}\langle\chi_\mu|\hat{f}|\chi_\nu\rangle = \epsilon_i \sum_{\nu} c_{\nu i}\langle\chi_\mu|\chi_\nu\rangle \tag{2.42}$$

which can be written in terms of the matrix element of the Fock operator in AO basis, $\mathbf{F}_{\mu\nu}$ and the overlap matrix element between the μ^{th} and ν^{th} AOs, $\mathbf{S}_{\mu\nu}$,

$$\sum_{\nu} c_{\nu i}\mathbf{F}_{\mu\nu} = \epsilon_i \sum_{\nu} c_{\nu i}\mathbf{S}_{\mu\nu} \tag{2.43}$$

Introducing the matrix $\mathbf{C}$ of molecular orbital (MO) coefficients, the generalised psuedo-eigenvalue equations can be written as,

$$\mathbf{FC} = \mathbf{SC}\epsilon. \tag{2.44}$$

The expectation value for the energy of a system can also be written in terms of

LCAOs,

$$\begin{aligned}\mathcal{E}(\Phi) &= \sum_i \langle i|\hat{h}|i\rangle + \frac{1}{2}\sum_{ij}\left(\langle ij|ij\rangle - \langle ij|ji\rangle\right) \\ &= \sum_i \sum_{\mu\nu} c^*_{\mu i} c_{\nu i} \langle \mu|\hat{h}|\nu\rangle + \frac{1}{2}\sum_{ij}\sum_{\mu\nu} c^*_{\mu i} c_{\nu i} \sum_{\lambda\sigma} c^*_{\lambda i} c_{\sigma i}\left(\langle \mu\lambda|\nu\sigma\rangle - \langle \mu\lambda|\sigma\nu\rangle\right) \\ &= \sum_{\mu\nu} D_{\mu\nu}\left[h_{\mu\nu} + \frac{1}{2}\sum_{\lambda\sigma} D_{\lambda\sigma}\left(\langle \mu\lambda|\nu\sigma\rangle - \langle \mu\lambda|\sigma\nu\rangle\right)\right]\end{aligned} \tag{2.45}$$

where $h_{\mu\nu}$ refers to the core Hamiltonian matrix and the density matrix $D_{\mu\nu} = \sum_i^n c^*_{\mu i} c_{\nu i}$ has been introduced, from which the electron density can be calculated as,

$$\rho(\mathbf{r}) = 2\sum_i^{n/2} |\varphi_i(\mathbf{r})|^2 = \sum_{\mu\nu} D_{\mu\nu} \chi^*_\mu(\mathbf{r})\,\chi_\nu(\mathbf{r}), \tag{2.46}$$

assuming a restricted formalism. The same process can be applied to the Fock operator giving,

$$F_{\mu\nu} = h_{\mu\nu} + \sum_{\lambda\sigma} D_{\lambda\sigma}\left(\langle \mu\lambda|\nu\sigma\rangle - \langle \mu\lambda|\sigma\nu\rangle\right) \tag{2.47}$$

Substituting this into Eq. (2.45) gives the following expression for the Roothaan-Hall energy of a system,

$$\mathcal{E}(\{c_{\mu i}\}) = \frac{1}{2}\sum_{\mu\nu} D_{\mu\nu}\left(h_{\mu\nu} + F_{\mu\nu}\right). \tag{2.48}$$

If the basis set $\{\chi_\mu\}$ is complete, the molecular orbitals are represented exactly, however, this, in practice, is not possible. Therefore, an incomplete set must be employed giving only an approximate representation of the molecular orbitals. Two types of basis functions are commonly employed in electronic structure calculations. Slater type orbitals (STOs) are the exact orbitals for the hydrogen atom, representing the correct nuclear cusp and decay behaviours. They are given by,

$$\chi^{\mathrm{STO}}(\mathbf{r}) = (R_x - r_x)^l (R_y - r_y)^m (R_z - r_z)^n \exp\left[-\alpha|\mathbf{R} - \mathbf{r}|\right], \tag{2.49}$$

where $l + m + n$ gives the orbital angular momentum and α is the exponent controlling how spatially diffuse the function is. Calculating integrals over STOs however, is non-trivial therefore Gaussian type orbitals (GTOs) are more commonly employed,

$$\chi^{\mathrm{GTO}}(\mathbf{r}) = (R_x - r_x)^l (R_y - r_y)^m (R_z - r_z)^n \exp\left[-\alpha|\mathbf{R} - \mathbf{r}|^2\right]. \tag{2.50}$$

GTOs allow the use of the Gaussian product theorem when calculating two-electron integrals resulting in a much greater computational efficiency, however, as shown in Fig. 2.1, they do not produce an accurate representation of the cusp and decay behaviours of the atomic orbitals resulting in more GTOs, in comparison to STOs, being required in the expansion, to give an accurate approximation to the molecular orbitals. The faster evaluation of GTO two electron integrals generally compensates for this however, making GTOs the go-to for forming accurate and efficient basis functions for finite systems. The computational cost

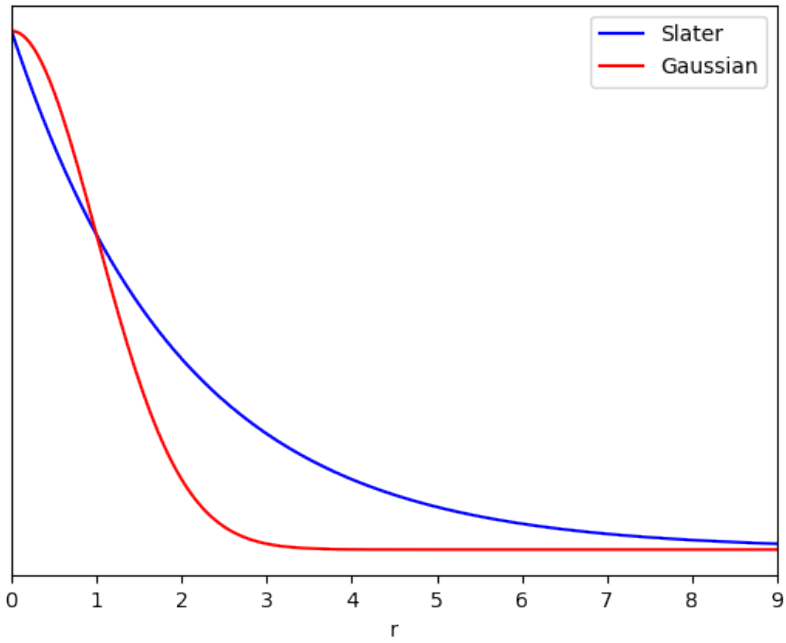

Figure 2.1: A visual representation of the difference between Slater and Gaussian type functions given by Eqs. (2.49) and (2.50).

when using GTOs can be further reduced by forming a *contracted* set of GTOs where a number of primitive GTO functions, with different exponents, are collected together as a fixed linear combination. Once the integrals have been calculated, the remaining steps in the calculation scale with number of basis functions not primitive functions. This contracted set does present a less flexible basis set, compared to the equivalent uncontracted set however, but enables more primitive functions to be used, generally increasing the quality. Many GTO basis sets have been produced optimising the α parameter, contraction lengths and coefficients per atom to attempt to reduce the overall number of functions required.

Self-Consistent Field Approach

The variation principle is employed to minimise the energy in Eq. (2.48) with respect to the MO coefficients, $\{c_{\mu i}\}$. Due to the dependence of $\mathbf{F}$ on $\mathbf{C}$ the problem becomes highly non-linear requiring an iterative method referred to as the self-consistent field (SCF) method to solve the Roothaan-Hall equations. The general SCF approach can be outlined as,

1. The relevant one- and two-electron integrals are evaluated over the given basis functions, these can be stored without need for re-calculation for small systems.

2. A suitable guess density is constructed and the initial Fock matrix is constructed from $\mathbf{D}^{\text{guess}}$ and the two-electron integrals.

3. The Fock matrix is then diagonalised to produce a new set of orbital coefficients $\mathbf{C}'$, eigenvalues ϵ and density matrix $\mathbf{D}'$.

4. A new Fock matrix, $\mathbf{F}'$, is constructed from $\mathbf{D}'$ via the aufbau principle - the orbitals are occupied with the lowest eigenvalues to give the ground state occupation.

5. This process is then repeated until a pre-defined convergence criteria on the change in the energy and density matrix $\mathbf{D}$ is met.

2.2 Correlated Methods

The solutions to the HF approach are exact, to within the defined finite basis limit, for a one-electron system. However, this method neglects the effects of instantaneous interactions between individual electrons, therefore, can only present an upper-bound to the true electronic energy for a multi-electron system, by consequence of the variational principle. The difference between the true ground state energy and that of the HF solution was defined by Löwdin as the correlation energy of the system,[56]

$$E_c = E_0 - E_{\text{HF}}. \tag{2.51}$$

Chemical processes often involve relatively small changes in energy, e.g. between reactants, transition states and products, which may be highly sensitive to changes in the total energy. In principle the correlation energy only constitutes a small fraction of the total energy however, it can be vital in providing quantitative accuracy from electronic structure calculations.

2.2.1 Configuration Interaction

The correlation energy can typically be accounted for by constructing a more flexible wavefunction ansatz, for example from a linear combination of Slater determinants Φ_I, including the HF determinant Φ_0,

$$\Psi \approx c_0\Phi_0 + \sum_I c_I\Phi_I. \tag{2.52}$$

For a given system, a number of basis functions m are used to construct $2m$ spinorbitals. The ground-state determinant will contain an electron in the $m_{\text{occ.}}$ spinorbitals with the lowest orbital energy, referred to as occupied spinorbitals. The remaining spinorbitals are unoccupied and are referred to as virtual orbitals. In configuration interaction (CI) theory, the wavefunction is represented as a linear combination of the HF determinant and its *excited determinants*,[57] generated by replacing one (or more) occupied orbitals, (i, j) with virtual orbitals (a, b), the expansion coefficients optimised using the variation principle,

$$\Psi = c_0\Phi_0 + \sum_{ia} c_i^a\Phi_i^a + \frac{1}{4}\sum_{ijab} c_{ij}^{ab}\Phi_{ij}^{ab} + \ldots \tag{2.53}$$

This can be extended to the limit of all possible excited determinants, which is referred to as *full configuration interaction* (FCI). Grouping together the determinants and coefficients, according to the number of orbitals replaced, results in a simplified expression for the CI

wavefunction,

$$|\Psi\rangle = c_0|0\rangle + c_S|S\rangle + c_D|D\rangle + c_T|T\rangle + ... = \sum_I c_I|I\rangle, \tag{2.54}$$

where each term represents the blocks of ground-state, singly, doubly, triply etc. excited determinants, respectively.

Although in principle FCI represents an exact solution in a given basis set, which is then considered to be formally exact in the limit of a complete basis set, it presents an extremely complex computational problem to solve, which increases significantly with basis set and system size, on the order of $m!$. Therefore, it can only readily be applied to very small systems with only a few basis functions. Common methods to reduce the computational complexity include truncating the CI expansion, only considering up to doubles for example, or alternatively restricting the active space by *freezing* certain orbitals or excluding particularly high energy orbitals.

2.2.2 Coupled-Cluster Theory

Truncation of the CI expansion however, breaks *size consistency* and the resulting energies are not *size extensive*, with errors increasing with system size.[58] An alternative approach to account for correlation by including excited state determinants is coupled-cluster (CC) theory, which addresses the issues when truncating the CI expansion. Analogous to CI theory, the CC method accounts for electron correlation by constructing a more-flexible wavefunction from the HF reference and its excited determinants, however, this is achieved via the exponential ansatz,[59–61]

$$\Psi = \exp\left(\hat{T}\right)\Phi_0 \tag{2.55}$$

where $\hat{T}$ is the cluster operator, defined as the sum of excitation operators to a given order,

$$\hat{T} = \hat{T}_1 + \hat{T}_2 + \hat{T}_3 + ... = \sum_\lambda \hat{T}_\lambda. \tag{2.56}$$

The action of a cluster operator on the HF determinant gives CC wavefunction contributions of the form,

$$\hat{T}_\lambda\Phi_0 = \left(\frac{1}{\lambda!}\right)^2 \sum_{ij...}\sum_{ab...} t_{ij...}^{ab...}\Phi_{ij...}^{ab...}. \tag{2.57}$$

where $\Phi_{ij...}^{ab...}$ are the excited state determinants with corresponding excitation amplitudes $t_{ij...}^{ab...}$.

Considering the common example of CCSD,[62] where the expansion is truncated after the singles and doubles excitation terms, into Eq. (2.55) and utilising a Taylor series

expansion of the exponential,

$$\begin{aligned}\Psi_{\text{CCSD}} &= \left(1 + \hat{T}_1 + \hat{T}_2 + \frac{1}{2}\hat{T}_1^2 + \hat{T}_1\hat{T}_2 + \frac{1}{2}\hat{T}_2^2 + \dots\right)\Phi_0 \\ &= \Phi_0 + \sum_i \sum_a t_i^a \Phi_i^a + \frac{1}{4}\sum_{ij}\sum_{ab} t_{ij}^{ab}\Phi_{ij}^{ab} + \frac{1}{2}\sum_{ij}\sum_{ab} t_i^a t_j^b \Phi_{ij}^{ab} \\ &\quad + \frac{1}{4}\sum_{ijk}\sum_{abc} t_{ij}^{ab} t_k^c \Phi_{ijk}^{abc} + \frac{1}{32}\sum_{ijkl}^{abcd} t_{ij}^{ab} t_{kl}^{cd} \Phi_{ijkl}^{abcd} + \dots\end{aligned} \tag{2.58}$$

The linear cluster operator terms are referred to as connected clusters and those that are products of cluster operators are referred to as disconnected clusters. Comparing this to the equivalent CI singles and doubles (CISD) wavefunction, reveals that CISD lacks the disconnected cluster terms which introduce higher-order excited determinants, which make CC size-consistent.

2.2.3 Perturbation Theory

Another alternative approach to calculating the electron correlation energy, is via perturbation theory - if the solution to a similar but simpler problem is known, then the solution to a related more complex problem can be approximated by applying a small correction to the known solution. This requires that the two problems differ only by a small correction which, as the correlation energy typically only makes up approximately 1% of the total energy, makes it applicable to determining the electron correlation energy of a given system.

Rayleigh and Schrödinger proposed splitting the Hamiltonian into the sum of a zeroth-order component $\hat{\mathcal{H}}_0$ and a perturbative operator $\hat{\mathcal{V}}$ scaled by a coefficient λ,

$$\hat{\mathcal{H}} = \hat{\mathcal{H}}_0 + \lambda\hat{\mathcal{V}}. \tag{2.59}$$

This approach is known as Rayleigh-Schrödinger perturbation theory (RSPT) and results in the Schrödinger equation Eq. (2.1) being written as,

$$\hat{\mathcal{H}}\Psi = \left(\hat{\mathcal{H}}_0 + \lambda\hat{\mathcal{V}}\right)\Psi = \mathcal{E}\Psi, \tag{2.60}$$

The exact eigenfunctions and eigenvalues of which, can be approximated using a series expansion in λ.

$$\Psi = \Psi^{(0)} + \lambda\Psi^{(1)} + \lambda^2\Psi^{(2)} + \dots \tag{2.61}$$

$$\mathcal{E} = \mathcal{E}^{(0)} + \lambda\mathcal{E}^{(1)} + \lambda^2\mathcal{E}^{(2)} + \dots \tag{2.62}$$

where $\Psi^{(k)}$ and $\mathcal{E}^{(k)}$ are the k^{th} order corrections to the eigenfunctions and corresponding eigenvalues of $\hat{\mathcal{H}}_0$.

The application of RSPT to wavefunction-based electronic structure methods was devised by Møller and Plesset, using the HF wavefunction as the zeroth-order approximation.[63] This approach is known as Møller-Plesset (MP) perturbation theory, for which the

zeroth-order operator is taken to be the sum of the Fock operators for each electron,

$$\hat{\mathcal{H}}_0 = \sum_i \hat{f}(i) = \sum_i \hat{h}(i) + \sum_{ij} \left(\hat{J}_j(i) - \hat{K}_j(i) \right), \tag{2.63}$$

and the perturbation operator is given by the difference between the exact and zeroth-order Hamiltonians,

$$\begin{aligned} \hat{\mathcal{V}} &= \left(\sum_i \hat{h}(i) + \sum_{i>j} \hat{w}(i,j) \right) = \left(\sum_i \hat{h}(i) + \sum_{ij} \left(\hat{J}_j(i) - \hat{K}_j(i) \right) \right) \\ &= \sum_{i>j} \hat{w}(i,j) - \sum_{ij} \left(\hat{J}_j(i) - \hat{K}_j(i) \right). \end{aligned} \tag{2.64}$$

The expressions for the first three energy terms for MP perturbation theory for a given Slater determinant Φ_0, are given by,

$$\mathcal{E}_0^{(0)} = \langle \Phi_0 | \hat{\mathcal{H}}_0 | \Phi_0 \rangle = \sum_i \langle \Phi_0 | \hat{f}(i) | \Phi_0 \rangle = \sum_i \langle i | \hat{f} | i \rangle = \sum_i \epsilon_i \tag{2.65}$$

$$\mathcal{E}_0^{(1)} = \langle \Phi_0 | \hat{\mathcal{V}}_0 | \Phi_0 \rangle = -\frac{1}{2} \sum_{ij} \langle ij || ij \rangle \tag{2.66}$$

$$\mathcal{E}_0^{(2)} = \sum_{n \neq 0} \frac{|\langle \Phi_n | \hat{\mathcal{V}}_0 | \Phi_0 \rangle|^2}{\varepsilon_0^{(0)} - \varepsilon_n^{(0)}} = \frac{1}{4} \sum_{ijab} \frac{|\langle ab || ij \rangle|^2}{\epsilon_i + \epsilon_j - \epsilon_a - \epsilon_b} \tag{2.67}$$

Here the second-order energy correction $\mathcal{E}_0^{(2)}$ includes only contributions from doubly-excited determinants. Simply summing the zeroth and first-order MP energy terms returns the ground-state HF energy, $\mathcal{E}_0^{(0)} + \mathcal{E}_0^{(1)} = \mathcal{E}_{\text{HF}}$. Therefore, the correlation corrections first appear within the second-order term, commonly referred to as the MP2 correlation energy,

$$\mathcal{E}_c^{\text{MP2}} = \frac{1}{4} \sum_{ijab} \frac{|\langle ab || ij \rangle|^2}{\epsilon_i + \epsilon_j - \epsilon_a - \epsilon_b} \tag{2.68}$$

2.3 Density-Functional Theory

The various different methods discussed so far have been widely applied to studying molecular systems however, they suffer from a major limitation, their poor computational scaling with system size (number of basis functions). On its own HF theory scales as $O\left(m^4\right)$, with m being the number of basis functions. Going beyond HF theory the scaling gets progressively worse, MP2 scales as $O\left(m^5\right)$, CISD/CCSD and MP3 scale as $O\left(m^6\right)$, MP4 and CCSD(T) scale as $O\left(m^7\right)$, CISDT/CCSDT and MP5 scale as $O\left(m^8\right)$ and using FCI scales as $O(m!)$. This scaling severely limits the system size that can be feasibly studied, particularly if electron correlation is important within the given system. Density-Functional theory (DFT) offers a different route to performing electronic-structure calculations at an improved computational cost scaling, allowing more accurate treatments of systems with many more basis functions. Fundamentally DFT attempts to describe a system in terms of its *electron density* $\rho(\mathbf{r})$ which would reduce the number of variables required to

represent a system from $4n$, where n is the number of electrons, to three spatial coordinates. This represents a much more cost-efficient method for calculating electronic structure of molecules. Initially DFT was thought to be an approximate model, rather than an exact theory. However, it was Pierre C. Hohenberg and Walter Kohn who first proved, in 1964, that the ground state of an electronic system in an external potential can be completely described by the one-electron density ρ.[64] From this modern DFT was conceived which can exhibit accuracies rivalling that of correlated methods whilst maintaining a much more manageable scaling of computational cost with respect to the number of basis functions.

2.3.1 The Rayleigh-Ritz Variational Principle

The non-relativistic time independent electronic Hamiltonian, as given in Eq. (2.5), can be written as,

$$\hat{\mathcal{H}}(v) = \hat{T} + \hat{V} + \hat{W}, \tag{2.69}$$

where $\hat{T}$ is the kinetic energy operator, and $\hat{W}$ is the electron-electron repulsion operator, which are both independent of the nuclear structure for systems with equivalent numbers of electrons. The final term $\hat{V}$ is the multiplicative external potential, typically representing the nuclear potential, which is not universal for all n-electron systems, since it explicitly depends on the nuclear charges and positions, see Eq. (2.2). Requiring that the external potential $v(\mathbf{r})$ belongs to the set of ρ-representable potentials,

$$\mathcal{V}_n = \left\{ v \quad | \quad \hat{\mathcal{H}}(v) \text{ has an } n\text{-electron ground state} \quad \Psi_v \right\}, \tag{2.70}$$

the existence of a ground state is guaranteed such that,

$$\hat{\mathcal{H}}(v)\,\Psi_v = \mathcal{E}(v)\,\Psi_v \qquad \forall v \in \mathcal{V}_n. \tag{2.71}$$

This implies that the ground-state energy $\mathcal{E}(v)$ can be defined by mapping the ρ-representable potentials to real numbers,

$$\mathcal{E} : \mathcal{V}_n \mapsto \mathbb{R}. \tag{2.72}$$

Consider the set $\mathcal{W}_n$ antisymmetric n-electron wavefunctions for which $\hat{\mathcal{H}}(v)$ has a finite expectation value,

$$\mathcal{W}_n = \left\{ \Psi_v \quad | \quad \langle \Psi_v | \Psi_v \rangle = 1; \quad \langle \Psi_v | \hat{\mathcal{H}}(v) | \Psi_v \rangle < \infty \right\}. \tag{2.73}$$

The Rayleigh-Ritz variation principle can be used to define the ground-state solution, for all pairs of potentials and wavefunctions $(v, \Psi) \in \mathcal{V}_n \times \mathcal{W}_n$,

$$\mathcal{E}(v) \leq \langle \Psi | \hat{\mathcal{H}}(v) | \Psi \rangle. \tag{2.74}$$

For each $v \in \mathcal{V}_n$, one or more ground-state solutions $\Psi_v \in \mathcal{W}_n$ exist as the global minimisers for the Rayleigh-Ritz variation principle, with,

$$\mathcal{E}(v) = \langle \Psi_v | \hat{\mathcal{H}}(v) | \Psi_v \rangle, \quad \Psi_v \in \underset{\Psi \in \mathcal{W}_n}{\arg\min} \langle \Psi | \hat{\mathcal{H}}(v) | \Psi \rangle. \tag{2.75}$$

From this theorem, it's possible to construct a linear combination of the x normalised, degenerate ground-state eigenfunctions as the global minimiser Ψ_v for a system with x-fold degenerate wavefunctions.

2.3.2 The Hohenberg-Kohn Theorems

In general the ideas set out by Hohenberg and Kohn[64] are presented as two fundamental theorems.

The First Hohenberg-Kohn Theorem

Consider shifting the external potential by an additive constant,

$$v_2 = v_1 + c \qquad c \in \mathbb{R} \tag{2.76}$$

The corresponding n-electron Hamiltonian and ground state energy are transformed as,

$$\hat{\mathcal{H}}(v_2) = \hat{\mathcal{H}}(v_1 + c) = \hat{\mathcal{H}}(0) + \sum_i (v_1(\mathbf{r}_i) + c) = \hat{\mathcal{H}}(v_1) + nc, \tag{2.77}$$

$$\mathcal{E}(v_2) = \mathcal{E}(v_1 + c) = \mathcal{E}(v_1) + nc, \tag{2.78}$$

therefore, it can be seen that the ground-state wavefunction is invariant to a gauge transformation of this form. Considering two potentials $v_1, v_2 \in \mathcal{V}_n$ assumed to share the same ground-state wavefunction Ψ, the difference between their corresponding Schödinger equations can be written as,

$$\left[\hat{\mathcal{H}}(v_1) - \hat{\mathcal{H}}(v_2)\right]\Psi = \sum_i \left[v_1(\mathbf{r}_i) - v_2(\mathbf{r}_i)\right]\Psi = \left[\mathcal{E}(v_1) - \mathcal{E}(v_2)\right]\Psi \tag{2.79}$$

The contributions from $\hat{T}$ and $\hat{W}$ are equivalent in each Hamiltonian since the number of electrons is the same, and therefore, cancel. Eliminating Ψ leads to,

$$\sum_i \left[v_1(\mathbf{r}_i) - v_2(\mathbf{r}_i)\right] = \mathcal{E}(v_1) - \mathcal{E}(v_2) \Rightarrow v_1(\mathbf{r}_i) - v_2(\mathbf{r}_i) = c \in \mathbb{R}. \tag{2.80}$$

This demonstrates that v_1 and v_2 must be equal to within an additive constant $c \in \mathbb{R}$, otherwise they could not yield the same wavefunction.

This idea can be extended to electron densities, given a v-representable ground-state density, $\rho \in \mathcal{A}_n$,

$$\mathcal{A}_n = \{\rho | \rho \text{ is yielded from an } n\text{-electron ground state of } \mathcal{H}(v) \quad v \in \mathcal{V}_n\}, \tag{2.81}$$

related to a potential $v_1 \in \mathcal{V}_n$, the Rayleigh-Ritz variational principle and Eq. (2.80) can be applied showing that for all $v_2 \in \mathcal{V}_n$,

$$\begin{aligned} \mathcal{E}(v_2) &\leq \langle\Psi|\hat{\mathcal{H}}(v_1)|\Psi\rangle + (v_2 - v_1|\rho) \\ &\leq \mathcal{E}(v_1) + (v_2 - v_1|\rho), \end{aligned} \tag{2.82}$$

showing that the ground state is concave in the external potential. Here, the notation $(v|\rho) = \int v(\mathbf{r}) \cdot \rho(\mathbf{r})\, d\mathbf{r}$ has been introduced and is used hereafter. Following on from this, it can be shown that,

$$\mathcal{E}(v_2) = \mathcal{E}(v_1) + (v_2 - v_1|\rho), \quad \text{for all } v_2 = v_1 + c, \quad v \in \mathcal{V}_n, \quad c \in \mathbb{R}, \tag{2.83}$$

$$\mathcal{E}(v_2) < \mathcal{E}(v_1) + (v_2 - v_1|\rho), \quad \text{for all } v_2 \neq v_1 + c, \quad v \in \mathcal{V}_n, \quad c \in \mathbb{R}, \tag{2.84}$$

leading to the principle that two external potentials that differ by more than a constant cannot have a common ground-state. This is more concisely defined as the first Hohenberg-Kohn theorem; A ground-state electron density determines the external potential uniquely up to an additive constant.

$$v_1 - v_2 \neq c \rightarrow \rho_1 - \rho_2 \neq 0 \qquad \rho_1, \rho_2 \in \mathcal{A}_n \quad \& \quad v_1, v_2 \in \mathcal{V}_n \tag{2.85}$$

Considering two densities ρ_1, $\rho_2 \in \mathcal{A}_n$ with two corresponding potentials v_1, $v_2 \in \mathcal{V}_n$ which differ by more than an additive constant, from Eq. (2.84) the following subgradient strict inequalities can be formed,

$$\begin{aligned} \mathcal{E}(v_2) &< \mathcal{E}(v_1) - (v_1 - v_2|\rho_1), \\ \mathcal{E}(v_1) &< \mathcal{E}(v_2) + (v_1 - v_2|\rho_1), \end{aligned} \tag{2.86}$$

Adding these together leads to,

$$(v_1 - v_2|\rho_1 - \rho_2) < 0 \qquad for v_1 - v_2 \neq c. \tag{2.87}$$

Hence, proving the first Hohenberg-Kohn theorem.

The Second Hohenberg-Kohn Theorem

The second Hohenberg-Kohn theorem defines the variational relationship for the ground-state energy in terms of the electron density. First, the Hohenberg-Kohn inequality is defined as,

$$\mathcal{E}(v) \leq F_{\mathrm{HK}}(\rho) + (v|\rho) \tag{2.88}$$

where F_{HK} is the *Hohenberg-Kohn universal density functional*, given by,

$$F_{\mathrm{HK}}(\rho) = \mathcal{E}(v_\rho) - (v_\rho|\rho), \tag{2.89}$$

and $\rho \in \mathcal{A}_n$ is a ground-state density of $v_\rho \in \mathcal{V}_n$. This can additionally be rearranged to produce a second important inequality,

$$F_{\mathrm{HK}}(\rho) \geq \mathcal{E}(v) - (v|\rho). \tag{2.90}$$

Both the inequalities Eq. (2.88) and Eq. (2.90) can be sharpened to an equality by respectively minimising or maximising the right-hand sides, producing two variational

principles. For $v \in \mathcal{V}_n$ & $\rho \in \mathcal{A}_n$,

$$\textbf{Hohenberg-Kohn Variation Principle:} \qquad \mathcal{E}(v) = \min_{\rho \in \mathcal{A}_n} \{F_{\mathrm{HK}}(\rho) + (v|\rho)\} \tag{2.91}$$

$$\textbf{Lieb Variation Principle:} \qquad F_{\mathrm{HK}}(\rho) = \max_{v \in \mathcal{V}_n} \{\mathcal{E}(v) - (v|\rho)\} \tag{2.92}$$

Through the Hohenberg-Kohn variational principle, it is possible to compute the ground-state energy for a given potential using the Hohenberg-Kohn functional,

$$F_{\mathrm{HK}}(\rho) = \langle \Psi_\rho | \hat{\mathcal{H}}(0) | \Psi_\rho \rangle = \langle \Psi_\rho | \hat{T} + \hat{W} | \Psi_\rho \rangle. \tag{2.93}$$

The exact form of $F_{\mathrm{HK}}(\rho)$ in terms of the density however, is unknown, requiring approximations to be constructed for it to be practically applied.

2.3.3 The Levy-Lieb Constrained Search

The Hohenberg-Kohn theorems represented a ground breaking method for approaching electronic structure problems, however, they are difficult to apply in practice due to the requirement that $v \in \mathcal{V}_n$ and $\rho \in \mathcal{A}_n$, where the sets $\mathcal{V}_n$ and $\mathcal{A}_n$ are unknown. This led to the work of Levy[65] and Lieb[66], who built upon this work improving the definitions such that a more generalised formulation of DFT could be presented, improving its practical utility.

To add some clarity to the following sections a brief discussion of some of the foundational mathematical concepts is considered. A full mathematical understanding of the following theorems is beyond the scope of this work, however, more in depth discussions can be found in the works of Eschrig[67], Helgaker[68]

Vector Spaces

A mathematical field is defined as a set of elements that satisfy the field axioms for addition and multiplication;

Axiom	Addition	Multiplication
Associativity	$(a+b)+c = a+(b+c)$	$(ab)c = a(bc)$
Commutativity	$a+b = b+a$	$ab = ba$
Distributivity	$a(b+c) = ab+ac$	$(a+b)c = ac+bc$
Identity	$a+0 = 0+a = a$	$a \cdot 1 = 1 \cdot a = a$
Inverses	$a+(-a) = (-a)+a = 0$	$aa^{-1} = a^{-1}a = 1, \quad (a \neq 0)$

A vector space $\mathcal{V}$ can be constructed over a scalar field $\mathbb{F}$ if the elements $\mathbf{x}, \mathbf{y}, \mathbf{z} \in \mathcal{V}$ and $a, b \in \mathbb{F}$ satisfy,

A norm may be defined for a vector space $\mathcal{V}$ as $\|\cdot\| : \mathcal{V} \to \mathbb{R}$ if the following conditions are met $\forall \mathbf{xy} \in \mathcal{V}$ and $a \in \mathbb{R}$,

- $\|\mathbf{x}\| \geq 0$ and $\|\mathbf{x}\| = 0$ if and only if $\mathbf{x} = \mathbf{0}$,
- $\|\mathbf{x}+\mathbf{y}\| \leq \|\mathbf{x}\| + \|\mathbf{y}\|$,

Vector Space Axioms	Operations
Associativity of Addition	$\mathbf{x}+(\mathbf{y}+\mathbf{z})=(\mathbf{x}+\mathbf{y})+\mathbf{z}$
Commutativity of Addition	$\mathbf{x}+\mathbf{y}=\mathbf{y}+\mathbf{x}$
Zero Vector	$\exists\mathbf{0}\in\mathcal{V}$ where $\mathbf{x}+\mathbf{0}=\mathbf{x},\ \forall\mathbf{x}\in\mathcal{V}$
Additive Inverse	$\forall\mathbf{x}\in\mathcal{V},\ \exists\mathbf{y}\in\mathcal{V}$ where $\mathbf{x}+\mathbf{y}=\mathbf{0}$
Associativity of Multiplication	$a\,(b\mathbf{x})=(ab)\,\mathbf{x}$
Distributivity	$a\,(\mathbf{x}+\mathbf{y})=a\mathbf{x}+a\mathbf{y}$
Multiplicative Identity	$\exists 1\in\mathbb{F}$ where $1\cdot\mathbf{x},\ \forall\mathbf{x}\in\mathcal{V}$

- $\|a\mathbf{x}\|=|a|\,\|\mathbf{x}\|$.

If a vector space has a defined norm it is known as a normed vector space. It is also considered complete if and only if every Cauchy sequence, a sequence $\{x_i\}$ for which $\forall\epsilon>0$ there is an $N\in\mathbb{N}$ such that $|x_i-x_j|\leq\epsilon$ when $i,j\geq N$, in $\mathcal{V}$ converges to an element of $\mathcal{V}$. If a given vector space is both normed and complete it is considered a Banach space within which a p-norm can be defined as,

$$||\mathbf{x}||_p=\left(\sum_i|x_i|^p\right)^{\frac{1}{p}}. \tag{2.94}$$

An inner product on the vector space $\mathcal{V}$ is a mapping $(\cdot,\cdot):\mathcal{V}\times\mathcal{V}\mapsto\mathbb{R}$ such that $\forall\mathbf{x},\mathbf{yz}\in\mathcal{V}$ and $\forall\alpha\in\mathbb{R}$:

- $(\mathbf{x},\mathbf{x})\geq 0$ and $(\mathbf{x},\mathbf{x})=0$ if and only if $\mathbf{x}=\mathbf{0}$,
- $(\mathbf{x}+\mathbf{y},\mathbf{z})=(\mathbf{x},\mathbf{z})+(\mathbf{y},\mathbf{z})$
- $(\alpha\mathbf{x},\mathbf{y})=\alpha(\mathbf{x},\mathbf{y})$
- $(\mathbf{x},\mathbf{y})=(\mathbf{y},\mathbf{x})^*$

If a vector space has a defined inner-product it is considered an inner product space. Additionally if a Banach space has a defined inner product it as referred to as a Hilbert space.

An important subset of the Banach spaces are the Lebesgue spaces, which can be defined as a Banach space which consists of functions whose p-norm, defined in Eq. (2.94), is Lebesgue p-integrable. They are denoted as $L^p(S)$ giving the space of measurable functions f over the field S which satisfy the identity,

$$||f||_p=\left(\int_S|f\,(\mathbf{r})\,|^p d\mathbf{r}\right)^{\frac{1}{p}}<+\infty. \tag{2.95}$$

The Generalised Rayleigh-Ritz Variation Principle

The requirement that $v\in\mathcal{V}_n$ was made to ensure that, for any n-electron system, the ground state Ψ_0 exists in the Rayleigh-Ritz variation principle, introduced in section 2.3.1. Considering instead the n-electron ground state as the infimum[i] of the expectation

[i] If the subset $\mathcal{S}\subset\mathcal{A}$ has lower bounds a_l, the element $a\in a_l$ for which $a\geq\alpha\in a_l$ is the greatest lower bound of $\mathcal{S}$ termed its *infimum*. Equivalently the *supremum* can be defined as the least upper bound of $\mathcal{S}$.

value of the Hamiltonian,

$$\mathcal{E}(v) = \inf_{\Psi \in \mathcal{W}_n} \langle \Psi | \hat{\mathcal{H}}(v) | \Psi \rangle \quad \forall v \in \mathcal{U}, \tag{2.96}$$

in which the set of all admissible potentials $\mathcal{U}$ (and normalised wave-functions $\mathcal{W}_n$) are defined by,

$$|\langle \Psi | \hat{\mathcal{H}}(v) | \Psi \rangle| < \infty \qquad \forall \Psi \in \mathcal{W}_n, \quad v \in \mathcal{U}. \tag{2.97}$$

This defines a general formulation of the Rayleigh-Ritz variation principle which doesn't require $v \in \mathcal{V}_n$. For a subset of $\mathcal{U}$ there exists a Ψ_0 of $\hat{\mathcal{H}}$ and $v \in \mathcal{V}_n$, giving a minimum for the Rayleigh-Ritz variation principle. When this is not the case, $v \notin \mathcal{V}_n$, no minimising wavefunction can exist and $\mathcal{E}(v)$ is the infimum over all expectation values for all $\Psi \in \mathcal{W}_n$. The set of admissible n-electron wavefunctions, $\mathcal{W}_n$, can therefore, be characterised as the set of normalised, antisymmetric n-electron wavefunctions, Ψ, with a finite expectation value,

$$\mathcal{W}_n = \left\{ \Psi \,\middle|\, \|\Psi\|_2 = 1,\ |\langle \Psi | \hat{\mathcal{H}}(v) | \Psi \rangle| < \infty,\ v \in \mathcal{V}_C,\ n\text{-elec},\ \text{antisymmetric} \right\}, \tag{2.98}$$

where $\mathcal{V}_C$ is the set of all point charge Coulomb potentials,

$$\mathcal{V}_C = \left\{ v \,\middle|\, v(\mathbf{r}) = -\sum_A \frac{Z_A}{|\mathbf{r} - \mathbf{R}_A|}, \quad N_{\text{nuc}} \in \mathbb{N}, \quad Z_A \in \mathbb{R} \right\}. \tag{2.99}$$

As $\mathcal{W}_n$ includes systems where $Z_A = 0$, resulting in $v = 0$, for Eq. (2.98) to be satisfied it is necessary for the expectation values of the kinetic and two electron operators to be finite for all possible wavefunctions,

$$|\langle \Psi | \hat{\mathcal{H}}(0) | \Psi \rangle| < \infty \quad \Longrightarrow \quad \langle \Psi | \hat{T} | \Psi \rangle < \infty \quad \& \quad \langle \Psi | \hat{W} | \Psi \rangle < \infty \tag{2.100}$$

From this it can be shown that any admissible n-electron wavefunction must belong to the first-order Sobolev space, $\Psi \in \hat{\mathcal{H}}^1_n$,[66] where the inner product of a given function must be finite,

$$\hat{\mathcal{H}}^1_n = \left\{ \Psi \;\middle|\; |\langle \Psi | \Psi \rangle + \sum_i \langle \nabla_i \Psi | \nabla_i \Psi \rangle| < \infty \right\}. \tag{2.101}$$

n-Representable Electron Densities

The next step would be to identify which density functions $\rho(\mathbf{r})$, correspond to an antisymmetric wavefunction. First, consider that any n-electron density function must satisfy,

$$\rho(\mathbf{r}) \geq 0 \qquad \forall \mathbf{r} \in \mathbb{R}^3 \qquad \int \rho(\mathbf{r})\, d\mathbf{r} = n. \tag{2.102}$$

That is, that the function must be non-negative and integrate to n over all space, where n is the total number of electrons in the system. If a function satisfies these two constraints then it can be considered as belonging to a subset of the Lebesgue space $L^1\left(\mathbb{R}^3\right)$, denoted

L_n^1,

$$L_n^1 = \left\{ \rho \in L_n^1\left(\mathbb{R}^3\right) | \rho \geq 0, \quad \int \rho\left(\mathbf{r}\right) d\mathbf{r} = n \right\}. \tag{2.103}$$

This on its own is not enough to ensure any density $\rho \in L_n^1$ is yielded by an n-electron wavefunction $\Psi \in \mathcal{W}_n$. We define the set of n representable densities as,

$$\mathcal{I}_n = \left\{ \rho \,|\rho \text{ can be obtained from } \Psi \in \mathcal{W}_n \right\}. \tag{2.104}$$

The set of n-representable densities must be determined such that $\rho \in L_n^1$ for which $\rho \in \mathcal{I}_n$ can be determined without evaluating the wavefunction $\Psi \in \mathcal{H}_n^1$ that gives ρ.

From Eq. (2.98), only densities pertaining to antisymmetric wavefunctions are n-representable, however, it can be shown that each $\rho \in L_n^1$ corresponds to an n-electron antisymmetric wavefunction, which may be taken to be a Slater determinant. Considering a set of n complex orbitals,

$$\phi_k\left(\mathbf{r}\right) = \sqrt{\frac{\rho\left(\mathbf{r}\right)}{n}} \exp\left[2\pi i \left(k-1\right) q\left(x\right)\right], \qquad k = 1, 2, \ldots, n \tag{2.105}$$

where $q\left(x\right)$ is defined as,

$$q\left(x\right) = \frac{1}{n} \int_{-\infty}^{x} \int_{-\infty}^{\infty} \int_{-\infty}^{\infty} \rho\left(t, y, z\right) dt dy dz, \tag{2.106}$$

and is real and non-negative. A Slater determinant to give any electron density $\rho \in L_n^1$ can be constructed from the set of orbitals $\{\phi_k\}$ and the spin functions σ_α and σ_β,

$$\rho_{\text{SD}}\left(\mathbf{r}\right) = \sum_k \left|\phi_k\left(\mathbf{r}\right)\right|^2 = \sum_k n^{-1} \rho\left(\mathbf{r}\right) = \rho\left(\mathbf{r}\right). \tag{2.107}$$

However, this still doesn't ensure that all the expectation values of the Hamiltonian are finite. To do this we can consider the von Weizsäcker kinetic energy functional,

$$T^{vW} : L_n^1 \rightarrow \left(0, +\infty\right], \tag{2.108}$$

$$T^{vW}\left(\rho\right) = \frac{1}{8} \int \frac{\left|\nabla \rho\left(\mathbf{r}\right)\right|^2}{\rho\left(\mathbf{r}\right)} d\mathbf{r}. \tag{2.109}$$

The von Weizsäcker kinetic energy is exact for a one-electron, or spin paired two-electron system and can be considered a lower bound to the kinetic energy of all n-electron wavefunctions with the same density,

$$T^{vW}\left(\rho\right) \leq \inf_{\Psi \rightarrow \rho} \langle \Psi | \hat{T} | \Psi \rangle < \infty, \rho \in \mathcal{I}_n. \tag{2.110}$$

Considering some density $\rho \in L_n^1$, which can be obtained from a Slater determinant Ψ_ρ^{SD}, it can be shown that,

$$\langle \Psi_\rho^{\text{SD}} | \hat{T} | \Psi_\rho^{\text{SD}} \rangle \leq \frac{16\pi^2 n^2}{3} T^{vW}\left(\rho\right) \tag{2.111}$$

From this it follows that if $T^{vW}\left(\rho\right) < \infty$ then $\Psi_\rho^{\text{SD}} \in \mathcal{W}_n$ and $\rho \in \mathcal{I}_n$. Therefore, a function

$\rho \in L_n^1\left(\mathbb{R}^3\right)$ can only be n-representable if and only if $T^{vW}\left(\rho\right)$ is finite,

$$\mathcal{I}_n = \left\{ \rho \in L_n^1\left(\mathbb{R}^3\right) | \rho \geq 0, \quad \int \rho\left(\mathbf{r}\right) d\mathbf{r} = n, \quad T^{vW}\left[\rho\right] < \infty \right\}. \tag{2.112}$$

The constraint requiring $T^{vW}\left[\rho\right]$ to be finite can be re-cast in the form,

$$|\nabla \rho^{\frac{1}{2}}| \in L^2\left(\mathbb{R}^3\right) \rightarrow \rho \in L^3\left(\mathbb{R}^3\right), \tag{2.113}$$

therefore, resulting in the Banach space of admissible densities,

$$\mathcal{X} = L^3\left(\mathbb{R}^3\right) \cap L^1\left(\mathbb{R}^3\right) \tag{2.114}$$

The Levy-Lieb Constrained-Search Functional

Now that the set of n-representable densities have been properly characterised, the generalised Rayleigh-Ritz minimisation from Eq. (2.96) can be reformulated to give a two-step minimisation, first over all $\rho \in \mathcal{I}_n$ then over all $\Psi \in \mathcal{W}_n$ that correspond to the density ρ,

$$\begin{aligned} \mathcal{E}\left(v\right) &= \inf_{\Psi \in \mathcal{W}_n} \langle \Psi | \hat{\mathcal{H}}\left(v\right) | \Psi \rangle = \inf_{\rho \in \mathcal{I}_n} \inf_{\Psi \rightarrow \rho} \langle \Psi | \hat{\mathcal{H}}\left(v\right) | \Psi \rangle \\ &= \inf_{\rho \in \mathcal{I}_n} \left\{ \inf_{\Psi \rightarrow \rho} \langle \Psi | \hat{T} + \hat{W} | \Psi \rangle + \left(v|\rho\right) \right\} \qquad \forall v \in \mathcal{V}_C. \end{aligned} \tag{2.115}$$

Here, the contribution of the potential v has been removed when performing the optimisation over the wavefunctions, as the value of $\left(v|\rho\right)$ will be equal for all $\Psi \rightarrow \rho$. From this an analogous functional, to the Hohenberg-Kohn functional, can be defined as the *Levy-Lieb constrained search functional*,

$$F_{LL} : \mathcal{I}_n \rightarrow \mathbb{R} \qquad F_{LL}\left(\rho\right) = \inf_{\Psi \rightarrow \rho} \langle \Psi | \hat{T} + \hat{W} | \Psi \rangle \qquad \forall \rho \in \mathcal{I}_n \tag{2.116}$$

representing a minimum for the kinetic and Coulomb repulsion energies for a given density ρ. It can be shown that a minimising wavefunction exists for all $\rho \in \mathcal{I}_n$, allowing the infimum in Eq. (2.116) to be replaced by a minimum,[66]

$$F_{LL}\left(\rho\right) = \min_{\Psi \rightarrow \rho} \langle \Psi | \hat{T} + \hat{W} | \Psi \rangle \qquad \forall \rho \in \mathcal{I}_n \tag{2.117}$$

for which a minimising, positive finite density always exists. This can be combined with the Hohenberg-Kohn variation principle Eq. (2.91),

$$\mathcal{E}\left(v\right) = \inf_{\rho \in \mathcal{I}_n} \left\{ F_{LL}\left(\rho\right) + \left(v|\rho\right) \right\} \qquad \forall v \in \mathcal{V}_C, \tag{2.118}$$

generalising the minimum to an infimum and requiring only the explicitly known sets of densities and potentials, $\mathcal{I}_n$ and $\mathcal{V}_C$, solving the representability problem of Hohenberg and Kohn's original formulation.

2.3.4 The Lieb Functional

Before continuing with the discussion of Lieb's reformulation to ensure a unique solution, the concept of a convex function is first introduced.

Convex Functions

A given function can be considered convex when the interpolation characteristic inequality is satisfied, that is, if any point on a linear interpolation between two points $f(x_1)$ and $f(x_2)$ is greater than the value of the function at that point,

$$\alpha f(x_1) + (1-\alpha) f(x_2) \geq f(\alpha x_1 + (1-\alpha) x_2) \qquad 0 \leq \alpha \leq 1. \tag{2.119}$$

This is demonstrated in Fig. 2.2. A function is further considered *strictly* convex if the interpolant is always greater than the function hence sharpening the inequality to a strict inequality ($>$ in the place of $\geq$) giving it a unique minimiser. A continuum set of lines defined at each point of the function, known as *supporting lines*, can be used to define a convex function, also shown in Fig. 2.2. Each supporting line is defined such that it only intersects the convex function $f(x)$, at a single value and does not exceed the value of $f(X)$ at any point. The resulting slope of the supporting line, which intersects $f(x)$ at x, is defined as the subgradient of $f(x)$ at x, which leads to the definition of the supporting line as,

$$l_y(x) = xy - g(y), \tag{2.120}$$

where y is the slope and $-g(y)$ is the intersection of the line with the function axis. At any given point x, the value of $f(x)$ is given exactly by the largest value of any of its supporting lines at x, otherwise referred to as the pointwise supremum of its supporting lines,

$$f(x) = \sup_y \{xy - g(y)\} \tag{2.121}$$

Therefore, the convex function $f(x)$ can is shown to be completely described by the function $g(y)$, the function that defines the point at which the supporting line with slope y crosses the function axis. This representation of $f(x)$ by $g(y)$ is known as the Legendre-Fenchel transformation, which has the more general definition; for any convex function $f : \mathbb{R} \mapsto \mathbb{R}$, there exists a conjugate function f^* such that,

$$f(x) = \sup_{y \in \mathbb{R}} \{xy - f^*(y)\} \tag{2.122}$$

$$f^*(y) = \sup_{y \in \mathbb{R}} \{xy - f(x)\} \tag{2.123}$$

An additional Legendre-Fenchel transform can be applied to f^* giving f^{**}, the biconjugate function of f, which will have the following identities,

$$f^{**} \leq f \qquad \& \qquad f^{**} = f \text{ if } f \text{ is convex}, \tag{2.124}$$

from which it can be inferred that applying the Legendre-Fenchel transform to a convex

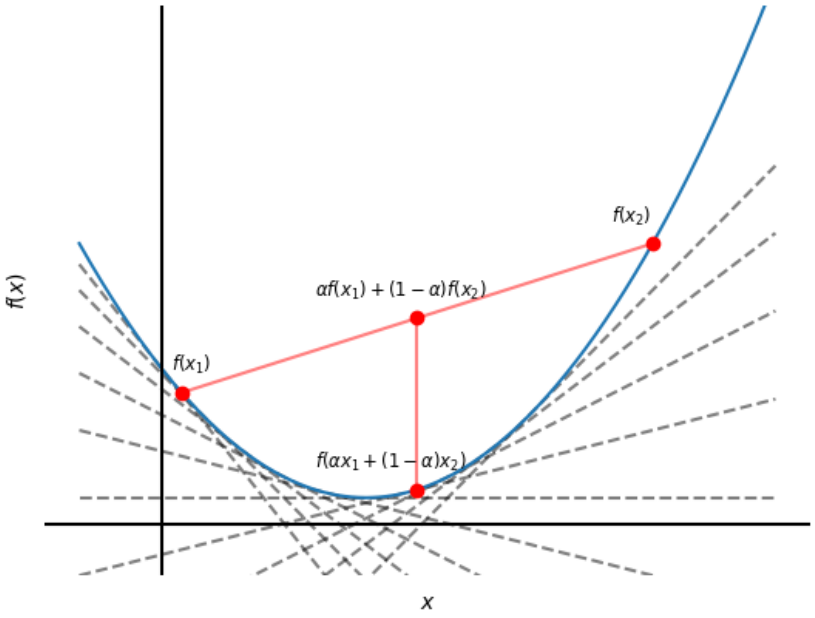

Figure 2.2: A subset of supporting lines for a convex function $f(x)$, with a demonstration of the linear interpolation characteristic inequality between two points $f(x_1)$ and $f(x_2)$.

function results in no loss of information and can be completely reversed. It is important to note that the functions f^* and f^{**} are always closed convex functions, even if the original function f is not convex itself. Following on from this therefore, the Fenchel-Moreau biconjugate theorem can be defined which states that, through conjugation a bijective mapping between the sets of closed convex functions $\Gamma(\chi)$ & $\Gamma(\chi^*)$ can be established over the dual spaces of χ & χ^* respectively. A pair of functions $f \in \Gamma(\chi)$ & $g \in \Gamma(\chi^*)$ are defined as dual functions, in which f can be fully reconstructed from g and *vice verse*. In the cases where f is not convex the biconjugate function gives the largest convex lower bound to f, known as the *convex envelope* or the *lower semi-continuous hull*.

In addition to convex functions, a concave function can be defined in a similar manner, whereby the concave conjugate is denoted,

$$f^{\circ}(y) = -f^*(-y), \tag{2.125}$$

which results in the accompanying *skew-conjugate* relations,

$$f^{\circ}(y) = \inf_{x \in \chi} \{f(x) + xy\} \tag{2.126}$$

$$f^{**}(x) = \sup_{y \in \chi^*} \{f^{\circ}(y) - xy\}. \tag{2.127}$$

From which the bijective mapping $\Gamma(\chi) \Leftrightarrow -\Gamma^*(\chi^*)$ can be formed from the closed convex functions on χ and the closed concave functions on χ^*.

Ensemble State Densities

So far it has been assumed that densities pertain to wavefunctions that can be described by a single normalised n-electron wavefunction, known as *pure-state* wavefunctions. This however, is not always appropriate for accurately representing the electronic state of a given system, leading to the need to consider an *ensemble* state instead, which is determined as a convex combination of pure-state wavefunctions. This can be particularly important when considering systems with multiple degenerate states. An ensemble density matrix γ represents the probability distribution for the set of n-electron states and can be constructed as,

$$\gamma = \sum_i \lambda_i |\Psi_i\rangle\langle\Psi_i| \qquad \lambda_i \geq 0 \qquad \sum_i \lambda_i = 1 \qquad \Psi_i \in \mathcal{W}_n. \tag{2.128}$$

The generalised Rayleigh-Ritz variation principle can then be applied to canonical ensembles, where the canonical ensemble ground state energy can be defined as,

$$\mathcal{E}(v) = \inf_{\gamma \in \mathcal{K}_n} \mathrm{tr}\gamma\hat{\mathcal{H}}(v), \tag{2.129}$$

where, $\mathcal{K}_n$ is the set of admissible ensemble density matrices,

$$\mathcal{K}_n = \left\{ \gamma = \sum_i \lambda_i |\Psi_i\rangle\langle\Psi_i| \;\middle|\; \lambda_i \geq 0, \quad \sum_i \lambda_i = 1, \quad \Psi_i \in \mathcal{W}_n \right\}. \tag{2.130}$$

This approach can also be applied with the Levy-Lieb constrained search producing the Lieb density-matrix constrained search functional,

$$F_{DM}(\rho) = \inf_{\gamma \to \rho} \mathrm{tr}\gamma\hat{\mathcal{H}}(0), \tag{2.131}$$

which is convex in ρ and a lower bound to F_{LL}, where $F_{DM} = F_{LL}$ if the density is pure-state representable.

The Lieb Functional

Recalling the second Hohenberg-Kohn theorem, Eq. (2.91) and Eq. (2.92) can be re-written as an infimum and supremum respectively,

$$\begin{aligned} \mathcal{E}(v) &= \inf_{\rho} \{F(\rho) + (v|\rho)\}, \\ F(\rho) &= \sup_{v} \{\mathcal{E}(v) - (v|\rho)\}. \end{aligned} \tag{2.132}$$

It can then be shown that $\mathcal{E}$ is a concave functional of v,

$$\begin{aligned} \mathcal{E}[\lambda v_1 + (1-\lambda) v_2] &= \inf_{\Psi} \left[\lambda \langle\Psi|\hat{\mathcal{H}}(v_1)|\Psi\rangle + (1-\lambda)\langle\Psi|\hat{\mathcal{H}}(v_2)|\Psi\rangle \right] \\ &\geq \lambda \inf_{\Psi} \left[\langle\Psi|\hat{\mathcal{H}}(v_1)|\Psi\rangle \right] + (1-\lambda) \inf_{\Psi} \left[\langle\Psi|\hat{\mathcal{H}}(v_2)|\Psi\rangle \right] \\ &= \lambda\mathcal{E}(v_1) + (1-\lambda)\mathcal{E}(v_2), \qquad 0 < \lambda < 1. \end{aligned} \tag{2.133}$$

From this it can be deduced that $\mathcal{E}(v)$ is a concave functional and $F(\rho)$ is its convex conjugate, meaning that $F(\rho)$ provides an exact description for $\mathcal{E}(v)$ and v and ρ are conjugate variables, belonging to dual vector spaces.

From the constraints that the density must be normalised and integrate to n over all space $\left(\rho \in L^1\right)$ and that the kinetic energy must be finite $\left(\nabla \rho^{1/2} \in L^2\right)$, a vector space for the admissible densities $\mathcal{X}$ can be defined as $\rho \in L^3 \cap L^1$. However, from the Levy-Lieb constrained search formalism, the potential is also required to have a finite interaction with the density, which was shown to only occur if $v \in L^{3/2} + L^{\infty}$ defined as $\mathcal{X}^*$.[66] Together $\mathcal{X}$ and $\mathcal{X}^*$ are dual vector spaces, and therefore, the Lieb functional can be formulated as,

$$F(\rho) = \sup_{v \in \mathcal{X}^*} \{\mathcal{E}(v) - (v|\rho)\} \qquad \rho \in \mathcal{X}, \tag{2.134}$$

with the dual energy functional given by,

$$\mathcal{E}(v) = \inf_{\rho \in \mathcal{X}} \{F(\rho) + (\rho|v)\} \qquad v \in \mathcal{X}^*. \tag{2.135}$$

The Hohenberg-Kohn universal functional, the Levy-Lieb constrained search functional and the Lieb functional are all equivalent for non-degenerate ground state densities, however, only the later two are defined when ρ corresponds to a non-ground state density. The Lieb functional additionally has a unique optimiser, due to it being the convex envelope of the constrained search functional, which itself is not convex and so may not have a unique optimiser.

2.3.5 Kohn-Sham Density-Functional Theory

Density-functional theory in its form as discussed up to this point is formally exact, however, in practice this is not the case due to the inability to form an exact analytical expression for the universal functional $F(\rho)$ as it includes the fully interacting two-electron term, in analogy to the discussion for HF theory in section 2.1.3. Therefore, approximations are required to enable the practical use of DFT.

The Kohn-Sham Equations

In an attempt to address this problem, Kohn and Sham proposed a different formalism based on the concept that for any n-electron system, an n-electron non-interacting system with equivalent density can be constructed.[69] The following break down of the universal functional was proposed,

$$\begin{aligned} F(\rho) &= \inf_{\Psi \to \rho} \langle \Psi | \hat{T} + \hat{W} | \Psi \rangle = T(\rho) + W(\rho) \\ &= T_s(\rho) + J(\rho) + (T(\rho) - T_s(\rho)) + (W(\rho) - J(\rho)) \\ &= T_s(\rho) + J(\rho) + E_{xc}(\rho), \end{aligned} \tag{2.136}$$

where $T_s(\rho)$ is the non-interacting kinetic energy functional,

$$T_s(\rho) = \inf_{\Psi_0 \to \rho} \langle \Psi_0 | \hat{T} | \Psi_0 \rangle = \min_{\sum_i |\phi_i|^2 \to \rho} \sum_i \langle \phi_i | -\frac{1}{2}\nabla_i^2 | \phi_i \rangle \tag{2.137}$$

where Ψ_0 defines a non-interacting n-electron wavefunction for which the density can be evaluated as,

$$\rho(\mathbf{r}) = \sum_\sigma \sum_i |\phi_i(\{\mathbf{r}, \sigma\})|^2. \tag{2.138}$$

The classical Coulomb electron-electron interaction term is,

$$J(\rho) = \frac{1}{2} \int \int \frac{\rho(\mathbf{r}_1)\rho(\mathbf{r}_2)}{|\mathbf{r}_1 - \mathbf{r}_2|} d\mathbf{r}_1 d\mathbf{r}_2 \tag{2.139}$$

Finally $E_{xc}(\rho)$ is defined as the *exchange-correlation energy functional* which can be broken down into two constituent components,

$$E_{xc}(\rho) = T_c(\rho) + W_{xc}(\rho), \tag{2.140}$$

which are in turn defined as; the *kinetic energy correlation correction*,

$$T_c(\rho) = T(\rho) - T_s(\rho) \geq 0, \tag{2.141}$$

and the *two-electron exchange and correlation*,

$$W_{xc}(\rho) = W(\rho) - J(\rho) \leq 0. \tag{2.142}$$

As both $T_s(\rho)$ and $J(\rho)$ are known analytically, this reduces the problem to finding an approximation to $E_{xc}(\rho)$, which, is a relatively small component of $F(\rho)$.

The expression for the total Kohn-Sham energy can be written as,

$$\mathcal{E}(v) = T_s(\rho) + J(\rho) + E_{xc}(\rho) + (v|\rho), \tag{2.143}$$

which can be variationally minimised over the density, which is represented by a set of n orthonormal, one-electron slater determinants, in a manner similar to that discussed for HF theory in section 2.1.3. This implies that the ground state energy corresponds to the point at which the functional derivative of the energy with respect to ρ is zero. This can be expressed as a Euler equation,

$$\frac{\delta}{\delta\rho(\mathbf{r})} \left\{ F(\rho) + \int v(\mathbf{r})\rho(\mathbf{r})\, d\mathbf{r} - \mu \int \rho(\mathbf{r}) \right\} = 0 \tag{2.144}$$

where μ is a Lagrange multiplier enforcing the constraints of Eq. (2.102). If $F(\rho)$ is assumed to be differentiable[70;71] this can be re-written as,

$$\frac{\delta F(\rho)}{\delta\rho(\mathbf{r})} + v(\mathbf{r}) = \mu. \tag{2.145}$$

In reality, $F(\rho)$ is not differentiable, see Ref. 70 for discussion. However, it may be regularised

via Moreau-Yosida regularisation, as described in Ref. 71. For such regularised forms the Euler equations can be rigorously constructed.

For a non-interacting system this can be written in terms of the non-interacting kinetic energy functional and a potential, termed the Kohn-Sham potential $v_s(\mathbf{r})$,

$$\frac{\delta T_s(\rho)}{\delta \rho(\mathbf{r})} + v_s(\mathbf{r}) = \mu. \tag{2.146}$$

The Kohn-Sham definition for $F(\rho)$ leads to the following breakdown of $v_s(\mathbf{r})$ for a fully interacting system,

$$v_s(\mathbf{r}) = v_{ext}(\mathbf{r}) + v_J(\mathbf{r}) + v_{xc}(\mathbf{r}), \tag{2.147}$$

where,

$$v_J(\mathbf{r}) = \frac{\delta J(\rho)}{\delta \rho(\mathbf{r})}, \tag{2.148}$$

$$v_{xc}(\mathbf{r}) = \frac{\delta E_{xc}(\rho)}{\delta \rho(\mathbf{r})} \tag{2.149}$$

and $v_{ext}(\mathbf{r})$ is the potential that the electrons experience due to the nuclear charges within the system. This leads to a set of one-electron equations in terms of molecular orbitals,

$$\left[-\frac{1}{2}\nabla^2 + v_s(\mathbf{r})\right]\phi_i(\{\mathbf{r},\sigma\}) = \varepsilon_i \phi_i(\{\mathbf{r},\sigma\}), \tag{2.150}$$

where ε_i is the energy of the corresponding Kohn-Sham orbitals ϕ_i. These equations can be solved self-consistently in analogy to the canonical Hartree-Fock equations.

2.3.6 Exchange-Correlation Functionals

The exact form of the exchange-correlation functional is not known, however, several logical constraints can be used to guide the development of sensible approximations required for the practical use of DFT. The first is that exchange is always present in any given system, but correlation is only present when the system contains more than one electron. Both however, lower the electronic energy of any given system, $E_x(\rho) < 0$ & $E_c(\rho) \leq 0$. The second constraint is that the exact exchange energy of any given one-electron system directly cancels the Coulomb self-repulsion term, $E_x(\rho) = -J(\rho)$. Additionally, as the exchange energy for a uniform electron gas is known, it follows that, in the limit of slowly-varying density,

$$\lim_{\nabla\rho(\mathbf{r})\to 0} E_x(\rho) = -\frac{3}{4}\left(\frac{3}{\pi}\right)^{1/3}\int \rho^{4/3}(\mathbf{r})\, d\mathbf{r}. \tag{2.151}$$

Lieb and Oxford[72] provided a bound on the exchange-correlation energy of a given system,

$$E_x(\rho) \geq E_{xc}(\rho) \geq -1.68\int \rho^{4/3}(\mathbf{r}). \tag{2.152}$$

Finally, Levy[65] provided a scaling relation for the density with respect to uniform scaling of the coordinates. Many constraints can be derived from these relations, some of the most

important of which are,

$$E_x(\rho) = \lambda E_x(\rho), \tag{2.153}$$

$$\lim_{\lambda\to\infty} E_c(\rho) > -\infty, \tag{2.154}$$

$$\lim_{|\mathbf{r}|\to\infty} v_{xc}(\mathbf{r}) = -\frac{1}{|\mathbf{r}|}, \tag{2.155}$$

$$\lim_{|\mathbf{r}|\to\infty} w_{xc}(\mathbf{r}) = -\frac{1}{2|\mathbf{r}|}, \tag{2.156}$$

where $w_{xc}(\mathbf{r})$ defines the exchange-correlation energy per electron and unit volume, which can be related to the total exchange-correlation energy,

$$E_{xc}(\rho) = \int w_{xc}(\mathbf{r})\,\rho(\mathbf{r})\,d\mathbf{r}. \tag{2.157}$$

For a more complete discussion of the known constraints on E_{xc} see Ref. 73–75

Local Density Approximations

The first model for the exchange-correlation functional was proposed by Kohn & Sham and is dependent on the density at a given point in space, known as the local density approximation (LDA). Some approximations are built around the exchange-correlation energy for a uniform electron gas,

$$E_{xc}^{\text{LDA}}(\rho) = \int \rho(\mathbf{r})\,\epsilon_{xc}(\rho(\mathbf{r}))\,d\mathbf{r}, \tag{2.158}$$

where ϵ_{xc} is the LDA exchange-correlation energy density, which can be broken down into separate exchange and correlation contributions,

$$\epsilon_{xc}(\rho(\mathbf{r})) = \epsilon_x(\rho(\mathbf{r})) + \epsilon_c(\rho(\mathbf{r})). \tag{2.159}$$

The exchange energy of a uniform electron gas can be given exactly by,

$$\epsilon_x(\mathbf{r}) = -\frac{3}{4}\sqrt[3]{\frac{3\rho(\mathbf{r})}{\pi}}. \tag{2.160}$$

However, no exact form of ϵ_c exists therefore, approximations have been derived from interpolation methods[76], of which the most widely adopted form is that of Vosko, Wilk and Nusair (VWN)[77].

Generalised Gradient Approximation

Local density approximations represent a reasonable approximation for calculating the exchange-correlation energy of many different systems, in particular metallic systems have been shown to be accurately modelled by LDAs. However, often to achieve the desired level of chemical accuracy, more information about the surrounding density and its non-uniformity, must be included. One such approach to this is to include, not only the density at a given point in space but also its gradient. Functionals that include this addition are typically

referred to as *generalised gradient approximations* (GGA). Typically, a density gradient dependent correction term is introduced to LDA functionals,

$$E_{xc}^{\mathrm{GGA}}(\rho) = \int \epsilon_{xc}(\mathbf{r})\, F_{xc}(\rho, s)\, \rho(\mathbf{r})\, d\mathbf{r}, \tag{2.161}$$

where F_{xc} is an enhancement factor depending on the reduced density gradient,

$$s(\mathbf{r}) = \frac{|\nabla\rho(\mathbf{r})|}{\rho^{4/3}(\mathbf{r})}. \tag{2.162}$$

The enhancement factor is the distinguishing factor between various GGAs, where it is often fitted to empirical data. By ensuring that the enhancement factor is 1 for a uniform density the correct uniform electron gas limit can be ensured. An example of a commonly used exchange functional is the Becke-88 GGA,[78] for which,

$$F_x(\rho, s) = 1 + 4\beta \frac{|s|^2}{1 + 6\beta s \sinh^{-1}(s)}, \tag{2.163}$$

where $\beta = 0.0042$, determined by fitting to calculations for the HF exchange energy of a series of noble gas atoms.

Meta-Generalised Gradient Approximations

The development of GGAs has often been considered the point where DFT became a reliable tool for calculating accurate molecular energies, however, further improvements have been made. The next logical improvement is the set of functionals known as *meta*-GGAs. This set of functionals improves upon the accuracy of GGAs by including more non-local terms in the model energy density. There are many examples of these additional terms such as the inclusion of the second-order spatial derivative of the density, $\nabla^2\rho(\mathbf{r})$, or the kinetic energy density,

$$\tau(\mathbf{r}) = \frac{1}{2}\sum_i \sum_\sigma |\nabla\phi_i(\{\mathbf{r}, \sigma\})|^2 \tag{2.164}$$

Common examples include TPSS,[79] SCAN[73–75], and ωB97xD.[80] The use of τ in these functionals allows for the recognition of regions dominated by a single orbital and in doing so the self-interaction errors of common GGAs can be reduced.

Hybrid Functionals

Up to this point it had been widely assumed that a greater overall accuracy could be achieved from a pairing of correlation density functionals with exchange density functionals, instead of exact non-local exchange, E_x^{HF}. However, Becke showed that by scaling down the proportion of exchange from the density functional and including a fraction of exact non-local exchange, it was possible to achieve a level of accuracy often exceeding that of GGAs and meta-GGAs.[81] This led to the development of an additional category of exchange-correlation functionals known as *hybrid* functionals, which have the general form,

$$E_{xc} = aE_x^{\mathrm{HF}} + (1-a)E_x^{\mathrm{DFT}} + E_c^{\mathrm{DFT}} \tag{2.165}$$

Here, a is the scaling parameter determining what fraction of exact exchange is included which is often guided by fitting to experimental reference data. One of the most common functionals used to date is the B3LYP hybrid functional[78;81;82] which has the form,

$$\begin{aligned} E_{xc}^{\text{B3LYP}} =& E_x^{\text{LDA}} + 0.2\left(E_x^{\text{HF}} - E_x^{\text{LDA}}\right) + 0.72\left(E_x^{\text{B88}} - E_x^{\text{LDA}}\right) \\ &+ E_c^{\text{VWN}} + 0.81\left(E_c^{\text{LYP}} - E_c^{\text{VWN}}\right), \end{aligned} \tag{2.166}$$

where, E_x^{B88} is the Becke-88 exchange functional, and E_c^{VWN} and E_c^{LYP} are the correlation functionals of Vosko, Wilk & Nusair[77] and Lee, Yang & Parr[81] respectively.

2.4 Systems in Strong Magnetic Fields

Thus far, methods for modelling solutions to the non-relativistic electronic Schödinger equation have been discussed, however, they are all approximations which are unable to accurately model the response of a given molecule to significant changes in its external environment. In practice there are many reasons why including how the molecule reacts to its physical environment would be invaluable to a thorough theoretical treatment. In this work, the treatment of systems with arbitrary strength external magnetic fields is considered.

The effect of an external magnetic field $\mathbf{B}$ on a chemical system can be split into three regimes, dependent on whether the magnetic or Coulomb interactions are the dominant form of interaction. The first is the *Coulomb regime* where $|\mathbf{B}| \ll 1$ a.u., (1 a.u. $= 235{,}000$ T). This describes the standard conditions on Earth where the Coulomb interactions dominate and systems exhibit familiar chemistry. The second is the *intermediate regime*, where $|\mathbf{B}| \approx 1$ a.u. Here the magnetic and Coulomb interactions are of similar importance and compete, which can result in some exotic chemistry. These conditions are found on celestial bodies such as white dwarf stars. Finally, there is the *Landau regime* where $|\mathbf{B}| \gg 1$ a.u. Within this regime the magnetic interactions become dominant leading to very exotic chemistry. This regime can be found on certain types of celestial bodies such as neutron stars, pulsars and magnetars.

Treating systems within the *Coulomb regime*, where the magnetic field can be treated as a small perturbation, is well documented and widely employed.[83–85] Moving to the *intermediate regime* and beyond however, requires a more rigorous consideration of the external field as it can no longer be considered as a small perturbation. Instead, a non-perturbative approach is employed, where self-consistent field calculations are conducted using a Hamiltonian directly incoporating the external field contributions and the resulting molecular orbitals are directly optimised in the presence of the magnetic field.[12;15;86–89]

2.4.1 The Hamiltonian

Electromagnetic fields are nonconservative, therefore the force $\mathbf{F}$ acting on a particle is dependent on its position $\mathbf{r}$, velocity $\mathbf{v}$ and time t. Any given particle, with charge Z,

within an electromagnetic field experiences the *Lorentz force*,

$$\mathbf{F}(\mathbf{r}, \mathbf{v}, t) = Z\left[\mathbf{E}(\mathbf{r}, t) + \mathbf{v} \times \mathbf{B}(\mathbf{r}, t)\right], \tag{2.167}$$

where $\mathbf{E}$ is the electric field strength and $\mathbf{B}$ is the magnetic induction. These must satisfy Maxwell's equations,

$$\nabla \cdot \mathbf{E} = \frac{\rho}{\epsilon_0} \tag{2.168}$$

$$\nabla \cdot \mathbf{B} = 0 \tag{2.169}$$

$$\nabla \times \mathbf{E} + \frac{\partial \mathbf{B}}{\partial t} = \mathbf{0} \tag{2.170}$$

$$\nabla \times \mathbf{B} - \epsilon_0 \mu_0 \frac{\partial \mathbf{E}}{\partial t} = \mu_0 \mathbf{J} \tag{2.171}$$

where $\rho(\mathbf{v}, t)$ and $\mathbf{J}(\mathbf{r}, t)$ are the charge and current densities respectively and ϵ_0 and μ_0 are known constants, the permittivity and permeability of free space respectively. In Eqs. (2.168) - (2.171) the function dependencies have been removed for simplicity. In a real system the internal fields of a given molecule would respond to an applied external field. To simplify the problem it is assumed that the electromagnetic field is fixed and unaffected by the particles, creating a semi-classical approximation. It is possible to further simplify the overall problem by writing $\mathbf{E}$ and $\mathbf{B}$ in terms of a vector potential $\mathbf{A}$. It can be shown that Eq. (2.169) is satisfied when,

$$\nabla \cdot \mathbf{B} = 0 \implies \mathbf{B} = \nabla \times \mathbf{A}, \tag{2.172}$$

which, if then substituted into Eq. (2.170), results in,

$$\nabla \times \left(\mathbf{E} + \frac{\partial \mathbf{A}}{\partial t}\right) = 0 \implies \mathbf{E} = -\nabla \phi - \frac{\partial \mathbf{A}}{\partial t}, \tag{2.173}$$

where ϕ is a scalar potential. This reduces the number of components within the potentials to four, (ϕ, A_x, A_y, A_z) rather than six, $(E_x, E_y, E_z, A_x, A_y, A_z)$.

Inherently these potentials are not unique, when transformed by an arbitrary gauge function,

$$\phi' = \phi - \frac{\partial f}{\partial t} \qquad \& \qquad \mathbf{A}' = \mathbf{A} + \nabla f, \tag{2.174}$$

it can be shown through Eq. (2.172) and Eq. (2.173), that they yield the same observable electric and magnetic fields,

$$\mathbf{E}' = -\nabla \phi' - \frac{\partial \mathbf{A}'}{\partial t} = -\phi + \frac{\partial f}{\partial t} - \frac{\partial \mathbf{A}}{\partial t} - \frac{\partial \nabla f}{\partial t} = \mathbf{E}, \tag{2.175}$$

$$\mathbf{B}' = \nabla \times \mathbf{A}' = \nabla \times (\mathbf{A} + \nabla f) = \mathbf{B} + \nabla \times \nabla f = \mathbf{B}. \tag{2.176}$$

Using the results above, a Hamiltonian operator can be defined to describe the motion of a particle within an electromagnetic field,

$$\hat{\mathcal{H}}(\mathbf{r}, \mathbf{p}) = \frac{\pi^2}{2m} + Z\phi(\mathbf{r}), \tag{2.177}$$

where $\boldsymbol{\pi}$ is the kinetic momentum,

$$\boldsymbol{\pi} = \mathbf{p} - Z\mathbf{A} = -i\hbar\nabla - Z\mathbf{A}. \tag{2.178}$$

For a given electron, where $Z = -e$, it is necessary to include additional terms to account for the electron's spin[90], this results in the following Hamiltonian for an electron,

$$\hat{\mathcal{H}} = \frac{\boldsymbol{\pi}^2}{2m} + \frac{e\hbar}{2m}\mathbf{B}\cdot\boldsymbol{\sigma} - e\phi, \tag{2.179}$$

where $\boldsymbol{\sigma}$ is the set of Pauli spin matrices,

$$\boldsymbol{\sigma}_x = \begin{pmatrix} 0 & 1 \\ 1 & 0 \end{pmatrix} \qquad \boldsymbol{\sigma}_y = \begin{pmatrix} 0 & -i \\ i & 0 \end{pmatrix} \qquad \boldsymbol{\sigma}_z = \begin{pmatrix} 1 & 0 \\ 0 & -1 \end{pmatrix} \tag{2.180}$$

The Pauli spin term is often re-written as $\mathbf{s} = \hbar\boldsymbol{\sigma}/2$ to simplify Eq. (2.179) to,

$$\hat{\mathcal{H}} = \frac{\boldsymbol{\pi}^2}{2m} + \frac{e}{m}\mathbf{B}\cdot\mathbf{s} - e\phi. \tag{2.181}$$

In a molecular system the scalar potential is assumed to be dominated by the atomic Coulomb potential,

$$\phi(\mathbf{r}) = \frac{-e}{4\pi\epsilon_0}\sum_k \frac{Z_k}{|\mathbf{r} - \mathbf{R}_k|} + \phi_{\text{ext}}(\mathbf{r}), \tag{2.182}$$

where ϕ_{ext} represents any other terms present in the scalar potential. Therefore, combining this with the expansion of $\boldsymbol{\pi}^2$ returns the zeroth-order electronic Hamiltonian $\hat{\mathcal{H}}_0$, as given by Eq. (2.5), plus a first and second-order response terms, $\hat{\mathcal{H}}^{(1)}$ and $\hat{\mathcal{H}}^{(2)}$,

$$\begin{aligned} \hat{\mathcal{H}} &= \hat{\mathcal{H}}_0 + \hat{\mathcal{H}}^{(1)} + \hat{\mathcal{H}}^{(2)} \\ &= \hat{\mathcal{H}}_0 + \sum_i \mathbf{A}(\mathbf{r}_i)\cdot\mathbf{p}_i + \sum_i \mathbf{B}(\mathbf{r}_i)\cdot\mathbf{s}_i + \frac{1}{2}\sum_i \mathbf{A}^2(\mathbf{r}_i) - \sum_i \phi_{\text{ext}}(\mathbf{r}_i) \end{aligned} \tag{2.183}$$

The first two additional terms in Eq. (2.183) are the first-order orbital and spin paramagnetic terms respectively. They are linear in $\mathbf{B}$ and can result in either a raising or lowering of the energy of the system relative to zero-field. The third additional term in Eq. (2.183) is the second-order diamagnetic term which is quadratic in $\mathbf{B}$ therefore, will always raise the energy of the system relative to zero-field.

2.4.2 Gauge-Origin Invariance

As previously described however, the potentials ϕ and $\mathbf{A}$ are not uniquely defined and can be altered by a gauge transformation whilst leaving the observable electromagnetic field unchanged. For a uniform static external magnetic field, the vector potential can be written as,

$$\mathbf{A}_{\mathbf{O}}(\mathbf{r}) = \frac{1}{2}\mathbf{B}\times(\mathbf{r} - \mathbf{O}), \tag{2.184}$$

where $\mathbf{O}$ is the arbitrary gauge origin, defined as the point in space where the vector potential vanishes,

$$\mathbf{A}_{\mathbf{O}}(\mathbf{O}) = 0. \tag{2.185}$$

This directly enters the Hamiltonian and calculated observables should be unaltered by a gauge transformation. The transformed Hamiltonian is related to the original via a unitary transform,

$$\hat{\mathcal{H}}' = \exp(-if)\,\hat{\mathcal{H}}\exp(if) \tag{2.186}$$

where f is the gauge function characterising the transformation. A common and important example is a shift in the gauge origin $\mathbf{O} \rightarrow \mathbf{G}$,

$$\mathbf{A}_{\mathbf{G}}(\mathbf{r}) = \mathbf{A}_{\mathbf{O}}(\mathbf{r}) - \mathbf{A}_{\mathbf{O}}(\mathbf{G}) = \mathbf{A}_{\mathbf{O}}(\mathbf{r}) + \nabla f, \qquad f(\mathbf{r}) = -\mathbf{A}_{\mathbf{O}}(\mathbf{G})\cdot\mathbf{r}. \tag{2.187}$$

In order for the expectation value of a given observable to be gauge origin invariant, the transformation of the Hamiltonian must be accompanied by a simultaneous transformation of the wavefunction,

$$\Psi' = \exp(-if)\,\Psi. \tag{2.188}$$

London Atomic Orbitals

Considering the transformation given by Eq. (2.188), it follows that the exact wave function is transformed as,

$$\Psi_{\mathbf{G}} = \exp\left[i\mathbf{A}_{\mathbf{O}}(\mathbf{G})\cdot\mathbf{r}\right]\Psi_{\mathbf{O}} = \exp\left[i\frac{1}{2}\mathbf{B}\times(\mathbf{G}-\mathbf{O})\cdot\mathbf{r}\right]\Psi_{\mathbf{O}} \tag{2.189}$$

The phase factor $\exp\left[i\mathbf{A}_{\mathbf{O}}(\mathbf{G})\cdot\mathbf{r}\right]$ introduces oscillations in the wave function dependent on the gauge-origin. Standard atomic orbitals, described by a finite basis set of GTOs or STOs, cannot accurately capture the change in phase required when the gauge origin is changed, however. In 1937, London proposed a modification to standard atomic orbitals by introducing the phase-factor $\exp(i\mathbf{A}(\mathbf{G};\mathbf{O})\cdot\mathbf{r})$ directly into the orbital functions,[86]

$$\omega(\mathbf{r},\mathbf{B},\mathbf{G}) = \exp\left[-i\frac{1}{2}\mathbf{B}\times(\mathbf{G}-\mathbf{K})\cdot\mathbf{r}\right]\varphi(\mathbf{r}) \tag{2.190}$$

where $\varphi(\mathbf{r})$ is a standard GTO centred at $\mathbf{K}$, as described in Eq. (2.50), $\mathbf{B}$ is the magnetic field and $\mathbf{G}$ is the gauge-origin. Utilizing this modified form of atomic orbitals makes the calculation of observables rigorously gauge-origin invariant, due to the atomic orbitals now exhibiting the correct response, to first order, to the external field for any choice of gauge-origin. They also have similar convergence with respect to system size as would be expected for field-independent quantities. These modified basis functions are referred to as *London atomic orbitals* (LAOs) or gauge-origin including atomic orbitals (GIAO) and have been used extensively for studying systems in arbitrary strength external magnetic fields.[12;13;23;37;84;85;89;91–93]

2.4.3 Current-Density-Functional Theory

When using LAOs with HF theory, although the integrals now require complex algebra, the general structure of the method remains the same. This is also largely true for correlated methods, with some modifications to the relevant CC, CI or MP equations. Due to how DFT is defined however, the variables need to be expanded to include a direct-dependence on the magnetic field, a method known as magnetic field DFT (BDFT),[94;95] or the paramagnetic current density, giving rise to *current*-DFT (cDFT),[14;96;97] which is employed throughout this work.

The Current-Density

The observable physical current density, induced by the magnetic field in the charge density of a given system, can be defined as,

$$\mathbf{j}(\mathbf{r}) = \sum_{ij}^{occ.} \left(\int \left(\phi_i^* \hat{\mathbf{p}}_j \phi_i + \rho \mathbf{A} \right) d\sigma_1 d\mathbf{x}_2 \dots d\mathbf{x}_n \right), \tag{2.191}$$

where the integral is over the spin coordinates of all electrons and the spatial coordinates of all except electron one. This is an observable quantity and therefore, must be invariant to a shift in the gauge origin. It can be decomposed into two components, the *paramagnetic current density*,

$$\mathbf{j}_p(\mathbf{r}) = -\frac{i}{2} \sum_{i}^{occ.} \left[\phi_i^*(\mathbf{r}) \nabla \phi_i(\mathbf{r}) - \phi_i(\mathbf{r}) \nabla \phi_i^*(\mathbf{r}) \right], \tag{2.192}$$

and the *diamagnetic current density*,

$$\mathbf{j}_d(\mathbf{r}) = \rho(\mathbf{r}) \mathbf{A}(\mathbf{r}). \tag{2.193}$$

The two individual components themselves are gauge dependent and therefore, vary with a gauge transformation in a compensating manner.

Constrained Search Formalism

A constrained search formalism can be applied to cDFT in the same manner as previously discussed. The energy is now dependent on both the scalar potential $u = v + \frac{1}{2}A^2$ and a vector potential $\mathbf{A}$,

$$\mathcal{E}(u, \mathbf{A}) = \inf_{\rho, \mathbf{j}_p} \left\{ F_{\mathrm{VR}}(\rho, \mathbf{j}_p) + (u|\rho) + (\mathbf{A}|\mathbf{j}_p) \right\}, \tag{2.194}$$

where $(\mathbf{A}|\mathbf{j}_p) = \int \mathbf{j}_p(\mathbf{r}) \cdot \mathbf{A}(\mathbf{r}) d\mathbf{r}$, and the Vignale-Rasolt constrained search functional, $F_{\mathrm{VR}}(\rho, \mathbf{j}_p)$, is defined as,

$$F_{\mathrm{VR}}(\rho, \mathbf{j}_p) = \sup_{u, \mathbf{A}} \left\{ \mathcal{E}(u, \mathbf{A}) - (u|\rho) - (\mathbf{A}|\mathbf{j}_p) \right\}, \tag{2.195}$$

and is dependent on both the charge density and the paramagnetic current density. This leads to a formalism which is dependent on a non-observable quantity which is in contrast to

standard DFT which is only dependent on the observable charge density. Many attempts to reformulate CDFT in terms of the observable physical current density have been made[98–100] however, to date none have proven successful. Moreover, the Vignale-Rasolt formulation has been shown to be valid and amenable to a similar treatment as given by Lieb[72] for standard DFT. For further discussion see Refs. 14 and 101

Kohn-Sham Decomposition

To make CDFT accessible for use in studying practical systems it is necessary to apply the Kohn-Sham decomposition to the Vignale-Rasolt universal functional yielding the following universal functional,

$$F_{\mathrm{VR}}\left(\rho, \mathbf{j}_p\right) = T_s\left(\rho, \mathbf{j}_p\right) + J\left(\rho\right) + E_{xc}\left(\rho, \mathbf{j}_p\right), \tag{2.196}$$

where both the non-interacting kinetic energy T_s and the exchange-correlation energy E_{xc} now depend on both the charge density and the paramagnetic current density. The non-interacting auxiliary system is constructed in the same manner as for standard Kohn-Sham DFT, as a Slater determinant of complex valued orbitals, with,

$$\rho\left(\mathbf{r}\right) = \sum_{i}^{occ.} \left|\phi_i\left(\mathbf{r}\right)\right|^2, \tag{2.197}$$

$$\mathbf{j}_p\left(\mathbf{r}\right) = -\frac{i}{2}\sum_{i}^{occ.}\left[\phi_i^*\left(\mathbf{r}\right)\nabla\phi_i\left(\mathbf{r}\right) - \phi_i\left(\mathbf{r}\right)\nabla\phi_i^*\left(\mathbf{r}\right)\right] \tag{2.198}$$

ensuring it has the same total number of electrons and paramagnetic current density as the fully interacting system. It follows that the Kohn-Sham equations for CDFT are given as,

$$\left[\frac{1}{2}\hat{\mathbf{p}}^2 + \hat{\mathbf{p}}\cdot\mathbf{A}_s\left(\mathbf{r}\right) + u_s\left(\mathbf{r}\right)\right]\phi_i\left(\mathbf{r}\right) = \varepsilon_i\phi_i\left(\mathbf{r}\right) \tag{2.199}$$

The corresponding Kohn-Sham potentials can be defined as,

$$u_s\left(\mathbf{r}\right) = v_{\mathrm{ext}}\left(\mathbf{r}\right) + v_J\left(\mathbf{r}\right) + v_{\mathrm{xc}}\left(\mathbf{r}\right) + \frac{1}{2}A_s^2\left(\mathbf{r}\right), \tag{2.200}$$

$$\mathbf{A}_s\left(\mathbf{r}\right) = \mathbf{A}_{\mathrm{ext}}\left(\mathbf{r}\right) + \mathbf{A}_{\mathrm{xc}}\left(\mathbf{r}\right) \tag{2.201}$$

where $v_{\mathrm{ext}}\left(\mathbf{r}\right)$ and $\mathbf{A}_{\mathrm{ext}}\left(\mathbf{r}\right)$ are the external potentials arising from the nuclei and external magnetic field respectively, $v_J\left(\mathbf{r}\right)$ is the potential defined in Eq. (2.148), and the exchange-correlation potentials are defined respectively as,

$$v_{\mathrm{xc}}\left(\mathbf{r}\right) = \frac{\delta E_{\mathrm{xc}}\left(\rho, \mathbf{j}_p\right)}{\delta\rho\left(\mathbf{r}\right)}, \tag{2.202}$$

$$\mathbf{A}_{\mathrm{xc}}\left(\mathbf{r}\right) = \frac{\delta E_{\mathrm{xc}}\left(\rho, \mathbf{j}_p\right)}{\delta\mathbf{j}_p\left(\mathbf{r}\right)}. \tag{2.203}$$

In analogy to standard DFT, once a suitable approximation to the exchange-correlation functional is formulated, Eq. (2.199) could be solved using the self-consistent field procedure.

Exchange-Correlation Functionals in CDFT

Due to the required dependence on the paramagnetic current density $\mathbf{j}_p$, most existing exchange-correlation functionals cannot be directly applied in CDFT. Additionally, it has been shown that $E_{\mathrm{xc}}(\rho, \mathbf{j}_p)$ must be independently gauge invariant[96], posing constraints on how $\mathbf{j}_p$ dependence is introduced in to exchange-correlation functionals. Two methods exist for adapting existing functionals for use within CDFT, vorticity dependent functionals and current modified kinetic energy based functionals.

Vorticity dependent functionals introduce $\mathbf{j}_p$ dependence through the introduction of the gauge-invariant vorticity,

$$\nu(\mathbf{r}) = \nabla \times \frac{\mathbf{j}_p(\mathbf{r})}{\rho(\mathbf{r})} = \frac{\rho(\mathbf{r}) \nabla \times \mathbf{j}_p(\mathbf{r}) - \nabla\rho(\mathbf{r}) \times \mathbf{j}_p(\mathbf{r})}{\rho(\mathbf{r})^2} \tag{2.204}$$

which leads to an exchange-correlation vector potential expressed in terms of the vorticity,

$$\mathbf{A}_{\mathrm{xc}} = \frac{1}{\rho(\mathbf{r})} \nabla \times \frac{\delta E_{\mathrm{xc}}(\rho, \nu)}{\delta \nu}. \tag{2.205}$$

These functionals typically take the form proposed by Vignale, Rasolt and Geldart (VRG),[96;97]

$$E_{\mathrm{xc}}^{\mathrm{VRG}}(\rho, \nu) = \int g(\rho(\mathbf{r})) |\nu(\mathbf{r})|^2 d\mathbf{r}, \tag{2.206}$$

where approximations to $g(\rho(\mathbf{r}))$ have been constructed from the uniform electron gas model, fitted to reference data.[102–108] Vorticity dependent functionals, whilst theoretically convenient, typically exhibit stability issues in self-consistent calculations since $\nu(\mathbf{r})$ is numerically ill-behaved, see Ref. 15.

The second method for constructing CDFT exchange correlation functionals was proposed by Becke[109] with a more elaborate variation being proposed by Pittalis[110], which utilise the observation that gauge-invariant kinetic energy densities can be formed from combining Kohn-Sham canonical-kinetic-energy density and the paramagnetic current density. Typically, most meta-GGAs are constructed with a dependence on the spin resolved kinetic energy density,

$$\tau_\sigma = \sum_i^{occ.} \nabla\phi_{i\sigma}^* \cdot \nabla\phi_{i\sigma}, \tag{2.207}$$

however, this is gauge-origin dependent, making it alone unsuitable for constructing exchange-correlation functionals for use with CDFT. Work by Dobson[111;112] and Becke[109] proposed a modification to the kinetic energy density to remove its dependence on gauge-origin,

$$\tau_\sigma \rightarrow \tilde{\tau}_\sigma = \tau_\sigma - \frac{|\mathbf{j}_{\mathrm{p}\sigma}|^2}{\rho_\sigma} \tag{2.208}$$

where $\mathbf{j}_{\mathrm{p}\sigma}$ is the spin resolved paramagnetic current density. The associated Kohn-Sham vector potential is given as,

$$\mathbf{A}_{\mathrm{xc}} = -\frac{\delta E_{\mathrm{xc}}(\rho, \tilde{\tau})}{\delta\tilde{\tau}} \frac{\mathbf{j}_p}{\rho} \tag{2.209}$$

Functionals with this modification are denoted by a prefix 'c' before the functional abbreviation, a common example, and one that is used throughout this work is the current modified TPSS (cTPSS) functional of Tao, Perdew, Staroverov and Scuseria.[79;113]

2.4.4 Computational Impact

The main advantage of LAOs is they can be employed to perform a full self-consistent field procedure, providing a non-perturbative route to studying the effect of external magnetic fields on molecular systems.[12] For both wavefunction methods and CDFT methods however, the computational cost when using LAOs is significantly increased compared to when utilising standard GAOs. Any floating point operations now require complex arithmetic, and the permutational symmetry of the two electron integrals is reduced from eight-fold to four-fold.[12;23] Furthermore, the field leads to reduction in spatial symmetry. Many new developments have been made to improve the computational efficiency when using LAOs, including efficient integral algorithms,[23] integral derivative algorithms[24], RI and Cholesky decomposition approximations[114;115]. In spite of these advances, utilising LAOs is still somewhat restrictive on the size of system that can be addressed.

2.5 Acceleration Using Density Fitting

Within most electronic structure methods, the evaluation of the electron-repulsion integrals (ERIs) is essential but one of the most computationally costly steps. Therefore, attempts to reduce the impact of ERIs are widely developed and employed. One such approach used throughout this work is the resolution-of-the-identity (RI) approximation,[116] where products of the orbital basis functions, $\{\chi_\mu\}$, are expanded over a set of auxiliary basis functions, $\{\varphi_p\}$,

$$\chi_\mu(\mathbf{r})\,\chi_\nu(\mathbf{r}) \approx \sum_p C^p_{\mu\nu}\varphi_p(\mathbf{r})\,. \tag{2.210}$$

The expansion coefficients $C^P_{\mu\nu}$ are typically obtained through minimisation of the self-repulsion of the residual $(R_{\mu\nu}|R_{\mu\nu})$, where,

$$R_{\mu\nu}(\mathbf{r}) = \chi_\mu(\mathbf{r})\,\chi_\nu(\mathbf{r}) - \sum_P C^P_{\mu\nu}\varphi_P(\mathbf{r})\,. \tag{2.211}$$

Using this expansion, the ERIs can be written as integrals over two and three centres instead of four,

$$(\mu\nu|\kappa\lambda) \approx (\mu\nu|\kappa\lambda)_{\mathrm{RI}} = \sum_{PQ}(\mu\nu|P)\,(P|Q)^{-1}\,(Q|\kappa\lambda)\,, \tag{2.212}$$

where μ, ν, κ and λ are labels for the orbital basis functions and P and Q are labels for the auxiliary basis functions. This can significantly improve the performance of ERI calculations, which, from the discussion in section 2.4, is even more important when considering integrals over LAOs where the complex algebra and reduction in permutational symmetry increases the cost of ERI evaluation significantly. Additionally, Reynolds and Shiozaki[117] showed that the auxiliary basis functions, for LAO based calculations, can be real, resulting in $(P|Q)^{-1}$ being real and reintroducing some permutational symmetry elements in the calculation of

the three centre integrals. For a more detailed discussion of the implementation of RI with LAOs see Ref. 114 This is also important when considering the embedded fragment method, introduced within chapter 3, where the reduction in the memory required for storing the ERIs proves vital for an efficient parallel implementation.

One of the main considerations when utilising the RI approximation is in the choice of auxiliary basis set, which must be chosen such that it provides a good fit for the product basis $|\mu\nu)$. This inherently implies that the choice of auxiliary basis is dependent on the choice of orbital basis set. There are many methods for constructing a suitable auxiliary basis set such as; using a Cholesky decomposition of the ERIs,[118;119] using a linear combination of atomic distributions,[120;121] or by utilising auxiliary basis sets that have already been optimised for calculating given properties. Constructing these optimised basis sets however, can be costly, and may be limited to certain applications or properties. Therefore, within this work the AutoAux procedure[122] for constructing suitable auxiliary basis sets is employed, which defines a conservative density-fitting basis set applicable to any electronic structure method and corresponding basis set, which has been shown to be accurate for a wide range of external field strengths.

3 An Embedded Fragment Method for Large Molecular Clusters in Strong Magnetic Fields

3.1 The Embedded Fragment Method

Until now, the LAO approach discussed in chapter 2 has only been applied to small molecules and atoms. However, it is not just small simple systems that are of interest, larger and more complex systems can play very significant roles in modern chemistry, making understanding them a very attractive prospect for current and future research. However, the high-rank polynomial dependence of computational cost with respect to system size for modern electronic structure techniques can impose a restrictive limitation on the size of the system that may be studied, as discussed in chapter 2. As an example, DFT, at the LDA or GGA levels, scales as $O\left(n^3\right)$ with the size of the system n. More complex wavefunction methods, often considered more accurate, have even worse scaling e.g. MP2 which scales as $O\left(n^5\right)$. This is complicated further when considering methods that utilise LAOs, due to the introduction of complex algebra and the reduction in permutational and point group symmetries which can be exploited. Whilst this doesn't change the overall scaling of each approach, it does significantly increase the 'prefactor' amplifying the effects of the high-rank scaling. Reducing this poor scaling is one of the most important current areas of research within the field of computation chemistry today. Many different approaches have been developed, of which, common approaches include semi-empirical methods[123–125], linear-scaling methods[126;127] orbital-free approaches[128–131] and fragmentation approaches,[132–145] which will be the focus of this work.

Many more complex systems are composed of reasonably discrete elements, for example, liquids or molecular crystals. Moreover, systems like this, that are held together via weak intermolecular interactions, may be more susceptible to magnetic fields. To simulate such systems electronic structure methods can be developed that take advantage of this discrete nature through fragmentation, in doing so making calculations on increasingly large systems more tractable. In *Modern Methods for Theoretical Physical Chemistry*[132], three categories of fragmentation based approaches are defined. The first is divide-and-conquer techniques,[133–135] where subsystems are treated within their surroundings using local Hamiltonians, which can then be combined to give the total density matrix for the full system. The second is transferable approaches,[136;137] based on the well-known additivity property of heat of formation, which can be approximately equated to the sum of bond (or other subunit) energies. The final category is fragmentation-interaction techniques,[138–141;143;144] based in the theory of molecular interactions, where the total energy of a system can be obtained by a sum of the fragment energies and intermolecular interaction energies between groups of fragments (dimers, trimers, tetramers etc.). Most fragmentation based

approaches ignore the environment around a given fragment, or opt to include only adjacent pairs, however, one such fragment-interaction method known as the Embedded Fragment Method[144] (EFM) attempts to include the total system environment whilst still retaining the benefits of applying a fragmentation method.

3.1.1 Overview of EFM Approaches for Non-Periodic Systems

The embedded fragment method, also commonly known as the fragment molecular orbital method (FMO), is a type of fragment approach first introduced by Kitaura and co-workers.[141;142] For a large molecular system that comprises many discrete fragments, the total electronic energy may be represented as the sum of fragment energies according to the many-body expansion (MBE),[146–150]

$$\begin{aligned}\mathcal{E}^{\text{total}} = &\sum_i \mathcal{E}_i + \sum_{j>i} (\mathcal{E}_{ij} - \mathcal{E}_i - \mathcal{E}_j) \\ &+ \sum_{k>j>i} (\mathcal{E}_{ijk} - \mathcal{E}_{ij} - \mathcal{E}_{jk} - \mathcal{E}_{ik} + \mathcal{E}_i + \mathcal{E}_j + \mathcal{E}_k) \\ &+ \ldots\end{aligned} \tag{3.1}$$

where $\mathcal{E}_i$ is the single point energy of fragment/monomer i, $\mathcal{E}_{ij}$ is the single point energy of the fragment pair/dimer containing fragments i and j and $\mathcal{E}_{ijk}$ is the single point energy of the trimer containing fragments i, j and k. Higher order terms are similarly defined. In principle this sum contains N terms, where N is the number of fragments, and is formally exact. However, in practice it is common to truncate the sum at a given number of terms to form an approximation of the total energy. This reduces the computational expense required to evaluate $\mathcal{E}^{\text{total}}$ as each higher-order term is individually more computationally expensive than its predecessor, therefore the more this series can be truncated, without significant loss in accuracy, the cheaper the calculation will be.

One of the main benefits of EFM, is that it is not limited in the choice of electronic structure method used for the individual calculations. Typically, the largest individual calculations required will be that of trimers, consisting of three small molecules, making it readily accessible to higher-levels of theory which would usually be too expensive when considering the system as a whole. Therefore, EFM provides a route to calculating approximate energies and properties of increasingly large systems with methods that would normally be inaccessible at such system sizes.

Convergence of the Many-Body Expansion

The act of truncating the MBE in practice, however, is not trivial. Many studies have shown that the convergence of the MBE can be very system dependent and often very slow, requiring many high-order terms, significantly increasing the computational complexity.[147;151–158] The most significant contributions to the energy of weakly interacting water clusters can be identified by considering the different many-body components of the energy[147]. Since the electron density of neutral species decays exponentially with distance r, the same is true of the exchange interaction[159–161] and therefore its contribution to the

higher order interaction terms will be small and only arise at small separations between monomers. Similarly, correlation interactions decay rapidly as r^{-6} and are thought to be near-pairwise additive for systems such as water clusters[158;162;163]. By contrast the Coulomb interaction exhibits a much slower asymptotic decay, to first order decaying as r^{-3} for neutral systems[164;165]. As a result, each monomer has a non-negligible interaction with potentially many other monomers in the cluster; the resulting polarisation effects[166–168] dominate the contributions to the energy, beyond two-body interactions, and become more significant with increasing cluster size[169;170]. In order to limit the number of terms within the many-body expansion therefore, it was proposed that the energy of each fragment could be calculated within an electrostatic potential, defining the longer range Coulomb interactions which are the most significantly impacted interactions when higher order terms were not explicitly considered.

The Hamiltonian operator for the energy of a single fragment is defined as,

$$\hat{\mathcal{H}}'_i = \hat{\mathcal{H}}_i + \sum_n \sum_{j \neq i} V_j(\mathbf{r}_n), \tag{3.2}$$

where $\hat{\mathcal{H}}_i$ is the standard electronic Hamiltonian for fragment i, as shown in Eq. (2.5), and $V_j(\mathbf{r}_n)$ is an electrostatic embedding potential term, exerted on electron n, due to fragment j. Similar expressions can be written for the dimer Hamiltonian,

$$\hat{\mathcal{H}}'_{ij} = \hat{\mathcal{H}}_{ij} + \sum_n \sum_{k \neq i,j} V_k(\mathbf{r}_n), \tag{3.3}$$

where $\hat{\mathcal{H}}_{ij}$ is the Hamiltonian for the dimer constructed from monomers i and j, as well as larger combinations of fragments. In the work by Kitaura and co-workers[141;142] a multiplicative Coulomb potential was used,

$$V_j^{\text{Coulomb}}(\mathbf{r}) = \sum_{a \in j} \frac{Z_a}{|\mathbf{r} - \mathbf{r}_a|} - \int \frac{\rho_j(\mathbf{r}')}{|\mathbf{r} - \mathbf{r}'|} d\mathbf{r}' \tag{3.4}$$

where Z_a and $\mathbf{r}_a$ are the charge and position of nucleus a within fragment j, and ρ_j is its electron density. The electron density and Coulomb potential of each fragment must be determined self-consistently therefore, including all many-body polarisation effects whilst enabling the truncation of the MBE.

Controlling Basis-Set Superposition Errors

Of the many studies on the convergence of the MBE, one additional factor has been shown to be of significant importance. Due to the very nature of fragmentation methods they are susceptible to the effects of the basis set superposition error (BSSE) on the MBE.[154;171–174] BSSE arises from the monomers or dimers effectively borrowing basis functions from other monomers to compensate for their basis set incompleteness, therefore, simply calculating the dimer interaction energy, for example, where the monomers are only calculated with their own basis sets introduces a BSSE. This will be amplified in the MBE due to the large number of terms susceptible to BSSE, creating an imbalance in the

computed many-body interactions. The two simplest methods for counteracting this error are to either increase the basis set size until the basis set limit is reached, effectively creating a near complete basis set, or to calculate all the individual monomer/dimer energies within the basis set of the total system. Both these methods would significantly undermine the cost-effectiveness of using an EFM and therefore, are not widely used to counteract BSSEs. For dimeric systems, Boys and Bernardi[175] proposed the counterpoise (CP) correction,

$$\mathcal{E}_{ij}^{\mathrm{CP}} = \left(\mathcal{E}_i^i - \mathcal{E}_i^{ij}\right) + \left(\mathcal{E}_j^j - \mathcal{E}_j^{ij}\right) \tag{3.5}$$

where $\mathcal{E}_i^{ij}$ is the energy of monomer i calculated with the combined basis functions of monomers i and j. This fairly simple correction has been the basis for most of the development for BSSE correction methods to date. Some of the most prominent variants of the CP methods are: the pairwise additive function counterpoise (PAFC)[176], the site-site function counterpoise (SSFC)[177] and the Valiron-Mayor function counterpoise (VMFC)[178]. Also of note, is the many-body counterpoise (MBCP) method[179;180] as an approximate BSSE correction method using an MBE like deconstruction of the effects of the present ghost functions. Many of these approaches have been adapted and integrated with existing EFM implementations.[172]

3.1.2 Designing Cost-Effective Embedding Potentials

There are many different approaches available when determining the embedding potential terms, such as the multiplicative Coulomb potential, defined in Eq. 3.4, however, Hirata and coworkers[144] formulated a method which provides a low-cost approach, specifically adapted to describe weak inter-molecular interactions within molecular clusters. Fragmenting molecular clusters into the individual molecules results in the many-body interactions being dominated by the long-range Coulomb interactions between the molecules, of which, for neutral systems consiting of monomers with well separated charge-distributions, the leading term is the dipole-dipole interaction. The potential due to a dipole moment $\boldsymbol{\mu}$ is given by,[181]

$$V_{\mu}\left(\mathbf{r}\right) = -\frac{\boldsymbol{\mu}\cdot\mathbf{r}}{r^3}, \tag{3.6}$$

Therefore, for this type of system it is appropriate to approximate the Coulomb interaction by simply evaluating the dipole-dipole interactions between the fragments, then modelling them via point charges to give the potential due to a given monomer as,

$$V_j\left(\mathbf{r}_n\right) = \frac{e_j}{|\mathbf{r}_n - \mathbf{R}_j - \left(\frac{\mathbf{d}}{2}\right)|} - \frac{e_j}{|\mathbf{r}_n - \mathbf{R}_j + \left(\frac{\mathbf{d}}{2}\right)|}, \tag{3.7}$$

where $e_j\mathbf{d}$ is equivalent to the dipole moment of fragment j, calculated within the embedding potential for monomer j, with the length of vector $\mathbf{d}$ set to an arbitrary constant, often set to 0.01 bohr which has been shown to be within the limit where the lengths of the dipole moment becomes negligible in the overall calculation, and the potential of Eq. (3.7) approaches that of Eq. (3.6). $\mathbf{R}_j$ is the point at which the nuclear component of the dipole moment for fragment j becomes zero. The dipole moments of all fragments must be determined self-consistently such that e_j for all monomers converges within a given threshold,

set to 10^{-4}a.u. throughout this work. The isolated monomer's dipole moments are used to construct the initial embedding potential for the iterative procedure. This approach proves to be much cheaper computationally than calculating the full Coulomb interaction between fragments whilst retaining reasonable accuracy, when considering systems with well-defined molecular fragments.

Although this dipole based approximation is well suited for molecular clusters it lacks an accurate short-range electrostatic representation, resulting in higher-order MBE terms being required when a system includes larger individual fragments or a more intricate short-range electrostatic field. This is undesirable due to the increased computational cost resulting from calculating the higher-order MBE terms, therefore, it would be beneficial to find adaptations to improve the dipole based approximation without significant increase in cost. One such method is to combine the dipole potential with an electrostatic potential (ESP) partial point charge approximation,[172] where some fixed position(s) within each fragment, such as each nucleus, are assigned a partial point charge,

$$V_i^{\mathrm{ESP}}(\mathbf{r}) = \sum_{a \in i} \frac{\zeta_a}{|\mathbf{r} - \mathbf{r}_a|}, \tag{3.8}$$

where ζ_a is the partial charge at the arbitrarily chosen position a. Each partial charge is determined such that V_i^{ESP} reproduces V_i^{Coulomb} as closely as possible,[182–184] minimizing,

$$\sigma = \sum_g \{V_i^{\mathrm{ESP}}(\mathbf{r_g}) - V_i^{\mathrm{Coulomb}}(\mathbf{r_g})\}^2, \tag{3.9}$$

where $\mathbf{r}_g$ are grid points distributed around the fragment i. This approach only requires three-centre, one-electron integrals which means it is less computationally intense compared to the full Coulomb potential, which requires four-center, two-electron integrals, but has a higher computational cost than the dipole approximation alone.

Within this work an alternative solution is proposed, based around a modified dipole embedding potential which is shown to be a reliable fix for the shortcomings of Eq. (3.7) whilst retaining its computational cost benefits, this is presented in section 3.3.

3.1.3 Computational Algorithm

An overview of the general computational implementation of a single point EFM energy calculation used within this work, can be summarized into the following steps:

1. The dipole moments of each isolated fragment are calculated.
2. These dipole moments are used to construct an embedding potential within which updated dipole moments are calculated. This is then iterated until self-consistency.
3. The energy of each monomer is calculated within the field due to the converged dipole moments.
4. The energy of any dimers/trimers/tetramers etc. are calculated within the field due to the converged dipole moments.

5. The total energy of the system is determined from the MBE of the monomer/dimer/trimer etc. energies.

3.1.4 Property Evaluation

The embedded fragment method is not just limited to calculating total energies of systems, the MBE can additionally be applied to a variety of different response properties. One such property is the derivative of the total energy with respect to atomic positions, also referred to as the force on each atom within the system. In a similar approach to how the MBE can be written in terms of single point energies in Eq. (3.1), the geometric derivative can be re-written in terms of energy derivatives of individual fragments,

$$\begin{aligned}\frac{\partial \mathcal{E}^{\text{total}}}{\partial x} = &\sum_i \frac{\partial \mathcal{E}_i}{\partial x} + \sum_{j>i} \left(\frac{\partial \mathcal{E}_{ij}}{\partial x} - \frac{\partial \mathcal{E}_i}{\partial x} - \frac{\partial \mathcal{E}_j}{\partial x} \right) \\ &+ \sum_{k>j>i} \left(\frac{\partial \mathcal{E}_{ijk}}{\partial x} - \frac{\partial \mathcal{E}_{ij}}{\partial x} - \frac{\partial \mathcal{E}_{jk}}{\partial x} - \frac{\partial \mathcal{E}_{ik}}{\partial x} + \frac{\partial \mathcal{E}_i}{\partial x} + \frac{\partial \mathcal{E}_j}{\partial x} + \frac{\partial \mathcal{E}_k}{\partial x} \right) \ldots,\end{aligned} \tag{3.10}$$

where $\frac{\partial \mathcal{E}_i}{\partial x}$ is the partial derivative of the energy of fragment i with respect to its position along the x axis. Similar expressions can be written for the derivatives along y and z and these can be combined to form the full $3 \times N_{\text{nuc}}$ matrix, where N_{nuc} is the total number of nuclei within the given system, for the total energy derivative of the system. This can then be fed into an optimisation algorithm allowing structural optimisations to be performed. It is additionally possible to calculate the second derivative of the total energy in the same manner opening the door to vibrational analysis via EFM. Additional EFM property evaluation methods are discussed throughout this work.

3.1.5 Computational Considerations

Precision in the Many-Body Summation

Many implementations exist for running EFM calculations, however, the majority are developed as wrappers around an existing quantum chemistry software package, essentially launching several standard single point energy calculations and reading the result from a set of resulting output files. This approach possess a potential flaw due to a well-known issue when employing a large summation such as the MBE, the accumulation of finite-precision errors. This results in EFM being particularly sensitive to threshold values within the electronic structure code. When EFM is employed as a *wrapper* type code, this can be amplified due to the final energy values being rounded to some arbitrary precision when printed within output files. These small errors can quickly accumulate within the final sum causing a significant error in the final value. In order to prevent this potential flaw, it is necessary to integrate EFM directly within a specific quantum chemistry software package, this would result all values for the final sum being stored in local memory, therefore, avoiding any rounding or precision errors. It will also be necessary to carefully consider the convergence thresholds iterative procedures in the electronic structure program and any potential floating point errors in numerical calculations when computing values.[170;185]

Exploiting the Embarrassingly Parallel Algorithm

At its core, EFM requires performing many different electronic structure calculations on individual monomers, dimers, trimers etc. All these calculations are entirely independent therefore, making EFM an embarrassingly parallel algorithm. Modern high performance compute (HPC) facilities are often built with parallel processing in mind, therefore, making use of this modern architecture to perform multiple single point energy calculations simultaneously would be a high priority for any new implementations of EFM. Although introducing parallel processing won't reduce the polynomial dependence of the cost scaling for EFM, it can drastically reduce the pre-scaling factor, significantly impacting the time required to perform an EFM calculation making increasingly large systems more readily accessible for computational analysis.

As pointed out by Herbert[158], exploiting parallel algorithms for EFM only impacts the so called *wall-time*, or the total time experienced by the user to perform an EFM calculation. This can often be deceptive as it hides the true computational expense for a single calculation. Often metrics such as power consumption or central processing unit (CPU) time have been discussed as potentially more accurate measures of computational efficiency, and indeed are often used by HPC facilities to price their computational resources. However, this does not negate the impact of using fragmentation based methods in the first place, but does raise some interesting ethical questions about the field of computational modelling which are beyond the scope of this work.

A Pythonic Approach – QUEST

Within this work all new methods have been implemented within the QUEST[35] quantum chemistry package. QUEST is a predominantly python based, rapid development platform for quantum electronic structure techniques with a significant motivation for developing new LAO based methods. Due to its python base, it is very accessible to adapt, particularly when considering the development and testing of new methods. The trade-off however, is that python is generally slower than pre-compiled coding languages, therefore, exploiting any techniques to improve the efficiency of calculations becomes a very significant factor in the method development.

3.2 Implementing EFM for Systems in External Electromagnetic Fields

3.2.1 The Binary and Tertiary Interaction Methods

Typically, EFM returns reasonable accuracy when only considering the first two or three terms in the MBE, treating all other N-body terms as purely Coulombic and therefore approximated by the embedding potential. Truncating the MBE at either the second or third term are known as the *binary* or *tertiary interaction approximations* respectively. They can be written as,

$$\mathcal{E}^{\text{binary}} = \sum_i \mathcal{E}_i + \sum_{j>i} \left(\mathcal{E}_{ij} - \mathcal{E}_i - \mathcal{E}_j\right), \tag{3.11}$$

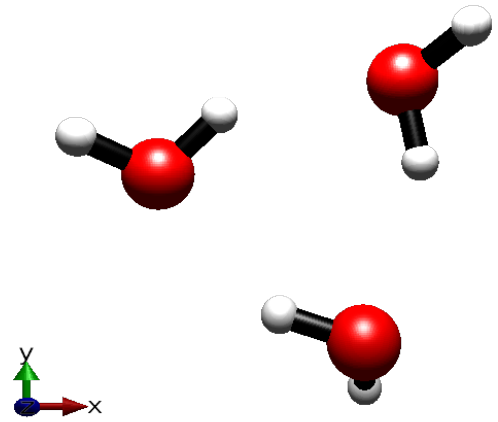

Figure 3.1: The geometry of the cyclic water trimer, optimised with HF theory and the aug-cc-pVDZ basis set.

$$\mathcal{E}^{\text{tertiary}} = \mathcal{E}^{\text{binary}} + \sum_{k>j>i} \left(\mathcal{E}_{ijk} - \mathcal{E}_{ij} - \mathcal{E}_{jk} - \mathcal{E}_{ik} + \mathcal{E}_i + \mathcal{E}_j + \mathcal{E}_k\right), \tag{3.12}$$

where $\mathcal{E}_i$ is the energy of monomer i within the embedding potential, calculated with the Hamiltonian from Eq. (3.2). $\mathcal{E}_{ij}$ is the equivalent for the dimer constructed from monomers i and j and $\mathcal{E}_{ijk}$ is the equivalent for the trimer constructed from monomers i, j and k. Both Eqs. (3.11) and (3.12) have been implemented within the QUEST software package and have been combined with the dipole based approximate embedding potential, described in Eq. (3.7), which presents a good approximation for longer-range intermolecular interactions whilst being reasonably computationally inexpensive. The implementation of Eq. (3.7) makes use of the existing nuclear attraction integral algorithms,[23] where the nuclear charges and positions are replaced by the partial charges and positions representing the self-consistent dipole moments $e_j\mathbf{d}$. This is directly appropriate for studying large, neutral, molecular clusters, such as those discussed within this chapter, where each molecule within the system is treated as a single fragment.

As an example, table 3.1 compares the single point energies for a cyclic water trimer using both conventional electronic structure methods and EFM based electronic structure methods using the *binary interaction approximation*, Eq. (3.11), with and without the

Table 3.1: Total EFM energies in E_h, EFM binding energies in kcal mol^{-1} (in parentheses) and their error with respect to conventional calculations, in mE_h and kcal mol^{-1} respectively, for a cyclic water trimer using a range of electronic structure methods, with the aug-cc-pVDZ basis set.

	No Embedding Potential		Dipole Embedding Potential	
	Energy	Error	Energy	Error
HF	-228.14205 (-10.5)	2.1 (1.3)	-228.14435 (-11.9)	-0.2 (-0.1)
BLYP	-229.29264 (-10.7)	2.4 (1.5)	-229.29590 (-12.8)	-0.8 (-0.6)
PBE	-229.09508 (-13.3)	2.9 (1.8)	-229.09823 (-15.3)	-0.3 (-0.2)
TPSS	-229.35380 (-11.8)	2.1 (1.9)	-229.35681 (-13.7)	-0.9 (-0.6)
MP2	-228.81045 (-14.3)	1.9 (1.2)	-228.81299 (-15.9)	-0.6 (-0.4)
CCSD	-228.83233 (-13.7)	1.9 (1.2)	-228.83481 (-15.3)	-0.6 (-0.4)

Table 3.2: Geometry of a cyclic water trimer optimised at using HF theory and the aug-cc-pVDZ basis set.

	Position / Å		
Atom	x	y	z
O1	-1.6527176	0.2922510	-0.2322186
H1	-2.3904046	0.6644842	0.2209743
H2	-0.9705371	0.9532540	-0.2350245
O2	0.6138554	-1.5247809	0.0807375
H3	-0.2902290	-1.2357228	0.0377337
H4	0.6989303	-2.2254475	-0.5444539
O3	1.0812597	1.3457061	-0.2361562
H5	1.6971547	1.8057715	0.3091461
H6	1.2624616	0.4190401	-0.1288747

dipole based embedding potential. The geometry of the water trimer was optimised at the HF/aug-cc-pVDZ level using QChem[186], and is shown in Fig. 3.1 with the geometrical coordinates given in table 3.2, to replicate the geometry used in Ref. 144, enabling a more reliable comparison. Therefore, demonstrating that our implementation within QUEST is a faithful implementation of EFM with the dipole approximation. It additionally demonstrates the sub-mE_h errors in the total energy across a range of electronic structure methods, when utilising EFM with the dipole approximation. This highlights the main strength of EFM, its applicability to any molecular electronic structure method, resulting in the traditionally more expensive methods becoming more accessible under this approximation without significant loss in accuracy. Also highlighted in table 3.1 is the importance of the embedding potential when calculating EFM energies. When employing a pure MBE, truncated at the second term, without the potential term from Eq. (3.2), the average error in the binding energy of the water trimer is 10.2%, however, this is reduced to 2.5% when the approximate dipole potential is introduced to the energy calculations.

To understand and implement the EFM, it was important to understand how this error behaved when increasing the system size, as the aim of this method is to treat increasingly large molecular systems. A set of over 70 of the lowest energy conformer water clusters, $(H_2O)_n$, where $n = 3 - 10$, presented by Bates *et. al*[187] was utilised for this analysis. The geometries, obtained from Ref. 187, were determined at the MP2 level with the aug-cc-pVTZ basis set for the oxygen atoms and the cc-pVTZ basis set for the hydrogen atoms.[188;189] The error in the EFM single point energies of these molecular clusters, determined at a range of theory levels, with respect to conventional methods, were calculated. The results of this are shown in Fig. 3.2. From this analysis it can be observed that increasing the system size retains a consistent level of error, in all cases the mean error is below 0.01% further confirming the accuracy of this method and its implementation within QUEST. The only outlier from this observation is the water trimer, where the error was observed to be much smaller than the larger clusters, which would not be unexpected as its MBE is *near complete* when truncated at 2$^{\mathrm{nd}}$ order. Another observation from Fig. 3.2 is that there is no significant difference in the errors when using either the aug-cc-pVDZ or the larger aug-cc-pVTZ basis sets and when using either of the three electronic structure methods, HF,

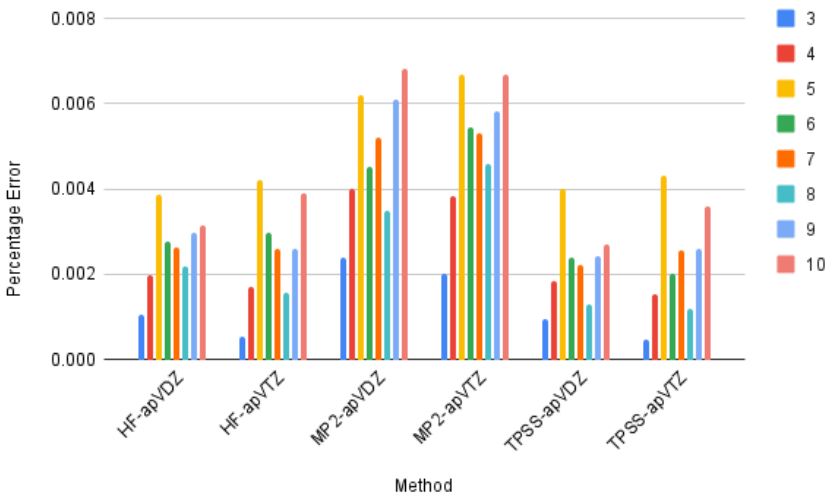

Figure 3.2: Mean percentage errors in the total energy calculated by EFM, compared to conventional approaches, for a series of different size water clusters at different levels of theory with both the aug-cc-pVDZ (apVDZ) and aug-cc-pVTZ (apVTZ) basis sets.

DFT(TPSS) or MP2. For the basis set comparison it is important to note that the EFM calculations included a BSSE correction as discussed in section 3.1.1 for which a detailed discussion of its implementation and impact on results is discussed in section 3.2.3.

It is still important however, to consider the effect of higher-order terms. This is considered for a $(H_2O)_{10}$ cluster in table 3.3 where it is clear that even with a reasonable embedding potential, including the three body terms within the MBE can have a non-negligible impact on the relative error of the calculations. Here it reduces the error in the EFM from $< 0.01\%$ to $< 0.001\%$. Therefore, when considering the EFM, it is not possible to assume the three body terms have a completely negligible contribution, however, will increase the cost of the calculations significantly as they now will exhibit cubic scaling. From this point forth only the binary interaction approximation is considered as it presents a more computationally inexpensive approximation to the energy of the system and still provides a reasonable accuracy, particularly when only considering qualitative analysis.

Table 3.3: Total EFM energies in E_h and their difference from conventionally calculated energies, in mE_h, for $(H_2O)_{10}$ using a range of electronic structure methods, with the aug-cc-pVDZ basis set.

	binary approximation		tertiary approximation	
	Energy	Error	EFM	Error
HF	-760.51936316	-13.8	-760.49967692	5.9
BLYP	-764.43677251	-42.6	-764.39689244	2.7
PBE	-763.80032365	-52.4	-763.74278278	5.2
TPSS	-764.64893471	-44.1	-764.59979207	5.0

Combining EFM With LAOs

The embedded fragment method itself is not new however, it has been implemented within several electronic structure software packages and has been used for many years as a cost-effective method for studying increasingly large or complex systems. It has never previously been applied to an LAO based electronic structure approach however, enabling the study of these complex systems within arbitrary external magnetic and electric fields. Therefore, this chapter discusses the implementation of a combined EFM/LAO approach and how it can be used to study the response of large molecular clusters to external fields.

Due to the fundamental nature of EFM, it only relies on simple molecular energy calculations, therefore, the only requirement for introducing an LAO based EFM is an existing implementation of an LAO based electronic structure method, such as that provided within QUEST. With only minor alterations the QUEST EFM implementation can be linked with the available LAO based techniques providing an implementation of LAO based EFM. Table 3.4 provides a comparison of the total energies and binding energies for the same cyclic water trimer calculated using a variety of electronic structure methods with and without EFM. This is analogous to the results presented in table 3.1 and those presented by Hirata *et. al*[144] however, the results here have been calculated using LAOs with an applied external magnetic field of $|\mathbf{B}| = 0.1$ a.u. (23.5×10^3 Tesla) perpendicular to the plane of the oxygen atoms in the cluster. These results do not contain any correction for BSSE, to enable a clearer comparison with table 3.1 and Ref. 144. Even at this relatively high field strength the error in the total energies for the water trimer remain well bellow 0.01%. The accuracy of the EFM in strong magnetic fields is further confirmed by calculating the error at a series of field strengths in the range $|\mathbf{B}| = 0.0$ a.u. to $|\mathbf{B}| = 0.1$ a.u. using each of the methods in table 3.4, for which the errors remain consistently bellow 0.01%. The mean errors for this data series for each electronic structure method are as follows: HF = 0.0005%, BLYP = 0.0005%, cTPSS = 0.0003%, MP2 = 0.002%, MP3 = 0.001% and CCSD = 0.002%. From this comparison, it is clear that using EFM with LAOs, and a strong applied magnetic field, retains the accuracy reported for the same method with GTOs, whilst also maintaining that level of accuracy across different electronic structure methods.

The use of LAOs enables the inclusion of even stronger field strengths up to 1 a.u., therefore, it is useful to discuss whether EFM can be reliably utilised with such field strengths

Table 3.4: Total energies in E_h, binding energies in kcal mol^{-1} (in parentheses) and their difference, in mE_h and kcal mol^{-1} respectively, of a water trimer using a range of electronic structure methods, with the aug-cc-pVDZ basis set and an applied magnetic field of 0.1 a.u. (2.35×10^4 Tesla).

	Conventional	EFM	Error
HF	-228.10169 (-12.7)	-228.10189 (-12.8)	-0.2 (-0.1)
BLYP	-229.25179 (-13.5)	-229.25258 (-14.0)	-0.8 (-0.5)
cTPSS	-229.31308 (-14.2)	-229.31393 (-14.7)	-0.8 (-0.5)
MP2	-228.76859 (-16.5)	-228.76904 (-16.8)	-0.5 (-0.3)
MP3	-228.78673 (-15.7)	-228.78718 (-16.0)	-0.5 (-0.3)
CCSD	-228.79094 (-15.9)	-228.79141 (-16.1)	-0.5 (-0.2)

Table 3.5: The error in the total water trimer energy evaluated using EFM relative to conventional evaluation at increasing magnetic field strengths, from $|\mathbf{B}| = 0.0$ a.u. to $|\mathbf{B}| = 0.9$ a.u., in the aug-cc-pVDZ basis for a range of electronic structure methods, given in kcal mol^{-1}.

$\lvert\mathbf{B}\rvert$ / a.u.	0.00	0.10	0.20	0.30	0.40	0.50	0.60	0.70	0.80	0.90
HF	-0.14	-0.12	-0.19	-0.24	-0.52	-0.74	-0.32	0.91	1.92	0.92
BLYP	-0.56	-0.49	-0.57	-0.61	-1.41	-1.87	-1.14	0.71	1.26	0.41
cTPSS	-0.58	-0.54	-0.61	-0.70	-1.37	-1.79	-1.00	0.92	1.55	0.54
MP2	-0.37	-0.28	-0.30	-0.32	-0.68	-0.92	-1.68	1.16	2.24	2.50
MP3	-0.36	-0.27	-0.29	-0.31	-0.63	-0.84	-1.75	1.02	2.14	1.48
CCSD	-0.37	-0.28	-0.29	-0.31	-0.64	-0.84	-0.40	1.05	2.13	2.47

as the chemistry becomes increasingly complex. Table 3.5 shows how the error in the total energy of the cyclic water trimer, Fig. 3.1, changes when the field strength is increased well beyond $|\mathbf{B}| = 0.1$ a.u. The magnetic field is applied in the same direction as with the analysis in table 3.4, perpendicular to the plane of the three oxygen atoms. It can be seen that the errors in the energies do not change significantly up to $|\mathbf{B}| = 0.3$ a.u. for all the methods presented within table 3.5. However, there is a sharp increase in error as the field strength increases from $|\mathbf{B}| = 0.3$ a.u. to $|\mathbf{B}| = 0.5$ a.u. Beyond $|\mathbf{B}| = 0.5$ a.u. the magnitude of the errors increases significantly. The behaviour of the errors beyond $|\mathbf{B}| \approx 0.3$ a.u. does not have a single obvious cause; there may be several contributing factors. One potential contributory factor is due to the change in the importance of the Coulomb interactions at very high field strengths, see chapter 2.4. The current implementation of EFM enables the significant truncation of the MBE by including an electrostatic embedding potential approximating the Coulomb interactions between the monomers, which dominate at long range when considering systems within the Coulomb regime. Beyond the Coulomb regime, this potential may no longer capture enough of the longer-range interaction contributions to present an accurate picture of the system. This may imply that either the embedded potential needs to be more thoroughly considered for systems at arbitrary field strengths, or that more terms within the MBE are required to accurately account for the more nuanced intermolecular interactions. Another important consideration could be the changes in ground state electronic configuration for molecules as they are exposed to an increasing external magnetic field strength.[24;25] This could cause complications when calculating interaction energy contributions to the MBE for fragments that may exhibit these state crossings. Further investigation into the cause of this apparent breakdown in the EFM at very high-field strengths would be required before a detailed understanding can be achieved. However, table 3.5 does imply that, up to a limit, EFM provides an accurate approach for studying these type of systems with an applied magnetic field.

Computational Scaling

It has been shown that using the binary approximation effectively reduces the cost scaling, with relation to the system size, to $O(n^2)$, regardless of what underlying electronic structure method is chosen. It can be further reduced to effectively linear scaling for very large clusters, if a radial cut-off is introduced when calculating the dimer energies employing

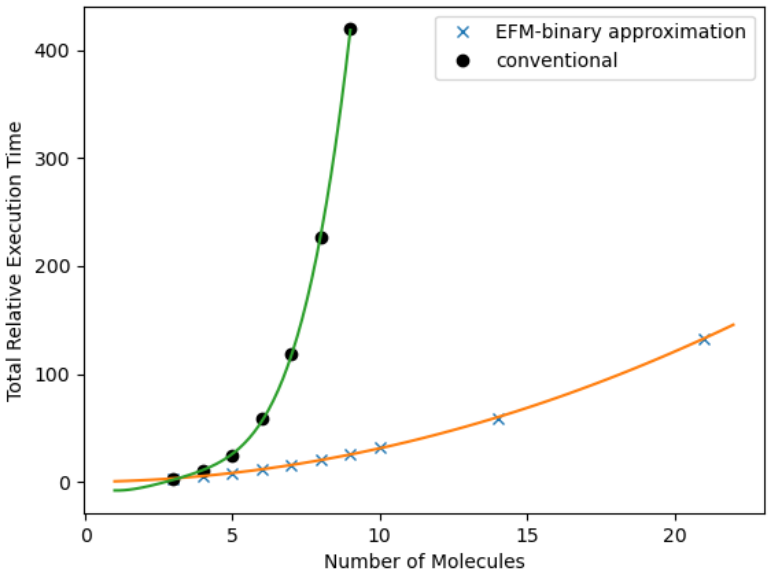

Figure 3.3: Total CPU time required to perform LAO based MP2 single point energy calculations on a series of water clusters, with and without EFM. The aug-cc-pVDZ basis set was used along with the RI approximation.

the assumption that the total energy of a well separated dimer is equal to the sum of the individual monomer energies within the embedding potential, since the 2-body electron-correlation contributions decay much faster than the Coulomb contributions. This all holds true when we consider using LAO based electronic structure methods, since inherently the cost is still only dependent on a series of dimer calculations, which are very cheap relative to the total system. Fig 3.3 demonstrates the reduction in scaling from $O\left(n^5\right)$ to the expected $O\left(n^2\right)$ for MP2 calculations, with the aug-cc-pVDZ basis set and resolution of the identity (RI) approximation, on a series of different size water clusters at $|\mathbf{B}| = 0.1$ a.u. All execution times are measured relative to the time required to calculate the energy of a single water molecule.

3.2.2 The Importance of the Initial Guess

Typically, when performing electronic structure calculations, an initial guess for the density matrices must be made. Common methods for this involve utilising the MOs obtained from a diagonalised core Hamiltonian matrix, or by taking a superposition of spherically averaged atomic densities (SAD). This step incurs a computational cost and may not provide a universally accurate guess for the SCF calculation, which leads to extra SCF iterations being required before the calculation reaches convergence. Considering the core foundations of EFM, a different approach for the initial guess has been implemented. Here we utilise information that has already been computed in previous steps, constructing the dimer/trimer initial guess as a superposition of monomer density matrices,

$$D^{ij} = D^i \oplus D^j. \tag{3.13}$$

The impact of this can be shown by performing a calculation on a $(H_2O)_{21}$ cluster, which contains 210 unique dimers. From a HF calculation with the aug-cc-pVDZ basis set and the RI approximation with the AutoAux auxiliary basis, the average number of SCF iterations required when using a SAD guess was ∼13. Compared to this, the same calculation using the superposition of monomer density matrices as the initial guess in all dimer calculations reduced the average number of SCF iterations to ∼9, it also approximately halved the overall time for the 210 dimer calculations, performed across 20 processors. Both calculations arrived at the same total energy value. This will be amplified when the number of dimer calculations is increased, which is related to the number of monomers as $N_{\text{dim}} = \frac{N_{\text{mon}}(N_{\text{mon}}-1)}{2!}$. From this it is clear that using a superposition of monomers as the initial SCF guess for the dimer calculations makes them more efficient and potentially more stable, removing the possibility for a poor initial guess to cause convergence problems. However, it does require the storage of all monomer density matrices which will increase the overall memory footprint of the calculation. Therefore, the balance of the total memory available vs the desired total computational time must be considered for increasingly large systems.

3.2.3 Corrections for the Basis-Set Superposition Error

As described in section 3.1.1 BSSE can be a very significant factor when considering the convergence of the MBE, therefore, a *truncated* form of the VMFC method has been implemented within QUEST.

$$\mathcal{E}^{\text{Total}} = \mathcal{E}^{\text{binary}} + \sum_{j>i} \left(\tilde{\mathcal{E}}_i^i - \tilde{\mathcal{E}}_i^{ij} + \tilde{\mathcal{E}}_j^j - \tilde{\mathcal{E}}_j^{ij} \right) \tag{3.14}$$

where $\tilde{\mathcal{E}}_i^{ij}$ is the single point energy of monomer i calculated in the basis set of dimer ij with self-consistent dipoles placed on all monomers n where $n \neq i, j$. This represents a non-negligible increase in computational cost however, due to the need to perform an additional $4N_{\text{dim}}$ single point energy calculations, where $N_{\text{dim}} = \frac{N(N-1)}{2!}$, is the total number of unique dimers within the system. This still presents a more computationally efficient approach for improving the MBE convergence than introducing the trimer terms, however.

3.2.4 Exploiting Parallelism

As introduced in section 3.1.3, the general structure of an EFM calculation is inherently embarrassingly parallel, owing to the independent nature of the individual monomer/dimer energy calculations. The current implementation within QUEST can be generalised and divided into several distinct sections, as shown in Fig 3.4, within which parallelism can be exploited. Although each step in the main EFM computation may require information from previous steps, each individual section, at its core, is a series of independent energy calculations which can all be performed simultaneously, in an attempt to decrease the overall time required. This introduces several important considerations. Firstly, there are several different methods to introduce distributed programming capabilities within python, each with there own pros and cons, therefore, determining the most appropriate approach for this implementation, but also for potentially expanding the existing code base in the future,

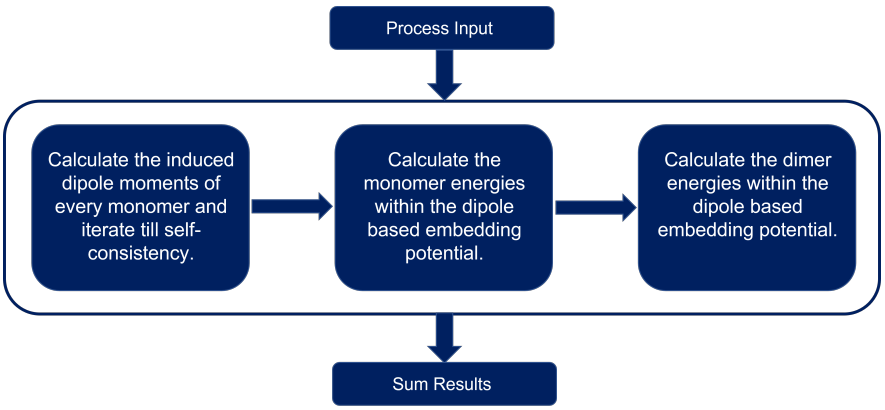

Figure 3.4: Flow diagram demonstrating the rough breakdown of an EFM single point energy calculation as implemented within QUEST. The main computation is within the central block which can be split into three distinct sections (for the binary interaction approximation), within which parallelism can be exploited.

must be carefully considered. Secondly, introducing parallelism without proper optimisation, such as efficient batching and memory management, could introduce complications which would restrict the overall benefit.

Parallel Programming in Python

Many different python libraries exist for the introduction of distributed programming, all with their own approaches, ranging from symmetric multiprocessing, to cluster/grid architecture programming, to dedicated cloud computing.[i] It can even be used to interface with GPUs using libraries such as CUDA or OpenCL. Due to the embarrassingly parallel nature of EFM, it can easily be applied to a cluster architecture approach enabling efficient scaling to any large high-performance computing (HPC) facility. For this reason, two libraries were selected to focus on.

The first was mpi4py[190–193], which provides python equivalents for commands from the *Message Passing Interface*[194;195] (MPI) which is a standardized and portable message-passing system providing syntax and semantics of library routines in several different scientific programming languages - Fortran, C or C++. MPI is applicable to a wide variety of parallel computers and has become the leading standard for message-passing libraries. It functions by initiating a specified number of simultaneous processes running the given program. Each of these processes is assigned an integer rank from 0 to $n-1$, where n is the total number of processors requested. Each processor manages its own function and memory whilst MPI provides an interface for communication between them such as the `send()` and `receive()` commands.

The second is RAY[196], which aims to provide a simpler API to introduce distributed programming options within Python, Java and C++. It is a reasonably new approach that consists of a master process with specified functions, labelled as tasks, which can be looped over, with each iteration being sent to any idle worker processes. This allows concepts such as shared memory to be employed. One of the main benefits of this type of

[i] See a more detailed list of available libraries at https://wiki.python.org/moin/ParallelProcessing

```
def mon_init(self,size):
    while len(self.mon_data)%size != 0:
        self.mon_data.append(None)
    self.mIndx = []
    x = 0
    u = numpy.zeros((len(self.mon_data)//size,size))
    for c in range(len(self.mon_data)//size):
        for i in range(size):
            u[c,i] = i + c*size
    for i in range(size):
        for c in range(len(self.mon_data)//size):
            self.mIndx.append(u[c,i])
    return
```

Figure 3.5: Example python function from QUEST[35] to set up efficient batches of monomer energy calculations over a given number of processors. The labels are subsequently distributed using the command `comm.Scatter(numpy.asarray(QEfm.mIndx,dtype=int),mIndx_pn,root=0)`.

approach is that the RAY module deals with a large portion of the process management, such as task batching and master/worker balance, which can often lead to inefficient parallel implementations if left purely to the developer.

Within this work the MPI based python package mpi4py was utilised due to its wide support, particularly with the many different high performance computing systems, therefore, hopefully providing a reduced chance for issues when utilising QUEST on a range of different compute systems.

Ensuring Maximum Efficiency

Improving the efficiency of a parallel implementation is vital when attempting to maximise the possible gains. Within the implementation of EFM several key concepts had to be considered. Firstly, the load balancing of the processors had to be optimised, to ensure no process was sitting idle whilst others handled an unequal proportion of the computational work. This was achieved by implementing efficient batching of the individual energy calculations across the available processors. At each stage in the overall EFM calculation, the number of individual energies to be computed is determined alongside the total number of available processes. Each energy calculation is given a label $0 - n$ where n is the total number of single point energy calculations at a given EFM stage. These labels are then distributed evenly across all available processors, such that any given processor will perform the same number of energy calculations, to within ± 1, as each of the other processors . Due to the nature of the `MPI.Scatter()` command however, this list of label must have length l such that the remainder of l/n_{proc} is 0, where n_{proc} is the total number of available processors. If when setting up the batches this is not satisfied, additional labels are introduced which when read by a given process, are understood as *do nothing on this iteration*. An example function, taken from QUEST, for setting up these batches is shown in Fig. 3.5.

The second major consideration was the efficient use of memory throughout an EFM

calculation. At each stage individual energy calculations are performed which generate a large subset of results, such as energies, integrals, density matrices etc. Storing all these results throughout the entire EFM calculation would result in a build up of unnecessary memory usage, which would limit the total size of the systems which could be treated with EFM. Additionally, there are several places within the implementation of EFM where each processor requires a copy of certain data to perform its set of tasks. Therefore, careful consideration of the values being stored by each single point calculation was required, discarding anything that was deemed unnecessary in the scope of the full EFM calculation.

Computational Scaling of the Implementation

Measuring the efficiency of a parallel implementation is a common and very useful technique throughout any form of computational based science. The absolute speed up gained can be defined as the ratio of the time taken to perform a single calculation on a single processor, t_0, to the time taken on n processors, t, represented as $\left(\frac{t}{t_0}\right)^{-1}$. Under ideal conditions, this would produce a linear trend where if the number of processors is doubled, the speed-up achieved also doubles, however, in reality this is not possible. Therefore, we can define the efficiency of a calculation as the ratio of the achieved speed up to the ideal speed up, which is often represented in the form of a percentage.

Fig 3.6 shows how the implementation in QUEST performs when a single, binary-interaction approximation, calculation on a water cluster consisting of 103 molecules is performed with different number of processors. To account for variable frequency scaling, three ideal lines have been plotted. The first is the traditional ideal line, $y = mx$ with $m = 1$. The two dashed lines represent the same ideal line scaled down such that $m = 1 - 0.15$ and $m = 1 - 0.33$ respectively, in accordance with the quoted clock speeds for AMD EPYC 7551 processors. From Fig 3.6 it is clear that, at a low number of processors, the achieved speed up follows the ideal line very closely. When using higher numbers of processors, the trend starts to deviate from the ideal line, but remains between the scaled lines, thus, indicating the QUEST implementation to be efficient and scalable. It is also important to note that there is an expected drop off in speed up at 103 processors due to the fact that the first two stages of the calculation, determining the embedding potential and calculating the monomer energies, will only perform a maximum of 103 energy calculations simultaneously. Therefore, will not benefit from including more processors than there are energy calculations to be performed. However, the dimer calculation stage will tend to dominate the time required for any reasonable size calculation, resulting in the expected drop off to be small, which is also observed.

3.3 Improving the Embedding Field by Short-Range Attenuation of the Dipole Model

The dipole potential is a good approximation to the Coulomb potential between two neutral subunits, in the asymptotic region of the potential, in which higher-order terms of the multipole expansion make a vanishing contribution. However, if the two charge

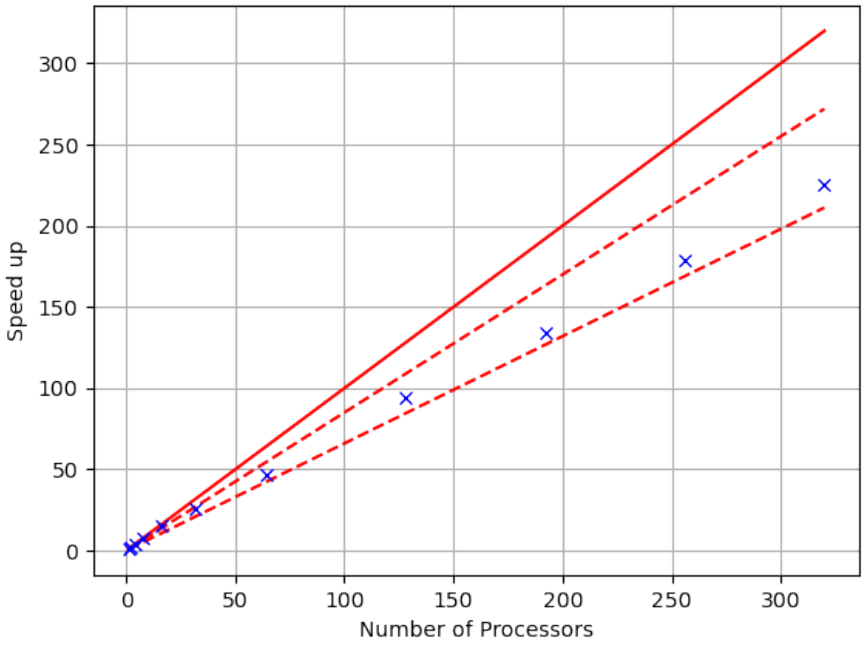

Figure 3.6: Measured speed up when increasing the number of processors for a HF/aug-cc-pVDZ EFM, binary-interaction approximation, calculation on a cluster consisting of 103 water molecules, compared to the ideal speed up at three different clock speeds, which accounts for variable frequency scaling.

distributions are not well separated and have a closer approach, the absence of the higher-order multipole terms results in an unphysical potential. As the system size was increased, the probability that two monomers were within this unphysical region was increased, where the interaction of their charge density with this potential would result in convergence issues within their individual calculations. This error would accumulate throughout the MBE causing significant errors in the final energies. This break down of the dipole based embedding potential approximation was amplified when utilising DFT based methods due to the increased polarisability of the orbitals, which is an artifact of the delocalisation error when using approximate exchange-correlation functionals[197]. These errors in the short-range truncated multipole expansion are widely documented and many methods for dealing with them have been proposed.[172;198] In work by Hirata and co-workers,[172] and discussed within section 3.1.2, this issue was observed and dealt with by augmenting the potential with partial charges for each monomer, optimising them to reproduce the Coulomb potential of the given monomer as closely as possible.

In this work, to overcome the inaccuracy of the dipole potential at short range, without introducing a new, and potentially more costly, embedding potential term, a short-range attenuation factor, based on the error function, was introduced,

$$V_j^{\mu}(\mathbf{r}_n) = \frac{e_j \mathrm{erf}\left(\mu|\mathbf{r}_n - \mathbf{R}_j - \left(\frac{\mathbf{d}}{2}\right)|\right)}{|\mathbf{r}_n - \mathbf{R}_j - \left(\frac{\mathbf{d}}{2}\right)|} - \frac{e_j \mathrm{erf}\left(\mu|\mathbf{r}_n - \mathbf{R}_j + \left(\frac{\mathbf{d}}{2}\right)|\right)}{|\mathbf{r}_n - \mathbf{R}_j + \left(\frac{\mathbf{d}}{2}\right)|} \tag{3.15}$$

where μ is a parameter which controls the rate of attenuation: as $\mu \to 0$, $\mathrm{erf}(\mu) \to 0$ whilst

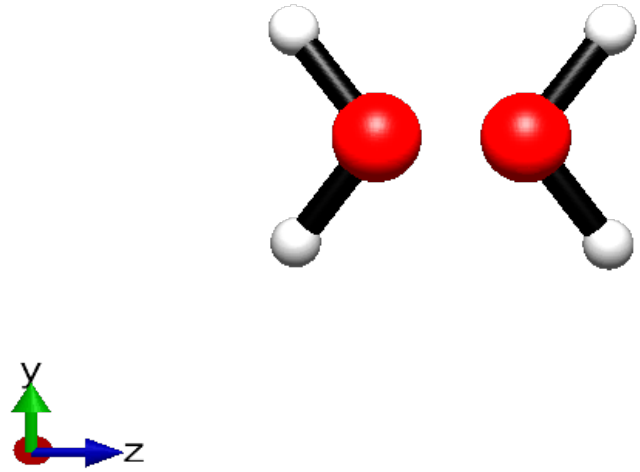

Figure 3.7: The orientation of a water dimer with a separation of 2.0 bohr between the oxygen atoms. The point $z = 0$ is placed directly between the two oxygen atoms.

as $\mu \to \infty$, $\mathrm{erf}(\mu) \to 1$. The resulting effect of Eq. (3.15) on the potential can be observed by considering the effective Coulomb potential of a water molecule a in the presence of another water molecule b with a separation of 2.0 bohr, the orientation of which is shown in Fig 3.7. The effective Coulomb potential in a can be represented by the difference between the Coulomb potentials of the total dimer and that of molecule b,

$$\tilde{v}_a^{\mathrm{J}}(\mathbf{r}) \approx v_{ab}(\mathbf{r}) - v_b(\mathbf{r}), \tag{3.16}$$

in which the Coulomb potentials are as defined in Eq. (3.4). This can then be compared to the effective attenuated dipole potential constructed from the Coulomb potential of a and the dipole potential of b,

$$\tilde{v}_a^{\mu}(\mathbf{r}) \approx v_a(\mathbf{r}) + v_b^{\mu}(\mathbf{r}). \tag{3.17}$$

The potentials due to Eqs. (3.16) and (3.17) are plotted in Fig. 3.8 for a range of attenuation parameters μ. Fig 3.8 clearly demonstrates how this attenuates the unphysical features of the dipole based potential in the vicinity of water molecule b, bringing it much closer to the full Coulomb potential. Multiplication of the potential by the density at each point in space can make the picture somewhat clearer by highlighting the potential in areas that contribute to the energy of the molecule; these are shown in Fig 3.9 in analogy to Fig 3.8. From both these figures its clear that significant attenuation is required to remove the unphysical short range features of the dipole potential. To further understand the impact of the dipole potential on systems with an increased separation, Fig 3.10 reproduces the analysis of Fig 3.9 for a system where the separation between the oxygen atoms is 8 bohr (the oxygen

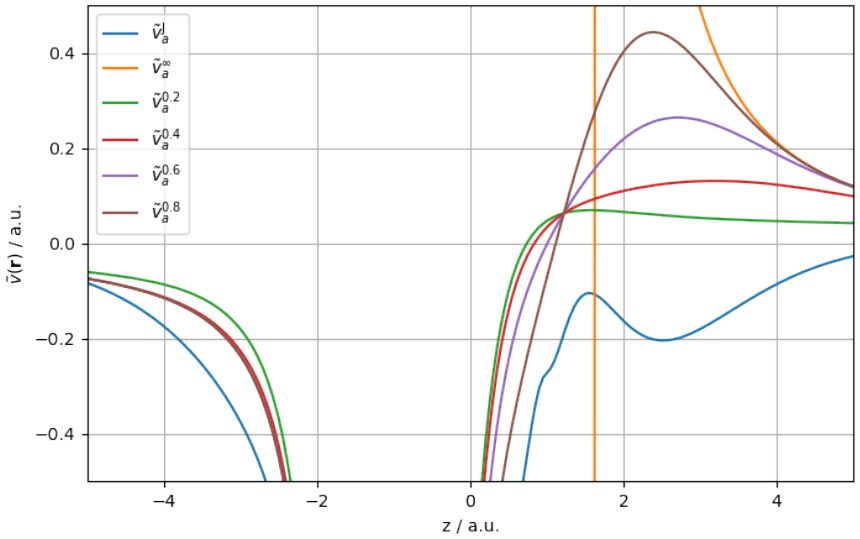

Figure 3.8: The effective potential for a water molecule, in the presence of another water molecule at a distance of 2.0 bohr, constructed from the full Coulomb potential $\tilde{v}_a^J$ and the attenuated dipole potential $\tilde{v}_a^\mu$ according to Eqs. (3.16) and (3.17) respectively.

atoms are placed at $z = +4$ and $z = -4$ bohr respectively). This clearly shows how the break down in the dipole potential only imposes errors on the energy of the system when the two atoms have a small separation. It also demonstrates that the attenuation doesn't introduce any unexpected behaviour when considering monomers that have an increased separation.

Even at these significant levels of attenuation however, it can be shown that the error with respect to a conventional all electron calculation rapidly approaches that of the unattenuated potential, this is demonstrated in Fig 3.11 and Fig 3.12. Also clear is that for calculations with HF and TPSS the error in the EFM calculation is decreased with $0.25 \lesssim \mu \lesssim 1$. An interesting observation is the fact that for certain cluster sizes, when calculated using DFT (TPSS), the error crosses 0, potentially indicating that for DFT, there is an optimum point at which the error is removed from the EFM calculation. This opens up a larger avenue for investigation into exactly how the attenuation impacts the DFT results and how geometry dependent it is, which is ongoing at the time of writing. It is important to note that this analysis is on optimised geometries for small water clusters, where in principle the individual molecules will be arranged such that they maximise favourable interactions, often leading to more tightly packed or specifically arranged systems. The analysis on larger systems within this chapter looks at systems obtained from molecular dynamics (MD) snapshots, which may introduce a potentially less optimally organised arrangement of molecules within the system. This may have an impact on how much the attenuation effects the energy of the total system. Ideally averaging over many MD snapshots, or optimising larger geometries (see chapter 4), would provide a more complete analysis, however, this goes beyond the scope of the analysis in this chapter.

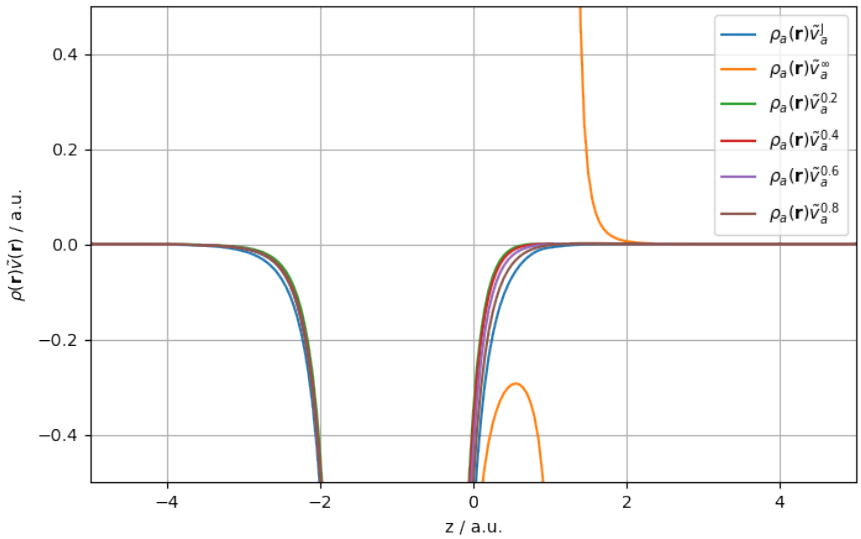

Figure 3.9: The effective potential for a water molecule multiplied by its density ρ_a, in the presence of another water molecule at a distance of 2.0 bohr, constructed from the full Coulomb potential $\tilde{v}_a^J$ and the attenuated dipole potential $\tilde{v}_a^\mu$ according to Eqs. (3.16) and (3.17)

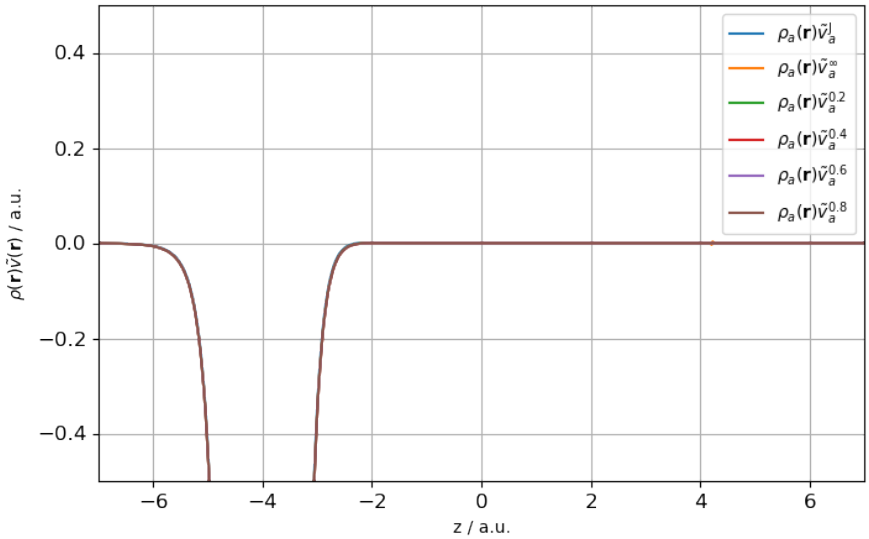

Figure 3.10: The effective potential for a water molecule multiplied by its density ρ_a, in the presence of another water molecule at a distance of 8.0 bohr, constructed from the full Coulomb potential $\tilde{v}_a^J$ and the attenuated dipole potential $\tilde{v}_a^\mu$ according to Eqs. (3.16) and (3.17)

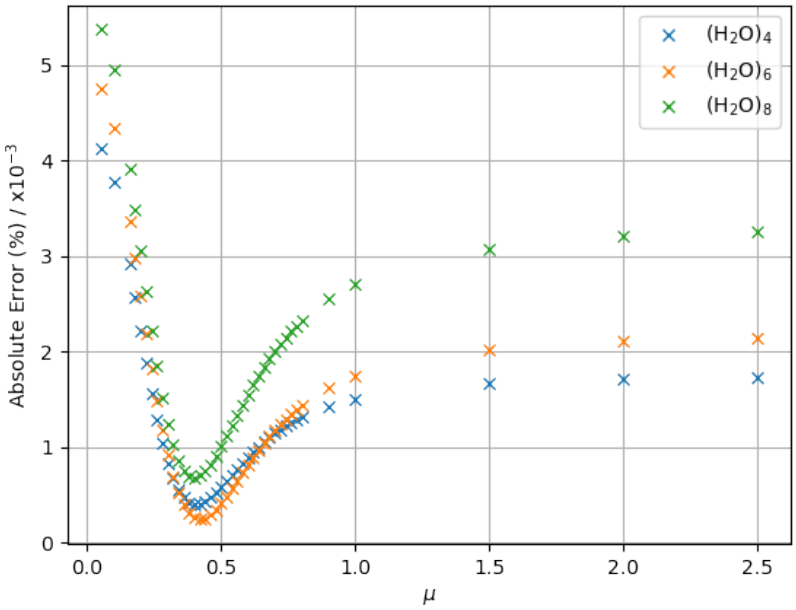

Figure 3.11: The error in the HF-EFM energy for three different water clusters taken from the data set provided in Ref. 187, at varying levels of embedding field attenuation.

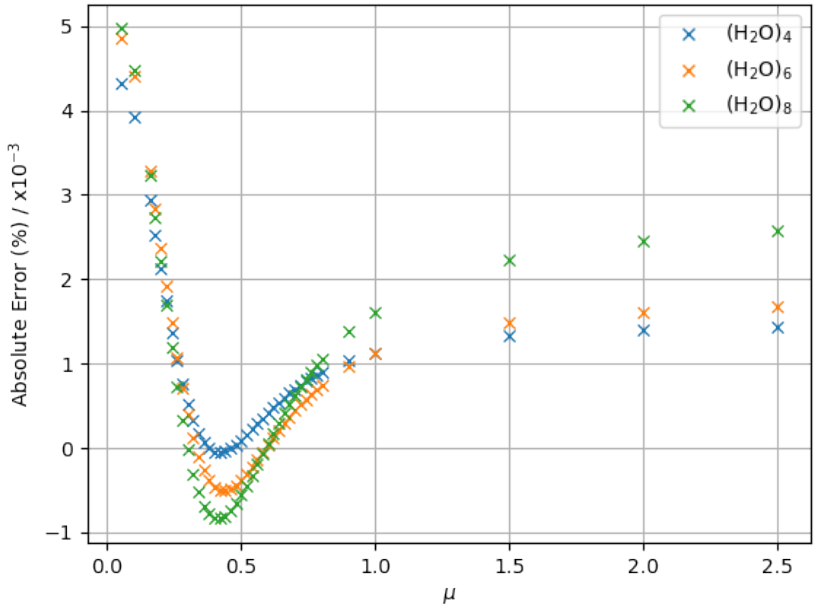

Figure 3.12: The error in the DFT(TPSS)-EFM energy for three different water clusters taken from the data set provided in Ref. 187, at varying levels of embedding field attenuation.

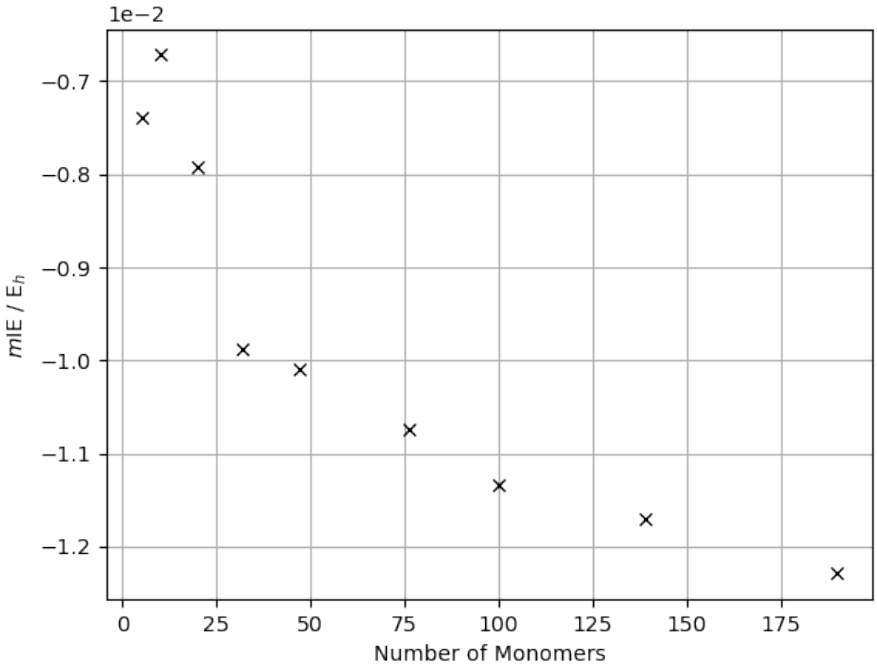

Figure 3.13: The *m*IE for a series of water clusters calculated using the EFM at the Hartree-Fock theory level with the aug-cc-pVDZ basis set and RI approximation.

3.4 Application to Water Clusters

Large molecular clusters are often used to model liquid structure and enable the study of solvation.[199–202] However, the high-rank polynomial dependence of computational cost with respect to system size for modern electronic structure techniques can be restrictive.[1;2] This limitation is often amplified when studying the complex behaviour of systems within an external magnetic field, see section 2.4. Many experimental studies have shown that an external magnetic field can create a measurable change in the properties of bulk liquid structures,[38–46] the rationale behind which, and in some cases the nature of these changes, is still a topic of significant debate. Though, the use of a magnetic fields to alter the properties of liquids within various industrial applications is well documented.[47–49] LAO based EFM would provide a possible route to gaining a theoretical understanding of bulk liquid structure and how it responds to external fields. Water represents a good model system, and has been frequently used when discussing fragmentation methods, due to the importance of intermolecular interactions within its structure, its general importance in every day life and its amenability to fragmentation based approaches.

3.4.1 Influence of Magnetic Fields on Water

Intermolecular Interaction Energy of Water

The total intermolecular interaction energy, E_{IE}, for a system can be defined as the difference between its total energy and the sum of the isolated molecule energies, however, when approximating bulk systems it is more useful to define the interaction energy

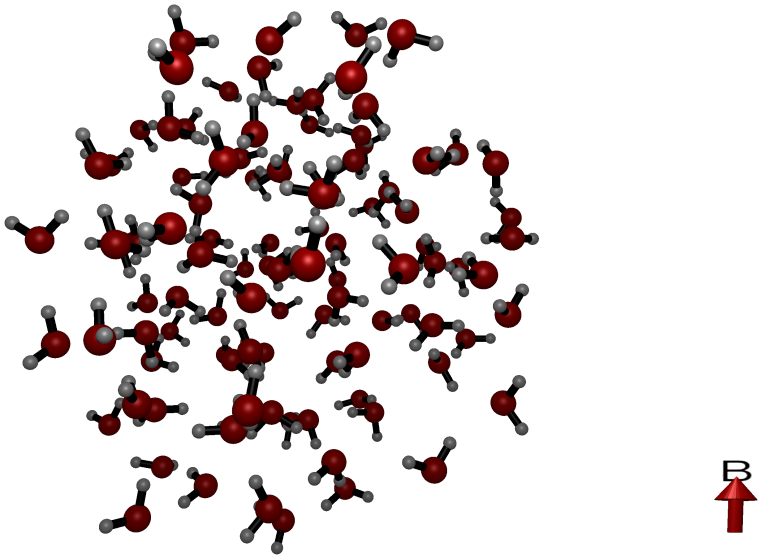

Figure 3.14: The structure of a $(H_2O)_{103}$ cluster determined from a snapshot of a molecular dynamics simulation. The direction of the applied field is shown by the red arrow.

per molecule, or the mean interaction energy (*m*IE), of the system, $\frac{E_{\text{IE}}}{N}$ where N is the total number of molecules within the system. By plotting the *m*IE against the number of molecules, shown in Fig. 3.13, it is clear that the *m*IE approaches a *bulk limit* as the system size is increased. This gives a good indication of how many molecules must be included within a molecular cluster to effectively approximate a bulk solution. For the example of water, Fig. 3.13, the systems were produced by taking a snapshot from an NVT ensemble molecular dynamics (MD) simulation of water, using the TIP3P force field[203;204] in the DL_POLY software package[205]. The simulation was carried out at 300 K on a cubic simulation cell of dimension 30 Å, allowed to equilibrate for 150 ps. It is import to note that the MD simulation was performed with no external magnetic field. Molecules were then systematically removed via a set radial cut-off to produce systems of varying size. Single point energy calculations were performed on these water clusters using the *binary interaction* approximation with Hartree-Fock theory, the aug-cc-pVDZ basis set[206] and an auto-generated auxiliary (AutoAux) basis set for density fitting[122]. Although this analysis shows that to truly approximate a bulk system quantitatively a system size of > 200 water molecules may be necessary, a system size of 103 water molecules, shown in Fig 3.14, was chosen for further investigation, as it represents a reasonable compromise between approaching this limit and allowing for computationally tractable calculations.

Single point EFM energy calculations, on the $(H_2O)_{103}$ cluster, were performed using various electronic structure methods, combined with the aug-cc-pVDZ/AutoAux basis sets. Some data utilising the larger aug-cc-pVTZ basis set[188;189] was also produced which demonstrated no significant deviation from the observed trend in the interaction energies for the smaller basis, thus confirming that aug-cc-pVDZ produced a sufficient level of accuracy at these field strengths. This is demonstrated in Fig 3.15 for DFT as the black circles. The applied magnetic field was varied in strength along the z axis. It is important to note

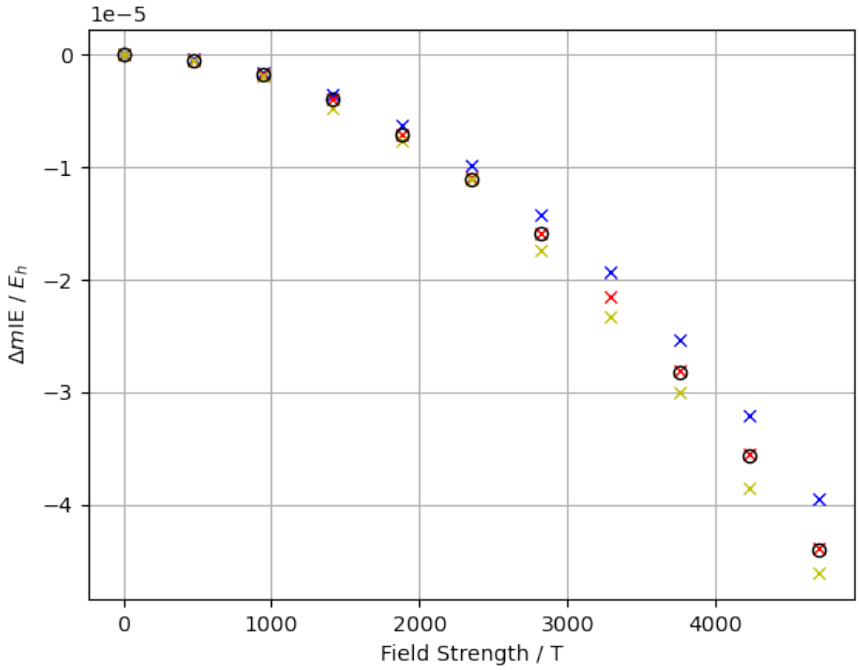

Figure 3.15: Change in *m*IE for a molecular cluster consisting of 103 water molecules, determined at the HF (blue), DFT/cTPSS (red) and MP2 (yellow) theory levels with the aug-cc-pVDZ basis set and RI approximation. Equivalent DFT/cTPSS calculations with the aug-cc-pVTZ basis set are also shown as black circles.

that these results don't include geometry relaxation within the external magnetic field, which will become significant at higher field strengths. However, the change in energy for a static geometry remains a good indication of how the system reacts to weaker fields where the effects on the geometry of bulk systems will be minimal. All DFT results in Fig. 3.15 include short-range attenuation of the embedding potential based on Eq. (3.15) with an attenuation parameter of $\mu = 0.45$. This was chosen by systematically reducing the parameter, increasing the attenuation, until the calculations became stable. It is also relevant to note that this value corresponds to the range that minimised the EFM error for small water clusters, as demonstrated in Figs. 3.11 and 3.12. The resulting trend demonstrates how, as the field strength is increased, the inter-molecular interactions, become stronger. This provides theoretical backing for the experimentally observed changes in the physical properties of water, under the influence of a magnetic field. However, the results presented in Fig 3.15 do not include geometry relaxation within the field and are restricted to including 2-body exchange and correlation interactions, which both could have an impact on the response to an external field.

Visualising the Electron Density from EFM Calculations

Simply studying the binding energies for a molecular cluster, such as water, is only one part of the picture, however. Expanding the method to enable the visualisation of the changes in the electronic structure around the individual molecules would give a more in depth picture of how the magnetic field is influencing the intermolecular interaction. This

can be achieved through applying the MBE to the total electron densities calculated for each monomer/dimer/trimer etc.,[207]

$$\rho\left(\mathbf{r}_m\right) = \sum_i \rho^i\left(\mathbf{r}_m\right) + \sum_{i<j} \Delta\rho^{ij}\left(\mathbf{r}_m\right), \tag{3.18}$$

where,

$$\rho^i\left(\mathbf{r}_m\right) = \sum_{\mu\nu\in i} D^i_{\mu\nu}\omega^*_\mu\left(\mathbf{r}_m\right)\omega_\nu\left(\mathbf{r}_m\right) \tag{3.19}$$

$$\Delta\rho^{ij}\left(\mathbf{r}_m\right) = \sum_{\mu\nu\in i,j} [D^{ij}_{\mu\nu} - \left(D^i_{\mu\nu} \oplus D^j_{\mu\nu}\right)]\omega^*_\mu\left(\mathbf{r}_m\right)\omega_\nu\left(\mathbf{r}_m\right). \tag{3.20}$$

Here D^i is the density matrix of monomer i and D^{ij} is the density matrix of the dimer made up of monomer i and monomer j. μ and ν are the indices of the basis functions.

Fig 3.16 shows, for the same fixed geometry water trimer as described previously within this chapter, with an applied magnetic field perpendicular to the plane of the cluster, how the electron density relative to the isolated water molecules, changes as the strength of the external magnetic field is increased up to 0.1 a.u. From the two images of Fig 3.16 the hydrogen bonding network is clearly visible and present with and without the applied magnetic field. From simply these two images however, it is very difficult to determine the change due to the applied field, suggesting that the influence of the field is very subtle even at such high field strengths. To get a clearer picture, the difference between the electron density at the two field strengths, relative to the isolated water molecules, can be calculated and has been shown in of Fig 3.17. Here it is clear that the applied magnetic field is drawing electron density into the centre of the cluster which could account for the increased binding energy, however, it also suggests that the increase in binding energy can't simply be explained as a strengthening of hydrogen bonds, at least at field strengths on the order of 0.1 a.u. This could be rationalised by a potential combination of strengthened hydrogen bonding as well as a new attractive effect due to the external magnetic field contracting the electron density perpendicular to the applied field creating the observed build up of density in the centre of the cluster. It is important to note the isovalues used for Figs 3.16 and 3.17 however, since the value used in Fig 3.17 is an order of magnitude smaller than that used for Fig 3.16. This highlights that whilst the magnetic field is influencing the electronic structure within the system as discussed, this influence is still relatively small compared to the standard Coulombic interactions already present within the system which continue to dominate the intermolecular interactions.

3.4.2 Influence of Electric Fields on Water

In addition to the application of arbitrary strength external magnetic fields to molecular systems, the electronic structure software, QUEST, can apply external electric fields either on their own, or in combination with magnetic fields. This opens an interesting avenue for comparison between the effects of both magnetic and electric fields. This can be demonstrating by applying the same analysis on the $(H_2O)_{103}$ within an external electric

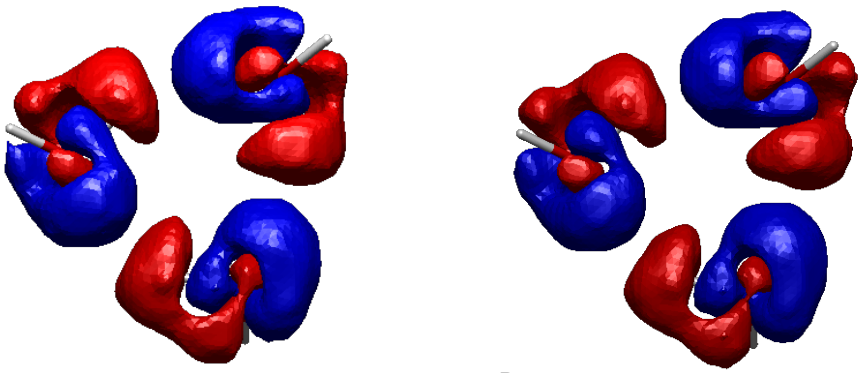

Figure 3.16: Density difference plots for a water trimer determined at two different field strengths (0.0 a.u. and 0.1 a.u.). All calculations performed using DFT with the cTPSS functional and the aug-cc-pVDZ basis set. Blue indicates a build up of electron density and red represents a depletion. The isovalue was set to 0.001.

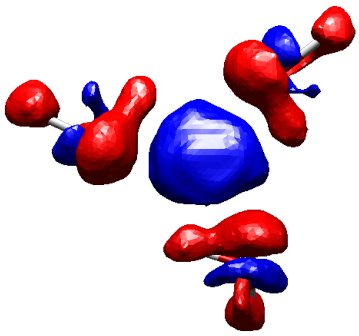

Figure 3.17: The change in electron density, relative to the isolated monomers, for a cyclic water trimer, from B=0.0 a.u. to B=0.1 a.u. calculated with the cTPSS DFT functional and the aug-cc-pVDZ basis set. Blue indicates a build up of electron density and red represents a depletion. The isovalue was set to 0.0001.

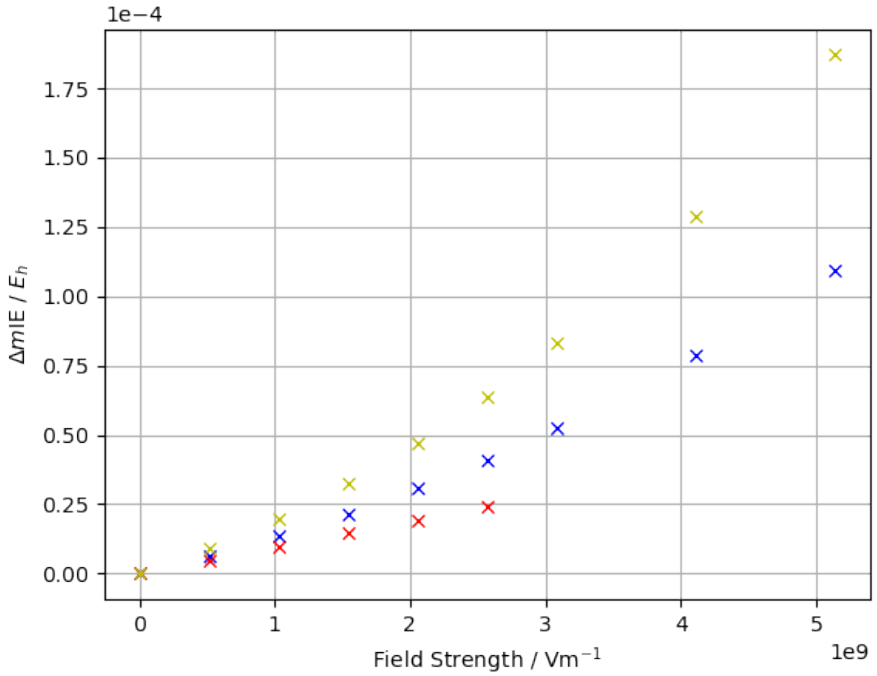

Figure 3.18: Change in *m*IE with respect to an applied electric field, for a molecular cluster consisting of 103 water molecules, determined at the HF (blue), DFT/cTPSS (red) and MP2 (yellow) theory levels with the aug-cc-pVDZ basis set and RI approximation.

field, shown in Fig 3.18. From this, it can be shown that an applied electric field seems to have the opposite effect on the *m*IE of water when compared to an applied magnetic field. As the field strength is increased, the *m*IE, and therefore, the intermolecular interaction strength decreases, weakening the binding between the water molecules. This however, has the same limitation that it does not involve geometry relaxation in the fields. It still provides a qualitative analysis on how the electric field influences the hydrogen bonding within the water cluster.

One interesting observation from these results was the erratic behaviours of the energy for the DFT results at field strengths above 0.08 a.u., where 1 a.u. $= 5.1422 \times 10^{11}$ Vm^{-1}. These results were considered anomalous and potentially not converged therefore have been left out of Fig. 3.18. The applied fields are significantly large which clearly has a significant impact on the embedding potential approximation, once again potentially amplified by the delocalisation error when using approximate exchange-correlation functionals as discussed in section 3.3. This presents an interesting discussion on how the dipole embedding potential is influenced by the electric field and if it remains a suitable approximation, also whether the attenuated dipole approximation of Eq. (3.15) can help fix this convergence issue. Since this work is primarily focused on the influence of external magnetic fields however, this analysis and discussion is reserved for future work.

4 Structural Optimisation of Large Molecular Clusters in Strong Magnetic Fields using EFM

Up to this point the implementation and use of EFM has been discussed for systems at static geometries, however, this can only go so far as an analytic tool. The changes in electronic structure due to an applied external field will lead to changes in the forces applied to the atoms within the system, therefore, to have a complete analytical tool for practical chemical investigations, the response of the forces on the atoms to the applied field must be considered. Molecular gradients in the presence on strong magnetic fields enables applications such as the study of chemical reactivity via geometric minima and transition states or *ab initio* molecular dynamics. Recent advances have presented an efficient and fully analytic approach to evaluate derivative integrals over LAOs.[24] This was demonstrated for a series of small molecular systems, however, it still retains the computational challenges when utilising LAOs, therefore, extension of the EFM method to include calculation energy derivatives would enable the application of structural optimisation within an external field, resulting in a more comprehensive tool for studying the effect of the field on large molecular clusters.

4.1 Implementation of Parallel Analytic Gradients in the EFM Approach

The equation for the total energy of a large molecular cluster can be written as a many-body expansion of specified fragments of the system, usually defined as the individual molecules. This is outlined in chapter 3 and written here up to the two-body interaction terms for reference,

$$\mathcal{E}^{\text{total}} = \sum_i \mathcal{E}_i + \sum_{j>i} (\mathcal{E}_{ij} - \mathcal{E}_i - \mathcal{E}_j) \dots \tag{4.1}$$

Here $\mathcal{E}_i$ is the total energy of monomer i and $\mathcal{E}_{ij}$ is the total energy of the dimer made up of fragments i and j. To enable the truncation of Eq. (4.1) and still retain a reasonable level of chemical accuracy, we define an electrostatic embedding potential included in a modified Hamiltonian given in Eqs. (3.2) and (3.3). Additionally introduced in chapter 3, first derivatives of the total energy can be obtained by a similar application of the many-body expansion, such as the derivative with respect to atomic positions. This can be written in terms of the binary interaction approximation as,

$$\frac{\partial \mathcal{E}^{\text{binary}}}{\partial x} = \sum_i \frac{\partial \mathcal{E}_i}{\partial x} + \sum_{j>i} \left(\frac{\partial \mathcal{E}_{ij}}{\partial x} - \frac{\partial \mathcal{E}_i}{\partial x} - \frac{\partial \mathcal{E}_j}{\partial x} \right), \tag{4.2}$$

where $\frac{\partial \mathcal{E}_i}{\partial x}$ and $\frac{\partial \mathcal{E}_{ij}}{\partial x}$ are the first derivatives, with respect to motion along x, of monomer i and dimer ij respectively, within the embedding potential.

If utilising a pure many-body based approach the individual derivative calculations are simply the molecular derivative of the specified fragment as provided by any electronic structure software package. It additionally maintains the embarrassingly parallel nature of EFM whereby each energy and its associated derivative can be calculated independently and simultaneously. However, to improve the convergence of the many-body expansion, enabling an increased level of truncation, an electrostatic embedding potential is included as described in Eq. (3.2). As a result, how this potential impacts the forces on the atoms and its response the to system must be considered.

4.1.1 Derivative of the Embedding Potential

In general, the response of the position of the point charges used to model the dipole potential is considered negligible and therefore is ignored within the current implementation of the analytical derivative expression. This results in the analytic gradient equations being approximate. Analytical derivatives have been presented for various forms of the embedding potential, however.[208;209] Instead this is considered in an optimisation by re-calculating the dipoles at each step. Each gradient calculation however, is performed within the self-consistent embedding potential, therefore, the impact of this fixed potential on the atomic coordinates must be considered. As the implementation of the dipole based embedding field was constructed as adapted nuclear-electron integrals, where the nuclear charge was replaced by the partial charges representing the self-consistent dipole moments, the derivative can be constructed in the same way,

$$\begin{aligned}\frac{\partial V^i_{ab}}{\partial N_x} = \sum_{j\neq i}\Bigg\{ & \delta_{NA}\left(\frac{\partial \mathbf{a}}{\partial A_x}\left|\frac{e_j}{|\mathbf{r}-\mathbf{R}-\frac{\mathbf{d}}{2}|}\right|\mathbf{b}\right) + \delta_{NA}\left(\frac{\partial \mathbf{a}}{\partial A_x}\left|\frac{-e_j}{|\mathbf{r}-\mathbf{R}+\frac{\mathbf{d}}{2}|}\right|\mathbf{b}\right) \\ & + \delta_{NB}\left(\mathbf{a}\left|\frac{e_j}{|\mathbf{r}-\mathbf{R}-\frac{\mathbf{d}}{2}|}\right|\frac{\partial \mathbf{b}}{\partial B_x}\right) + \delta_{NA}\left(\frac{\partial \mathbf{a}}{\partial A_x}\left|\frac{e_j}{|\mathbf{r}-\mathbf{R}+\frac{\mathbf{d}}{2}|}\right|\mathbf{b}\right) \\ & + \delta_{NB}\left(\mathbf{a}\left|\frac{-e_j}{|\mathbf{r}-\mathbf{R}+\frac{\mathbf{d}}{2}|}\right|\frac{\partial \mathbf{b}}{\partial B_x}\right)\Bigg\}.\end{aligned} \tag{4.3}$$

This is implemented by modifying the nuclear-attraction gradient terms for LAOs introduced in Ref. 24 and added to the existing gradient terms for the given monomer/dimer derivative calculation.

4.1.2 Optimisation Algorithms

Calculating the force on the atoms within a system can be informative however, they provide the most practical use when combined with an optimisation algorithm, to find the minimum energy structure of a system. Since, even when employing LAOs, the total energy and its derivatives must be real, standard optimisation algorithms can be employed without alteration.[24] However, whilst internal coordinates are often used for the optimisation as they present a convenient method of representing the structure of the system,[210;211] they can't

be conveniently applied for systems within an external field however, due to the dependence of the energy of the system on the orientation with respect to the external field. Therefore, Cartesian coordinates are used throughout this work. There are several different approaches when considering a geometry optimisation, which are generally grouped by the required variables; those that only require the energy, those that require the energy and its first derivative, and finally those that additionally require the Hessian or second derivative of the energy.[212;213] These all balance the cost of calculating the three variables, the energy, gradient and the Hessian, with the number of iterations required for convergence. Energy only algorithms are the most widely applicable however, generally require the largest number of iterations. Methods that employ the Hessian will, in general, converge in the fewest number of iterations but requires the Hessian evaluation with each step which itself can be extemely costly. Typically, gradient based methods are the most efficient algorithms as they provide a good compromise of rapid convergence without the need for costly higher order derivatives, and therefore, are the most widely employed.

Within this work a *quasi*-Newton line search method is employed, which can be considered as an approximation to Hessian based optimisation algorithms. For a Newton-based method the potential energy surface is approximated by a Taylor expansion about the current point, $\mathbf{r}_0$, which when truncated at second order can be written as,

$$\mathcal{E}(\mathbf{r}) = \mathcal{E}_0 + \mathbf{g}_0^{\mathsf{T}} \Delta\mathbf{r} + \frac{1}{2}\Delta\mathbf{r}^{\mathsf{T}}\mathbf{H}_0\Delta\mathbf{r}, \tag{4.4}$$

where $\mathcal{E}_0$, $\mathbf{g}_0$ and $\mathbf{H}_0$ are the energy, gradient and Hessian for the system at coordinates $\mathbf{r}_0$. The gradient of Eq. (4.4) which can be written as,

$$\mathbf{g}(\mathbf{r}) = \mathbf{g}_0 + \mathbf{H}_0\Delta\mathbf{r}. \tag{4.5}$$

At the minimum energy coordinate of the potential energy surface the gradient will be zero. Setting Eq. (4.5) equal to zero leads to,

$$\Delta\mathbf{r} = -\mathbf{H}_0^{-1}\mathbf{g}_0, \tag{4.6}$$

known as the Newton step. However, this requires the calculation of the Hessian. *Quasi*-Newton methods remove this dependence by approximating the Hessian, whilst still determining the step according to Eq. (4.6). This presents a generally more efficient approach compared to methods that only use the energy or the gradient directly in steepest descent methods, and doesn't require the costly calculation of the Hessian at each step. The initial Hessian can be formed from a variety of approximations, such as; empirical estimations, calculations with a lower level of theory or by simply setting it to the identity matrix. It is then updated at each step through a given update method, for which common examples include; the Murtagh-Sargent (MS) scheme,[214] the Davidson-Fletcher-Powell (DFP) scheme[215] or the Broyden-Fletcher-Goldfarb-Shanno (BFGS) scheme.[216–220] The latter of which is employed within this work and therefore, considered here, the expression for the

update of the approximate Hessian can be written as,

$$\mathbf{H}' = \mathbf{H} + \frac{\Delta\mathbf{g}\Delta\mathbf{g}^{\mathsf{T}}}{\Delta\mathbf{r}^{\mathsf{T}}\Delta\mathbf{g}} - \frac{\mathbf{H}\Delta\mathbf{r}^{\mathsf{T}}\Delta\mathbf{r}\mathbf{H}}{\Delta\mathbf{r}^{\mathsf{T}}\mathbf{H}\Delta\mathbf{r}} \tag{4.7}$$

Direct expressions for updating $\mathbf{H}^{-1}$ within this model can also be defined to remove the need to calculate Eq. (4.7) and then find its inverse. Within this work the BFGS update method is used for a *quasi*-Newton optimisation where the initial Hessian is given by the identity matrix.

Since the energy, gradients and Hessian for the total system can all be obtained from the EFM, the optimisation algorithms require no modification and can be directly integrated with EFM. In addition, the EFM energies/gradients/Hessians can all be calculated in a parallel manner at each iteration within the optimisation. This has all been implemented within the QUEST electronic structure package.

4.2 Application to Water Clusters - The Importance of Structural Relaxation

In chapter 3, many results were presented demonstrating how the effects of a magnetic field can influence the intermolecular binding energies for water clusters. It was observed that an external magnetic field would increase the strength of the intermolecular interactions within water clusters, with plots of the electron density showing that the origins of this response is complex and requires a more in depth study for a true understanding. This investigation, although informative, does not allow for a complete analysis of the effects of the applied magnetic field on the intermolecular interactions in the water clusters however, particularly when considering increasingly large external field strengths. The extensions presented within section 4.1 would produce a more complete toolset for the analysis of these interactions, enabling the response of the structural geometry of the system not just the electronic structure to be taken into account.

4.2.1 Application to a Cyclic Water Trimer

As a first test case, the cyclic water trimer, first considered in section 3.2.1 with geometry shown in Fig. 3.1, is once again considered here. This represents a system small enough that it can be treated with conventional computational methods within QUEST enabling a comparative test case for the EFM derivatives. Table 4.1 shows the absolute errors for the first derivative of the energy with respect to the motion of each atom along each cartesian axis. With HF theory the EFM results in a mean absolute difference of 1.2×10^{-4} $\mathrm{E_h}a_0^{-1}$ (4%), demonstrating how this EFM based derivative method can achieve results reasonably close to those for the conventional approach, within a modest deviation. More importantly the sign of each derivative component remains the same when comparing the conventional and EFM results. Additionally, this remains true when considering DFT which gives a mean absolute difference of 1.7×10^{-4} $\mathrm{E_h}a_0^{-1}$ (2%). Since the aim of this work is to apply the EFM to LAO based methods, it is important to ensure this general agreement

Table 4.1: The absolute difference, at $|\mathbf{B}| = 0$ a.u.,in the EFM and conventional forces acting upon each atom within a cyclic water trimer with, geomtry as given in table 3.2, shown in Fig. 3.1, calculated with both HF theory and DFT (with the TPSS exchange correlation functional) and the 6-31G basis set. All values are given in atomic units ($E_h a_0^{-1}$).

	HF / $\times 10^{-4}$			TPSS / $\times 10^{-4}$		
Atom	x	y	z	x	y	z
O1	0.9	1.3	1.1	1.5	2.8	2.4
H1	0.2	1.7	0.9	0.7	2.4	1.6
H2	1.7	0.7	1.3	1.9	0.1	2.4
O2	1.1	2.2	3.9	2.7	1.8	3.8
H3	1.4	0.4	4.6	2.2	0.4	6.2
H4	1.4	0.0	0.0	2.1	0.7	0.8
O3	0.9	0.4	0.2	0.2	1.3	0.3
H5	0.6	0.5	0.6	1.3	0.8	1.4
H6	0.5	2.7	0.5	0.1	3.6	0.2

Table 4.2: The absolute difference, at $|\mathbf{B}| = 0.1$ a.u.,in the EFM and conventional forces acting upon each atom within a cyclic water trimer with, geomtry as given in table 3.2, shown in Fig. 3.1, calculated with both HF theory and DFT (with the TPSS exchange correlation functional) and the 6-31G basis set. All values are given in atomic units ($E_h a_0^{-1}$).

	HF / $\times 10^{-4}$			TPSS / $\times 10^{-4}$		
Atom	x	y	z	x	y	z
O1	1.1	1.0	0.8	1.3	2.4	2.0
H1	0.2	1.5	0.8	0.5	2.1	1.3
H2	2.0	0.9	1.3	2.3	0.4	2.3
O2	0.9	2.7	4.1	2.4	2.2	4.2
H3	1.3	0.1	4.5	2.1	0.1	5.9
H4	1.3	0.1	0.2	1.9	0.5	0.5
O3	1.3	0.3	0.3	0.7	1.1	0.1
H5	0.5	0.4	0.5	1.0	0.8	1.2
H6	0.7	2.9	0.4	0.0	3.9	0.3

beyond the zero field case. Table 4.2 demonstrates this for the same cyclic water trimer exposed to an external field of strength $|\mathbf{B}| = 0.1$ a.u., with direction perpendicular to the plane of the oxygen atoms, in the same manner as within section 3.2.1. From table 4.2 its clear that applying the EFM to calculate gradients within an external field retains the same level of accuracy as with the zero field case. With HF theory the mean absolute difference is 1.2×10^{-4} $E_h a_0^{-1}$ ($\sim 5\%$) and for DFT with the TPSS functional it is 1.6×10^{-4} $E_h a_0^{-1}$ ($\sim 2\%$).

As the energy derivatives present a reasonable approximation, the next step is to consider a full geometry optimisation, once again comparing between conventional methods and EFM for the same water trimer. The EFM method has been implemented to calculate the energy and its first derivative which can be fed to a *quasi*-Newton optimiser using the BFGS Hessian update according to Eq. (4.7). For all optimisation calculations not using the EFM, the convergence criteria is set as; the largest element of the gradient and of the ensuing step $< 3 \times 10^{-4}$ a.u., the root-mean-square of the gradient and of the ensuing

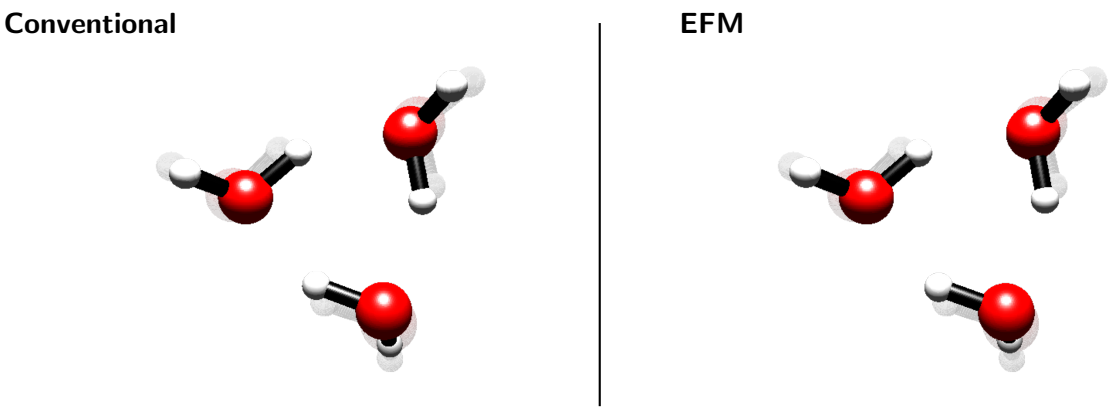

Figure 4.1: The initial (greyed out) and final geometries for the zero field optimisation of the cyclic water trimer from chapter 3. Optimisation was performed at the DFT level of theory with the TPSS functional and the 6-31G basis set.

step $< 2 \times 10^{-4}$ a.u., and the change in energy between steps $< 5 \times 10^{-6}$ a.u. However, due to the approximate nature of the gradient determined from the EFM, which neglects the response of the dipole moments, as described in section 4.1.1, it will not converge as accurately as with an all-electron fully analytic gradient. Therefore, when using the EFM, a slightly different set of criteria are defined, more focused on tightly converging the step and energy. For all EFM based optimisation calculations the convergence criteria is set to; the largest element of the step $< 6 \times 10^{-5}$ a.u., the root-mean-square of the step $< 4 \times 10^{-5}$ a.u., and the change in energy between steps $< 5 \times 10^{-6}$ a.u. Fig. 4.1 shows the optimised geometries, with the initial geometries greyed out, for the cyclic water trimer first presented in chapter 3, optimised both with and without the EFM at zero field. Both calculations used DFT and the TPSS exchange-correlation functional in combination with the 6-31G basis set. Both optimisations followed almost identical optimisation paths and resulted in near identical final geometries. The final energy of each equilibrium structure was; for conventional DFT $\mathcal{E} = -229.250947$ E_h and for EFM based DFT $\mathcal{E} = -229.252794$ E_h. The RMSD in the final atomic positions was 0.023615 Å and the RMSD in the final OH bond lengths and angles were 0.0037 Å and 0.56° respectively. From this its clear that the EFM based optimisation provides a reasonable approximation when determining minimum energy geometries, within a small tolerance.

Once again this analysis only considers the zero field case, therefore, it is beneficial to examine the efficacy of the EFM geometry optimisation to calculate equilibrium geometries of molecular clusters in strong magnetic fields. Here, the application of EFM geometry optimisation to the water trimer at $|\mathbf{B}| = 0.1$ a.u. is considered. In analogy to Fig. 4.1, Fig. 4.2 shows the initial and final geometries for conventional and EFM based DFT geometry optimisations for the cyclic water trimer. The final energies are $\mathcal{E} = -229.211643$ E_h and $\mathcal{E} = -229.199348$ E_h for the conventional and EFM calculations respectively. The RMSD in the final atomic positions were 0.0971 Å and the RMSD in the final OH bond lengths and angles were 0.0047 Å and 0.66° respectively. These deviations are similar to the those at zero field suggesting that the EFM can be expected to give a good approximation for a geometry optimisation with an external magnetic field.

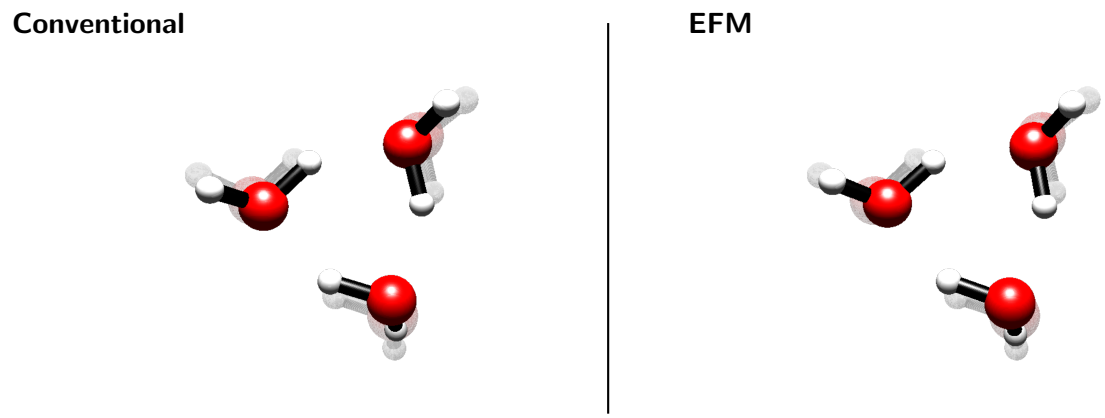

Figure 4.2: The initial (greyed out) and final geometries for the zero field optimisation of the cyclic water trimer from chapter 3. Optimisation was performed at the DFT level of theory with the TPSS functional and the 6-31G basis set. The initial geometry was taken form table 3.2.

Figure 4.3: The difference in the electron density between the full system and its isolated monomers, of the TPSS-EFM optimised water trimer at $|\mathbf{B}| = 0.1$ a.u. (left). The electron density at the $|\mathbf{B}| = 0$ a.u. equilibrium geometry (right).

Reassuringly, the interaction energy, taking into account the geometry relaxation effects, still decreases when the external field is introduced. For the cases presented here, shown in Figs. 4.1 and 4.2, the interaction energy decreases by 2.79 kcal mol^{-1}. The magnitude of this change is a factor of ~ 2 larger for the fixed trimer geometry presented in chapter 3, in the same field. This demonstrates the importance of geometry relaxation effects when a strong external field is applied. For this case the change in interaction energy from $|\mathbf{B}| = 0$ a.u. to $|\mathbf{B}| = 0.1$ a.u. was -1.15 kcal mol^{-1}. An analysis of the electron density, see Fig. 4.3 of this optimised geometry reveals that the dominant interaction is still the hydrogen bonding, however, when comparing to a calculation of the electron density at zero field with this geometry shows the same build up of density within the centre of the trimer. This also coincides with the difference in the final geometries of the water trimer at zero field and at $|\mathbf{B}| = 0.1$ a.u., this difference is very minimal but does show a compression of the cyclic trimer.

$\|\mathbf{B}\|$ / a.u.	Interaction Energy / E_h	
	Initial Geometry	Optimised Geometry
0.00	-0.12181011	-0.34090596
0.01	-0.12189308	-0.33897596
0.10	-0.12977458	-0.34435781

Table 4.3: The interaction energy for a $(H_2O)_{21}$ cluster with and without the response of the structural geometry within the external field.

4.2.2 Application to Larger Clusters

To this point it has been demonstrated that the EFM approach to geometry optimisation works with a comparative example for a water trimer, however, the aim of this work is to apply this to increasingly large clusters. Therefore, as a proof of concept the EFM based HF/6-31G geometry optimisation of a $(H_2O)_{21}$ cluster, taken from the same MD snapshot that generated the $(H_2O)_{103}$ cluster in chapter 3, is considered at three different field strengths, $|\mathbf{B}| = 0$ a.u., $|\mathbf{B}| = 0.01$ a.u. and $|\mathbf{B}| = 0.1$ a.u. The optimisations are shown in Figs. 4.4, 4.5 and 4.6 respectively. It is clear from each that, as expected, the optimisation compresses the overall geometry since the initial geomtetry is taken from a snapshot of a molecular dynamics (MD) simulation, following the steps outlined in chapter 3, the MD simulation includes a periodic cell with > 21 water molecules. Once again how the interaction energy varies when the geometry relaxation of the water cluster is considered, these values are shown in table 4.3. These results show how from $|\mathbf{B}| = 0.0$ a.u. to $|\mathbf{B}| = 0.1$ a.u., the expected decrease in the interaction energy is observed. However, for the much smaller change in field strength between $|\mathbf{B}| = 0.0$ a.u. to $|\mathbf{B}| = 0.01$ a.u., an increase in the interaction energy is observed corresponding to a decrease in the intermolecular interaction strength. This contradicts what was observed in the results from chapter 3 leading to the conclusion that geometry relaxation within the external field must be very significant in accurately describing the response to the change in field strength. However, the analysis in section 3.4 considers a much larger cluster in an attempt to approximate a bulk system. In addition, when considering these types of systems, they will exhibit potential energy surfaces with many local minima. This would imply that the use of conformer searching potentially using molecular dynamics is essential to locate the true equilibrium structures for an accurate discussion. This further highlights one of the potential uses of these types of EFM approaches, creating a very accessible option for combined quantum mechanical and molecular dynamics studies. Recent advances have introduced magnetic fields to molecular dynamics simulations,[221–224] therefore, opening the possibility of using these to generate conformers which can then be more accurately studied using EFM. Applying this approach to clusters of the size considered in section 3.4, to improve upon its analysis, is ongoing work.

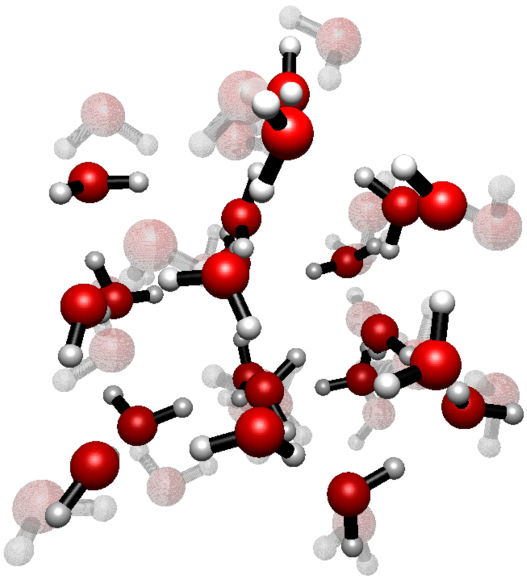

Figure 4.4: The initial (greyed out) and final geometries for the HF/6-31G optimisation of a $(H_2O)_{21}$ cluster at $|\mathbf{B}| = 0.00$ a.u. using the EFM.

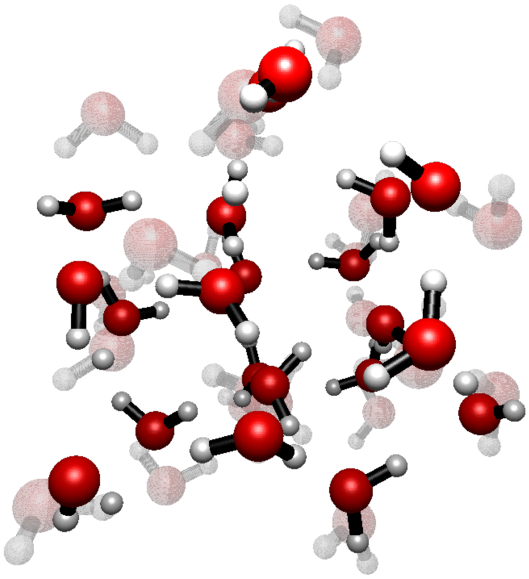

Figure 4.5: The initial (greyed out) and final geometries for the HF/6-31G optimisation of a $(H_2O)_{21}$ cluster at $|\mathbf{B}| = 0.01$ a.u. using the EFM.

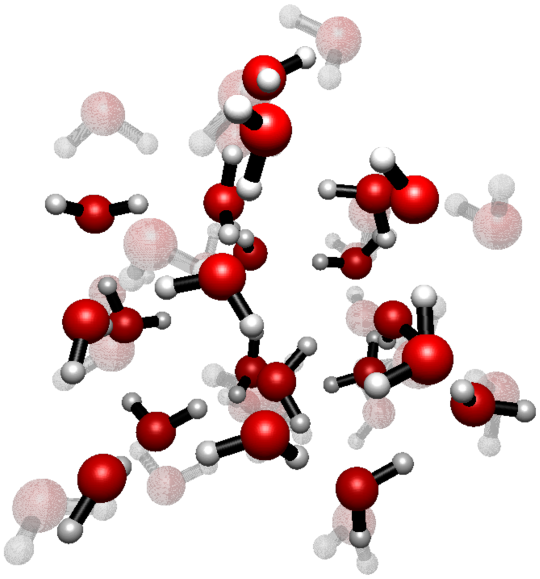

Figure 4.6: The initial (greyed out) and final geometries for the HF/6-31G optimisation of a $(H_2O)_{21}$ cluster at $|\mathbf{B}| = 0.10$ a.u. using the EFM.

5 Analysing Magnetically Induced Currents in Molecular Systems

The analysis of magnetically-induced current susceptibilities is a well-established approach that can provide a wealth of chemical information for understanding molecular magnetic properties and interactions[225–232]. Such current susceptibilities have been determined via a range of gauge-origin independent electronic-structure approaches. In the present work, LAOs have been utilised, as done by Jusélius, Gauss and Sundholm[233;234] to determine magnetically induced current susceptibilities in molecular systems. The physical current is routinely calculated in the application of non-perturbative current-density-functional approaches[15;19;235] for molecules in magnetic fields. The magnetically induced currents can then be easily computed by finite differences from the physical current, evaluated for a small perturbative magnetic field applied along one Cartesian axis. The use of such a non-perturbative approach also allows for the determination of current densities directly as a function of magnetic field strength.

5.1 The Magnetically Induced Current and Current Susceptibility

Existing implementations are available for determining the magnetically induced current susceptibilities, however, they typically require the calculation of magnetic response properties. This is widely accessible for traditional DFT, whereas, very few implementations of linear response calculations within a CDFT frameworks exist. The need for linear response calculations can be avoided however, since we can access these quantities as a direct byproduct of our nonperturbative calculations.

Within QUEST we can determine the LAO one-particle density matrix at both the HF and, more importantly, the CDFT levels in the presence of a static, arbitrary strength, uniform magnetic field. The charge density at a given grid point can then be calculated as,

$$\rho(\mathbf{r}) = \sum_{\sigma} \sum_{ab} D^{\sigma}_{ab} \omega_a(\mathbf{r}) \omega^*_b(\mathbf{r}), \tag{5.1}$$

and the paramagnetic current density as,

$$\mathbf{j}_{\mathrm{p}}(\mathbf{r}) = -\frac{i}{2} \sum_{\sigma} \sum_{ab} D^{\sigma}_{ab} \left[(\nabla \omega_a(\mathbf{r})) \omega^*_b(\mathbf{r}) - \omega_a(\mathbf{r}) (\nabla \omega_b(\mathbf{r}))^* \right]. \tag{5.2}$$

The physical current density is then constructed as,

$$\mathbf{j} = \mathbf{j}_d + \mathbf{j}_p = \rho \mathbf{A} + \mathbf{j}_p. \tag{5.3}$$

The induced-current susceptibility can be evaluated from three SCF calculations, in which

the external magnetic field is aligned along each of the three orthogonal Cartesian axes, respectively. With a weak field along each Cartersian direction τ, the partial derivative

$$J_{\nu}^{B_{\tau}}(r) = \frac{\partial j_{\nu}(\mathbf{r})}{\partial B_{\tau}} \tag{5.4}$$

can be evaluated numerically, yielding the current density susceptibility tensor.

Once the induced-current susceptibility tensor is determined, it is possible to determine the NMR shielding tensor for a nucleus, K with associated magnetic moment $\mathbf{M}_K$. To lowest order, the energy of a nuclear magnetic moment $\mathbf{M}_k$ with vector potential $\mathbf{A}_K(\mathbf{r}) = \frac{\mu_0}{4\pi}\frac{\mathbf{M}_K \times \mathbf{r}_K}{r_K^3}$ in an electronic system with current density $\mathbf{j}(\mathbf{r})$ is given by $\int \mathbf{A}_K(\mathbf{r}) \cdot \mathbf{j}(\mathbf{r}) \mathrm{d}\mathbf{r}$, yielding the following expression for the shielding constant:[236]

$$\sigma_{K;\alpha,\beta} = \int \frac{\mathrm{d}\mathbf{A}_K(\mathbf{r})}{\mathrm{d}M_{K,\beta}} \cdot \frac{\mathrm{d}\mathbf{j}(\mathbf{r})}{\mathrm{d}B_{\alpha}} \mathrm{d}\mathbf{r}. \tag{5.5}$$

5.1.1 Functional Dependence

The Biot-Savart Law in Eq (5.5) provides a direct way to assess the quality of magnetically induced currents in the vicinity of nuclei. Furness *et. al*[19] demonstrated how the cTPSS functional gives modest improvements over GGA level functionals such as the Perdew-Burke-Ernzerhof (PBE) functional when evaluating NMR shielding constants. Here, the use of hybrid (cTPSSh) and range-separated hybrid (cTPSSrsh) forms of the cTPSS functional are considered. The cTPSSh functional was constructed from 10% orbital-dependent exchange and 90% of the cTPSS exchange functional. The construction of cTPSSrsh follows that of Goll *et. al*[237]. Comparison between these functionals and a conventional linear response approach at the CCSD(T) level for the calculation of isotropic NMR shielding constants of a benchmark set of 27 small molecules has been investigated in the current work. In line with previous results, cTPSS offers modest improvements over GGA level approximations, with mean absolute error of 25.3 ppm. Moreover, cTPSSh and cTPSSrsh offer only small improvements with mean absolute errors of 24.6 and 25.3 ppm respectively. The following sections deal with current densities associated with chemical bonds. At the midpoint of a bond, the current density is sensitive to the delocalization of electronic charge, resulting in potentially less accurate current densities when using GGA-type functionals due to their associated delocalization errors[238]. To some extent this can be corrected for by using hybrid functionals, therefore, due to this observation, and the only limited additional improvement of cTPSSrsh, the cTPSSh functional will be used for the remainder of this chapter.

5.2 Quadrature Schemes for Analysis of Magnetically Induced Currents

The physical current density is a rich source of chemical information; its topology reflects the chemical structure of the molecule and the interaction of the electronic structure with an externally applied magnetic field. Magnetically induced current suscepti-

bilities have long been used in ring-current models to provide insight into nuclear-magnetic-resonance (NMR) chemical shifts[226;239–241] and as a criterion for assessing the aromaticity of molecules[242]. They give insight into electron delocalisation[243–246] and their analysis has also been applied to probe hydrogen bond strengths[245;247;248]. Nonetheless, the physical induced current **j** is a complicated vectorial quantity associated with a particular orientation of the applied magnetic field **B** with respect to the molecular frame. The induced current density susceptibility $J_\nu^{B_\tau}$ is a tensorial quantity, reflecting the vectorial nature of both the applied magnetic field and the induced physical current density. As such, the analysis of these quantities is less straightforward than that for simple scalar quantities.

In general, there are two main approaches that may be used for the analysis of currents induced in molecular systems by external magnetic fields. The first of these are integration techniques which, by constructing numerical quadratures over two-dimensional planes, allow the current density to be probed in specific parts of a molecule.[233;234]. Secondly, topological techniques employing concepts from vector-field analysis such as separatrices and stagnation graphs are used to analyse the induced current fields[232;249–251]. Both approaches can provide quantitative information on the nature of the electron delocalisation in chemical species and their interactions with external fields.

In this work, QUEST[35] was extended to include functionality to provide flexible quadratures to allow for integration of the current passing user-defined planes, giving measures of ring and bond currents in molecular systems. Fig. 5.1 demonstrates this for the napthalene molecule. On the left, the current is plotted for a plane 1 bohr above the molecular plane. This was determined by applying a weak field of 0.001 a.u. in the direction normal to the molecular plane. There is a strong global ring current following the C–C bonds, which can be measured by means of an integration plane. The right-hand panel of Fig. 5.1 demonstrates this, where the position of the plane is indicated by the red line. It bisects 3 C–C bonds and extends 10 bohr above and below the molecular plane. Integration over the whole plane gives zero current by symmetry, as seen from the bond-current profile, constructed by slicing this plane into 1000 segments and then integrating the current passing each segment. The resulting profile is symmetric and describes the main features of the magnetically induced current: the outer large peaks correspond to the global perimeter current, while the smaller central features correspond to current vortices localised on each ring.

For this small, highly symmetric molecule, one could analyse the strength of the magnetically induced current further by integrating over smaller planes that localise values to rings or bonds. An obvious approach would be to construct planes with their origin in one of the ring centres, bisecting a chosen bond and extending away from the molecule until the magnitude of the current is negligible. For the central C12–C13 bond (see Fig. 5.2 for numbering), the plane can be chosen to extend from one ring centre to the other; integration of the current passing through this plane gives zero by symmetry. Integration over a plane bisecting the C9–C10 bond gives an integrated current strength of 13.1 nA/T at the cTPSSh/6-31G* level. This relatively strong diatropic current is consistent with the magnetic criterion for aromaticity and the cTPSSh current profile is similar to those in

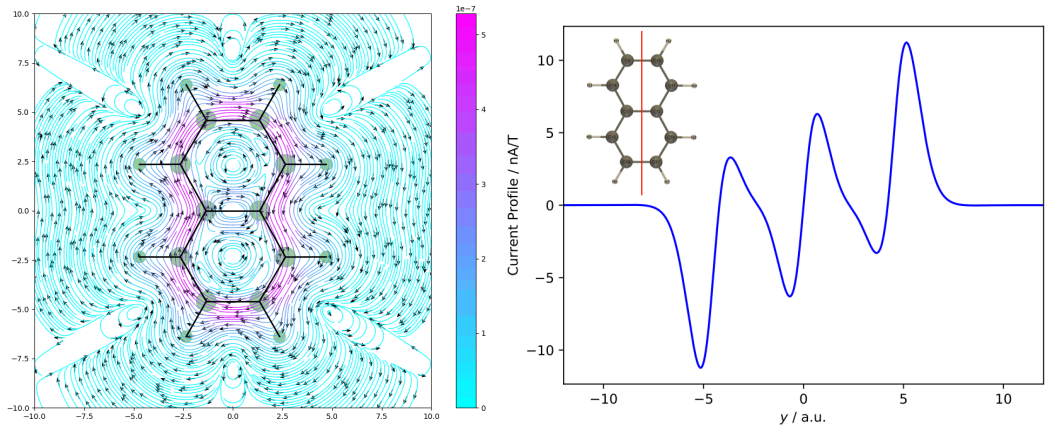

Figure 5.1: The magnetically induced current **j** (a.u.) in a field of 0.001 a.u. perpendicular to the molecular plane (left). The current profile (nA/T), calculated for a plane extending 10 bohr above and below the molecular frame along the red line shown in the inset, where $y = 0$ is positioned in the centre of the C12-C13 bond (right).

previous studies[226].

Whilst the naphthalene molecule is a simple planar system, it highlights two common issues encountered when attempting to analyse molecular currents by setting up local quadratures. Firstly, the integrated current susceptibility calculated is dependent on the area of the integration plane—in this case, a large plane is used to capture the whole ring current value. Secondly, it may not always be possible to use such large integration planes without intersecting another bond vector—for example, the plane used for the C9–C10 bond from ring centre to ring centre will have a different spatial extent to that starting at a ring centre, bisecting the C12–C13 bond and continuing to a distance far from the molecule. This issue is commonly encountered for more complex structures, particularly if they are non-planar.

5.2.1 Disc-based Quadrature Schemes

For the 2D square planar integration discussed so far, Gauss–Legendre quadrature is used, similar to that employed by the GIMIC program[233;234]. Here we set up bond-centred disc quadratures using the Elhay–Kautsky method[252;253], where the integral of a function F in the xy plane is calculated as

$$I(F) \approx \pi r_c^2 \sum_{j=1}^{n_\theta} \sum_{i=1}^{n_r} w_i F(x_i, y_i) \tag{5.6}$$

where r_c is the radius of the disc, n_θ is the number of angular nodes, n_r is the number of radial nodes and w_i are the quadrature weights. It is recommended to use $n_\theta = 2n_r$ for a balanced integration of angular and radial coordinates. QUEST provides structural analysis techniques to determine the bonded atom pairs, for which the average of the covalent radii is used as r_c. The quadrature is then constructed for each bond initially in the xy plane, before being translated to the bond centre and rotated so that the normal to the centre of the disc lays along the bond vector. In this manner, small 2D disc quadratures can be

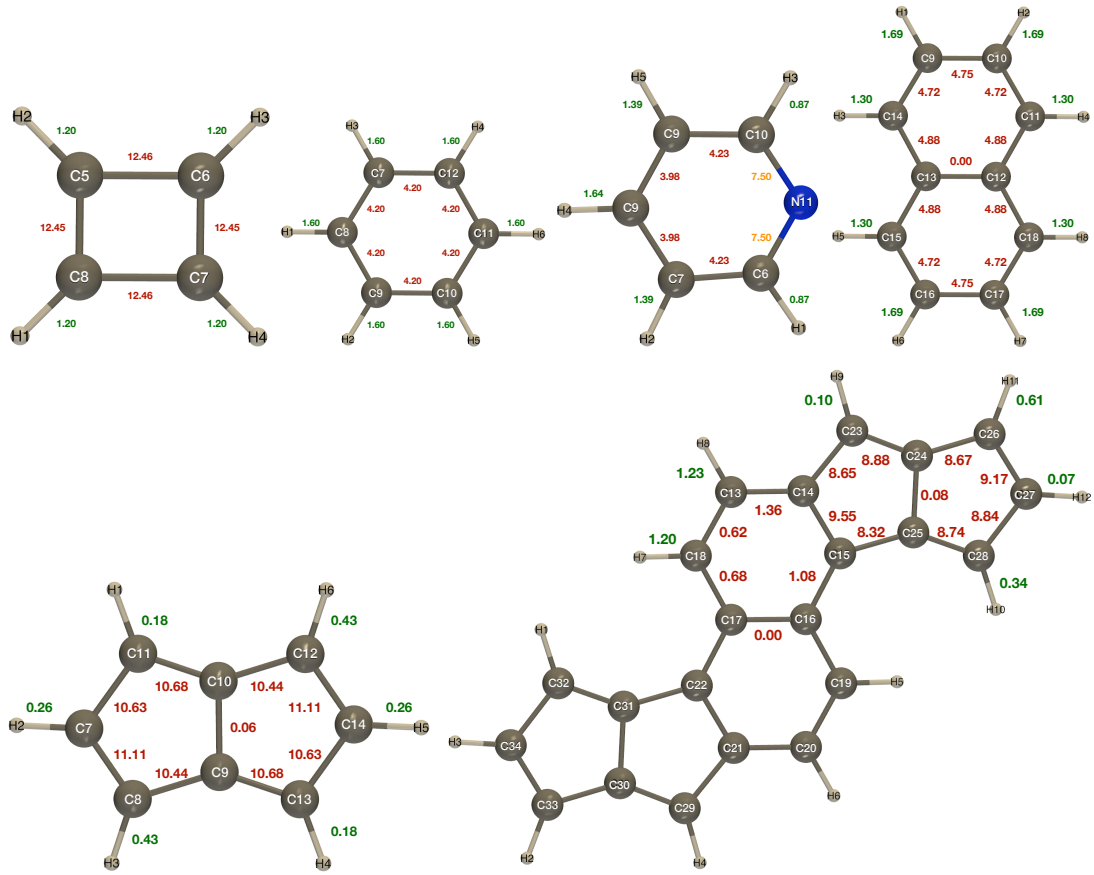

Figure 5.2: Bond currents assigned by use of the disc-based quadrature (nA/T) for cyclobutadiene, benzene, pyridine, naphthalene, pentalene and bispentalene annelated naphthalene. C-H currents are shown in green, C-C currents in red and C-N currents in orange. All values calculated at the cTPSSh/6-31G* level.

rapidly constructed for each bond in the molecule. The result of this procedure is illustrated for the benzene molecule in Fig. 5.3. Here a small quadrature with $n_\theta = 10$ and $n_\mathrm{r} = 5$ is shown for illustration purposes. From the top view, the different radial extent of the C–C and C–H quadratures is clear: from the oblique view, the radial and angular structures of the disc quadratures are visible. In practice, the values of n_θ and n_r are user inputs. In this work, $n_\theta = 100$ and $n_\mathrm{r} = 50$ quadratures were used for all bonds, as preliminary tests indicate that the current integrals evaluated with these quadratures are already tightly converged.

To test the utility of this quadrature to distill complex current-density vector fields into bond current susceptibilities, we have applied it to a range of previously studied planar ring structures. The results are shown in Fig. 5.2 and Table 5.1, where we report the integrated current norm. All molecules were optimized at the PBE0/6-31G* level[254;255] using density fitting[256;257] with the def2-QZVPP auxiliary basis and the auxiliary density matric methods (ADMMs) approximation[258;259], with 3-21G as the ADMM auxiliary basis using the LSDALTON program[260;261]. Clearly, the bond current susceptibilities give a good qualitative representation of the current density vector field. For example, the naphthalene bond current susceptibilities reflect the perimeter current in Fig. 5.1. The bond current susceptibilities in cyclobutadiene, benzene and pentalene reflect their highly symmetric

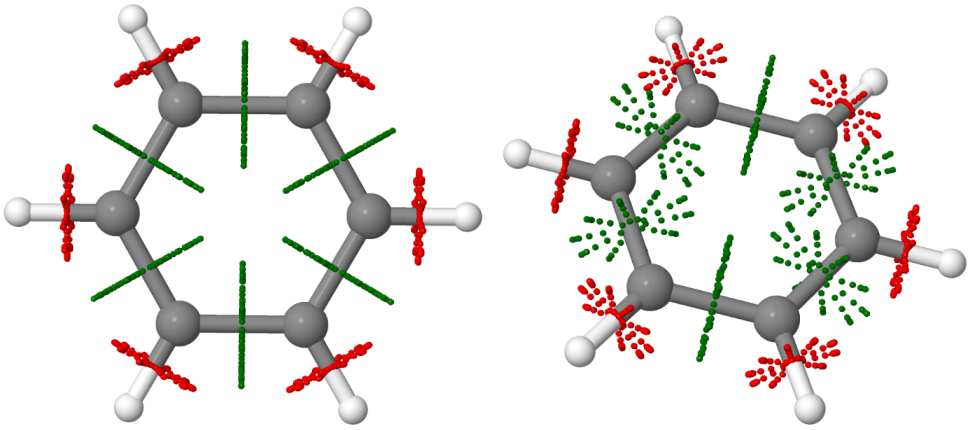

Figure 5.3: The disc-based quadrature applied to the benzene molecule, top view (left) and oblique view (right). In this case a modest quadrature with $n_\theta = 10$ and $n_r = 5$ is plotted to show the radial structure. The different spatial extents of the C-C (green) and C-H (red) quadratures are determined by the average of the covalent radii of the two atoms involved in each bond.

structures. Those in pyridine are most intense around the C–N bonds, as expected. By inspection of the current density plots in tandem with the bond current susceptibilities, it is clear that those for cyclobutadiene and pentalene are consistent with the anti-aromatic nature of these molecules, whilst those for benzene, naphthalene and pyridine are consistent with their aromatic nature. Numerically, the disc-quadrature-based bond current susceptibilities are smaller than those reported for the planar quadratures. In Ref. 234, for example, the benzene current is reported as 11.8 nA/T at the B3LYP/def2-TZVP level, compared with 4.2 nA/T in the present calculations. This difference is because the planar quadratures used in Ref. 234 are designed to capture the entire ring current, whilst the smaller quadratures used here capture only the environment local to the bond centre.

A more challenging case is bispentalene annelated naphthalene (BPAN), previously studied using GIMIC by Sunholm, Berger and Fliegl[262]. Cao *et al.*[239] synthesised and characterised organic compounds with two pentalene units annelated with a naphthalene moiety in 2015. As the molecule has 22π electrons, Hückel's rule would predict the molecule to be aromatic. However, an upfield shift of pentalene hydrogen atoms was measured using NMR spectroscopy indicating anti-aromaticity. The disc quadrature used in the present work leads to conclusions similar to those obtained via the GIMIC analysis in Ref. 262—namely, that the pentalene moieties remain strongly anti-aromatic, whilst the central naphthalene moiety is weakly aromatic. These observations have been used to rationalise the experimental observations of Cao *et al.*[239]. Here they further establish the validity of our simplified quadrature.

Furthermore, since all bond types are treated with the same averaged covalent radii, the intensity of the currents may be consistently compared between systems. In Table 5.1, for example, we see that the C–C bond currents in the anti-aromatic systems are generally more intense that those in the aromatic systems.

Table 5.1: Bond currents for the planar ring systems cyclobutadiene, benzene, pyridine, naphthalene, pentalene and bispentalene annelated naphthalene (nA/T). The atomic numbering is shown in Fig. 5.2.

Molecule	Bond	Bond Length	Atom Nos.	HF	LDA	PBE	PBE0	cTPSS	cTPSSh	cTPSSrsh
Cyclobutadiene	C-H	2.047	5-2, 6-3, 7-4, 8-1	0.93	1.21	1.29	1.17	1.25	1.20	0.84
	C-C	2.967	6-5, 8-7	12.69	13.15	12.65	12.73	12.41	12.46	12.85
	C-C	2.520	7-6, 8-5	12.80	13.13	12.61	12.72	12.39	12.45	12.84
Benzene	C-H	2.053	7-3,8-1, 9-2, 10-5, 11-6,12-4	1.82	1.66	1.52	1.68	1.54	1.60	1.85
	C-C	2.631	8-7, 9-8, 10-9, 11-10, 12-7, 12-11	4.40	4.13	4.08	4.17	4.17	4.20	4.26
Pyridine	C-H	2.057	6-1, 10-3	1.06	0.92	0.82	0.92	0.83	0.87	1.08
	C-H	2.051	7-2, 9-5	1.62	1.41	1.29	1.46	1.33	1.39	1.64
	C-C	2.631	7-6, 10-9	4.40	4.18	4.12	4.22	4.20	4.23	4.31
	C-H	2.053	8-4,	1.87	1.70	1.55	1.72	1.58	1.64	1.90
	C-C	2.628	8-7,9-8	4.13	3.90	3.87	3.95	3.96	3.98	4.02
	C-N	2.521	11-6,11-10	7.62	7.38	7.39	7.45	7.48	7.50	7.43
Pentalene	C-H	2.047	7-2, 14-5	0.32	0.23	0.34	0.16	0.33	0.26	0.30
	C-H	2.046	8-3, 12-6	0.94	0.48	0.35	0.56	0.35	0.43	0.96
	C-C	2.558	8-7, 14-12	8.10	12.14	11.64	10.85	11.38	11.11	9.15
	C-C	2.774	9-8, 12-10	7.44	11.41	10.97	10.15	10.72	10.44	8.43
	C-C	2.746	10-9,	0.04	0.06	0.06	0.06	0.06	0.06	0.05
	C-H	2.050	11-1, 13-4	0.67	0.20	0.13	0.28	0.13	0.18	0.66
	C-C	2.814	11-7, 14-13	7.64	11.62	11.15	10.35	10.90	10.63	8.73
	C-C	2.558	11-10, 13-9	7.57	11.73	11.26	10.38	10.98	10.68	8.60
Naphthalene	C-H	2.052	9-1, 10-2, 16-6, 17-7	1.89	1.77	1.62	1.77	1.64	1.69	1.92
	C-C	2.595	11-10, 14-9, 16-5, 18-17	4.85	4.67	4.62	4.69	4.70	4.72	4.70
	C-H	2.055	11-4, 14-3, 15-5, 18-8	1.53	1.30	1.20	1.36	1.24	1.30	1.51
	C-C	2.669	10-9, 17-16	4.86	4.70	4.65	4.72	4.73	4.75	4.72
	C-C	2.676	12-11, 14-13, 15-13, 18-12	4.96	4.83	4.76	4.84	4.86	4.88	4.85
	C-C	2.697	13-12,	0.00	0.00	0.00	0.00	0.00	0.00	0.00
BPAN	C-H	2.053	13-8, 20-6	1.62	1.28	1.14	1.35	1.15	1.23	1.64
	C-C	2.649	14-13, 21-20	2.85	1.28	1.22	1.60	1.21	1.36	2.58
	C-C	2.649	15-14, 22-21	9.92	9.38	9.20	9.81	9.27	9.55	10.01
	C-C	2.659	16-15, 22-17	2.91	0.62	0.66	1.39	0.78	1.08	2.59
	C-C	2.736	17-16	0.00	0.00	0.00	0.00	0.00	0.00	0.00
	C-H	2.049	18-7, 19-5	1.58	1.25	1.12	1.32	1.12	1.20	1.60
	C-C	2.605	18-13, 20-19	2.54	0.12	0.18	0.96	0.30	0.62	2.19
	C-C	2.676	18-17, 19-16	2.59	0.18	0.26	0.99	0.38	0.68	2.23
	C-H	2.051	23-9, 29-4	0.53	0.13	0.05	0.20	0.05	0.10	0.55
	C-C	2.788	23-14, 29-21	6.98	9.05	8.80	8.54	8.73	8.65	7.52
	C-C	2.772	25-15, 31-22	6.64	8.71	8.48	8.20	8.40	8.32	7.11
	C-C	2.760	25-24, 31-30	0.39	0.12	0.10	0.13	0.08	0.08	0.25
	C-H	2.045	26-11, 32-2	1.02	0.70	0.56	0.73	0.54	0.61	1.07
	C-C	2.757	26-24, 33-30	6.55	9.17	8.92	8.47	8.83	8.67	7.19
	C-H	2.047	27-12, 34-3	0.41	0.06	0.11	0.08	0.12	0.07	0.43
	C-C	2.564	27-26, 34-33	7.12	9.68	9.38	9.00	9.30	9.17	7.78
	C-H	2.048	28-10, 32-1	0.76	0.42	0.28	0.45	0.27	0.34	0.81
	C-C	2.562	28-25, 32-31	6.63	9.27	8.99	8.55	8.89	8.74	7.30
	C-C	2.797	28-27, 34-32	6.77	9.35	9.06	8.65	8.98	8.84	7.48
	C-C	2.558	24-23, 30-29	7.12	9.35	9.08	8.75	8.99	8.88	7.59

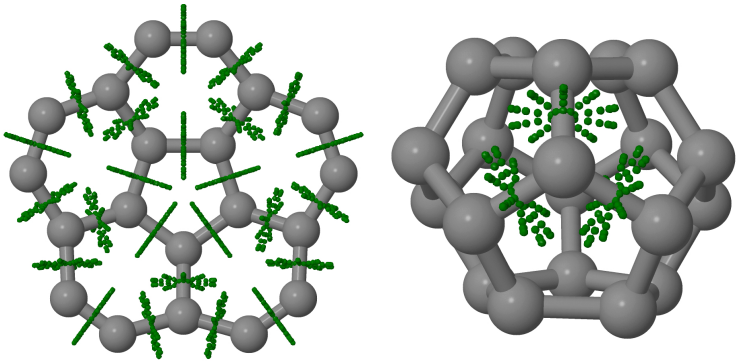

Figure 5.4: Disc quadratures for the bowl (left) and cage (right) isomers of C_{20}. The use of covalent radii to setup the bond centred quadratures avoids the discs intersecting, allowing their use for 3D structures. For clarity, simple quadratures with $n_\theta = 10$ and $n_r = 5$ are shown. For the cage isomer only the 3 closest discs are shown to avoid occlusion.

5.2.2 3D Structures

A potential advantage of the disc-based quadrature is its utility for compact 3D structures. To explore this, the ring, bowl and cage isomers of C_{20} are considered. The geometries were optimised at the PBE0/6-31G* level using density fitting in the df-def2 auxiliary basis and the ADMMS approximation in the 3-21G ADMM auxiliary basis, yeilding structures close to D_{10h}, C_{5v} and D_{3d} symmetries respectively. The stability of these isomers has been studied extensively[263–265], using a range of quantum-chemical methods, including accurate coupled-cluster methods[265].

Fig. 5.4 shows the disc-based quadratures for the bowl and cage isomers, as prototypical 3D cases. The bowl exhibits relatively weak curvature and the quadrature discs remain well separated. In the right panel of Fig. 5.4, only the three nearest disc quadratures are shown for clarity. Reassuringly, none of the disc quadratures intersect in this relatively compact structure, comfirming the applicability of this quadrature to general systems.

The bond current susceptibilities for each isomer are shown in Fig. 5.5. For the ring isomer alternating values are obtained, consistent with alternating bond lengths. The intensities of 33.59 and 31.31 nA/T are characteristic of strong anti-aromaticity. For the bowl isomer, the central pentagon exhibits bond current susceptibilities of 7.03 nA/T, with weaker values of 2.68 nA/T for the spokes bonds between inner ring and the perimeter, and alternating perimeter values of 2.18 and 4.59 nA/T at the cTPSSh/6-31G* level. The cage structure has a wider range of bond lengths and bond current susceptibilities; see Table 5.2 for details. Generally, the bond current susceptibilities are similar between the PBE, PBE0, cTPSS and cTPSSh functionals, with cTPSSrsh more closely resembling HF values and LDA giving somewhat different currents.

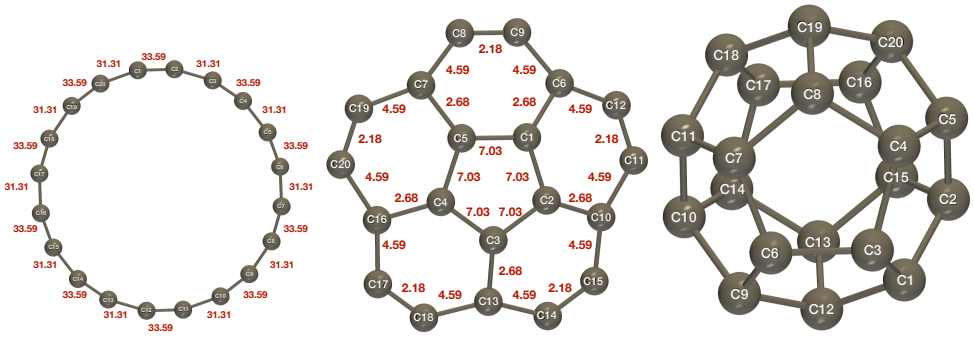

Figure 5.5: Bond currents, assigned using the disc-based quadrature for the ring (left) and bowl (centre) isomers of C_{20}. The atomic numbering is shown for the cage isomer and the bond current values are shown in Table 5.2

Table 5.2: Bond currents for the bowl, cage and ring isomers of C_{20}. The atomic numbering is shown in Fig. 5.5.

Molecule	Bond	Bond Length	Atom Nos.	HF	LDA	PBE	PBE0	cTPSS	cTPSSh	cTPSSrsh
C_{20} Ring	C-C	2.333	2-1,4-3,6-5,8-7,10-9,12-11,14-13,16-15,18-17,20-19	34.29	41.83	40.13	26.97	38.90	33.59	33.60
	C-C	2.541	3-2,5-4,7-6,9-8,11-10,13-12,15-14,17-16,19-18,20-0	31.97	38.84	37.34	25.06	36.29	31.31	31.24
C_{20} Bowl	C-C	2.688	2-1, 3-2, 4-3, 5-1, 5-4	7.36	6.94	6.87	7.13	6.92	7.03	7.17
	C-C	2.692	6-1,7-5, 10-2, 13-3, 16-4	2.08	2.48	2.63	2.51	2.75	2.68	2.20
	C-C	2.672	8-7, 9-6, 11-10, 12-6, 14-13, 15-10, 17-16, 18-13, 19-7, 20-16	4.66	4.49	4.51	4.51	4.61	4.59	4.46
	C-C	2.358	9-8, 12-11, 15-14, 18-17, 20-19	1.56	2.12	2.12	1.96	2.27	2.18	1.72
C_{20} Cage	C-C	2.725	2-1, 18-11	2.38	2.24	2.31	2.18	2.30	2.23	2.20
	C-C	2.653	3-1, 18-17	4.46	5.08	5.00	4.81	4.99	4.91	4.53
	C-C	2.870	4-3, 17-14	2.93	3.92	3.96	3.62	3.99	3.84	3.00
	C-C	2.719	5-2, 11-10	2.05	2.15	2.23	2.02	2.21	2.11	1.94
	C-C	2.654	5-4, 15-10	4.68	5.16	5.07	4.91	5.07	5.00	4.67
	C-C	2.709	6-3,	1.49	2.00	1.93	1.83	1.89	1.86	1.77
	C-C	2.716	7-6,16-15	1.50	0.67	0.64	0.83	0.67	0.74	1.20
	C-C	2.705	8-4,14-13	1.73	2.09	2.01	1.95	1.97	1.95	1.92
	C-C	2.716	8-7,15-13	1.42	0.49	0.46	0.67	0.49	0.56	1.11
	C-C	2.750	9-6,20-16	3.34	2.12	2.08	2.44	2.08	2.24	2.98
	C-C	2.833	10-9, 20-5	5.08	6.95	7.00	6.38	7.00	6.73	5.37
	C-C	2.715	11-7, 15-2	3.66	2.16	2.15	2.64	2.19	2.39	3.17
	C-C	2.827	12-1, 19-18	4.87	6.79	6.85	6.22	6.85	6.58	5.22
	C-C	2.639	12-9, 20-19	5.19	7.78	7.74	7.02	7.65	7.36	5.82
	C-C	2.752	13-12, 19-8	3.57	2.32	2.29	2.65	2.29	2.44	3.18

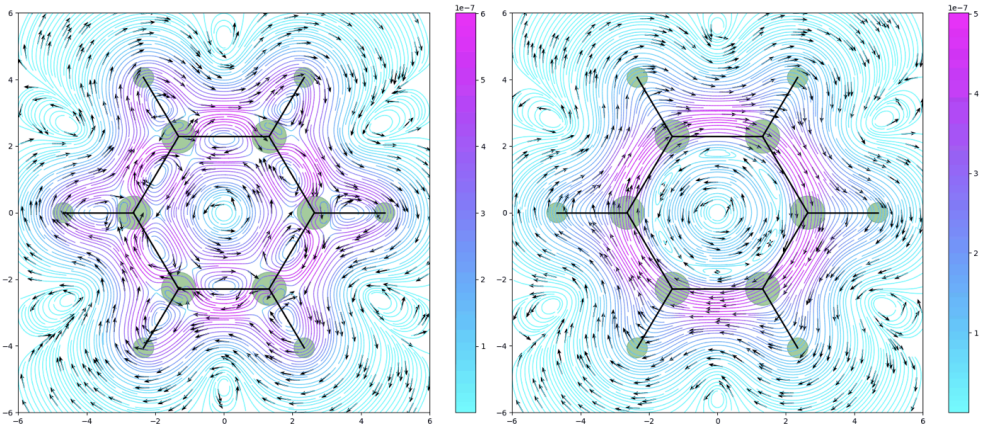

Figure 5.6: Magnetically induced currents (a.u.) for the benzene molecule in its ground state, for a field of 0.001 a.u. perpendicular to the molecular plane. The current is plotted in the molecular plane (left) and 1 bohr above the molecular plane (right).

5.3 Magnetically Induced Current Susceptibilities and Excited States

The disc-based and planar quadratures in QUEST provide a flexible suite of tools for the analysis of magnetically induced current densities in molecular systems. Additionally, the analysis of spin-resolved current densities is available within the QUEST implementation. This is particularly important if one wishes to examine the current densities of not only ground but also excited states. A prototypical example is the benzene molecule. In the ground state, the α and β spin currents are the same; these are plotted in Fig. 5.6. In the left panel, the in-plane currents show the current pathways in the σ framework, whilst the currents 1 bohr above the plane show the π currents.

Papadakis and Ottosson[266] have highlighted the 'Jekyl and Hyde' character of the benzene molecule, with its first triplet excited state exhibiting strong anti-aromaticity according to Baird's rule[267]. The spin-resolved magnetically induced currents are shown in Fig. 5.7 for a field of 0.001 a.u. perpendicular to the molecular plane. In such a field, the first excited state with two unpaired β electrons is lowest. The spin-resolved currents of this state can be directly accessed via an SCF calculation. The α current in the left-hand panel of Fig. 5.7 is slightly more compact relative to the ring centre than the β current in the right-hand panel. The intensity of the α current is also lower, reflecting the larger population of β spin electrons.

5.4 Magnetically Induced Currents in Strong Fields

An advantage of the non-perturbative approach to calculating magnetically induced currents is the ability to study systems explicitly as a function of field strength, beyond the perturbative regime. The BH molecule is a classic example of a closed-shell system exhibiting paramagnetism. This paramagnetism has been rationalised in terms of a simple two-state model in Ref. 13, which leads to a ground-state energy that first decreases in the

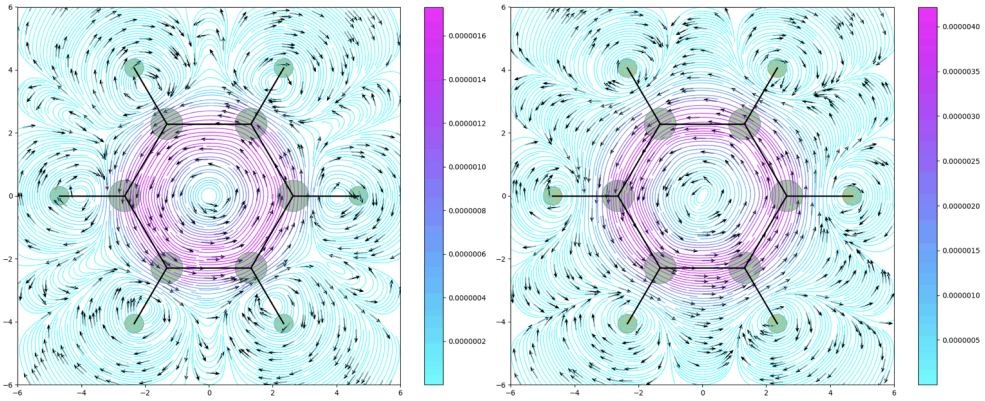

Figure 5.7: Magnetically induced currents (a.u.) for the benzene molecule in its first excited state, for a field of 0.001 a.u. perpendicular to the molecular plane. The α-spin current (left) and the β-spin current (right), plotted 1 bohr above the molecular plane.

presence of a magnetic field perpendicular to the bond axis, before rising diamagnetically. This behaviour is shown in the insets in Fig. 5.8. For reference, the behaviour of the ground state with the magnetic field oriented parallel to the bond axis is also shown, exhibiting a state crossing at approximately 0.25 a.u. Here we focus on a perpendicular field ranging from 0.0 to 1.0 a.u.

Fig. 5.8 presents the magnetically induced currents in fields of 0.05, 0.25, 0.45 and 0.80 a.u. perpendicular to the bond axis (corresponding to the ground-state orientation in a magnetic field). As expected, the currents at 0.05 a.u. are strongly reminiscent of the magnetic current susceptibilities presented for this molecule in Ref. 226. They feature a large paratropic vortex around the B atom (left) and a weaker diatropic vortex closer to the H atom (right). As the field strength increases, the paratropic vortex is attenuated at 0.25 a.u., close to the transition between paramagnetic and diamagnetic behaviour. The paratropic current becomes localised much more closely to the B atom and the magnitude of the paratropic and diatropic currents become essentially equal on the B and H atoms, respectively. At 0.50 a.u. the currents become weaker in magnitude, but the diatropic circulations now envelop the entire molecular volume and the energy of the system rises diamagnetically. This trend continues at higher fields as the energy of this state continues to rise.

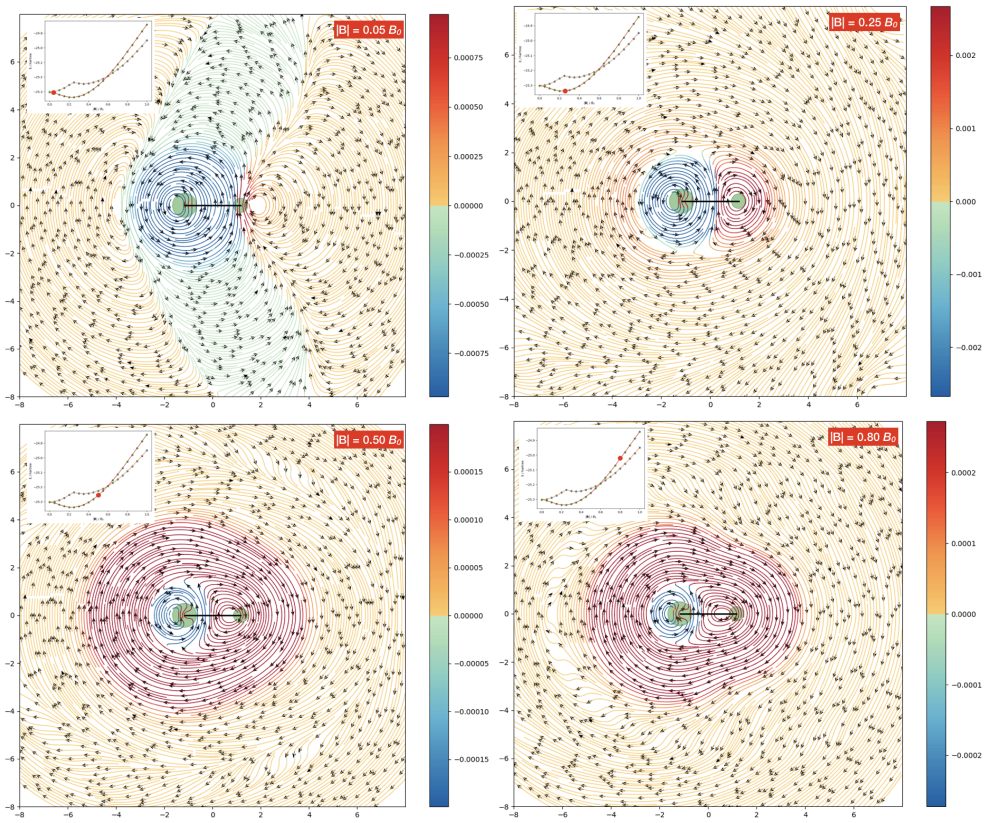

Figure 5.8: Magnetically induced currents (a.u.) for the BH molecule in strong magnetic fields calculated in the primitive aug-cc-pV5Z basis. The field is applied perpendicular to the bond axis with strengths of 0.05 (top left), 0.25 (top right), 0.50 (bottom left), 0.80 a.u. (bottom right). At fields significantly below 0.25 a.u. a paratropic vortex dominates around the B atom, as the field increases this vortex is attenuated and becomes spatially much more localised to the B atom. At very strong fields the current circulations become almost entirely diatropic as the energy rises diamagnetically.

6 Molecular Visualisation and Manipulation for EFM Applications

When studying molecular systems, a molecular editor and visualiser can be incredibly useful to quickly build and view complex 3D molecular systems. There are many different options when it comes to choosing a visualiser including popular options such as, IQMol, Avogadro, VMD etc. Each will have their own advantages over the rest, for example IQMol directly interfaces with the QChem software package and therefore, is the go to visualiser for QChem users. Whilst developing the various methods detailed within this thesis it became apparent that no single molecular visualiser contained all the features one might require when studying molecular systems with fragmentation methods, or systems exposed to external fields. Due to the general difficulty when attempting to introduce new features into existing visualisers, I have endeavoured to create a new molecular editor/visualiser, QuestView, with the aim that it presents all features one would require when using the techniques previously discussed in this work, whilst also providing an easy route to introducing new features in the future.

6.1 Development of a Python Based Desktop Application

As QUEST is predominantly python based, due to its overall accessibility when developing new features, it was chosen as the base coding language for developing an accompanying molecular visualiser. Python offers several different approaches when creating a graphical user interface (GUI) based desktop application, however, the Qt framework offered a wide range of functions which would lend themselves to the accessible development of a cross-platform python based GUI application. Qt is written in C++ therefore, requires bindings when being used within other coding languages. The relevant python bindings are available via the PyQt5 package.

6.1.1 PyQt5

Qt is a development framework for the creation of GUI based applications with a wide array of functionality going beyond the simple user-interface design including, but not limited to, abstractions for threading, structured query language (SQL), extensible markup language (XML), multimedia frameworks and OpenGL graphics rendering. Typically, applications consist of a collection of windows with embedded objects, called widgets, controlling the interactive functionality. It employs a signal/slot mechanism for communication between objects which is a type-safe method for interaction between the many widgets within a given application. It is cross-platform, supported across desktop, web and mobile integrating directly with the windowing system on the target platform. In addition, there is support for a wide range of platform specific plugins that can be added into a code base to adapt for specific situations if required.

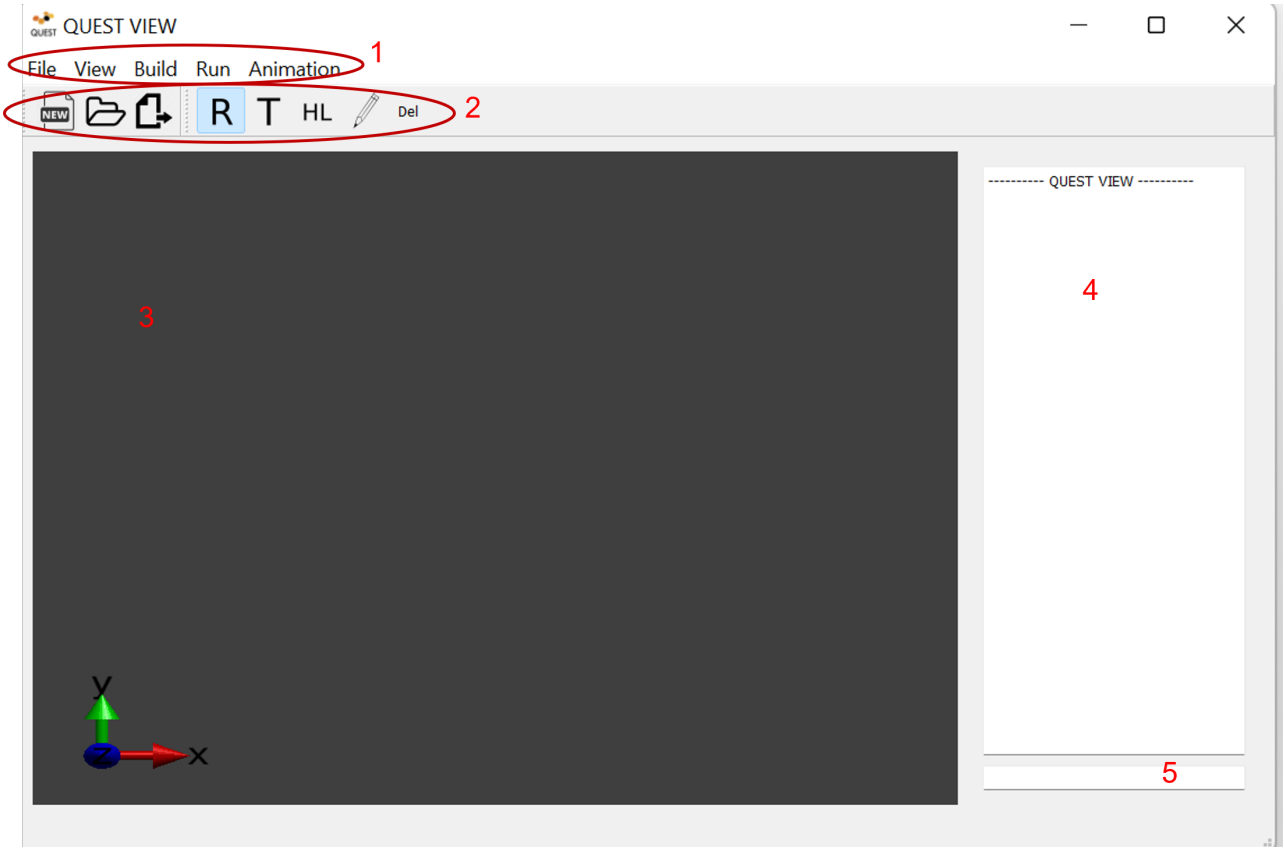

Figure 6.1: Main window for the QuestView application designed with PyQt5

Fig 6.1 shows the PyQt5 based main window for the QuestView application. It is designed as a QMainWindow object with several embedded widgets to add functionality. Some of the key features have been highlighted;

1. Main menus provided by the QMenuBar widget.
2. Quick access tools provided by the QToolBar widget, with icon images included via the QIcon method.
3. Main visualisation window for rendering 3D graphics, provided by the QOpenGLWidget widget.
4. A command console providing a text interface via a QTextBox widget.
5. A text box for inputting text commands, provided by a QLineEdit widget.

6.1.2 PyOpenGL

Once the main framework for a desktop application had been constructed, the next task was to develop the graphics processing engine for 3-dimensional visualisation of molecular data and properties. Due to the desire to ensure QuestView was entirely cross-platform, the OpenGL graphics application programming interface (API) was the obvious choice, when considering graphical rendering options, as it can be utilised across most major modern operating-systems (OS). Additionally, PyQt5 contains functionality specifically designed to work with the OpenGL API. OpenGL is developed by the Khronos Group, a non-profit

consortium who publish and maintain various interoperability standards, and is implemented directly via graphics processing unit (GPU) vendors. It can be used, within a python based application, via the python bindings in the PyOpenGL python package and with the built-in QOpenGLWidget from PyQt5.

The Qt5 OpenGL Widget

Alongside its other benefits, OpenGL was chosen as Qt5 contains a class specifically designed to display OpenGL graphics within a Qt application, the QOpenGLWidget class. When invoked it will create a viewport widget which can be placed anywhere within the application window, see Fig 6.1 for an example. QOpenGLWidget provides three main functions for controlling graphics rendering within the created viewport,

- `paintGL()` - Deals with the rendering of the OpenGL scene and is called any time the widget is updated.
- `resizeGL()` - Deals with creating the viewport and the 3D projections used when rendering. It is called whenever the widget is resized.
- `initializeGL()` - Deals with creating any OpenGL resources used throughout the program. This is called once when the widget is first created.

The main benefit of these functions within the OpenGLWidget class is the background tasks Qt performs when they are called, such as ensuring the viewports OpenGL framebuffer object is the currently bound context when calling `paintGL`. This can significantly ease the development process, particularly if dealing with multiple OpenGL contexts. In addition to these, Qt packages up many common OpenGL function calls within the functions of the QOpenGLWidget class for ease of use and to ensure correct cross-platform behaviour.

OpenGL Shaders

In general OpenGL controls how data is communicated between the main program, based on the CPU, and the graphics rendering which takes place on the GPU. However, it does not directly tell the GPU how to process the data it has been sent, for this we develop shaders. Shaders are programs, written in the OpenGL shading language (GLSL), which are compiled and run directly on the GPU and control how the data passed by the CPU is processed. There are two key types of shaders within any basic OpenGL based program, a vertex shader and a fragment shader.

Vertex shaders typically control where within the viewport an object will appear. In general OpenGL developers employ the $model \times view \times projection$ transformation model. An object's vertex data will have been loaded into a vertex buffer object (VBO) when passed to the GPU, however, this data is typically in *model space* or *local space*, where the object has been built around a fixed point in space, usually (0,0,0). This needs to undergo a series of transformations to enable OpenGL to correctly render the scene. First, it needs to be transformed into *world space*, relative to the coordinates of the scene being rendered. This transformation is carried out by a 4×4 matrix referred to as the *model* matrix. This matrix contains the necessary scaling, rotation and translation transformations required to move the

object into *world space*. Once in *world space*, the viewing direction needs to be taken into account. This is done via the *view* matrix, again rotating and translating the object such that the 'camera' is now positioned at the origin of the coordinate space, this is referred to as *view space*. Finally, the scene needs to be converted to *clip space* where all visible vertex positions within the scene are normalised to be between -1 and 1 in both the x and y directions, known as normalised device coordinates (NDC). This is also where any projection scaling is applied to create the illusion of 3 dimensionality when the scene is rendered on the 2-dimensional viewport. This transformation is carried out by the *projection* matrix. Once in *clip space* the scene can now be sent to OpenGL's viewport transformation function to be converted into *screen space* which maps all data to physical pixels within the viewport. The user must define the relevant matrices which are then passed as uniform variables to the vertex shader to enable the processing of the vertex data.

Once the position of the object's vertices has been determined, their properties must now be dealt with. The simplest example of a vertex's property is its colour, which can be combined with the vertex data in the VBO when sent to the GPU. How these properties are dealt with is controlled by the fragment shader. A simple fragment shader will just assign the colour value to each given pixel and pass this onto OpenGL's rendering function. However, it is possible to apply more complex concepts such as lighting and textures within, the fragment shader.

3D Matrix Transformations

Throughout the development of 3D graphics rendering, it is vital to understand how a fixed point, or vertex, can be manipulated within the given coordinate system. There are three main types of manipulation one can use on a given vertex; scaling, rotation and translation. The simplest of these is scaling. Each given point in 3D space has 3 coordinates, $\mathbf{v} = (x, y, z)$, therefore it can be written as a vector of length 3. To apply scaling to a given point a 3×3 diagonal matrix can be defined with scaling for each of the three coordinates located along its 3 diagonal elements.

$$\mathbf{S} = \begin{bmatrix} s_x & 0 & 0 \\ 0 & s_y & 0 \\ 0 & 0 & s_z \end{bmatrix} \tag{6.1}$$

When the vector representing the given point is multiplied by this matrix it will scale the three coordinates by the corresponding scaling factor $\mathbf{Sv} = (s_x x, s_y y, s_z z)$. Rotational transformation can also be represented, in a similar way, via a 3×3 matrix. For example, the rotation of a point $\mathbf{v}$, about the x axis through an angle θ can be written as,

$$\begin{bmatrix} \cos\theta & -\sin\theta & 0 \\ \sin\theta & \cos\theta & 0 \\ 0 & 0 & 1 \end{bmatrix} \cdot \begin{bmatrix} x \\ y \\ z \end{bmatrix} = \begin{bmatrix} x\cos\theta - y\sin\theta \\ x\sin\theta + y\cos\theta \\ z \end{bmatrix} \tag{6.2}$$

Translation proves slightly more complex however, as it can't be written as a 3×3 matrix. Instead, it is written as a 4×4 matrix and a translational unit must be added to the point

vector,

$$\begin{bmatrix} 1 & 0 & 0 & T_x \\ 0 & 1 & 0 & T_y \\ 0 & 0 & 1 & T_z \\ 0 & 0 & 0 & 1 \end{bmatrix} \cdot \begin{bmatrix} x \\ y \\ z \\ 1 \end{bmatrix} = \begin{bmatrix} x + T_x \\ y + T_y \\ z + T_z \\ 1 \end{bmatrix} \tag{6.3}$$

The final type of transformation that is required for graphics rendering is the *projection* matrix which is vital for rendering 3D scenes as 2D images on screen. It defines a *viewing box* called a frustum where, when applied to the scene, everything that ends up with NDCs within the frustum is rendered and everything else is *clipped*. It also provides a homogeneous w component ($\mathbf{v} = \{x, y, z, w\}$) to any given vertex, allowing OpenGL to perform perspective division, effectively mapping the 3D vertex to the 2D viewport. There are two types of projection matrix used commonly within 3D rendering, the orthographic and perspective projection matrices. Orthographic projection is a form of parallel projection creating a frustum where the projection lines are orthogonal to the projection plane, resulting in every plane of a given scene appearing as affine transformations on the viewport. It is given by,

$$\mathbf{P}_{\text{ortho}} = \begin{bmatrix} \frac{2}{r-l} & 0 & 0 & -\frac{r+l}{r-l} \\ 0 & \frac{2}{t-b} & 0 & -\frac{t+b}{t-b} \\ 0 & 0 & \frac{-2}{f-n} & -\frac{f+n}{f-n} \\ 0 & 0 & 0 & 1 \end{bmatrix} \tag{6.4}$$

where r, l, t, and b define the x and y components of the frustum, (right, left, top, bottom respectively) and f and n define the z components (far and near). After applying an orthographic projection a vectors w component is always equal to 1, resulting in directly mapping the vector to NDC. In 3D graphics however, it is often useful to apply *perspective* to the scene, essentially rendering objects smaller if they are further from the viewer. To do this we require changing a vectors w component. This can be performed via a perspective projection matrix, which has the form,

$$\mathbf{P}_{\text{persp}} = \begin{bmatrix} \frac{2n}{r-l} & 0 & \frac{r+l}{r-l} & 0 \\ 0 & \frac{2n}{t-b} & \frac{t+b}{t-b} & 0 \\ 0 & 0 & -\frac{f+n}{f-n} & \frac{-2fn}{f-n} \\ 0 & 0 & -1 & 0 \end{bmatrix} \tag{6.5}$$

The resulting xyz components of the NDC are then divided by the w component to introduce the illusion of perspective.

Blinn-Phong Lighting

To effectively render 3D graphics, some form of lighting effects need to be taken into account. Without any lighting it can be difficult to make out the 3-dimensionality of an image, see Fig 6.2. Lighting within the real world however, is extremely complex with many different factors. Therefore, for 3D rendering approximate models based on simple physics of light are used to create semi-realistic lighting scenes. One of the simplest models is the Blinn-Phong shading[268;269] model which considers three separate components,

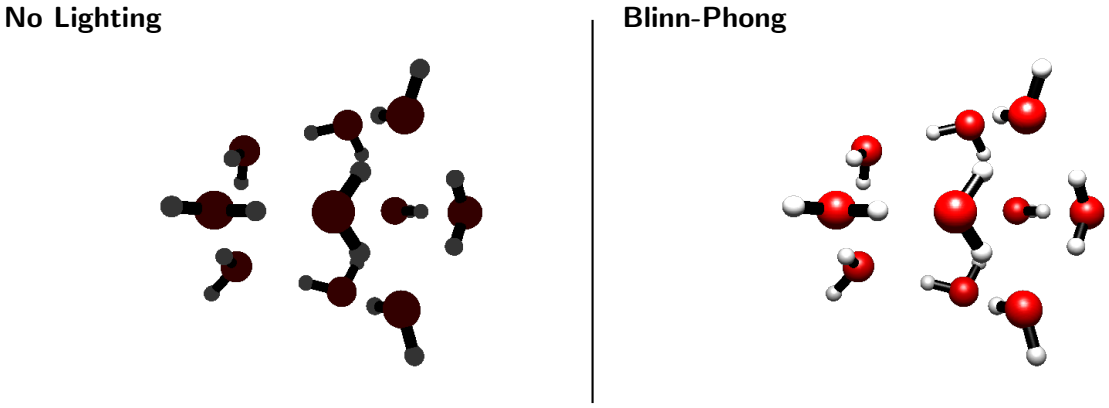

Figure 6.2: Three dimensional image of a water cluster generated using the QuestView software with and without blinn-phong lighting effects applied.

- Ambient lighting, or the neutral lighting on an object making its colour visible.
- Diffuse lighting which simulates a directional light source.
- Specular lighting which simulates the bright spot that appears on objects when directly facing a light source.

Ambient lighting is the simplest of the three components and accounts for the fact that under real conditions there are many light sources scattered around a given object including reflections of the main light source of surrounding objects. In computer graphics there are algorithms that can calculate these types of lighting effects and are referred to as *global illumination* algorithms, however, they are very complex and computationally expensive. Therefore, for the purposes of this 3D viewer we only need to consider a very simplified model for the ambient light. It is calculated by multiplying an objects colour, in red-green-blue (RGB) format, with values between 0 and 1 for each colour component, by an ambient light strength, which is set to 0.2 in the case of the QuestView main fragment shaders.

Diffuse lighting starts to become more complex as here, the angle of an object with respect to the light source needs to be taken into account. If the light source is directly perpendicular to the objects surface then the lighting effect is at its strongest. To measure this, the normal vector for the objects surface is required. The angle between the light source and the normal vector is then calculated, the closer this angle is to 0, the stronger the impact of the light source. See Fig 6.3 for reference. The dot product between the normal vector and the incoming lights direction can be used to give a scalar factor that will be used to calculate the object's resulting colour.

$$\mathbf{C}_{\text{pixel}} = S\mathbf{C}_{\text{light}}\frac{\mathbf{R}_{\text{light}} \cdot \mathbf{N}}{r^2}\mathbf{C}_{\text{base}} \tag{6.6}$$

where, $\mathbf{C}_{\text{light}}$ and $\mathbf{C}_{\text{base}}$ are the RGB colour values for the light source and object respectively and S is a scalar factor controlling the strength of the light source. $\mathbf{R}_{\text{light}}$ is the vector between the light and the object, $\mathbf{N}$ is the unit normal for the objects surface and r is the distance between the object surface and the light source. In practice the angle θ may be

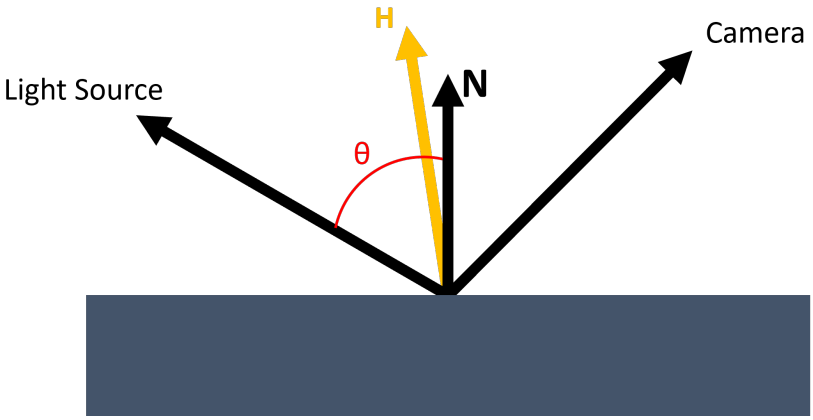

Figure 6.3: The components that are required for calculating lighting effects on a given pixel on an objects surface.

> 0 resulting in a negative value for the dot product in Eq. (6.6), in this case the result of the dot product is set to 0. When dealing with vertex normals it is important to note that the usual model matrix used to manipulate the vertices will not have the desired effect on its normal vector. Instead, the transpose of the inverse of the upper-left 3×3 part of the model matrix is used.

The final component of the Blinn-Phong shading model is the specular lighting. Here, the position of the object and light source is required, however, the viewing position is also required. Specular lighting is based around the reflective properties of the given object, as light is reflected from a given surface it is most intense along a vector with an angle $-\theta$ to the normal vector, where θ is the angle between the light source and the surface normal. Therefore, if the viewing position aligns along this vector, there is a much more intense lighting effect due to the light source. In practice this is measured using what is referred to as a halfway vector, $\mathbf{H}$. It is the unit vector exactly halfway between the view direction, $\mathbf{R}_{\text{view}}$, and light direction, $\mathbf{R}_{\text{light}}$. It is given by,

$$\mathbf{H} = \frac{\mathbf{R}_{\text{light}} + \mathbf{R}_{\text{view}}}{|\mathbf{R}_{\text{light}} + \mathbf{R}_{\text{view}}|} \tag{6.7}$$

The smaller the angle between $\mathbf{H}$ and $\mathbf{N}$ the more intense the specular lighting effect. The overall specular light component is given by,

$$\mathbf{C}_{\text{pixel}} = S\mathbf{C}_{\text{light}} \frac{(\mathbf{H} \cdot \mathbf{N})^s}{r^2} \tag{6.8}$$

where s is a scalar depicting the *shininess* of a surface.

Once these three components have been calculated the overall colour of the given pixel is determined by summing all three components giving a final RGB vector. This vector is then combined with an alpha value, controlling the opacity of the object. This final RGB-alpha (RGBA) vector, of length 4, is then sent to OpenGL's rendering function, see bellow. The calculation of lighting effects takes place within the *fragment* shader, written in GLSL. Several different fragment shaders are utilised within QuestView for various visual effects.

Alpha Blending

Several functions within QuestView require controlling the opacity of objects within the molecular viewing window. This is carried out by a process called alpha blending. When an object is sent to the GPU, the shader program is executed on its triangulated vertices and their colours. Each colour is represented by a vector of length 3 giving the RGB values, between 0 and 1. When the resulting pixel colour value is passed onto the OpenGL rendering function however, it is passed as an RGBA vector of length 4. The additional value is the α value for that given vertex and describes its opacity, 0 being completely transparent and 1 being completely opaque. The simplest method for calculating the total blended colour, of the given pixel, is given by,

$$\mathbf{C}_{\text{result}} = \mathbf{C}_{\text{source}} F_{\text{source}} + \mathbf{C}_{\text{destination}} F_{\text{destination}}, \tag{6.9}$$

where $\mathbf{C}_{\text{source}}$ is the RGB colour of the object and $\mathbf{C}_{\text{destination}}$ is the currently loaded RGB colour for that given pixel, which can be due to an already processed object or simply the background colour. F_{source} and $F_{\text{destination}}$ are the impact factors given by the objects α value; $F_{\text{source}} = \alpha$ and $F_{\text{destination}} = 1 - \alpha$. For demonstrations of how this is rendered see the optimised geometry figures within section 4.2.

6.2 The Molecular Viewer

QuestView consists of both a text-based interface and an interactive 3D viewer window, both of which enable the visualisation and manipulation of molecular systems. Visualisation of molecular structures can be rendered in three different styles; ball and stick, stick, wireframe and Van der Waals. These are shown in Fig. 6.4.

6.2.1 Text Based Input

The text input window to the right of the viewer enables simple text commands to be input, and text based results to be shown, these include but are not limited to,

- printing geometry/fragmentation information,
- removing atoms/fragments according to set conditions,
- adding charge/spin projection information,
- editing how the system is fragmented.

6.2.2 Click-and-Drag Molecule Building

Once the foundations for the application had been developed, implementing a parser for various molecular structure file types and displaying the resulting 3D structure was fairly trivial. However, most molecular viewing software can go beyond this, including tools to draw and edit molecular structures directly within the viewer window. PyQt5 includes functions to retrieve the mouse pointer position within a given widget as a 2D pixel value. The complexity lies in being able to reliably convert this into the viewport's *world space*

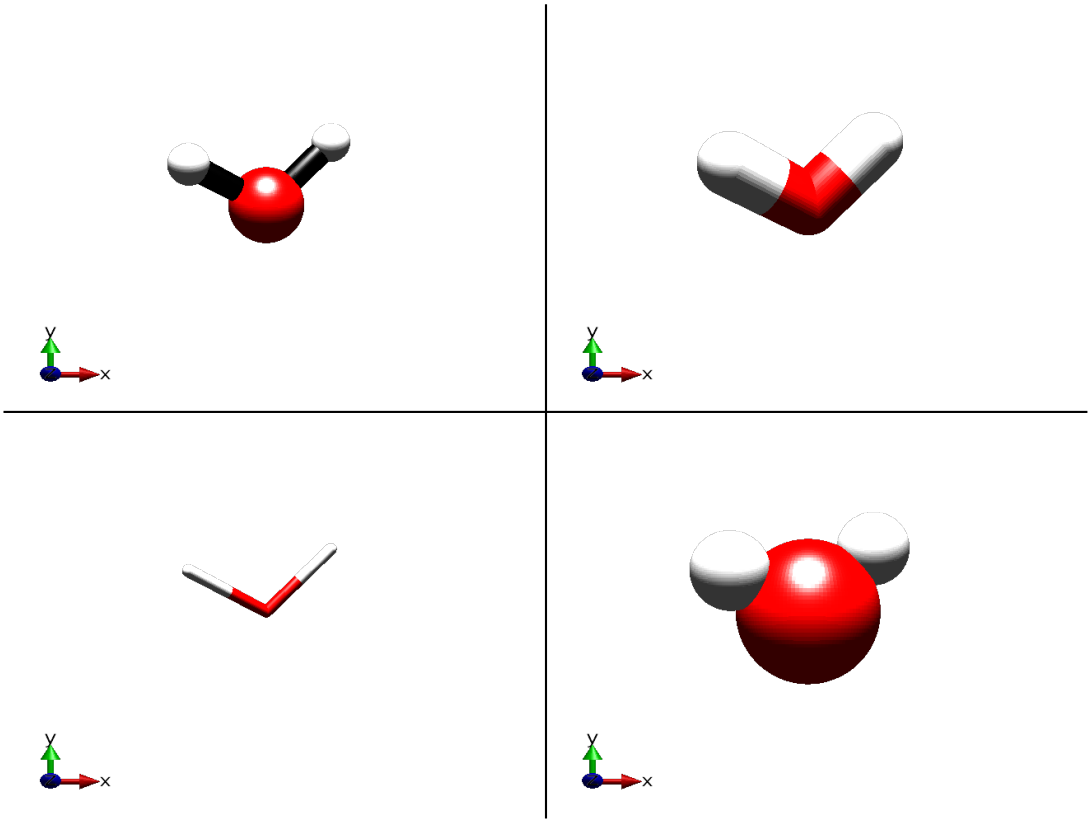

Figure 6.4: Examples of a water molecule in the different rendering styles available within QuestView.

and back. This requires taking the (x,y) positions of the mouse within the window, and multiplying this with the inverse of the model matrix to retain the position within world coordinates. The z coordinate is set to a fixed value. Once in world coordinates, a check is carried out as to whether an atom already exists at that point. If one does not exist then a new atom object is created. Otherwise, a new atom object is only created if the mouse action involves a *drag*, wherein the new atom object will follow the mouse pointer position and a new bond will be created linking to the atom at the original mouse click position. If the final mouse position after the drag motion is on top of an existing atom, it will create a bond from the first atom to the second without creating a new atom. Alongside this functionality, a highlighting tool enables the user to highlight specific atoms and edit their positions or bonding from the viewer. Together this provides presents a complete suite of tools for building and editing simple molecules in line with other molecular viewing software packages.

6.2.3 Interfacing With Open Babel

The Open Babel toolbox[270] is designed to give users access to many useful ready-to-use programs for chemical analysis. Therefore, it provides several functions that can significantly improve the user experience of molecular visualisers.

Molecular Input

Open Babel contains interfaces for generating molecular structures from many input formats. Although within QuestView, the handling of reading molecular structure input files is dealt with internally, the generation of molecular structures from simplified molecular-input line-entry system (SMILES) strings has been implemented utilising the Open Babel python library, enabling a more simplistic construction and visualisation of much more complex molecular structures. Additionally, once a molecular structure has been created, Open Babel can analyse the bond order of the atoms in the system, filling any vacancies with hydrogen atoms, following pre-defined valence rules.

Molecular Dynamics Optimisation

By interfacing with Open Babel, quick optimisation methods via molecular mechanics force fields are readily available. These have several parameters such as energy convergence, maximum number of steps or the algorithm used for the optimisation. There are three main force fields supported by OpenBabel;

- Generalised Amber Force Field[271] - parameterised for larger biomolecules with some support for smaller drugs/ligands.
- Merck Molecular Force Field[272–278] - parameterised for most atoms present in organic compounds.
- Universal Force Field[279] - generalised to be applicable to all atoms in the periodic table.

6.3 Iso-Surface Generation

One important feature for any given molecular visualiser is the ability to view properties of molecules, not just their 3D structures. As discussed within chapter 3, properties such as the total electron density of a system can be very important when performing a detailed analysis. This could be of additional interest when considering molecular systems within magnetic fields as the molecular orbitals contain a non-physical imaginary component, which could provide more insight into the response of the system to the field, this is not typically considered in most molecular viewer software packages. Most modern electronic structure packages can output data that can be used to plot properties such as the total electron density and molecular orbitals. This data takes the form of single values at given points, defined by an $n_x \times n_y \times n_z$ plotting grid. This data must be interpreted however, before it can be visualised.

6.3.1 Marching Cubes Algorithm

The most common approach to visualise properties such as electron densities, is to calculate an iso-surface, which is a 3-dimensional surface, where the value of the density (or any given property) is equivalent at all points along the surface and equal to a given iso-value. Within QuestView, this surface can be calculated by employing the marching

cubes algorithm (MCA).[280] The MCA can be split into two main steps, firstly the points along the surface corresponding to the iso-value must be determined, and secondly triangle vertexes and normals at these points must be calculated to direct the graphics engine on how to draw the surface.

To determine the iso-surface, cubic slices of data are generated from the plotting grid. The algorithm then determines how the surface intersects the given cube by comparing the values at each of the eight vertices and the given iso-value, giving them a value of 1 if they are $<$ the iso-value, therefore, outside the surface, or 0 if they are $>$ the iso-value, inside the surface. Given the cube has eight vertices with each having two possible states, 0 or 1, there are $2^8 = 256$ possible ways the surface can intersect the cube. Enumerating these 256 cases creates a lookup table corresponding to the surface-edge intersections for any given cube. These cases can be reduced by utilising the implicit symmetry of a cube. First, the topology of the triangulated surface remains unchanged if the relationship of the surface values to the cubes is reversed. Therefore, only cases with zero to four vertices greater than the iso-value need to be considered, effectively reducing the number of possible cases to 128. Secondly, this can be further reduced to 14 possible patterns by considering the rotational symmetry of the cube. These 14 patterns are shown in Fig 6.6. An index for each case can be created using the vertex numbering shown in Fig 6.5, which then points to a list of edge intersections within the lookup table. The precise point of intersection for the surface and any given edge is then calculated via linear interpolation,

$$\mathbf{v}_{\text{surface}} = \mathbf{v}_a + \left(\frac{x_{\text{iso}} - x_a}{x_a - x_b} \right) (\mathbf{v}_a - \mathbf{v}_b) \,, \tag{6.10}$$

where $\mathbf{v}_a$ and x_a are the grid point and property value for a given cube vertex a and x_{iso} is the iso-value.

Once a given cube has been analysed the algorithm *marches* onto the next one, periodically moving across the plotting grid.

The final step in the MCA is the calculation of unit normals for each triangle vertex to enable lighting effects to be applied when rendering the 3D surface. There are several different approaches for determining surface normals for the vertices, within QuestView the cross product is utilised. The unit normal, $\mathbf{N}_a$, for a given vertex $\mathbf{v}_a$, which makes a triangle with vertices $\mathbf{v}_a, \mathbf{v}_b, \mathbf{v}_c$, is given by,

$$\mathbf{N}_a = \frac{(\mathbf{v}_b - \mathbf{v}_a) \times (\mathbf{v}_c - \mathbf{v}_a)}{|\,(\mathbf{v}_b - \mathbf{v}_a) \times (\mathbf{v}_c - \mathbf{v}_a)\,|}. \tag{6.11}$$

These vertices and corresponding normals can then be fed into the OpenGL API and drawn within the viewer window, displaying a 3D surface plot for the given property.

6.3.2 Laplacian Smoothing

In practice, plotting grids can often be quite sparse, resulting in surfaces appearing *'blocky'* when fed through the MCA. To improve the look of the generated surfaces, a smoothing algorithm is applied to the surface data. The chosen smoothing function within

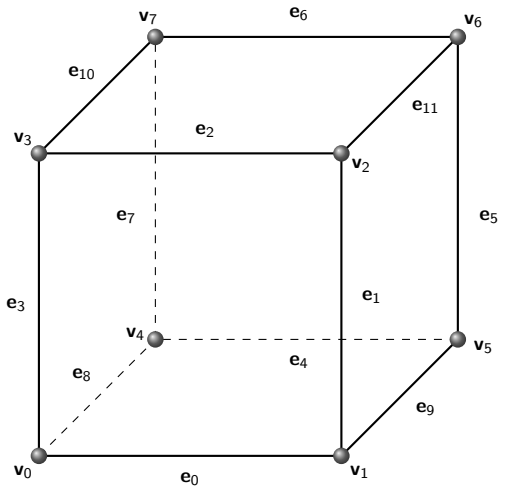

Figure 6.5: Cube vertex and edge numbering for the marching cubes algorithm. The resulting index is an 8 bit binary value with each bit corresponding to a state of a given vertex.

QuestView is the Laplacian smoothing algorithm[281;282], where a new position for a given vertex is determined from local vertex information. The new position for a given vertex i is,

$$\mathbf{v}_i = \frac{1}{N}\sum_{j=1}^{N}\mathbf{v}_j, \tag{6.12}$$

where N is the number of adjacent vertices to vertex i and $\mathbf{v}_j$ is the position of the j^{th} adjacent vertex. This algorithm can be iterated multiple times to improve the smoothing however, it can exhibit *shrinking* of the total surface if iterated too many times. By default, QuestView performs 3 iterations of the Laplacian smoothing algorithm, however, this can be changed by the user if desired. An example of how Laplacian smoothing improves the quality of the produced image is demonstrated in Fig 6.7.

6.4 3-Dimensional Vector Plotting

Throughout Chapter 5, the concept of magnetically-induced currents has been introduced. However, the resulting current vector, **j**, is a complex and 3-dimensional property which, within Chapter 5, has only been analysed using 2-dimensional vector plots. QuestView presents a potential opportunity to progress the analysis of these currents beyond simple 2-dimensional images. When calculating the magnetically-induced current, the 3-dimensional vectors are evaluated at a series of grid points. In the figures in Chapter 5, these vectors are visualised as arrows on a given 2-dimensional plane. To go beyond this analysis, the vectors can be plotted as 3-dimensional arrows around the visualised molecule enabling the detailed analysis of the 3 dimensionality of the vector field. Examples of this are shown in Fig 6.8.

There are some significant considerations if this is to be a useful tool moving forward. Within this implementation there is no visual account for the magnitude of the induced

current at each grid point, the addition of a colour gradient based visualisation for the magnitude would enable a more complete analysis of how the induced current varies in the space around the given molecule. Additionally, thresholds need to be determined for the visualisation of the current vectors to limit the number of arrows displayed around the molecule due to the typical density of plotting grids used during the electronic structure calculations. Further work in these directions and for alternate representations of 3D vector fields is in progress.

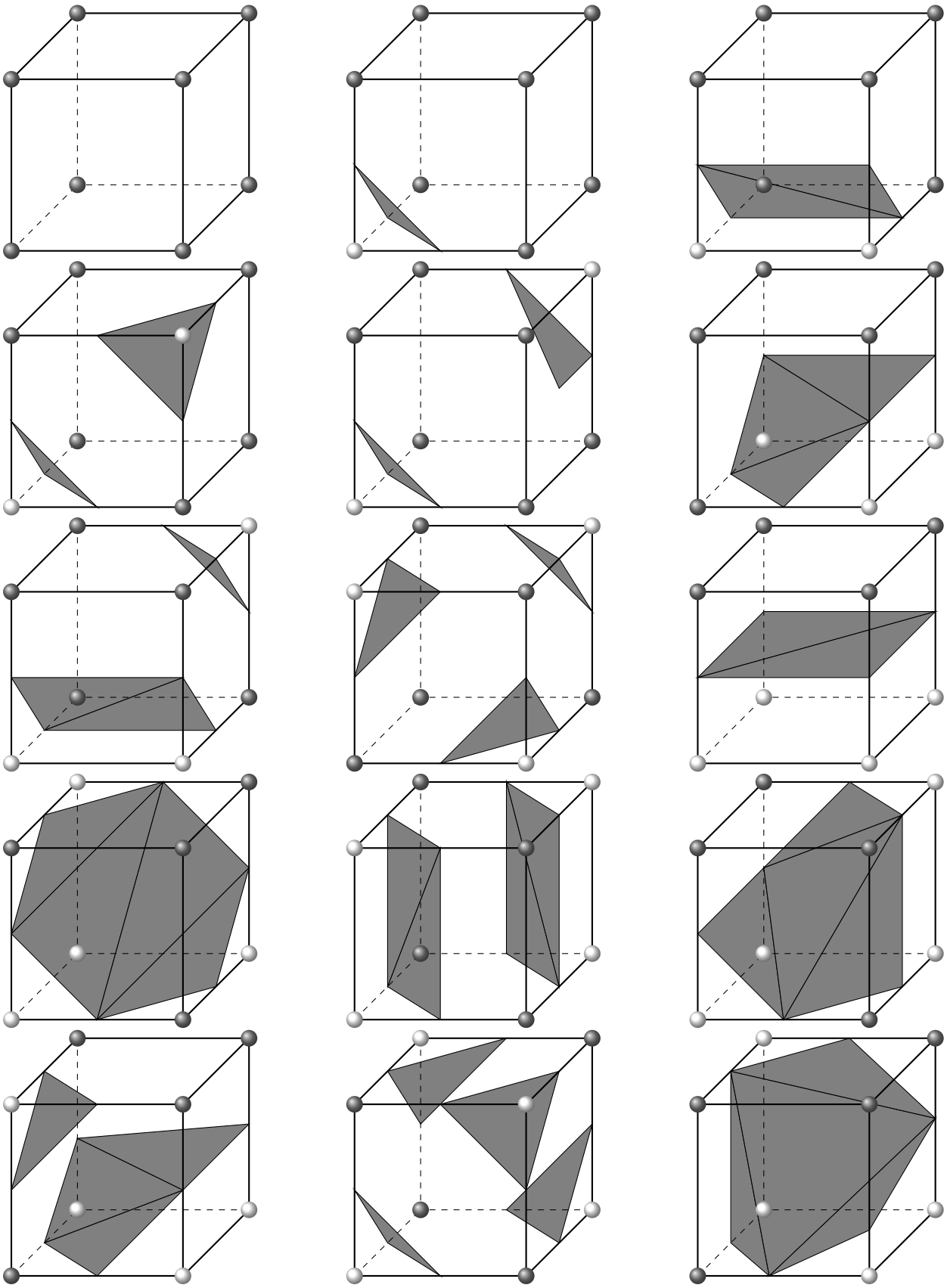

Figure 6.6: The 14 possible patterns that a given surface can take through any given cubic slice of data, split into triangles for display via a graphics engine.

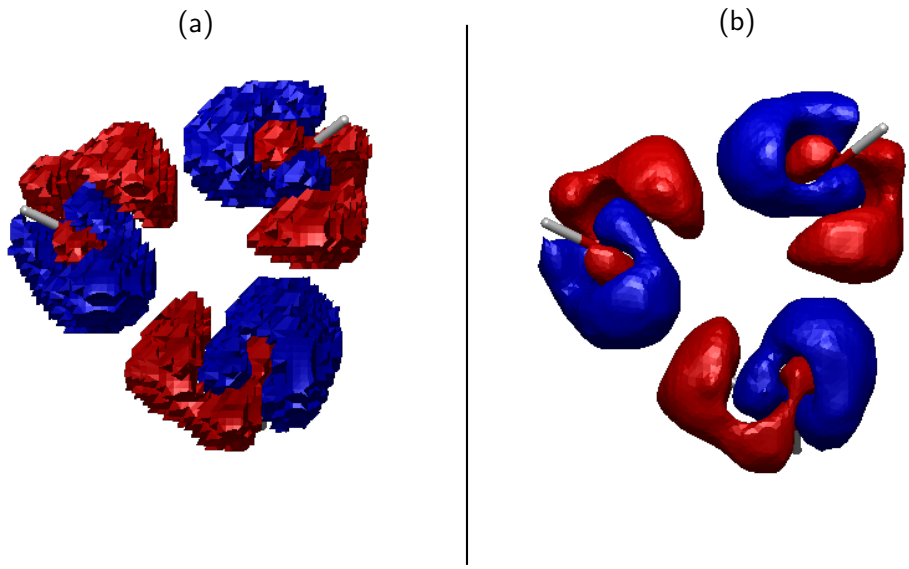

Figure 6.7: Electron density difference plots for a water trimer plotted with (b) and without (a) the use of the Laplacian smoothing algorithm.

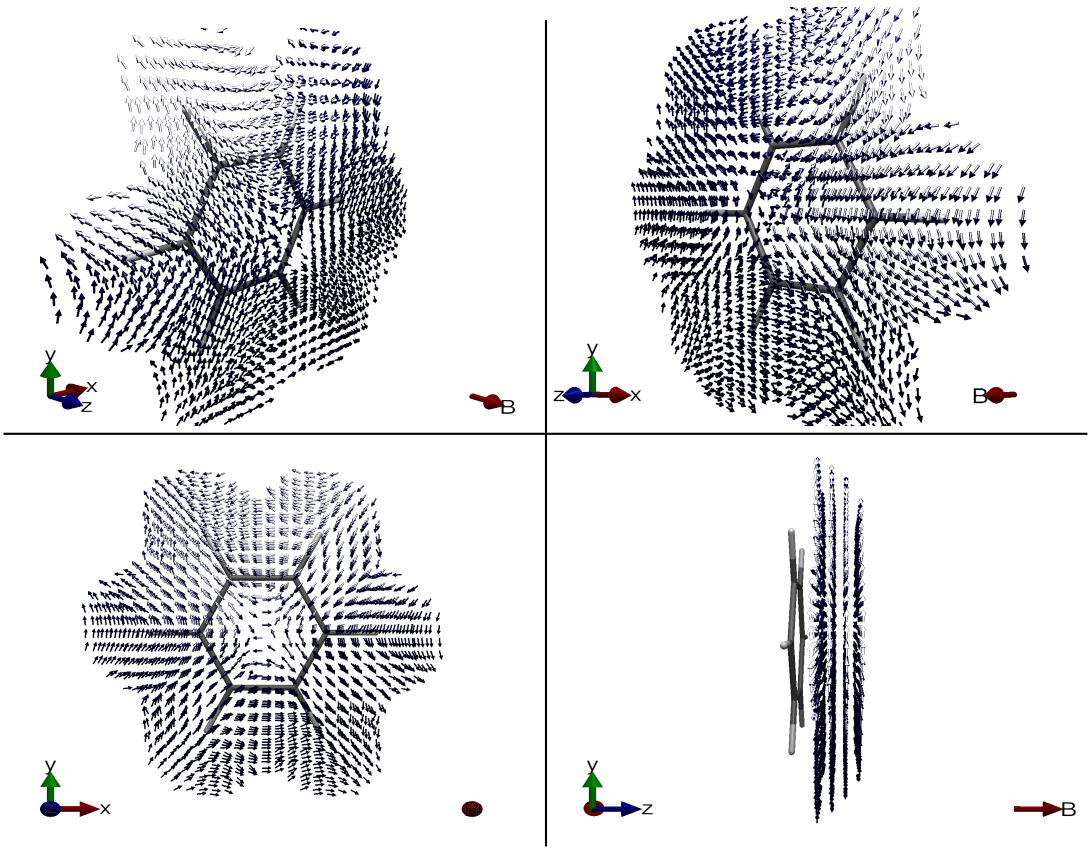

Figure 6.8: 3-Dimensional vector plots showing the induced current 1-2 bohr above a benzene ring due to an applied magnetic field of $|\mathbf{B}| = 0.001$ a.u. along the z-axis.

7 Ongoing Extensions to The EFM

Due to the nature of the EFM it has been shown to be incredibly adaptable, enabling its application to the calculation of a wide variety of chemical and physical properties across a wide variety of system types. Moving forward therefore, expanding the capabilities of the LAO based EFM implementation that has been the focus of most of this work proves a logical next step. This chapter briefly discusses some of the ongoing extensions to the work already presented, and how they can expand the scope of the EFM even more.

7.1 NMR of Molecules in Solution

The potential applications of LAO based EFMs extend beyond simply studying the energies and structures of molecular clusters in magnetic fields. LAO based electronic structure methods have been shown to provide an efficient route to calculating molecular magnetic properties such as magnetisabilities, hypermagnetisabilities and nuclear magnetic resonance (NMR) shielding constants.[15;283;284] Of particular note, although not directly used within this chapter, the use of cDFT has been shown to significantly improve the accuracy when calculating NMR shielding constants, over standard Kohn-Sham DFT.[15] However, to date the calculation of these properties with LAO based non-perturbative methods, such as cDFT, neglects the fact that most NMR experiments are conducted in solution, therefore, neglecting the impact of the solvent-solute interactions on the NMR chemical shifts. One potential route to including solvent effects is to utilise the polarisable continuum method (PCM)[285–288] which applies a constant electrostatic potential to mimic the effects of a solvent without including the solvent molecules explicitly. This can be applied to standard perturbative DFT methods but has yet to be applied to a cDFT approach. However, it has been shown that EFM presents a potential route to introducing explicit solvent effects without incurring a significant increase in the computational complexity of the calculations.[289–292] Whilst this has been demonstrated for calculations using LAOs and perturbation theory for both molecular cluster and crystals, see Ref. 292, extending this to the non-pertubative methods available in QUEST, for inclusion of arbitrary field strengths, is discussed here.

7.1.1 Non-Perturbative Calculation of NMR Shielding Constants

The dependence of the molecular electronic energy $E(\mathbf{B}, \mathbf{M}_k)$ on the external magnetic field, $\mathbf{B}$ and the nuclear magnetic moment $\mathbf{M}_k$ of nucleus k represented by the vector potential,

$$\mathbf{A}_k(\mathbf{r}) = \frac{\mu_0 \mathbf{M}_k \times (\mathbf{r} - \mathbf{K})}{4\pi |\mathbf{r} - \mathbf{K}|^3} = \frac{\mu_0}{4\pi} \mathbf{M}_k \times \frac{1}{\partial \mathbf{K}} \frac{1}{|\mathbf{r} - \mathbf{K}|}, \tag{7.1}$$

where $\mathbf{K}$ is the position of the nucleus, k, can be written as a Taylor expansion,

$$E\left(\mathbf{B},\mathbf{M}_K\right) = E\left(\mathbf{0},\mathbf{0}\right) + \sum_{\alpha\beta}\sigma_{k;\alpha\beta}B_\alpha M_{k;\beta} + \ldots \tag{7.2}$$

The leading-order mixed term of which is the nuclear shielding tensor,

$$\sigma_{k;\alpha\beta} = \left.\frac{\partial^2 E\left(\mathbf{B},\mathbf{M}_k\right)}{\partial B_\alpha \partial M_{k;\beta}}\right|_{\mathbf{B}=\mathbf{0},\mathbf{M}_k=\mathbf{0}} \tag{7.3}$$

The derivative of the energy with respect to $\mathbf{M}_k$ can be computed analytically,

$$\Xi_{k;\beta}\left(\mathbf{B}\right) = \left.\frac{\partial E\left(\mathbf{B},\mathbf{M}_k\right)}{\partial M_{k;\beta}}\right|_{\mathbf{B}=\mathbf{0},\mathbf{M}_k=\mathbf{0}} = \frac{e\mu_0}{4\pi m}\epsilon_{\alpha\beta\gamma}\frac{\partial}{\partial K_\gamma}\langle\psi|\{\hat{p}_\alpha + eA_\alpha, |\mathbf{r}-\mathbf{K}|^{-1}\}|\psi\rangle, \tag{7.4}$$

where $\{\hat{p}_\alpha + eA_\alpha, |\mathbf{r}-\mathbf{K}|^{-1}\}$ denotes the anti-commutator. The expectation value in Eq. (7.4) can be written in a form similar to a nuclear attraction integral and therefore, can be evaluated using a modification of the code to calculate nuclear attraction integrals with LAO basis functions. The second differentiation, with respect to $\mathbf{B}$, can be computed directly by finite difference numerical differentiation, using a central difference method about $|\mathbf{B}| = 0$ a.u. Considering the function $\Xi_{k;\beta}\left(\mathbf{B}\right)$ is symmetric about this point, this can be written as,

$$\sigma_{k;\alpha\beta} \approx \frac{\Xi_{k;\beta}\left(\mathbf{B}\right) - \Xi_{k;\beta}\left(-\mathbf{B}\right)}{2\epsilon} \simeq \frac{\Xi_{k;\beta}\left(\mathbf{B}\right)}{\epsilon}. \tag{7.5}$$

The isotropic NMR shielding constant is then calculated as $\sigma_k^{\text{iso}} = \frac{1}{3}\text{Tr}\sigma_k$.

7.1.2 NMR Shielding Constants Calculated Using EFM

The most common form of experimental NMR is solution based, therefore, NMR shielding constants determined by gas phase calculations, such as those in Ref. 15, typically only serve as a computational benchmark, due to the absence of the solvent effects. Calculating NMR shielding constants within an EFM framework, however, could provide a low-cost approach for including solvent effects within a given calculation.

The NMR shielding constant for a specific nucleus can be calculated by a many-body summation in the same way as the derivatives with respect to atomic position, used when calculating forces on atoms. Here we can calculate the analytic first derivative with respect to nuclear magnetic moment $\mathbf{M}_k$ for a specified nucleus at each stage within an EFM calculation. These can then be combined to give the total energy derivative for a given nucleus,

$$\Xi_{k;\beta}^{i,\text{total}} = \Xi_{k;\beta}^{i} + \sum_{j>i}\left(\Xi_{k;\beta}^{ij} - \Xi_{k;\beta}^{i}\right)\ldots, \tag{7.6}$$

where $\Xi_{k;\beta}^{i}$ is the derivative of the energy of monomer i and $\Xi_{k;\beta}^{ij}$ is the derivative of the i^{th} monomer atoms of the dimer constructed from monomers i and j. Finite difference in the magnetic field strength can then be used to determine the total NMR shielding tensor, $\sigma_{\mathbf{k}}$ for a given monomer i.

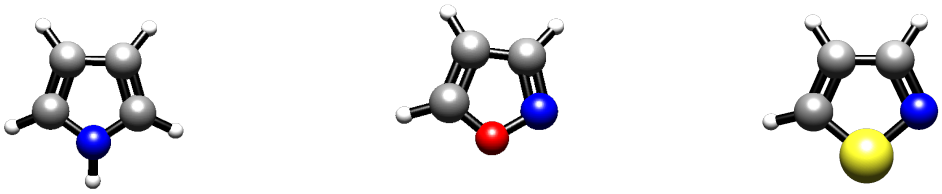

Figure 7.1: The structure of the pyrrole (left), isoxazole (centre) and isothiazole (right) molecules.

7.1.3 Application to Solvated Molecules

To test how EFM can reproduce NMR shielding constants, several molecules solvated in water are considered, the isolated structures of which are shown in Fig. 7.1. Within the work of Semenov and coworkers[293], it is shown that for a collection of azoles and azines, including the molecules considered here, solvent effects can have a significant impact on the NMR chemical shifts, particularly when considering polar solvents and therefore, need to be properly treated. From the results presented in Ref. 293 it was demonstrated how using solvent methods such as PCM and a supermolecule approach can significantly improve the calculated chemical shifts. In this work, the pyrrole, isoxazole and isothiazole molecules are considered solvated in water. The geometries for the individual molecules were determined at the MP2 theory level with the 6-311++G** basis set. The geometry of the surrounding solvent molecules was determined using the universal force field[279] (UFF) where a single molecule was placed at the Cartesian origin, surrounded by 50 explicit solvent molecules. An example of the solvated geometries is shown in Fig. 7.2, for the pyrrole molecule. The absolute NMR shielding constants for the nitrogen atom were then calculated using DFT and the EFM, with the KT3 exchange-correlation functional of Keal and Tozer[294] in combination with the pcS-3 basis set for the nitrogen atom and the pc-2 basis set for all other atoms.[295–300] Whilst cDFT functionals, such as the cTPSS functional utilised in chapter 3, are available and have been shown to be more accurate for calculating magnetic response properties, the KT3 functional is used here to provide a direct comparison with the results in Ref. 293. The gas phase and IEF-PCM values are taken from Ref. 293, calculated using the same DFT functional and basis sets with the geometries being optimised at the MP2 theory level with the 6-311++G** basis set. Nitrogen NMR chemical shifts, δ, are calculated with reference to neat nitro-methane (CH_3NO_2) as recommended by IUPAC,[301;302]

$$\delta = \frac{\sigma_{CH_3NO_2} - \sigma}{1 - 10^{-6}\sigma_{CH_3NO_2}}, \tag{7.7}$$

where σ is the calculated absolute NMR shift and $\sigma_{CH_3NO_2} = -135.8$ ppm.[303]

From the results in table 7.1, it is clear the EFM based approach is a good qualitative method for calculating NMR chemical shifts in solution. It shifts the values in the correct direction compared to those performed in gas phase however, from this analysis it doesn't produce an improvement when compared to the values calculated using IEF-PCM. This is an interesting result, particularly when comparing to Ref. 293 where they present a

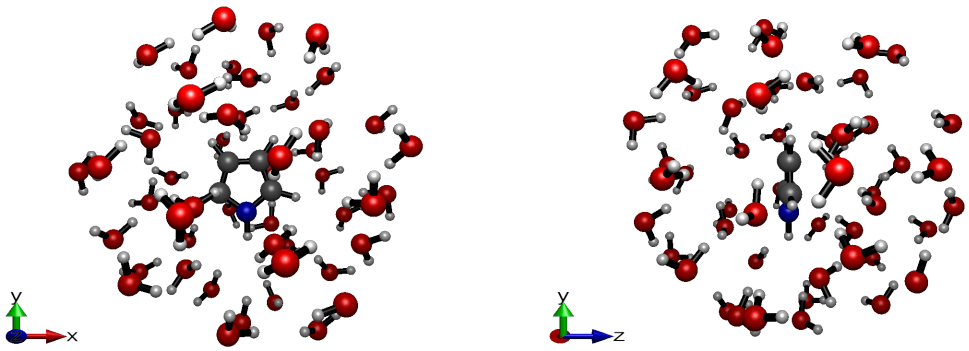

Figure 7.2: The geometry of pyrrole solvated in 50 water molecules optimised using the UFF molecular dynamics force field.

Compound	Gas Phase	IEF-PCM	EFM	Experiment
Pyrrole	-232.5	-224.7	-217.3	-226.5
Isoxazole	12.7	-3.9	4.2	-10.3
Isothiazole	-73.0	-85.2	-76.5	-95.8

Table 7.1: NMR chemical shifts, in ppm, for various molecules, with and without solvent effects. Gas phase, IEF-PCM and experimental reference values are taken from Ref. 293.

supermolecule method which introduces a single explicit solvent molecule and is shown to, in general, deliver an improvement over the IEF-PCM values. There are several factors that could influence the quantitative accuracy of the EFM method. The first could be the requirement for including more explicit solvent molecules, however, this seems somewhat unlikely in light of the results presented in Ref. 293 for the supermolecule approach, and the idea that NMR is a relatively local property given that nuclear shielding tensors are determined mostly by the local environment of the nucleus. The more likely influencing factor is the geometry of the total system. NMR shielding constants are very susceptible to the environment that a nucleus exists in, which is one of the factors that make it such a powerful analytic tool in experiments. As an example, the EFM NMR chemical shift for isoxazole was calculated where the geometry of the total system, including the isoxazole molecule, was determined using the UFF molecule force field. The resulting chemical shift was 40.7 ppm, which is significantly different compared to the calculation where the central isoxazole molecule was optimised using MP2. As an additional comparison a gas phase calculation was performed on the geometry of the isoxazole molecule extracted from the UFF optimisation. This gave a chemical shift value of 54.7 ppm, demonstrating the impact the geometry of the system has on the calculation of the NMR chemical shift. Therefore, to improve upon the quantitative accuracy when calculating NMR chemical shifts with the EFM, it would make sense to couple this approach with the geometry optimisation procedure discussed in chapter 4. This is not considered within this work but is an area of ongoing research. It also once again highlights the possible need for a more complete conformer based analysis using a combined quantum mechanical and molecular dynamics approach.

	$\|\mathbf{B}\| = 0$ a.u.		$\|\mathbf{B}\| = 0.1$ a.u.	
Excitation	Isolated	$(H_2O)_{51}$	Isolated	$(H_2O)_{51}$
ω^1	3.024	3.130	3.120	1.370
ω^2	4.362	5.137	4.642	2.923
ω^3	7.430	6.554	7.394	4.686
ω^4	13.714	9.566	11.758	6.902
ω^5	14.904	12.272	13.686	9.592

Table 7.2: Excitation energies in eV, determined through the RPA, for an isolated water molecule, and the same water molecule in the center of a $(H_2O)_{51}$ cluster both at zero field and with an applied field strength of $|\mathbf{B}| = 0.1$ a.u. The calculations were performed at using DFT with the TPSS exchange correlation functional and the 6-31G basis set.

7.2 Excited States of Molecules in Solution Under the Influence of an External Magnetic Field

Another property that can be computed for large molecular clusters with EFM calculations, is the calculation of excitation energies for a given monomer within a larger system, often representing a solvated molecule. The EFM excitation energy of a given monomer i is given by,

$$\omega_i = \sum_{j \neq i}^{n} \left(\omega_{ij}^{'} - \omega_i^{'} \right) + \omega_i^{'}, \tag{7.8}$$

where $\omega_{ij}^{'}$ and $\omega_i^{'}$ are the excitation energies of dimer ij and monomer i respectively. Typical methods used to determine the excitation energies involve real-time electron dynamics methods such as real-time time-dependent density functional theory (RT-TDDFT)[304;305] for which an LAO based RT-TDDFT approach has recently been developed to describe excitations in strong magnetic fields.[22] This section presents a qualitative analysis using a preliminary implementation of EFM based linear response TDDFT (LR-TDDFT)[306–310] with the random phase approximation (RPA), to investigate how important a full implementation of EFM based excitation energies within an external magnetic field could be. Within the current implementation, the full EFM approach is not used directly, instead the linear response calculations are performed on a given monomer within the self-consistently converged electrostatic embedding potential, yielding $\omega_i^{'}$ from Eq. (7.8).

Table 7.2 contains the excitation energies for the lowest five excitations calculated using the RPA for LR-TDDFT. The geometry of the water cluster was taken from the MD simulations used to generate the $(H_2O)_{103}$ cluster within chapter 3. The excitation energy calculations were calculated at the DFT level with the TPSS functional and the 6-31G basis set. Calculations are presented at both zero field and at a field strength of $|\mathbf{B}| = 0.1$ a.u. From the results in table 7.2 its clear that including some form of environment interactions can have a noticeable effect on the lowest excitations of a water molecule, generating what is referred to as the solvatochromatic shift. This effect is significantly amplified when considering a molecule within a larger cluster, in a strong external magnetic field. It is well known that an applied external magnetic field causes Zeeman splitting leading to a removal in the degeneracy of orbitals creating more possible transitions. It is also known

to lower the spatial symmetry of the system and molecular orbitals, resulting in transitions that are symmetry forbidden at zero field, being present in high field spectra.[22] From this simple analysis this effect seems to be significantly impacted by the external embedding potential modelling the external electrostatic environment. This only includes approximate electrostatic contributions from molecular interactions, within the full EFM approach this would be extended to include quantum effects. This therefore, highlights the value of an EFM for determining excited states of molecules within molecular clusters. Performing the many body sum from Eq. (7.8), however, requires a clear assignment of each excitation in a monomer and its corresponding excitation in each dimer it is a part of. This may be possible for the lowest energy valence excitations but is progressively more difficult for higher excitations. This adds an extra layer of complexity when considering the division and MBE of the total system, compared to the calculation of properties such as NMR shielding constants, presented in section 7.1.

7.3 Treating Periodic Molecular Crystals in Strong Magnetic Fields using EFM

A crystalline solid is defined as an ordered repetition of a specific group of atoms, in 1-, 2- or 3-dimensions. This creates a system with translational periodicity, where, in a pure crystal, each repetition is a perfect reproduction of the original set of atoms. This periodicity can be defined by a set of translational symmetry operations,

$$\mathbf{T} = n_1\mathbf{a}_1 + n_2\mathbf{a}_2 + n_3\mathbf{a}_3 \qquad n_1, n_2, n_3 \in \mathbb{R}. \tag{7.9}$$

The set of points defined by the translation vector $\mathbf{T}$ are termed lattice points, each defined by a set of integers n_1, n_2 and n_3 and the non-coplanar vectors $\mathbf{a}_1, \mathbf{a}_2$ and $\mathbf{a}_3$, which define the translation. The parallelepiped formed by these three basis vectors, and encompassing the specified arrangement of repeated atomic positions, is termed the unit cell of the system. In reality, any given crystalline system will be finite, however, typically the effects of the crystal's surface is assumed to be negligible when considering the *bulk* properties of the material. The finite crystalline system is therefore, often considered as an $N = N_1 \times N_2 \times N_3$ unit cell subset, of the infinite system, known as a *supercell*.

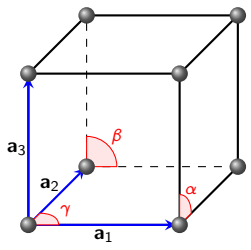

Figure 7.3: A primitive unit cell, with the lattice vectors $\mathbf{a}_1$, $\mathbf{a}_2$ & $\mathbf{a}_3$ and the angles between them, α, β & γ indicated.

The Schrödinger equation for an electron in a periodic potential defined as,

$$\left[-\frac{1}{2}\nabla^2 + v\left(\mathbf{r}\right)\right]\phi_i\left(\mathbf{r};\mathbf{k}\right) = \varepsilon_i\left(\mathbf{k}\right)\phi_i\left(\mathbf{r};\mathbf{k}\right), \tag{7.10}$$

where the eigenfunctions are known as Bloch functions,

$$\phi\left(\mathbf{r};\mathbf{k}\right) = \exp\left(i\mathbf{k}\cdot\mathbf{r}\right)\varphi\left(\mathbf{r};\mathbf{k}\right) \tag{7.11}$$

with wave vector $\mathbf{k}$ which defines how the phase of $\phi\left(\mathbf{r};\mathbf{k}\right)$ changes between adjacent unit cells. As introduced in chapter 2, when performing electronic structure calculations, the molecular orbitals are typically expanded in a finite basis of atom-centred atomic orbitals,

$$\varphi_i\left(\mathbf{r}\right) = \sum_{\nu} c_{\nu i}\chi_\nu\left(\mathbf{r}\right). \tag{7.12}$$

This can be adapted to model electronic structure within a periodic system by constructing a translationally-invariant basis from periodic images of the atom-centred basis,

$$\tilde{\chi}_\mu\left(\mathbf{r};\mathbf{k}\right) = \frac{1}{\sqrt{N}}\sum_{\mathbf{T}}\exp\left[-i\mathbf{k}\cdot\left(\mathbf{r}-\mathbf{T}\right)\right]\chi_\mu\left(\mathbf{r}-\mathbf{T}\right). \tag{7.13}$$

From this a series of corresponding Bloch functions can be constructed,

$$\omega_\mu\left(\mathbf{r};\mathbf{k}\right) = \exp\left(i\mathbf{k}\cdot\mathbf{r}\right)\tilde{\chi}_\mu\left(\mathbf{r};\mathbf{k}\right) = \frac{1}{\sqrt{N}}\sum_{\mathbf{T}}\exp\left(i\mathbf{k}\cdot\mathbf{T}\right)\chi_\mu\left(\mathbf{r}-\mathbf{T}\right). \tag{7.14}$$

This can then be substituted into (7.12) to produce a periodic equivalent, often termed *crystalline orbitals*,

$$\phi_i\left(\mathbf{r};\mathbf{k}\right) = \sum_{\mu} c_{\mu i}\left(\mathbf{k}\right)\omega_\mu\left(\mathbf{r};\mathbf{k}\right). \tag{7.15}$$

The self-consistent field equations can be derived for the periodic system using crystalline orbitals rather than molecular orbitals.

Whilst attempts to introduce external magnetic fields within periodic electronic structure calculations do exist,[311;312] it is a non-trivial theoretical exercise. In the preceding chapters it has been discussed how EFM can be applied to weakly bound molecular clusters however, sources throughout the literature demonstrate that EFMs can be readily applied to certain types of periodic systems, with some adaptations.[145;313–319] Therefore, the application of an LAO based EFM to molecular crystals is explored in the following chapter.

7.3.1 Extending EFM to Periodic Systems

Molecular crystals define a class of solids that constitute well-defined molecular units bound by weak interactions. They are common across many fields of chemistry from medical drugs,[320] to high pressure chemistry[321–325] and are often used as starting points for solid-state chemical reactions.[326] However, all electron periodic electronic structure theories can be complex and introducing external fields is non-trivial. A potentially more straightforward approach could be the extension of EFM to periodic molecular crystals. The benefit of this

type of periodic method, is that the individual monomer/dimer energies can be calculated using any non-periodic molecular electronic structure method, which in theory should include those derived to use LAOs for non-perturbative inclusions of external fields.

Adapted Many-Body Expansion

Molecular crystals can be defined as a supercell, or a periodic repetition of a specific arrangement of the molecules defining the unit cell of the system, as described above. The fragmentation then occurs within the periodically repeated unit cell, typically fragmenting the system within the unit cell according to the individual molecules which are bound by weak intermolecular interactions. The many-body expansion outlined and employed in the previous chapters, can be adapted to approximate the electronic energy per unit cell of a 3-dimensional, infinitely extended, periodic molecular crystal. For which, within the binary interaction approximation, is given by,

$$\begin{aligned} E^{\text{cell}} = &\sum_{i} E_{i(0)} + \sum_{i<j} \left(E_{i(0)j(0)} - E_{i(0)} - E_{j(0)} \right) \\ &+ \frac{1}{2} \sum_{\mathbf{n}\neq 0} \sum_{i,j} \left(E_{i(0)j(\mathbf{n})} - E_{i(0)} - E_{j(\mathbf{n})} \right) + E_{\text{LR}} \end{aligned} \tag{7.16}$$

where $E_{i(0)}$ is the energy of the i^{th} monomer in the central (0^{th}) unit cell, $E_{i(0)j(\mathbf{n})}$ is the energy of the dimer constructed from the i^{th} monomer in the central unit cell and the j^{th} monomer in the $\mathbf{n}^{\text{th}}$ unit cell, where $\mathbf{n}$ is a 3-dimensional index with origin at $\mathbf{0}$. E_{LR} is a classical long-range electrostatic energy correction. As introduced in the preceding chapters, all the individual energies are calculated in accordance to Eq. (3.2), including a self-consistently optimised dipole based embedding potential to account for the polarization or electrostatic induction effects. Within the work presented in this chapter the embedding potential is given by (3.7), and can contain the improvements depicted in chapter 3. Additionally, the corrections for BSSE defined in chapter 3 can also be included.

As demonstrated in chapter 4, EFM can be used to calculate derivatives of the total energy of the system. This can be applied to molecular crystal in a similar way, the first and second derivatives of the energy with respect to the atomic coordinates are given, within the binary interaction approximation, by,

$$\begin{aligned} \frac{\partial E^{\text{cell}}}{\partial x} = &\sum_{i} \frac{\partial E_{i(0)}}{\partial x} + \sum_{i<j} \left(\frac{\partial E_{i(0)j(0)}}{\partial x} - \frac{\partial E_{i(0)}}{\partial x} - \frac{\partial E_{j(0)}}{\partial x} \right) \\ &+ \frac{1}{2} \sum_{\mathbf{n}\neq 0} \sum_{i,j} \left(\frac{\partial E_{i(0)j(\mathbf{n})}}{\partial x} - \frac{\partial E_{i(0)}}{\partial x} - \frac{\partial E_{j(\mathbf{n})}}{\partial x} \right) + \frac{\partial E_{\text{LR}}}{\partial x}, \end{aligned} \tag{7.17}$$

$$\begin{aligned} \frac{\partial^2 E^{\text{cell}}}{\partial x \partial y} = &\sum_{i} \frac{\partial^2 E_{i(0)}}{\partial x \partial y} + \sum_{i<j} \left(\frac{\partial^2 E_{i(0)j(0)}}{\partial x \partial y} - \frac{\partial^2 E_{i(0)}}{\partial x \partial y} - \frac{\partial^2 E_{j(0)}}{\partial x \partial y} \right) \\ &+ \frac{1}{2} \sum_{\mathbf{n}\neq 0} \sum_{i,j} \left(\frac{\partial^2 E_{i(0)j(\mathbf{n})}}{\partial x \partial y} - \frac{\partial^2 E_{i(0)}}{\partial x \partial y} - \frac{\partial^2 E_{j(\mathbf{n})}}{\partial x \partial y} \right) + \frac{\partial^2 E_{\text{LR}}}{\partial x \partial y}. \end{aligned} \tag{7.18}$$

Additionally, when dealing with crystal structures, the derivative with respect to the lattice

parameters is often required, which can be formulated in the same way,

$$\frac{\partial E^{\text{cell}}}{\partial a} = \frac{1}{2}\sum_{\mathbf{n}}\sum_{i,j}\left(\frac{\partial E_{i(\mathbf{0})j(\mathbf{n})}}{\partial a} - \frac{\partial E_{j(\mathbf{n})}}{\partial a}\right) + \frac{\partial E_{\text{LR}}}{\partial a} \tag{7.19}$$

where a is a lattice constant along one of the Cartesian axes. Typically, when calculating energy derivatives within an EFM approach, the response of the self-consistent cell dipole moments and E_{LR} to the changes in atomic coordinates is considered negligible and neglected[142]. However, it has been shown that their response to changes in the lattice constants is non-negligible and therefore, is often included in some form.[315] In particular the response of the long range classical correction, E_{LR}, can have a significant contribution. Depending on the aim of the calculation, the variables x and y can be defined to represent either collective, in-phase coordinates or the individual atomic coordinates. A significant result of this is that derivatives of dipole moments and polarizabilities can be constructed from a similar analysis, overcoming the typical issues when defining these properties in solids,[313;327;328] providing a convenient method for calculating infrared and Raman intensities.

Once the total energy and its geometric derivatives have been calculated, standard solid state analysis can be performed, such as the evaluation of Gibbs energy,[314]

$$G = H_e + U_V - TS_V, \tag{7.20}$$

where H_e is the electronic enthalpy given by, $H_e = E^{\text{cell}} + pV$ where p is pressure and V the volume of the unit cell, U_V is the vibrational internal energy, T is the temperature and S_V is the entropy per unit cell. The values U_V and S_V are related to the partition function Z_V,

$$U_v = \frac{k_{\text{B}}T^2}{K}\frac{\partial Z_v}{\partial T}, \tag{7.21}$$

$$S_v = \frac{k_{\text{B}}T}{K}\frac{\partial \ln Z_V}{\partial T} + \frac{k_{\text{B}}}{K}\ln Z_V, \tag{7.22}$$

where K is the number of wave vectors in the reciprocal cell.

Long-Range Electrostatic Energy Correction

Within solid state electronic structure theory, it is often difficult to consider enough unit cells to effectively converge the energy per unit cell. To reduce the number of cells that are explicitly considered, a long-range electrostatic correction is often applied. Typically, this takes the form of the (long-range) Madelung constant, from which the electric potential V_i at point r_i due to all point charges within a lattice, can be determined,

$$V_i = \frac{e}{4\pi\epsilon_0 \mathbf{r}_0}\sum_{j\neq i}\frac{z_j \mathbf{r}_0}{r_{ij}} = \frac{e}{4\pi\epsilon_0 \mathbf{r}_0}m_i. \tag{7.23}$$

where m_i is the Madelung constant on the i^{th} charge. Within the EFM approach, the electrostatic potential due to the atoms within the unit cell has been determined as that due to the induced dipoles, which for the explicitly considered supercell, consisting of **M**

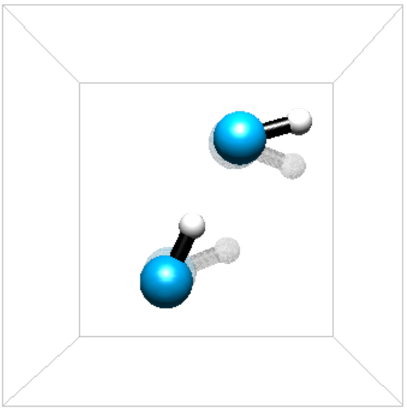

Figure 7.4: Initial (greyed out) and final geometry for two hydrogen fluoride molecules within a cubic unit cell of dimension 10 bohr, optimised with HF theory and the 3-21G basis set with a 1 dimensional supercell constructed from 5 unit cells.

unit cells, is included via Eq. (3.7). For E_{LR}, the Madelung constant can be considered as the electrostatic interaction between the dipole moments of the fragments within the central unit cell and those within a set of unit cells between **M** and a long-range supercell defined by **L**,[316]

$$E_{\mathrm{LR}} = \frac{1}{2}\sum_{\mathbf{n}=-\mathbf{L}}^{-\mathbf{M}-1} E_{\mathbf{n}}^{\mathrm{LR}} + \frac{1}{2}\sum_{\mathbf{n}=\mathbf{M}+1}^{\mathbf{L}} E_{\mathbf{n}}^{\mathrm{LR}}, \tag{7.24}$$

where,

$$E_{\mathbf{n}}^{\mathrm{LR}} = \sum_{i\in\mathbf{0}}\sum_{j\in\mathbf{n}}\left\{\frac{R_{ij}^2\mu_i\cdot\mu_j - 3\left(\mu_i\cdot\mathbf{R}_{ij}\right)\left(\mu_j\cdot\mathbf{R}_{ij}\right)}{4\pi\epsilon_0 R_{ij}^5}\right\} \tag{7.25}$$

7.3.2 Molecular Crystal Structure in External Magnetic Fields

As an example, this method has been applied to a linear chain of hydrogen fluoride molecules. The HF forces on each atom, calculated via Eq. (7.17), are shown in table 7.3 where the corresponding total energy per unit cell is -198.921696 E_h. The 3-21G basis was used, with a 1-dimensional supercell of length 5 in the x direction with a fixed cubic unit cell with dimensions 10 bohr, which is based of the optimised parameters found in Ref. 317. This structure was then optimised resulting in the structure shown in Fig. 7.4. From Ref. 317, a stack of linear chains of hydrogen fluoride molecules form a zig-zag structure. From Fig. 7.4, the hydrogen fluoride molecules do approach a zig-zag based structure but remain close to the gas phase optimisation therefore, implying that more unit cells or a more accurate consideration of the unit cell parameters, would be required to accurately generate the correct structure. This is not considered any further here however, using these results as a proof of concept, with more in depth analysis ongoing, including how a magnetic field will influence the equilibrium geometry.

When using calculations over periodic supercells, it is known that if the dimensions of the unit cell approach infinity the calculation should approach that of a gas phase calculation of the system within the unit cell. This is often used as a basic check when trying to determine the validity of periodic electronic structure codes. This has been carried out for the system of two hydrogen fluoride molecules and the cyclic water trimer from Fig. 3.1. For both systems, a cubic unit cell of dimension 1000 bohr reproduced the gas phase single point energy of -198.915337 E_h and -226.819908 E_h respectively and their gradient terms. This further remains true when applying an external magnetic field. For the same two systems, with an applied external magnetic field of $|\mathbf{B}| = 0.1$ a.u., the energy per unit cell returns the gas phase single point energies of -198.895491 E_h and -226.777606 E_h respectively as well as their respective first derivatives.

7.3.3 Limitations and Potential Extension To All Electron Periodic Methods

The EFM requires that the system being considered can be sensibly fragmented, which proves trivial for systems such as molecular crystals, but can prove more challenging for ionic or covalent crystals, metals or superconductors. This is not to say it is impossible[138;329–333] but does impose a limitation on the efficient applicability of the EFM. It is also an approximation, that will yield reasonable results however, it can still be advantageous to consider a full periodic electronic structure treatment. Additionally, having access to an all electron periodic electronic structure code, even at $|\mathbf{B}| = 0.0$ a.u., could provide a useful test mechanism when considering how appropriate the EFM based periodic method is. Periodic electronic structure methods are widely employed across many fields of research however, as previously stated, adapting them to include the effects of an external magnetic field is non-trivial. The remainder of this chapter presents some basic theoretical foundations for an all electronic periodic HF calculation, the implementation of which within QUEST is ongoing work, then outlines the problems which must be addressed to construct an LAO based periodic HF approach.

Periodic RHF

A linear combination of crystalline orbitals, constructed from atom centred Gaussian type orbitals is given by Eq. (7.15). The orbital coefficients and energy bands, $\mathcal{E}_p$, where p is the band index, are determined through the HF Roothaan-Hall equations, as introduced

	Position / a_0			q	Force / $E_h a_0^{-1}$		
Atom	x	y	z		x	y	z
F1	2.14103	0.94562	0.00000		0.027491	-0.017696	0.00000
H2	3.80225	0.27553	0.00000		0.002763	-0.022810	0.00000
F3	0.25130	-2.83535	0.00000		0.049990	0.006223	0.00000
H4	1.91252	-2.16526	0.00000		0.043935	0.015633	0.00000

Table 7.3: Forces on each of the four atoms within the unit cell given in $E_h a_0^{-1}$

in chapter 2.1.3,

$$\sum_{\nu} F_{\mu\mathbf{k}}^{\nu\mathbf{k}} C_{p\mathbf{k}}^{\nu\mathbf{k}} = \mathcal{E}_{p\mathbf{k}} \sum_{\nu} S_{\mu\mathbf{k}}^{\nu\mathbf{k}} C_{p\mathbf{k}}^{\nu\mathbf{k}}. \tag{7.26}$$

The Fock, F and overlap matrices, S, can be obtained directly from their AO-based expressions as,

$$F_{\mu\mathbf{k}}^{\nu\mathbf{k}} = \sum_{\mathbf{n}=-\mathbf{L}}^{\mathbf{L}} F_{\mu(\mathbf{0})\nu(\mathbf{n})} \exp\left(i\mathbf{k}\cdot\mathbf{r}_{\mathbf{n}}\right), \tag{7.27}$$

$$S_{\mu\mathbf{k}}^{\nu\mathbf{k}} = \sum_{\mathbf{n}=-\mathbf{S}}^{\mathbf{S}} S_{\mu(\mathbf{0})\nu(\mathbf{n})} \exp\left(i\mathbf{k}\cdot\mathbf{r}_{\mathbf{n}}\right), \tag{7.28}$$

where $S_{\mu(\mathbf{0})\nu(\mathbf{n})}$ is the overlap integral of the μ^{th} and ν^{th} AOs from the $\mathbf{0}^{\text{th}}$ and $\mathbf{n}^{\text{th}}$ unit cells respectively,

$$S_{\mu(\mathbf{0})\nu(\mathbf{n})} = \int \chi_{\mu(\mathbf{0})}^{*}(\mathbf{r})\,\chi_{\nu(\mathbf{n})}(\mathbf{r})\,d\mathbf{r}. \tag{7.29}$$

The supercell is defined by **L** with **S** defining a short-range cut-off which is typically noticeably smaller due to the rapid decay of the Gaussian functions of the AOs. This can all be carried out in the same manner as with standard RHF theory discussed in chapter 2.

Extension to Arbitrary Magnetic Fields

Adapting this method to include an LAO based treatment of an arbitrary strength magnetic field is not a straightforward task. This is due to the fact that we deal with the external field explicitly within the Hamiltonian according to Eq. (2.183). This results in a Hamiltonian whose periodicity is no longer solely dependent on the external potential $v(\mathbf{r})$ therefore, our definition of crystalline orbitals based on Bloch functions, Eq. 7.11, is no longer appropriate. A method for dealing with both the periodicity of the external field as well the crystal itself must be designed. In work by Lee, Cai and Galli[311;312] they describe the so-called *magnetic periodic boundary conditions* (MPBC) for which the wavefunction of the periodic system is written as,

$$\Psi(\mathbf{r}-\mathbf{T}) = \left[i\frac{e}{\hbar}\mathbf{A}(\mathbf{T})\cdot\mathbf{r} - i\mathbf{k}\cdot\mathbf{T}\right]\cdot\Psi(\mathbf{r}-\mathbf{T}). \tag{7.30}$$

Within their work they implement this approach for *ab initio* calculations on periodic supercells using a plane wave approach. The next steps therefore, would be to extend this approach to atom centred LAOs.

8 Conclusions and Future Work

An implementation of the embedded fragment method has been presented and combined with recent advances in non-perturbative electronic structure methods for calculations within arbitrary strength magnetic fields. It has been shown that this approach retains the same level of accuracy when an external magnetic field is applied to the given system. It has also been shown to retain the general computational advantages of fragmentation-based approaches, reproducing the expected reduction in computational scaling - to $O\left(N^2\right)$ for the binary interaction approximation. The presented implementation takes full advantage of the embarrassingly parallel nature of the embedded fragment method, whilst also including several other cost saving approximations, potentially reproducing the near linear scaling that this method has been shown to achieve.

In the limit of very large systems, a known flaw in the dipole based embedding potential was observed, causing convergence issues in fragment pair calculations. Whilst corrections for this exist they typically involve introducing additional terms to the potential, impacting its computational cost. A new method for addressing the issues has been proposed, presenting an effective and lower cost improvement to the dipole based potential. The error analysis for the new attenuated dipole based potential seems to suggest that this method could be optimised to significantly reduce, the error in the binary interaction approximation. This requires a more thorough analysis particularly with extension to much larger clusters.

This new implementation of EFM was applied to a large water cluster, to demonstrate how it can be used to develop an understanding of how external magnetic fields influence intermolecular interactions in large or even bulk systems. It is important to note that a conventional calculation on the $(H_2O)_{103}$ cluster with the largest basis set used (aug-cc-pVTZ) would require an LAO-based calculation with over 12,000 basis functions. Calculations on this scale are simply not feasable with any current implementation of the utilised LAO based methods, therefore highlighting the benefits of using EFM. The results showed agreement with experimental observations showing that the intermolecular binding is strengthened by the external field. However, they also highlighted how the change in the intermolecular interactions is due to complex responses to the external field and therefore, is difficult to explicitly quantify in terms of simply a strengthening of the existing hydrogen bonding network. Further investigations on how the electronic density responds to the external field would help improve the understanding of where this increased intermolecular interaction strength originates. In particular studies that include the response of the geometric structure of the systems must be considered.

Chapter 4 expanded on the foundations set out in chapter 3, implementing the calculation of the first derivatives of the total energy with respect to the positions of the nuclei. This required modification of existing derivative algorithms implemented within QUEST, including modifying existing nuclear attraction integral derivatives to include the

response due to the embedding potential term. However, the response of the external potential itself was considered negligible and therefore, not required. The calculation of the EFM derivatives is efficiently implemented making use of its inherent parallel nature, enabling the application of the derivative calculations for increasingly large systems. This was incorporated into the *quasi*-Newton geometry optimiser within QUEST, creating an approach to perform EFM based geometry optimisations on large molecular clusters within arbitrary strength magnetic fields. A comparison is made for the cyclic water trimer introduced in chapter 3, whereby its geometry was further optimised at the DFT theory level with and without the approximation of the EFM. This was done at zero field and in a strong magnetic field strength of $|\mathbf{B}| = 0.1$ a.u. $= 23500$ T. From this comparison its clear that the EFM is an approximate method, particularly with the further caveat that the gradient of the embedding potential is not considered here in line with previous implementations of EFM based energy derivatives. However, it does present a reasonable accuracy for the geometry optimisation of the water trimer. Therefore, the real purpose of this method is then showcased with the optimisation of a $(H_2O)_{21}$ cluster at the same two field strengths. This presents an efficient method for scaling up geometry optimisations and potentially property calculations on increasingly large molecular clusters.

Chapter 5 presents a suite of tools to analyse the complex current vector field induced by exposing a molecule to an external field. This includes the well-established 2D planar Gaussian-Legendre quadrature approach as well as a new disc-based quadrature for analysing bond currents. It has been demonstrated that, for a range of planar ring systems, the qualitative insights offered by this procedure mirror those of the 2D planar Gauss-Legendre quadrature. Furthermore, the bond currents were shown to provide an accurate distillation of the complex features of the current density to simple chemical diagrams. A key advantage of the proposed disc quadrature is its applicability to 3D structures. This was demonstrated for the ring, bowl and cage isomers of the C_{20} molecule, in which the disc quadratures remain well-defined and deliver bond currents that match with expectations based on the symmetry of these systems. The flexibility of our implementation for open-shell systems and excited states was demonstrated for the benzene molecule in its ground and first excited state, the former having aromatic character and the latter having strongly anti-aromatic character. Finally, the utility of these tools for the analysis of magnetically induced currents was demonstrated for the BH molecule. At weak fields the currents reflect those obtained from the analysis in using response theory. At higher fields, the currents reflect the transition from para- to dia-magnetism, an effect that cannot be visualised using the linear-response approach to study magnetically induced current susceptibilities.

Throughout the completion of this work many software programs were utilised, however, the need for a more suitable and adaptable molecular viewing and editing package became clear. The successful development of a fully featured molecular viewer has directly fed into all other chapters within this work. All the figures of 3D molecular structures and properties, excluding those presented in Chapter 5, have been produced via the QuestView software package. It has also streamlined the general workflow when working with the EFM within QUEST, enabling quick and accessible generation of complex input files, containing specific fragmentation and fragment properties, as well as visualisation of outputs. It has been

efficiently implemented for full cross-platform support thanks to the OpenGL graphics API and includes direct integration with the QUEST electronic structure program and the Open Babel chemistry toolbox. There are still many features that are yet to be implemented within QuestView, with aims of adapting it for both teaching and research. With further development still underway, it may potentially become a worthy competitor against more established software options within the near future. A particular goal is to make it easily extensible by community contributions particularly since it uses the python framework.

Due to the adaptability of the EFM its applications extend well beyond the scope of what has presently been discussed. Therefore, within Chapter 7 several extensions to the EFM and how they are being implemented within an LAO based framework is discussed. This chapter therefore, focuses on ongoing and future work based on the foundations provided within this thesis. Chapter 4 describes how the EFM can be used to calculate energy derivative-based properties such as the forces on the atoms within a given system. In Chapter 7 this is extended to include the calculation of NMR shielding constants and excitation energies. NMR shielding constants can be calculated through the second derivative of the energy with respect to the magnetic moment and the external magnetic field. This presents a potential method for the treatment of explicit solvent interactions and is therefore demonstrated for several molecules dissolved in water. These results are compared with experimental results as well as calculations in the gas phase and calculations utilising the IEM-PCM approximate solvation method. From the results it can be observed that the EFM reproduced the correct direction of the shift in NMR shielding constants, however, the results presented here do not show an improvement over existing approximate solvation-based methods. This could be due to inaccurate geometries for the solvation shells, therefore, future work should consider the use of a more accurate optimisation method, such as that defined in chapter 4.

Also briefly discussed within chapter 7, is the possibility of calculating excitation energies with the EFM. A brief analysis of how excitation energies can be affected by both chemical environment and an external field, with particular interest in the interplay between both environmental factors. The results show a significant change in the observed excitations for a water molecule when changing both its chemical and physical environment. This demonstrates how useful an approach the EFM could be for conducting a more in depth analysis on how excitation energies are influenced by a molecule's environment, without looking at much more computationally challenging approaches. The full implementation of EFM excited state calculations within arbitrary strength magnetic fields is ongoing.

The extension of EFM for periodic crystals has additionally been implemented for calculation of total unit cell energies as well as the first derivatives of the energy with respect to the geometry of the system within the unit cell, and is presented in chapter 7. This method once again makes use of the embarrassingly parallel nature of the EFM in analogy to the molecular clusters approach depicted in chapter 3, to enable the more efficient calculation of unit cell energies and derivatives. In this implementation the dipole based embedding potential defined in chapter 3, is used and extended such that the self-consistent dipoles of the unit cell are additionally used to create a long range electrostatic energy

correction term. The next steps in building upon this work involve completing the energy derivatives implementation enabling the geometrical optimisation of the lattice parameters of the unit cell. Whilst the current implementation enables the optimisation of the crystal structure with a fixed unit cell volume, to enable full crystal structure optimisation, the derivative with respect to the lattice constants would need to be implemented. This could then be extended to calculating useful properties of periodic crystals. In addition to the periodic EFM approach a brief discussion of an all electron periodic HF theory approach is presented, alongside an introductory discussion of the ongoing work to extend this to arbitrary magnetic fields. This is in the early stages of development but would present a nice suite of tools for analysing periodic systems with external fields as well as providing a benchmark method for comparison with the periodic EFM.

Bibliography

[1] W. Kohn. 'Density functional theory for systems of very many atoms.' *International Journal of Quantum Chemistry*, **56**, 229–232, 1995.

[2] M. Head-Gordon. 'Multiscale Modeling and Analysis of Microtubule Self-Assembly Dynamics.' *Journal Physical Chemistry*, **100**, 13213–13225, 1996.

[3] J. Almlöf, K. Faegri, and K. Korsell. 'Principles for a direct SCF approach to LICAO - MO *ab - initio* calculations.' *Journal of Computational Chemistry*, **3**, 385–399, 1982.

[4] S. Reine, E. Tellgren, A. Krapp, T. Kjærgaard, T. Helgaker, B. Jansik, S. Høst, and P. Salek. 'Variational and robust density fitting of four-center two-electron integrals in local metrics.' *The Journal of Chemical Physics*, **129**, 104101, 2008.

[5] F. Neese, F. Wennmohs, A. Hansen, and U. Becker. 'Efficient, approximate and parallel Hartree–Fock and hybrid DFT calculations. A 'chain-of-spheres' algorithm for the Hartree–Fock exchange.' *Chemical Physics*, **356**, 98–109, 2009.

[6] T. M. Henderson. 'Embedding wave function theory in density functional theory.' *The Journal of Chemical Physics*, **125**, 014105, 2006.

[7] T. Dresselhaus and J. Neugebauer. 'Part and whole in wavefunction/DFT embedding.' *Theoretical Chemistry Accounts*, **134**, 97, 2015.

[8] S. J. R. Lee, M. Welborn, F. R. Manby, and T. F. Miller. 'Projection-Based Wavefunction-in-DFT Embedding.' *Accounts of Chemical Research*, **52**, 1359–1368, 2019.

[9] M. S. Gordon, D. G. Fedorov, S. R. Pruitt, and L. V. Slipchenko. 'Fragmentation Methods: A Route to Accurate Calculations on Large Systems.' *Chemical Reviews*, **112**, 632–672, 2012.

[10] G. A. Cisneros, K. T. Wikfeldt, L. Ojamäe, J. Lu, Y. Xu, H. Torabifard, A. P. Bartók, G. Csányi, V. Molinero, and F. Paesani. 'Modeling Molecular Interactions in Water: From Pairwise to Many-Body Potential Energy Functions.' *Chemical Reviews*, **116**, 7501–7528, 2016.

[11] R. M. Richard, K. U. Lao, and J. M. Herbert. 'Aiming for Benchmark Accuracy with the Many-Body Expansion.' *Accounts of Chemical Research*, **47**, 2828–2836, 2014.

[12] E. I. Tellgren, A. Soncini, and T. Helgaker. 'Nonperturbative ab initio calculations in strong magnetic fields using London orbitals.' *Journal of Chemical Physics*, **129**, 154114, 2008.

[13] E. I. Tellgren, T. Helgaker, and A. Soncini. 'Non-perturbative magnetic phenomena in closed-shell paramagnetic molecules.' *Physical Chemistry Chemical Physics*, **11**, 5489–5498, 2009.

[14] E. I. Tellgren, S. Kvaal, E. Sagvolden, U. Ekström, A. M. Teale, and T. Helgaker. 'Choice of basic variables in current-density-functional theory.' *Physical Review A*, **86**, 062506, 2012.

[15] E. I. Tellgren, A. M. Teale, J. W. Furness, K. K. Lange, U. Ekström, and T. Helgaker. 'Non-perturbative calculation of molecular magnetic properties within current-density functional theory.' *Journal of Chemical Physics*, **140**, 034101, 2014.

[16] S. Stopkowicz, J. Gauss, K. K. Lange, E. I. Tellgren, and T. Helgaker. 'Coupled-cluster theory for atoms and molecules in strong magnetic fields.' *The Journal of Chemical Physics*, **143**, 074110, 2015.

[17] S. Sun, D. Williams-Young, and X. Li. 'An ab Initio Linear Response Method for Computing Magnetic Circular Dichroism Spectra with Nonperturbative Treatment of Magnetic Field.' *Journal of Chemical Theory and Computation*, **15**, 3162–3169, 2019.

[18] S. Sun, D. B. Williams-Young, T. F. Stetina, and X. Li. 'Generalized Hartree–Fock with Nonperturbative Treatment of Strong Magnetic Fields: Application to Molecular Spin Phase Transitions.' *Journal of Chemical Theory and Computation*, **15**, 348–356, 2019.

[19] J. W. Furness, J. Verbeke, E. I. Tellgren, S. Stopkowicz, U. Ekström, T. Helgaker, and A. M. Teale. 'Current Density Functional Theory Using Meta-Generalized Gradient Exchange-Correlation Functionals.' *Journal of Chemical Theory and Computation*, **11**, 4169–4181, 2015.

[20] F. Hampe and S. Stopkowicz. 'Equation-of-motion coupled-cluster methods for atoms and molecules in strong magnetic fields.' *The Journal of Chemical Physics*, **146**, 154105, 2017.

[21] S. Reimann, A. Borgoo, J. Austad, E. I. Tellgren, A. M. Teale, T. Helgaker, and S. Stopkowicz. 'Kohn–Sham energy decomposition for molecules in a magnetic field.' *Molecular Physics*, **117**, 97–109, 2019.

[22] M. Wibowo, T. J. P. Irons, and A. M. Teale. 'Modeling Ultrafast Electron Dynamics in Strong Magnetic Fields Using Real-Time Time-Dependent Electronic Structure Methods.' *Journal of Chemical Theory and Computation*, **17**, 2137–2165, 2021.

[23] T. J. Irons, J. Zemen, and A. M. Teale. 'Efficient Calculation of Molecular Integrals over London Atomic Orbitals.' *Journal of Chemical Theory and Computation*, **13**, 3636–3649, 2017.

[24] T. J. P. Irons, G. David, and A. M. Teale. 'Optimizing Molecular Geometries in Strong Magnetic Fields.' *Journal of Chemical Theory and Computation*, **17**, 2166–2185, 2021.

[25] G. David, T. J. P. Irons, A. E. A. Fouda, J. W. Furness, and A. M. Teale. 'Self-Consistent Field Methods for Excited States in Strong Magnetic Fields: a Comparison between Energy- and Variance-Based Approaches.' *Journal of Chemical Theory and Computation*, **17**, 5492–5508, 2021.

[26] M. J. Pemberton, T. J. P. Irons, T. Helgaker, and A. M. Teale. 'Revealing the exotic structure of molecules in strong magnetic fields.' *The Journal of Chemical Physics*, **156**, 204113, 2022.

[27] J. R. P. Angel and J. D. Landstreet. 'A Determination by the Zeeman Effect of the Magnetic Field Strength in the White Dwarf G99-37.' *The Astrophysical Journal*, **191**, 457, 1974.

[28] J. R. P. Angel. 'Magnetism in white dwarfs.' *The Astrophysical Journal*, **216**, 1, 1977.

[29] M. Ivanov. 'Hartree-Fock calculation of the $1s^2 2s^2$ state of the Be atom in external magnetic fields from $\gamma = 0$ up to $\gamma = 1000$.' *Physics Letters A*, **239**, 72–80, 1998.

[30] M. V. Ivanov and P. Schmelcher. 'Ground state of the lithium atom in strong magnetic fields.' *Physical Review A*, **57**, 3793–3800, 1998.

[31] M. V. Ivanov and P. Schmelcher. 'Ground state of the carbon atom in strong magnetic fields.' *Physical Review A*, **60**, 3558–3568, 1999.

[32] LONDON. 'A quantum chemistry program for plane–wave/GTO hybrid basis sets and finite magnetic field calculations.'

[33] BAGEL. 'Brilliantly Advanced General Electronic-structure Library. Available at http://www.nubakery.org under the GNU General Public License.'

[34] 'TURBOMOLE V7.3 2018, a development of University of Karlsruhe and Forschungszentrum Karlsruhe GmbH, 1989-2007, TURBOMOLE GmbH, since 2007; available from
`http://www.turbomole.com.`'

[35] 'QUEST; A rapid development platform for Quantum Electronic Structure Techniques. http://quest.codes.', since 2017.

[36] D. B. Williams-Young, A. Petrone, S. Sun, T. F. Stetina, P. Lestrange, C. E. Hoyer, D. R. Nascimento, L. Koulias, A. Wildman, J. Kasper, J. J. Goings, F. Ding, A. E. DePrince, E. F. Valeev, and X. Li. 'The Chronus Quantum software package.' *WIREs Computational Molecular Science*, **10**, 2020.

[37] K. K. Lange, E. I. Tellgren, M. R. Hoffmann, and T. Helgaker. 'A Paramagnetic Bonding Mechanism for Diatomics in Strong Magnetic fields.' *Science*, **337**, 327–331, 2012.

[38] M. Iwasaka and S. Ueno. 'Structure of water molecules under 14 T magnetic field.' *Journal of Applied Physics*, **83**, 6459–6461, 1998.

[39] H. Hosoda, H. Mori, N. Sogoshi, A. Nagasawa, and S. Nakabayashi. 'Refractive indices of water and aqueous electrolyte solutions under high magnetic fields.' *Journal of Physical Chemistry A*, **108**, 1461–1464, 2004.

[40] M. C. Amiri and A. A. Dadkhah. 'On reduction in the surface tension of water due to magnetic treatment.' *Colloids and Surfaces A: Physicochemical and Engineering Aspects*, **278**, 252–255, 2006.

[41] L. Holysz, A. Szczes, and E. Chibowski. 'Effects of a static magnetic field on water and electrolyte solutions.' *Journal of Colloid and Interface Science*, **316**, 996–1002, 2007.

[42] E. J. Toledo, T. C. Ramalho, and Z. M. Magriotis. 'Influence of magnetic field on physical-chemical properties of the liquid water: Insights from experimental and theoretical models.' *Journal of Molecular Structure*, **888**, 409–415, 2008.

[43] R. Cai, H. Yang, J. He, and W. Zhu. 'The effects of magnetic fields on water molecular hydrogen bonds.' *Journal of Molecular Structure*, **938**, 15–19, 2009.

[44] M. Iino and Y. Fujimura. 'Surface tension of heavy water under high magnetic fields.' *Applied Physics Letters*, **94**, 261902, 2009.

[45] Y. Wang, B. Zhang, Z. Gong, K. Gao, Y. Ou, and J. Zhang. 'The effect of a static magnetic field on the hydrogen bonding in water using frictional experiments.' *Journal of Molecular Structure*, **1052**, 102–104, 2013.

[46] Y. Wang, H. Wei, and Z. Li. 'Effect of magnetic field on the physical properties of water.' *Results in Physics*, **8**, 262–267, 2018.

[47] S. Kobe, G. D. Z. C. A, P. J. Mcguiness, and J. S. Z. Sar. 'The influence of the magnetic field on the crystallisation form of calcium carbonate and the testing of a magnetic water-treatment device.' *Journal of Magnetism and Magnetic Materials*, **236**, 71–76, 2001.

[48] B. Liu, B. Gao, X. Xu, W. Hong, Q. Yue, Y. Wang, and Y. Su. 'The combined use of magnetic field and iron-based complex in advanced treatment of pulp and paper wastewater.' *Chemical Engineering Journal*, **178**, 232–238, 2011.

[49] H. Wei, Y. Wang, and J. Luo. 'Influence of magnetic water on early-age shrinkage cracking of concrete.' *Construction and Building Materials*, **147**, 91–100, 2017.

[50] E. Schrödinger. 'Quantisierung als eigenwertproblem.' *Annalen der Physik*, **384**, 361–376, 1926.

[51] M. Born and R. Oppenheimer. 'Zur Quantentheorie der Molekeln.' *Annalen der Physik*, **389**, 457–484, 1927.

[52] D. R. Hartree. 'The Wave Mechanics of an Atom with a Non-Coulomb Central Field. Part I. Theory and Methods.' *Mathematical Proceedings of the Cambridge Philosophical Society*, **24**, 89–110, 1928.

[53] C. C. J. Roothaan. 'Self-Consistent Field Theory for Open Shells of Electronic Systems.' *Reviews of Modern Physics*, **32**, 179–185, 1960.

[54] C. C. J. Roothaan. 'New Developments in Molecular Orbital Theory.' *Reviews of Modern Physics*, **23**, 69–89, 1951.

[55] G. G. Hall. 'The molecular orbital theory of chemical valency VIII. A method of calculating ionization potentials.' *Proceedings of the Royal Society of London. Series A. Mathematical and Physical Sciences*, **205**, 541–552, 1951.

[56] P.-O. Löwdin. 'Exchange, Correlation, and Spin Effects in Molecular and Solid-State Theory.' *Reviews of Modern Physics*, **34**, 80–87, 1962.

[57] R. Nesbet. 'Configuration interaction in orbital theories.' *Proceedings of the Royal Society of London. Series A. Mathematical and Physical Sciences*, **230**, 312–321, 1955.

[58] R. J. Bartlett. 'Many-Body Perturbation Theory and Coupled Cluster Theory for Electron Correlation in Molecules.' *Annual Review of Physical Chemistry*, **32**, 359–401, 1981.

[59] J. Čížek. 'On the Correlation Problem in Atomic and Molecular Systems. Calculation of Wavefunction Components in Ursell-Type Expansion Using Quantum-Field Theoretical Methods.' *The Journal of Chemical Physics*, **45**, 4256–4266, 1966.

[60] J. Čížek and J. Paldus. 'Correlation problems in atomic and molecular systems III. Rederivation of the coupled-pair many-electron theory using the traditional quantum chemical methods.' *International Journal of Quantum Chemistry*, **5**, 359–379, 1971.

[61] J. Paldus, J. Čížek, and I. Shavitt. 'Correlation Problems in Atomic and Molecular Systems. IV. Extended Coupled-Pair Many-Electron Theory and Its Application to the BH_3 Molecule.' *Physical Review A*, **5**, 50–67, 1972.

[62] G. D. Purvis and R. J. Bartlett. 'A full coupled-cluster singles and doubles model: The inclusion of disconnected triples.' *The Journal of Chemical Physics*, **76**, 1910–1918, 1982.

[63] C. Møller and M. S. Plesset. 'Note on an Approximation Treatment for Many-Electron Systems.' *Physical Review*, **46**, 618–622, 1934.

[64] P. Hohenberg and W. Kohn. 'Inhomogeneous Electron Gas.' *Physical Review*, **136**, 864–871, 1964.

[65] M. Levy. 'Electron densities in search of Hamiltonians.' *Physical Review A*, **26**, 1200–1208, 1982.

[66] E. H. Lieb. 'Density functionals for coulomb systems.' *International Journal of Quantum Chemistry*, **24**, 243–277, 1983.

[67] H. Eschrig. *The Fundamentals of Density Functional Theory*, volume 32. Vieweg+Teubner Verlag, 1996.

[68] T. Helgaker, P. Jorgensen, and J. Olsen. *Density-Functional Theory: A Convex Treatment*. Wiley, 2023.

[69] W. Kohn and L. Sham. 'Self-Consistent Equations Including Exchange and Correlation Effects.' *Physical Review*, **140**, 1133–1138, 1965.

[70] P. E. Lammert. 'Differentiability of Lieb functional in electronic density functional theory.' *International Journal of Quantum Chemistry*, **107**, 1943–1953, 2007.

[71] S. Kvaal, U. Ekström, A. M. Teale, and T. Helgaker. 'Differentiable but exact formulation of density-functional theory.' *The Journal of Chemical Physics*, **140**, 18A518, 2014.

[72] E. H. Lieb and S. Oxford. 'Improved lower bound on the indirect Coulomb energy.' *International Journal of Quantum Chemistry*, **19**, 427–439, 1981.

[73] J. Sun, A. Ruzsinszky, and J. Perdew. 'Strongly Constrained and Appropriately Normed Semilocal Density Functional.' *Physical Review Letters*, **115**, 036402, 2015.

[74] J. Sun, R. C. Remsing, Y. Zhang, Z. Sun, A. Ruzsinszky, H. Peng, Z. Yang, A. Paul, U. Waghmare, X. Wu, M. L. Klein, and J. P. Perdew. 'Accurate first-principles structures and energies of diversely bonded systems from an efficient density functional.' *Nature Chemistry*, **8**, 831–836, 2016.

[75] A. P. Bartók and J. R. Yates. 'Regularized SCAN functional.' *The Journal of Chemical Physics*, **150**, 161101, 2019.

[76] D. M. Ceperley and B. J. Alder. 'Ground State of the Electron Gas by a Stochastic Method.' *Physical Review Letters*, **45**, 566–569, 1980.

[77] S. H. Vosko, L. Wilk, and M. Nusair. 'Accurate spin-dependent electron liquid correlation energies for local spin density calculations: a critical analysis.' *Canadian Journal of Physics*, **58**, 1200–1211, 1980.

[78] A. D. Becke. 'Density-functional exchange-energy approximation with correct asymptotic behavior.' *Physical Review A*, **38**, 3098–3100, 1988.

[79] J. Tao, J. P. Perdew, V. N. Staroverov, and G. E. Scuseria. 'Climbing the Density Functional Ladder: Nonempirical Meta–Generalized Gradient Approximation Designed for Molecules and Solids.' *Physical Review Letters*, **91**, 146401, 2003.

[80] J.-D. Chai and M. Head-Gordon. 'Long-range corrected hybrid density functionals with damped atom-atom dispersion corrections.' *Physical Chemistry Chemical Physics*, **10**, 6615, 2008.

[81] A. D. Becke. 'Density-functional thermochemistry. III. The role of exact exchange.' *The Journal of Chemical Physics*, **98**, 5648–5652, 1993.

[82] C. Lee, W. Yang, and R. G. Parr. 'Development of the Colle-Salvetti correlation-energy formula into a functional of the electron density.' *Physical Review B*, **37**, 785–789, 1988.

[83] R. Ditchfield, D. P. Miller, and J. A. Pople. 'Self-consistent Molecular-orbital methods. VII. Convergence of gaussian expansions of Slater-type atomic orbitals in calculations of First- And Second-order properties.' *The Journal of Chemical Physics*, **53**, 613–619, 1970.

[84] R. Ditchfield. 'Self-consistent perturbation theory of diamagnetism.' *Molecular Physics*, **27**, 789–807, 1974.

[85] J. R. Cheeseman, G. W. Trucks, T. A. Keith, and M. J. Frisch. 'A comparison of models for calculating nuclear magnetic resonance shielding tensors.' *The Journal of Chemical Physics*, **104**, 5497–5509, 1996.

[86] F. London. 'Théorie quantique des courants interatomiques dans les combinaisons aromatiques.' *Journal de Physique et le Radium*, **8**, 397–409, 1937.

[87] G. G. Hall. 'Gauge invariant gaussian orbitals and the ab initio calculation of diamagnetic susceptibility for molecules.' *International Journal of Quantum Chemistry*, **7**, 15–25, 1973.

[88] S. T. Epstein. 'Gauge invariance, current conservation, and GIAO's.' *The Journal of Chemical Physics*, **58**, 1592–1595, 1973.

[89] K. Wolinski, J. F. Hinton, and P. Pulay. 'Efficient implementation of the gauge-independent atomic orbital method for NMR chemical shift calculations.' *Journal of the American Chemical Society*, **112**, 8251–8260, 1990.

[90] W. Pauli. 'Zur Quantenmechanik des magnetischen Elektrons.' *Zeitschrift für Physik*, **43**, 601–623, 1927.

[91] R. Ditchfield, D. P. Miller, and J. A. Pople. 'Self-Consistent Molecular Orbital Methods. XI. Molecular Orbital Theory of NMR Chemical Shifts.' *The Journal of Chemical Physics*, **54**, 4186–4193, 1971.

[92] R. Ditchfield. 'Molecular Orbital Theory of Magnetic Shielding and Magnetic Susceptibility.' *The Journal of Chemical Physics*, **56**, 5688–5691, 1972.

[93] R. Ditchfield. 'On molecular orbital theories of NMR chemical shifts.' *Chemical Physics Letters*, **15**, 203–206, 1972.

[94] C. J. Grayce and R. A. Harris. 'Magnetic-field density-functional theory.' *Physical Review A*, **50**, 3089–3095, 1994.

[95] F. R. Salsbury and R. A. Harris. 'The current in magnetic field density functional theory and its application to the chemical shielding and magnetic susceptibility.' *The Journal of Chemical Physics*, **107**, 7350–7359, 1997.

[96] G. Vignale and M. Rasolt. 'Density-functional theory in strong magnetic fields.' *Physical Review Letters*, **59**, 2360–2363, 1987.

[97] G. Vignale and M. Rasolt. 'Current- and spin-density-functional theory for inhomogeneous electronic systems in strong magnetic fields.' *Physical Review B*, **37**, 10685–10696, 1988.

[98] X.-Y. Pan and V. Sahni. 'Density and physical current density functional theory.' *International Journal of Quantum Chemistry*, **110**, 2833–2843, 2010.

[99] X.-Y. Pan and V. Sahni. 'Generalization of the Hohenberg–Kohn theorem to the presence of a magnetostatic field.' *Journal of Physics and Chemistry of Solids*, **73**, 630–634, 2012.

[100] G. Diener. 'Current-density-functional theory for a nonrelativistic electron gas in a strong magnetic field.' *Journal of Physics: Condensed Matter*, **3**, 9417–9428, 1991.

[101] S. Kvaal, A. Laestadius, E. Tellgren, and T. Helgaker. 'Lower Semicontinuity of the Universal Functional in Paramagnetic Current–Density Functional Theory.' *The Journal of Physical Chemistry Letters*, **12**, 1421–1425, 2021.

[102] A. M. Lee, S. M. Colwell, and N. C. Handy. 'The calculation of magnetisabilities using current density functional theory.' *Chemical Physics Letters*, **229**, 225–232, 1994.

[103] A. M. Lee, N. C. Handy, and S. M. Colwell. 'The density functional calculation of nuclear shielding constants using London atomic orbitals.' *The Journal of Chemical Physics*, **103**, 10095–10109, 1995.

[104] E. Orestes, T. Marcasso, and K. Capelle. 'Density-functional calculation of ionization energies of current-carrying atomic states.' *Physical Review A*, **68**, 022105, 2003.

[105] J. Tao. 'Explicit inclusion of paramagnetic current density in the exchange-correlation functionals of current-density functional theory.' *Physical Review B*, **71**, 205107, 2005.

[106] J. Tao and G. Vignale. 'Analytic expression for the diamagnetic susceptibility of a uniform electron gas.' *Physical Review B*, **74**, 193108, 2006.

[107] K. Higuchi and M. Higuchi. 'Vorticity expansion approximation of the exchange-correlation energy functional in current density functional theory.' *Physical Review B*, **74**, 195122, 2006.

[108] M. Higuchi and K. Higuchi. 'Evaluation of vorticity expansion approximation of current-density functional theory by means of Levy's asymptotic bound.' *Physical Review B*, **75**, 195114, 2007.

[109] A. D. Becke. 'Current-density dependent exchange-correlation functionals.' *Canadian Journal of Chemistry*, **74**, 995–997, 1996.

[110] S. Pittalis, S. Kurth, S. Sharma, and E. K. U. Gross. 'Orbital currents in the Colle-Salvetti correlation energy functional and the degeneracy problem.' *The Journal of Chemical Physics*, **127**, 124103, 2007.

[111] J. F. Dobson. 'Spin-density functionals for the electron correlation energy with automatic freedom from orbital self-interaction.' *Journal of Physics: Condensed Matter*, **4**, 7877–7890, 1992.

[112] J. F. Dobson. 'Alternative expressions for the Fermi hole curvature.' *The Journal of Chemical Physics*, **98**, 8870–8872, 1993.

[113] J. Tao and J. P. Perdew. 'Nonempirical Construction of Current-Density Functionals from Conventional Density-Functional Approximations.' *Physical Review Letters*, **95**, 196403, 2005.

[114] A. Pausch and W. Klopper. 'Efficient evaluation of three-centre two-electron integrals over London orbitals.' *Molecular Physics*, **118**, e1736675, 2020.

[115] S. Blaschke and S. Stopkowicz. 'Cholesky decomposition of complex two-electron integrals over GIAOs: Efficient MP2 computations for large molecules in strong magnetic fields.' *The Journal of Chemical Physics*, **156**, 044115, 2022.

[116] J. L. Whitten. 'Coulombic potential energy integrals and approximations.' *The Journal of Chemical Physics*, **58**, 4496–4501, 1973.

[117] R. D. Reynolds and T. Shiozaki. 'Fully relativistic self-consistent field under a magnetic field.' *Physical Chemistry Chemical Physics*, **17**, 14280–14283, 2015.

[118] N. H. F. Beebe and J. Linderberg. 'Simplifications in the generation and transformation of two-electron integrals in molecular calculations.' *International Journal of Quantum Chemistry*, **12**, 683–705, 1977.

[119] F. Aquilante, R. Lindh, and T. B. Pedersen. 'Unbiased auxiliary basis sets for accurate two-electron integral approximations.' *The Journal of Chemical Physics*, **127**, 114107, 2007.

[120] S. Ten-no and S. Iwata. 'Three-center expansion of electron repulsion integrals with linear combination of atomic electron distributions.' *Chemical Physics Letters*, **240**, 578–584, 1995.

[121] S. Ten-no and S. Iwata. 'Multiconfiguration self-consistent field procedure employing linear combination of atomic-electron distributions.' *The Journal of Chemical Physics*, **105**, 3604–3611, 1996.

[122] G. L. Stoychev, A. A. Auer, and F. Neese. 'Automatic Generation of Auxiliary Basis Sets.' *Journal of Chemical Theory and Computation*, **13**, 554–562, 2017.

[123] P. Fuentealba, H. Stoll, L. V. Szentpily, P. Schwerdtfeger, and H. Preuss. 'On the reliability of semi-empirical pseudopotentials: simulation of Hartree-Fock and Dirac-Fock results.' *Journal of Physics B: Atomic and Molecular Physics*, **16**, 323–328, 1983.

[124] R. I. Eglitis, A. V. Postnikov, and G. Borstel. 'Semiempirical Hartree-Fock calculations for KNbO 3.' *Physical Review B*, **54**, 2421–2427, 1996.

[125] A. P. Scott and L. Radom. 'Harmonic Vibrational Frequencies: An Evaluation of Hartree-Fock, Møller-Plesset, Quadratic Configuration Interaction, Density Functional Theory, and Semiempirical Scale Factors.' *The Journal of Physical Chemistry*, **100**, 16502–16513, 1996.

[126] S. Goedecker. 'Linear scaling electronic structure methods.' *Reviews of Modern Physics*, **71**, 1085–1123, 1999.

[127] G. E. Scuseria and P. Y. Ayala. 'Linear scaling coupled cluster and perturbation theories in the atomic orbital basis.' *Journal of Chemical Physics*, **111**, 8330–8343, 1999.

[128] H. Chen and A. Zhou. 'Orbital-Free Density Functional Theory for Molecular Structure Calculations.' *Numerical Mathematics: Theory, Methods and Applications*, **1**, 1–28, 2008.

[129] J. Xia, C. Huang, I. Shin, and E. A. Carter. 'Can orbital-free density functional theory simulate molecules.' *Journal of Chemical Physics*, **136**, 084102, 2012.

[130] W. C. Witt, B. G. D. Rio, J. M. Dieterich, and E. A. Carter. 'Orbital-free density functional theory for materials research.' *Journal of Materials Research*, **33**, 777–795, 2018.

[131] M. S. Ryley, M. Withnall, T. J. Irons, T. Helgaker, and A. M. Teale. 'Robust All-Electron Optimization in Orbital-Free Density-Functional Theory Using the Trust-Region Image Method.' *Journal of Physical Chemistry A*, **125**, 459–475, 2021.

[132] E. B. Starikov, J. P. Lewis, and S. Tanaka. *Modern methods for theoretical physical chemistry of biopolymers*. Elsevier, 2006.

[133] W. Yang. 'Direct calculation of electron density in density-functional theory.' *Physical Review Letters*, **66**, 1438–1441, 1991.

[134] A. Imamura, Y. Aoki, and K. Maekawa. 'A theoretical synthesis of polymers by using uniform localization of molecular orbitals: Proposal of an elongation method.' *The Journal of Chemical Physics*, **95**, 5419–5431, 1991.

[135] G. P. Das, A. T. Yeates, and D. S. Dudis. 'Ab initio fragment orbital-based theory.' *International Journal of Quantum Chemistry*, **92**, 22–28, 2003.

[136] V. Deev and M. A. Collins. 'Approximate ab initio energies by systematic molecular fragmentation.' *Journal of Chemical Physics*, **122**, 2005.

[137] M. Svensson, S. Humbel, R. D. J. Froese, T. Matsubara, S. Sieber, and K. Morokuma. 'ONIOM: A Multilayered Integrated MO + MM Method for Geometry Optimizations and Single Point Energy Predictions. A Test for Diels-Alder Reactions and Pt(P(t-Bu)$_3$)$_2$ + H_2 Oxidative Addition.' *The Journal of Physical Chemistry*, **100**, 19357–19363, 1996.

[138] H. Stoll. 'Correlation energy of diamond.' *Physical Review B*, **46**, 6700–6704, 1992.

[139] D. W. Zhang and J. Z. Zhang. 'Molecular fractionation with conjugate caps for full quantum mechanical calculation of protein-molecule interaction energy.' *Journal of Chemical Physics*, **119**, 3599–3605, 2003.

[140] S. Li, W. Li, and T. Fang. 'An efficient fragment-based approach for predicting the ground-state energies and structures of large molecules.' *Journal of the American Chemical Society*, **127**, 7215–7226, 2005.

[141] K. Kitaura, E. Ikeo, T. Asada, T. Nakano, and M. Uebayasi. 'Fragment Molecular Orbital Method: An Approximate Computational Method For Large Molecules.' *Chemical Physics Letters*, **313**, 701–706, 1999.

[142] K. Kitaura, T. Sawai, T. Asada, T. Nakano, and M. Uebayasi. 'Pair interaction molecular orbital method: an approximate computational method for molecular interactions.' *Chemical Physics Letters*, **312**, 319–324, 1999.

[143] T. Nakano, T. Kaminuma, T. Sato, Y. Akiyama, M. Uebayasi, and K. Kitaura. 'Fragment molecular orbital method: application to polypeptides.' *Chemical Physics Letters*, **318**, 614–618, 2000.

[144] S. Hirata, M. Valiev, M. Dupuis, S. S. Xantheas, S. Sugiki, and H. Sekino. 'Fast electron correlation methods for molecular clusters in the ground and excited states.' *Molecular Physics*, **103**, 2255–2265, 2005.

[145] S. Hirata, K. Gilliard, X. He, J. Li, and O. Sode. 'Ab initio molecular crystal structures, spectra, and phase diagrams.' *Accounts of Chemical Research*, **47**, 2721–2730, 2014.

[146] D. Hankins, J. W. Moskowitz, and F. H. Stillinger. 'Water Molecule Interactions.' *The Journal of Chemical Physics*, **53**, 4544–4554, 1970.

[147] M. J. Elrod and R. J. Saykally. 'Many-Body Effects in Intermolecular Forces.' *Chem. Rev*, **94**, 1975–1997, 1994.

[148] A. D. Kulkarni, V. Ganesh, and S. R. Gadre. 'Many-body interaction analysis: Algorithm development and application to large molecular clusters.' *The Journal of Chemical Physics*, **121**, 5043–5050, 2004.

[149] S. R. Pruitt, C. Bertoni, K. R. Brorsen, and M. S. Gordon. 'Efficient and Accurate Fragmentation Methods.' *Accounts of Chemical Research*, **47**, 2786–2794, 2014.

[150] M. A. Collins and R. P. A. Bettens. 'Energy-Based Molecular Fragmentation Methods.' *Chemical Reviews*, **115**, 5607–5642, 2015.

[151] K. Hermansson. 'Many-body effects in tetrahedral water clusters.' *The Journal of Chemical Physics*, **89**, 2149–2159, 1988.

[152] S. S. Xantheas. 'Significance of higher-order many-body interaction energy terms in water clusters and bulk water.' *Philosophical Magazine B*, **73**, 107–115, 1996.

[153] S. S. Xantheas. 'Cooperativity and hydrogen bonding network in water clusters.' *Journal of Chemical Physics*, **258**, 225–231, 2000.

[154] J. Cui, H. Liu, and K. D. Jordan. 'Theoretical characterization of the $(H_2O)_21$ cluster: Application of an *n*-body decomposition procedure.' *Journal of Physical Chemistry B*, **110**, 18872–18878, 2006.

[155] Y. Chen and H. Li. 'Intermolecular Interaction in Water Hexamer.' *The Journal of Physical Chemistry A*, **114**, 11719–11724, 2010.

[156] K.-Y. Liu and J. M. Herbert. 'Understanding the many-body expansion for large systems. III. Critical role of four-body terms, counterpoise corrections, and cutoffs.' *The Journal of Chemical Physics*, **147**, 161729, 2017.

[157] S. Saha, M. R. Vivek, and G. N. Sastry. 'On the origin of spurious errors in many-body expansion for water cluster.' *Journal of Chemical Sciences*, **129**, 1053–1060, 2017.

[158] J. M. Herbert. 'Fantasy versus reality in fragment-based quantum chemistry.' *Journal of Chemical Physics*, **151**, 2019.

[159] J. D. Cloizeaux. 'Energy Bands and Projection Operators in a Crystal: Analytic and Asymptotic Properties.' *Physical Review*, **135**, A685–A697, 1964.

[160] L. Piela, J.-M. André, J. G. Fripiat, and J. Delhalle. 'On the behaviour of exchange in restricted hartree-fock-roothaan calculations for periodic polymers.' *Chemical Physics Letters*, **77**, 143–150, 1981.

[161] H. J. Monkhorst and M. Kertesz. 'Exact-exchange asymptotics in polymer Hartree-Fock calculations.' *Physical Review B*, **24**, 3015–3024, 1981.

[162] M. J. Gillan, D. Alfè, P. J. Bygrave, C. R. Taylor, and F. R. Manby. 'Energy benchmarks for water clusters and ice structures from an embedded many-body expansion.' *The Journal of Chemical Physics*, **139**, 114101, 2013.

[163] A. Heßelmann. 'Correlation effects and many-body interactions in water clusters.' *Beilstein Journal of Organic Chemistry*, **14**, 979–991, 2018.

[164] W. H. Keesom. 'On the second virial coefficient for di-atomic gases.' *Koninklijke Nederlandse Akademie van Wetenschappen Proceedings Series B Physical Sciences*, **15**, 417–431, 1912.

[165] F. London. 'The general theory of molecular forces.' *Transactions of the Faraday Society*, **33**, 8b, 1937.

[166] P. Debye. 'The van der Waals cohesion forces.' *Physikalische Zeitschrift*, **21**, 178–1877, 1920.

[167] P. Debye. 'Molecular forces and their electric explanation.' *Physikalische Zeitschrift*, **22**, 302–308, 1921.

[168] F. London. 'Zur Theorie und Systematik der Molekularkräfte.' *Zeitschrift für Physik*, **63**, 245–279, 1930.

[169] W. Chen and M. S. Gordon. 'Energy Decomposition Analyses for Many-Body Interaction and Applications to Water Complexes.' *The Journal of Physical Chemistry*, **100**, 14316–14328, 1996.

[170] K. U. Lao, K.-Y. Liu, R. M. Richard, and J. M. Herbert. 'Understanding the many-body expansion for large systems. II. Accuracy considerations.' *The Journal of Chemical Physics*, **144**, 164105, 2016.

[171] J. M. Pedulla, K. Kim, and K. D. Jordan. 'Theoretical study of the n-body interaction energies of the ring, ž / cage and prism forms of $(H_2O)_6$.' *Chemical Physics Letters*, **291**, 78–84, 1998.

[172] M. Kamiya, S. Hirata, and M. Valiev. 'Fast electron correlation methods for molecular clusters without basis set superposition errors.' *Journal of Chemical Physics*, page 074103, 2008.

[173] J. F. Ouyang, M. W. Cvitkovic, and R. P. Bettens. 'Trouble with the many-body expansion.' *Journal of Chemical Theory and Computation*, **10**, 3699–3707, 2014.

[174] R. M. Richard, B. W. Bakr, and C. D. Sherrill. 'Understanding the Many-Body Basis Set Superposition Error: Beyond Boys and Bernardi.' *Journal of Chemical Theory and Computation*, **14**, 2386–2400, 2018.

[175] S. F. Boys and F. Bernardi. 'The calculation of small molecular interactions by the differences of separate total energies. Some procedures with reduced errors.' *Molecular Physics*, **19**, 553–566, 1970.

[176] B. H. Wells and S. Wilson. 'van der Waals interaction potentials: Many-body basis set superposition effects.' *Chemical Physics Letters*, **101**, 429–434, 1983.

[177] L. Turi and J. J. Dannenberg. 'Correcting for basis set superposition error in aggregates containing more than two molecules: ambiguities in the calculation of the counterpoise correction.' *The Journal of Physical Chemistry*, **97**, 2488–2490, 1993.

[178] P. Valiron and I. Mayer. 'Hierarchy of counterpoise corrections for N-body clusters: Generalization of the Boys-Bernardi scheme.' *Chemical Physics Letters*, **275**, 45–55, 1997.

[179] R. M. Richard, K. U. Lao, and J. M. Herbert. 'Approaching the complete-basis limit with a truncated many-body expansion.' *Journal of Chemical Physics*, **139**, 224102, 2013.

[180] R. M. Richard, K. U. Lao, and J. M. Herbert. 'Achieving the CCSD(T) basis-set limit in sizable molecular clusters: Counterpoise corrections for the many-body expansion.' *Journal of Physical Chemistry Letters*, **4**, 2674–2680, 2013.

[181] A. Stone. *The Theory of Intermolecular Forces*. Oxford University Press, 2013.

[182] F. A. Momany. 'Determination of Partial Atomic Charges from Ab Initio Molecular Electrostatic Potentials. Application to Formamide, Methanol, and Formic Acid.' *The Journal of Physical Chemistry*, **82**, 1978.

[183] U. C. Singh and P. A. Kollman. 'An Approach to Computing Electrostatic Charges for Molecules.' *Journal of Computational Chemistry*, **5**, 129–145, 1984.

[184] C. I. Bayly, P. Cieplak, W. Cornell, and P. A. Kollman. 'A well-behaved electrostatic potential based method using charge restraints for deriving atomic charges: the RESP model.' *The Journal of Physical Chemistry*, **97**, 10269–10280, 1993.

[185] R. M. Richard, K. U. Lao, and J. M. Herbert. 'Understanding the many-body expansion for large systems. I. Precision considerations.' *The Journal of Chemical Physics*, **141**, 014108, 2014.

[186] Y. Shao, Z. Gan, E. Epifanovsky, A. T. Gilbert, M. Wormit, J. Kussmann, A. W. Lange, A. Behn, J. Deng, X. Feng, D. Ghosh, M. Goldey, P. R. Horn, L. D. Jacobson, I. Kaliman, R. Z. Khaliullin, T. Kuś, A. Landau, J. Liu, E. I. Proynov, Y. M. Rhee, R. M. Richard, M. A. Rohrdanz, R. P. Steele, E. J. Sundstrom, H. L. Woodcock, P. M. Zimmerman, D. Zuev, B. Albrecht, E. Alguire, B. Austin, G. J. O. Beran, Y. A. Bernard, E. Berquist, K. Brandhorst, K. B. Bravaya, S. T. Brown, D. Casanova, C.-M. Chang, Y. Chen, S. H. Chien, K. D. Closser, D. L. Crittenden, M. Diedenhofen, R. A. DiStasio, H. Do, A. D. Dutoi, R. G. Edgar, S. Fatehi, L. Fusti-Molnar, A. Ghysels, A. Golubeva-Zadorozhnaya, J. Gomes, M. W. Hanson-Heine, P. H. Harbach, A. W. Hauser, E. G. Hohenstein, Z. C. Holden, T.-C. Jagau, H. Ji, B. Kaduk, K. Khistyaev, J. Kim, J. Kim, R. A. King, P. Klunzinger, D. Kosenkov, T. Kowalczyk, C. M. Krauter, K. U. Lao, A. D. Laurent, K. V. Lawler, S. V. Levchenko, C. Y. Lin, F. Liu, E. Livshits, R. C. Lochan, A. Luenser, P. Manohar, S. F. Manzer, S.-P. Mao, N. Mardirossian, A. V. Marenich, S. A. Maurer, N. J. Mayhall, E. Neuscamman, C. M. Oana, R. Olivares-Amaya, D. P. O'Neill, J. A. Parkhill, T. M. Perrine, R. Peverati, A. Prociuk, D. R. Rehn, E. Rosta, N. J. Russ, S. M. Sharada, S. Sharma, D. W. Small, A. Sodt, T. Stein, D. Stück, Y.-C. Su, A. J. Thom, T. Tsuchimochi, V. Vanovschi, L. Vogt, O. Vydrov, T. Wang, M. A. Watson, J. Wenzel, A. White, C. F. Williams, J. Yang, S. Yeganeh, S. R. Yost, Z.-Q. You, I. Y. Zhang, X. Zhang, Y. Zhao, B. R. Brooks, G. K. Chan, D. M. Chipman, C. J. Cramer, W. A. Goddard, M. S. Gordon, W. J. Hehre, A. Klamt, H. F. Schaefer, M. W. Schmidt, C. D. Sherrill, D. G. Truhlar, A. Warshel, X. Xu, A. Aspuru-Guzik, R. Baer, A. T. Bell, N. A. Besley, J.-D. Chai, A. Dreuw, B. D. Dunietz, T. R. Furlani, S. R. Gwaltney, C.-P. Hsu, Y. Jung, J. Kong, D. S. Lambrecht, W. Liang, C. Ochsenfeld, V. A. Rassolov, L. V. Slipchenko, J. E. Subotnik, T. V. Voorhis, J. M. Herbert, A. I. Krylov, P. M. Gill, and M. Head-Gordon. 'Advances in molecular quantum chemistry contained in the Q-Chem 4 program package.' *Molecular Physics*, **113**, 184–215, 2015.

[187] D. M. Bates, J. R. Smith, and G. S. Tschumper. 'Efficient and accurate methods for the geometry optimization of water clusters: Application of analytic gradients for the two-body:many-body QM:QM fragmentation method to $(H_2O)_n$, $n = 3 - 10$.' *Journal of Chemical Theory and Computation*, **7**, 2753–2760, 2011.

[188] R. A. Kendall, T. H. Dunning, and R. J. Harrison. 'Electron affinities of the first-row

atoms revisited. Systematic basis sets and wave functions.' *The Journal of Chemical Physics*, **96**, 6796–6806, 1992.

[189] D. E. Woon and T. H. Dunning. 'Gaussian basis sets for use in correlated molecular calculations. III. The atoms aluminum through argon.' *The Journal of Chemical Physics*, **98**, 1358–1371, 1993.

[190] L. Dalcín, R. Paz, and M. Storti. 'MPI for Python.' *Journal of Parallel and Distributed Computing*, **65**, 1108–1115, 2005.

[191] L. Dalcín, R. Paz, M. Storti, and J. D'Elía. 'MPI for Python: Performance improvements and MPI-2 extensions.' *Journal of Parallel and Distributed Computing*, **68**, 655–662, 2008.

[192] L. D. Dalcin, R. R. Paz, P. A. Kler, and A. Cosimo. 'Parallel distributed computing using Python.' *Advances in Water Resources*, **34**, 1124–1139, 2011.

[193] L. Dalcin and Y. L. L. Fang. 'Mpi4py: Status Update after 12 Years of Development.' *Computing in Science and Engineering*, **23**, 47–54, 2021.

[194] M. P. Forum. 'MPI: A Message-Passing Interface Standard.' *International Journal of Supercomputer Applications*, **8**, 159–416, 1994.

[195] M. Forum. 'A Message Passing Interface Standard.' *High Performance Computing Applications*, **12**, 1–299, 1998.

[196] P. Moritz, R. Nishihara, S. Wang, A. Tumanov, R. Liaw, E. Liang, M. Elibol, Z. Yang, W. Paul, M. I. Jordan, and I. Stoica. 'Ray: A Distributed Framework for Emerging AI Applications.' In '13th USENIX Symposium on Operating Systems Design and Implementation (OSDI 18),' pages 561–577. USENIX Association, Carlsbad, CA, 2018.

[197] A. J. Cohen, P. Mori-Sánchez, and W. Yang. 'Insights into current limitations of density functional theory.' *Science*, **321**, 792–794, 2008.

[198] A. J. Stone. 'Electrostatic Damping Functions and the Penetration Energy.' *The Journal of Physical Chemistry A*, **115**, 7017–7027, 2011.

[199] S. S. Xantheas and T. H. Dunning. '*Ab intio* studies of cyclic water clusters $(H2O)_n$, n=1-6. I. Optimal structures and vibrational spectra.' *The Journal of Chemical Physics*, **99**, 8774–8792, 1993.

[200] S. S. Xantheas. '*Ab initio* studies of cyclic water clusters $(H2O)_n$, n=1-6. II. Analysis of many-body interactions.' *The Journal of Chemical Physics*, **100**, 7523–7534, 1994.

[201] C. J. Burnham and S. S. Xantheas. 'Development of transferable interaction models for water. IV. A flexible, all-atom polarizable potential (TTM2-F) based on geometry dependent charges derived from an ab initio monomer dipole moment surface.' *Journal of Chemical Physics*, **116**, 5115–5124, 2002.

[202] S. S. Xantheas, C. J. Burnham, and R. J. Harrison. 'Development of transferable interaction models for water. II. Accurate energetics of the first few water clusters from first principles.' *Journal of Chemical Physics*, **116**, 1493–1499, 2002.

[203] W. L. Jorgensen, J. Chandrasekhar, J. D. Madura, R. W. Impey, and M. L. Klein. 'Comparison of simple potential functions for simulating liquid water.' *The Journal of Chemical Physics*, **79**, 926–935, 1983.

[204] E. Neria, S. Fischer, and M. Karplus. 'Simulation of activation free energies in molecular systems.' *The Journal of Chemical Physics*, **105**, 1902–1921, 1996.

[205] I. T. Todorov, W. Smith, K. Trachenko, and M. T. Dove. 'DLPOLY.' *Journal of Materials Chemistry*, **16**, 1911–1918, 2006.

[206] T. H. Dunning. 'Gaussian basis sets for use in correlated molecular calculations. I. The atoms boron through neon and hydrogen.' *The Journal of Chemical Physics*, **90**, 1007–1023, 1989.

[207] T. Ishikawa. 'Ab initio quantum chemical calculation of electron density, electrostatic potential, and electric field of biomolecule based on fragment molecular orbital method.' *International Journal of Quantum Chemistry*, **118**, 2018.

[208] K. Kitaura, S. I. Sugiki, T. Nakano, Y. Komeiji, and M. Uebayasi. 'Fragment molecular orbital method: Analytical energy gradients.' *Chemical Physics Letters*, pages 163–170, 2001.

[209] T. Nagata, D. G. Fedorov, and K. Kitaura. 'Derivatives of the approximated electrostatic potentials in the fragment molecular orbital method.' *Chemical Physics Letters*, **475**, 124–131, 2009.

[210] J. Baker. 'Techniques for geometry optimization: A comparison of cartesian and natural internal coordinates.' *Journal of Computational Chemistry*, **14**, 1085–1100, 1993.

[211] J. Baker and F. Chan. 'The location of transition states: A comparison of Cartesian, Z-matrix, and natural internal coordinates.' *Journal of Computational Chemistry*, **17**, 888–904, 1996.

[212] H. B. Schlegel. 'Optimization of Equilibrium Geometries and Transition Structures.' In 'Advances in Chemical Physics,' chapter 4, pages 249–286. John Wiley & Sons, Ltd, 1987.

[213] H. P. Hratchian and H. B. Schlegel. 'Finding Minima, Transition States, and Following Reaction Pathways on ab initio Potential Energy Surfaces.' In C. Dykstra (editor), 'Theory and Applications of Computational Chemistry,' pages 195–249. Elsevier, 2005.

[214] B. A. Murtagh and R. W. H. Sargent. 'A Constrained Minimization Method With Quadratic Convergence.' In R. Fletcher (editor), 'Optimization,' pages 215–246. Academic Press New York, 1969.

[215] R. Fletcher and M. J. D. Powell. 'A Rapidly Convergent Descent Method for Minimization.' *The Computer Journal*, **6**, 163–168, 1963.

[216] C. G. Broyden. 'The Convergence of a Class of Double-rank Minimization Algorithms 1. General Considerations.' *IMA Journal of Applied Mathematics*, **6**, 76–90, 1970.

[217] C. G. Broyden. 'The Convergence of a Class of Double-rank Minimization Algorithms.' *IMA Journal of Applied Mathematics*, **6**, 222–231, 1970.

[218] R. Fletcher. 'A new approach to variable metric algorithms.' *The Computer Journal*, **13**, 317–322, 1970.

[219] D. Goldfarb. 'A family of variable-metric methods derived by variational means.' *Mathematics of Computation*, **24**, 23–26, 1970.

[220] D. F. Shanno. 'Conditioning of quasi-Newton methods for function minimization.' *Mathematics of Computation*, **24**, 647–656, 1970.

[221] T. Culpitt, L. D. M. Peters, E. I. Tellgren, and T. Helgaker. '*Ab initio* molecular dynamics with screened Lorentz forces. I. Calculation and atomic charge interpretation of Berry curvature.' *The Journal of Chemical Physics*, **155**, 024104, 2021.

[222] L. D. M. Peters, T. Culpitt, L. Monzel, E. I. Tellgren, and T. Helgaker. '*Ab Initio* molecular dynamics with screened Lorentz forces. II. Efficient propagators and rovibrational spectra in strong magnetic fields.' *The Journal of Chemical Physics*, **155**, 024105, 2021.

[223] T. Culpitt, L. D. M. Peters, E. I. Tellgren, and T. Helgaker. 'Analytic calculation of the Berry curvature and diagonal Born–Oppenheimer correction for molecular systems in uniform magnetic fields.' *The Journal of Chemical Physics*, **156**, 044121, 2022.

[224] L. Monzel, A. Pausch, L. D. M. Peters, E. I. Tellgren, T. Helgaker, and W. Klopper. 'Molecular dynamics of linear molecules in strong magnetic fields.' *The Journal of Chemical Physics*, **157**, 054106, 2022.

[225] P. Lazzeretti. 'Ring currents.' *Progress in Nuclear Magnetic Resonance Spectroscopy*, **36**, 1–88, 2000.

[226] D. Sundholm, H. Fliegl, and R. J. Berger. 'Calculations of magnetically induced current densities: theory and applications.' *WIREs Computational Molecular Science*, **6**, 639–678, 2016.

[227] J. Pople. 'Molecular orbital theory of aromatic ring currents.' *Molecular Physics*, **1**, 175–180, 1958.

[228] R. McWeeny. 'Ring currents and proton magnetic resonance in aromatic molecules.' *Molecular Physics*, **1**, 311–321, 1958.

[229] R. A. Hegstrom and W. N. Lipscomb. 'Magnetic Properties of the BH Molecule.' *The Journal of Chemical Physics*, **45**, 2378–2383, 1966.

[230] J. A. N. F. Gomes. 'Topological elements of the magnetically induced orbital current densities.' *The Journal of Chemical Physics*, **78**, 4585–4591, 1983.

[231] J. A. N. F. Gomes. 'Topology of the electronic current density in molecules.' *Physical Review A*, **28**, 559–566, 1983.

[232] T. A. Keith and R. F. W. Bader. 'Topological analysis of magnetically induced molecular current distributions.' *The Journal of Chemical Physics*, **99**, 3669–3682, 1993.

[233] J. Jusélius, D. Sundholm, and J. Gauss. 'Calculation of current densities using gauge-including atomic orbitals.' *The Journal of Chemical Physics*, **121**, 3952–3963, 2004.

[234] H. Fliegl, S. Taubert, O. Lehtonen, and D. Sundholm. 'The gauge including magnetically induced current method.' *Physical Chemistry Chemical Physics*, **13**, 20500, 2011.

[235] J. W. Furness, U. Ekström, T. Helgaker, and A. M. Teale. 'Electron localisation function in current-density-functional theory.' *Molecular Physics*, **114**, 1415–1422, 2016.

[236] S. Pelloni, A. Ligabue, and P. Lazzeretti. 'Ring-Current Models from the Differential Biot-Savart Law.' *Organic Letters*, **6**, 4451–4454, 2004.

[237] E. Goll, M. Ernst, F. Moegle-Hofacker, and H. Stoll. 'Development and assessment of a short-range meta-GGA functional.' *The Journal of Chemical Physics*, **130**, 234112, 2009.

[238] P. Mori-Sánchez, A. J. Cohen, and W. Yang. 'Many-electron self-interaction error in approximate density functionals.' *The Journal of Chemical Physics*, **125**, 201102, 2006.

[239] J. Cao, G. London, O. Dumele, M. von Wantoch Rekowski, N. Trapp, L. Ruhlmann, C. Boudon, A. Stanger, and F. Diederich. 'The Impact of Antiaromatic Subunits in [4 *n* +2] π-Systems: Bispentalenes with [4 *n* +2] π-Electron Perimeters and Antiaromatic Character.' *Journal of the American Chemical Society*, **137**, 7178–7188, 2015.

[240] G. V. Baryshnikov, N. N. Karaush, R. R. Valiev, and B. F. Minaev. 'Aromaticity of the completely annelated tetraphenylenes: NICS and GIMIC characterization.' *Journal of Molecular Modeling*, **21**, 136, 2015.

[241] G. V. Baryshnikov, R. R. Valiev, N. N. Karaush, D. Sundholm, and B. F. Minaev. 'Aromaticity of the doubly charged [8]circulenes.' *Physical Chemistry Chemical Physics*, **18**, 8980–8992, 2016.

[242] H. Fliegl, D. Sundholm, S. Taubert, J. Jusélius, and W. Klopper. 'Magnetically Induced Current Densities in Aromatic, Antiaromatic, Homoaromatic, and Nonaromatic Hydrocarbons.' *The Journal of Physical Chemistry A*, **113**, 8668–8676, 2009.

[243] S. Taubert, D. Sundholm, and F. Pichierri. 'Magnetically Induced Currents in Bianthraquinodimethane-Stabilized Möbius and Hückel [16]Annulenes.' *The Journal of Organic Chemistry*, **74**, 6495–6502, 2009.

[244] H. Fliegl, D. Sundholm, S. Taubert, and F. Pichierri. 'Aromatic Pathways in Twisted Hexaphyrins.' *The Journal of Physical Chemistry A*, **114**, 7153–7161, 2010.

[245] H. Fliegl, O. Lehtonen, D. Sundholm, and V. R. I. Kaila. 'Hydrogen-bond strengths by magnetically induced currents.' *Physical Chemistry Chemical Physics*, **13**, 434–437, 2011.

[246] T. K. Dickens, R. B. Mallion, and S. Radenković. 'Assessing the Extent of π-Electron Delocalization in Naphtho-Annelated Fluoranthenes by Means of Topological Ring-Currents.' *The Journal of Physical Chemistry A*, **123**, 1445–1450, 2019.

[247] G. Monaco, P. D. Porta, M. Jabłoński, and R. Zanasi. 'Topology of the magnetically induced current density and proton magnetic shielding in hydrogen bonded systems.' *Physical Chemistry Chemical Physics*, **17**, 5966–5972, 2015.

[248] P. D. Porta, R. Zanasi, and G. Monaco. 'Hydrogen-hydrogen bonding: The current density perspective.' *Journal of Computational Chemistry*, **36**, 707–716, 2015.

[249] S. Pelloni, F. Faglioni, R. Zanasi, and P. Lazzeretti. 'Topology of magnetic-field-induced current-density field in diatropic monocyclic molecules.' *Physical Review A*, **74**, 012506, 2006.

[250] S. Pelloni, P. Lazzeretti, and R. Zanasi. 'Topological models of magnetic field induced current density field in small molecules.' *Theoretical Chemistry Accounts*, **123**, 353–364, 2009.

[251] P. Lazzeretti. 'Topological definition of ring currents.' *Physical Chemistry Chemical Physics*, **18**, 11765–11771, 2016.

[252] P. Davis and P. Rabinowitz. *Mathematics of Numerical Integration*. Dover Publications, 2007.

[253] S. Elhay and J. Kautsky. 'Algorithm 655.' *ACM Transactions on Mathematical Software*, **13**, 399–415, 1987.

[254] J. P. Perdew, K. Burke, and M. Ernzerhof. 'Generalized Gradient Approximation Made Simple.' *Physical Review Letters*, **77**, 3865–3868, 1996.

[255] C. Adamo and V. Barone. 'Toward reliable density functional methods without adjustable parameters: The PBE0 model.' *The Journal of Chemical Physics*, **110**, 6158–6170, 1999.

[256] B. I. Dunlap, J. W. D. Connolly, and J. R. Sabin. 'On some approximations in applications of $X\alpha$ theory.' *The Journal of Chemical Physics*, **71**, 3396–3402, 1979.

[257] B. I. Dunlap, J. W. D. Connolly, and J. R. Sabin. 'On first-row diatomic molecules and local density models.' *The Journal of Chemical Physics*, **71**, 4993, 1979.

[258] M. Guidon, J. Hutter, and J. VandeVondele. 'Auxiliary Density Matrix Methods for Hartree-Fock Exchange Calculations.' *Journal of Chemical Theory and Computation*, **6**, 2348–2364, 2010.

[259] P. Merlot, R. Izsák, A. Borgoo, T. Kjærgaard, T. Helgaker, and S. Reine. 'Charge-constrained auxiliary-density-matrix methods for the Hartree–Fock exchange contribution.' *The Journal of Chemical Physics*, **141**, 094104, 2014.

[260] LSDalton. 'A linear scaling molecular electronic structure program, Release v2018.2 (2018), see http://daltonprogram.org.'

[261] K. Aidas, C. Angeli, K. L. Bak, V. Bakken, R. Bast, L. Boman, O. Christiansen, R. Cimiraglia, S. Coriani, P. Dahle, E. K. Dalskov, U. Ekström, T. Enevoldsen, J. J. Eriksen, P. Ettenhuber, B. Fernández, L. Ferrighi, H. Fliegl, L. Frediani, K. Hald, A. Halkier, C. Hättig, H. Heiberg, T. Helgaker, A. C. Hennum, H. Hettema, E. Hjertenaes, S. Høst, I.-M. Høyvik, M. F. Iozzi, B. Jansík, H. J. A. Jensen, D. Jonsson, P. Jørgensen, J. Kauczor, S. Kirpekar, T. Kjaergaard, W. Klopper, S. Knecht, R. Kobayashi, H. Koch, J. Kongsted, A. Krapp, K. Kristensen, A. Ligabue, O. B. Lutnaes, J. I. Melo, K. V. Mikkelsen, R. H. Myhre, C. Neiss, C. B. Nielsen, P. Norman, J. Olsen, J. M. H. Olsen, A. Osted, M. J. Packer, F. Pawlowski, T. B. Pedersen, P. F. Provasi, S. Reine, Z. Rinkevicius, T. A. Ruden, K. Ruud, V. V. Rybkin, P. Sałek, C. C. M. Samson, A. S. de Merás, T. Saue, S. P. A. Sauer, B. Schimmelpfennig, K. Sneskov, A. H. Steindal, K. O. Sylvester-Hvid, P. R. Taylor, A. M. Teale, E. I. Tellgren, D. P. Tew, A. J. Thorvaldsen, L. Thøgersen, O. Vahtras, M. A. Watson, D. J. D. Wilson, M. Ziolkowski, and H. Ågren. 'The Dalton quantum chemistry program system.' *Wiley Interdisciplinary Reviews: Computational Molecular Science*, **4**, 269–284, 2014.

[262] D. Sundholm, R. J. F. Berger, and H. Fliegl. 'Analysis of the magnetically induced current density of molecules consisting of annelated aromatic and antiaromatic hydrocarbon rings.' *Physical Chemistry Chemical Physics*, **18**, 15934–15942, 2016.

[263] W. An, Y. Gao, S. Bulusu, and X. C. Zeng. '*Ab Initio* calculation of bowl, cage, and ring isomers of C20 and C20-.' *The Journal of Chemical Physics*, **122**, 204109, 2005.

[264] S. Grimme and C. Mück-Lichtenfeld. 'Structural isomers of C20 revisited: the cage and bowl are almost isoenergetic.' *Chemphyschem : a European journal of chemical physics and physical chemistry*, **3**, 207–9, 2002.

[265] Y. Jin, A. Perera, V. F. Lotrich, and R. J. Bartlett. 'Coupled cluster geometries and energies of C20 carbon cluster isomers – A new benchmark study.' *Chemical Physics Letters*, **629**, 76–80, 2015.

[266] R. Papadakis and H. Ottosson. 'The excited state antiaromatic benzene ring: a molecular Mr Hyde?' *Chemical Society Reviews*, **44**, 6472–6493, 2015.

[267] N. C. Baird. 'Quantum organic photochemistry. II. Resonance and aromaticity in the lowest $^3\pi\pi^*$ state of cyclic hydrocarbons.' *Journal of the American Chemical Society*, **94**, 4941–4948, 1972.

[268] B. T. Phong. 'Graphics and Illumination for Computer Generated Pictures.' *Communications of the ACM*, **18**, 311–317, 1975.

[269] J. F. Blinn. 'Models of light reflection for computer synthesized pictures.' pages 192–198. ACM Press, 1977.

[270] N. M. O'Boyle, M. Banck, C. A. James, C. Morley, T. Vandermeersch, and G. R. Hutchison. 'Open Babel: An open chemical toolbox.' *Journal of Cheminformatics*, **3**, 33, 2011.

[271] J. Wang, R. M. Wolf, J. W. Caldwell, P. A. Kollman, and D. A. Case. 'Development and testing of a general amber force field.' *Journal of Computational Chemistry*, **25**, 1157–1174, 2004.

[272] T. A. Halgren. 'Merck molecular force field. I. Basis, form, scope, parameterization, and performance of MMFF94.' *Journal of Computational Chemistry*, **17**, 490–519, 1996.

[273] T. A. Halgren. 'Merck molecular force field. II. MMFF94 van der Waals and electrostatic parameters for intermolecular interactions.' *Journal of Computational Chemistry*, **17**, 520–552, 1996.

[274] T. A. Halgren. 'Merck molecular force field. III. Molecular geometries and vibrational frequencies for MMFF94.' *Journal of Computational Chemistry*, **17**, 553–586, 1996.

[275] T. A. Halgren and R. B. Nachbar. 'Merck molecular force field. IV. conformational energies and geometries for MMFF94.' *Journal of Computational Chemistry*, **17**, 587–615, 1996.

[276] T. A. Halgren. 'Merck molecular force field. V. Extension of MMFF94 using experimental data, additional computational data, and empirical rules.' *Journal of Computational Chemistry*, **17**, 616–641, 1996.

[277] T. A. Halgren. 'MMFF VI. MMFF94s option for energy minimization studies.' *Journal of Computational Chemistry*, **20**, 720–729, 1999.

[278] T. A. Halgren. 'MMFF VII. Characterization of MMFF94, MMFF94s, and other widely available force fields for conformational energies and for intermolecular-interaction energies and geometries.' *Journal of Computational Chemistry*, **20**, 730–748, 1999.

[279] A. K. Rappe, C. J. Casewit, K. S. Colwell, W. A. Goddard, and W. M. Skiff. 'UFF, a full periodic table force field for molecular mechanics and molecular dynamics simulations.' *Journal of the American Chemical Society*, **114**, 10024–10035, 1992.

[280] W. E. Lorensen and H. E. Cline. 'Marching Cubes: A High Resolution 3D Surface Construction Algorithm.' *ACM SIGGRAPH Computur Graphics*, **21**(4), 163–169, 1987.

[281] L. R. Herrmann. 'Laplacian-Isoparametric Grid Generation Scheme.' *Journal of the Engineering Mechanics Division*, **102**, 749–756, 1976.

[282] O. Sorkine, D. Cohen-Or, Y. Lipman, M. Alexa, C. Rössl, and H.-P. Seidel. 'Laplacian surface editing.' page 175. ACM Press, 2004.

[283] O. B. Lutnæs, A. M. Teale, T. Helgaker, D. J. Tozer, K. Ruud, and J. Gauss. 'Benchmarking density-functional-theory calculations of rotational g tensors and magnetizabilities using accurate coupled-cluster calculations.' *The Journal of Chemical Physics*, **131**, 144104, 2009.

[284] A. M. Teale, O. B. Lutnæs, T. Helgaker, D. J. Tozer, and J. Gauss. 'Benchmarking density-functional theory calculations of NMR shielding constants and spin–rotation constants using accurate coupled-cluster calculations.' *The Journal of Chemical Physics*, **138**, 024111, 2013.

[285] J. Tomasi, B. Mennucci, and E. Cancès. 'The IEF version of the PCM solvation method: an overview of a new method addressed to study molecular solutes at the QM ab initio level.' *Journal of Molecular Structure: THEOCHEM*, **464**, 211–226, 1999.

[286] J. Tomasi, B. Mennucci, and R. Cammi. 'Quantum Mechanical Continuum Solvation Models.' *Chemical Reviews*, **105**, 2999–3094, 2005.

[287] J. Tomasi, E. Cancés, C. S. Pomeli, M. Caricato, G. Scalmani, M. J. Frisch, R. Cammi, M. V. Basilevsky, G. N. Chuev, and B. Mennucci. 'Modern Theories of Continuum Models.' In B. Mennucci and R. Cammi (editors), 'Continuum Solvation Models in Chemical Physics: From Theory to Applications,' John Wiley & Sons Ltd, 2008.

[288] V. Weijo, B. Mennucci, and L. Frediani. 'Toward a General Formulation of Dispersion Effects for Solvation Continuum Models.' *Journal of Chemical Theory and Computation*, **6**, 3358–3364, 2010.

[289] J. D. Hartman, R. A. Kudla, G. M. Day, L. J. Mueller, and G. J. Beran. 'Benchmark fragment-based 1H, 13C, 15N and 17O chemical shift predictions in molecular crystals.' *Physical Chemistry Chemical Physics*, **18**, 21686–21709, 2016.

[290] S. T. Holmes, R. J. Iuliucci, K. T. Mueller, and C. Dybowski. 'Density functional investigation of intermolecular effects on 13C NMR chemical-shielding tensors modeled with molecular clusters.' *Journal of Chemical Physics*, **141**, 164121, 2014.

[291] J. D. Hartman, S. Monaco, B. Schatschneider, and G. J. O. Beran. ' Fragment-based 13 C nuclear magnetic resonance chemical shift predictions in molecular crystals: An alternative to planewave methods .' *The Journal of Chemical Physics*, **143**, 102809, 2015.

[292] J. D. Hartman and G. J. Beran. 'Fragment-based electronic structure approach for computing nuclear magnetic resonance chemical shifts in molecular crystals.' *Journal of Chemical Theory and Computation*, **10**, 4862–4872, 2014.

[293] V. A. Semenov, D. O. Samultsev, and L. B. Krivdin. 'Solvent effects in the GIAO-DFT calculations of the15N NMR chemical shifts of azoles and azines.' *Magnetic Resonance in Chemistry*, **52**, 686–693, 2014.

[294] T. W. Keal and D. J. Tozer. 'A semiempirical generalized gradient approximation exchange-correlation functional.' *The Journal of Chemical Physics*, **121**, 5654–5660, 2004.

[295] F. Jensen. 'Polarization consistent basis sets: Principles.' *The Journal of Chemical Physics*, **115**, 9113–9125, 2001.

[296] F. Jensen. 'Erratum: "Polarization consistent basis sets: Principles" .' *The Journal of Chemical Physics*, **116**, 3502–3502, 2002.

[297] F. Jensen. 'Polarization consistent basis sets. II. Estimating the Kohn-Sham basis set limit.' *The Journal of Chemical Physics*, **116**, 7372–7379, 2002.

[298] F. Jensen. 'Polarization consistent basis sets. III. The importance of diffuse functions.' *The Journal of Chemical Physics*, **117**, 9234–9240, 2002.

[299] F. Jensen and T. Helgaker. 'Polarization consistent basis sets. V. The elements Si-Cl.' *The Journal of Chemical Physics*, **121**, 3463–3470, 2004.

[300] F. Jensen. 'Polarization Consistent Basis Sets. 4: The Elements He, Li, Be, B, Ne, Na, Mg, Al, and Ar.' *The Journal of Physical Chemistry A*, **111**, 11198–11204, 2007.

[301] R. K. Harris, E. D. Becker, S. M. C. de Menezes, R. Goodfellow, and P. Granger. 'NMR nomenclature. Nuclear spin properties and conventions for chemical shifts(IUPAC Recommendations 2001).' *Pure and Applied Chemistry*, **73**, 1795–1818, 2001.

[302] R. K. Harris, E. D. Becker, S. M. C. D. Menezes, P. Granger, R. E. Hoffman, and K. W. Zilm. 'Further Conventions for NMR Shielding and Chemical Shifts (IUPAC Recommendations 2008).' *Magnetic Resonance in Chemistry*, **46**, 582–598, 2008.

[303] C. J. Jameson, A. K. Jameson, D. Oppusunggu, S. Wille, P. M. Burrell, and J. Mason. '^{15}N nuclear magnetic shielding scale from gas phase studies.' *The Journal of Chemical Physics*, **74**, 81–88, 1981.

[304] J. J. Goings, P. J. Lestrange, and X. Li. 'Real-time time-dependent electronic structure theory.' *WIREs Computational Molecular Science*, **8**, 2018.

[305] X. Li, N. Govind, C. Isborn, A. E. DePrince, and K. Lopata. 'Real-Time Time-Dependent Electronic Structure Theory.' *Chemical Reviews*, **120**, 9951–9993, 2020.

[306] E. Runge and E. K. U. Gross. 'Density-Functional Theory for Time-Dependent Systems.' *Physical Review Letters*, **52**, 997–1000, 1984.

[307] M. E. Casida. 'Time-Dependent Density Functional Response Theory for Molecules.' In 'Recent Advances in Density Functional Methods,' pages 155–192, 1995.

[308] M. Petersilka, U. J. Gossmann, and E. K. U. Gross. 'Excitation Energies from Time-Dependent Density-Functional Theory.' *Physical Review Letters*, **76**, 1212–1215, 1996.

[309] S. Sen, K. K. Lange, and E. I. Tellgren. 'Excited States of Molecules in Strong Uniform and Nonuniform Magnetic Fields.' *Journal of Chemical Theory and Computation*, **15**, 3974–3990, 2019.

[310] S. Sun, D. Williams-Young, and X. Li. 'An ab Initio Linear Response Method for Computing Magnetic Circular Dichroism Spectra with Nonperturbative Treatment of Magnetic Field.' *Journal of Chemical Theory and Computation*, **15**, 3162–3169, 2019.

[311] W. Cai and G. Galli. 'Ab Initio Calculations in a Uniform Magnetic Field Using Periodic Supercells.' *Physical Review Letters*, **92**, 186402, 2004.

[312] E. Lee, W. Cai, and G. A. Galli. 'Electronic structure calculations in a uniform magnetic field using periodic supercells.' *Journal of Computational Physics*, **226**, 1310–1331, 2007.

[313] X. He, O. Sode, S. S. Xantheas, and S. Hirata. 'Second-order many-body perturbation study of ice Ih.' *Journal of Chemical Physics*, page 204505, 2012.

[314] K. Gilliard, O. Sode, and S. Hirata. 'Second-order many-body perturbation and coupled-cluster singles and doubles study of ice VIII.' *Journal of Chemical Physics*, **140**, 174507, 2014.

[315] S. Hirata. 'Quantum chemistry of macromolecules and solids.' *Physical Chemistry Chemical Physics*, **11**, 8397–8412, 2009.

[316] S. Hirata. 'Fast electron-correlation methods for molecular crystals: An application to the α, $\beta 1$, and $\beta 2$ modifications of solid formic acid.' *Journal of Chemical Physics*, **129**, 204104, 2008.

[317] O. Sode and S. Hirata. 'Second-order many-body perturbation study of solid hydrogen fluoride.' *Journal of Physical Chemistry A*, **114**, 8873–8877, 2010.

[318] O. Sode and S. Hirata. 'Second-order many-body perturbation study of solid hydrogen fluoride under pressure.' *Physical Chemistry Chemical Physics*, **14**, 7765–7779, 2012.

[319] T. Fujita, T. Nakano, and S. Tanaka. 'Fragment molecular orbital calculations under periodic boundary condition.' *Chemical Physics Letters*, **506**, 112–116, 2011.

[320] S. Wen and G. J. O. Beran. 'Accidental Degeneracy in Crystalline Aspirin: New Insights from High-Level ab Initio Calculations.' *Crystal Growth & Design*, **12**, 2169–2172, 2012.

[321] R. J. Hemley. 'The element of uncertainty.' *Nature*, **404**, 240–241, 2000.

[322] R. J. Hemley. 'Effects of High Pressure on Molecules.' *Annual Review of Physical Chemistry*, **51**, 763–800, 2000.

[323] C. G. Salzmann, P. G. Radaelli, B. Slater, and J. L. Finney. 'The polymorphism of ice: five unresolved questions.' *Physical Chemistry Chemical Physics*, **13**, 18468, 2011.

[324] M. Santoro and F. A. Gorelli. 'High pressure solid state chemistry of carbon dioxide.' *Chemical Society Reviews*, **35**, 918, 2006.

[325] J. M. McMahon, M. A. Morales, C. Pierleoni, and D. M. Ceperley. 'The properties of hydrogen and helium under extreme conditions.' *Reviews of Modern Physics*, **84**, 1607–1653, 2012.

[326] L. Lieserowitz and J. Stoddart. 'Molecular crystals.' *Current Opinion in Solid State and Materials Science*, **3**, 397–398, 1998.

[327] E. Blount. 'Formalisms of Band Theory.' volume 13 of *Solid State Physics*, pages 305–373. Academic Press, 1962.

[328] R. Resta. 'Macroscopic polarization in crystalline dielectrics: the geometric phase approach.' *Reviews of Modern Physics*, **66**, 899–915, 1994.

[329] R. Podeszwa, B. M. Rice, and K. Szalewicz. 'Predicting Structure of Molecular Crystals from First Principles.' *Physical Review Letters*, **101**, 115503, 2008.

[330] M. A. Collins. '*Ab initio* lattice dynamics of nonconducting crystals by systematic fragmentation.' *The Journal of Chemical Physics*, **134**, 164110, 2011.

[331] H. Stoll. 'On the correlation energy of graphite.' *The Journal of Chemical Physics*, **97**, 8449–8454, 1992.

[332] H. Stoll, B. Paulus, and P. Fulde. 'An incremental coupled-cluster approach to metallic lithium.' *Chemical Physics Letters*, **469**, 90–93, 2009.

[333] J. Gräfenstein, H. Stoll, and P. Fulde. 'Computation of the valence band of diamond by means of local increments.' *Chemical Physics Letters*, **215**, 611–616, 1993.